Development of subgrid models for a periodic circulating fluidized bed of binary mixture of particles

Solène Chevrier

▶ To cite this version:

Solène Chevrier. Development of subgrid models for a periodic circulating fluidized bed of binary mixture of particles. Fluid Dynamics [physics.flu-dyn]. Institut National Polytechnique de Toulouse - INPT, 2017. English. NNT : 2017INPT0072 . tel-04223134

HAL Id: tel-04223134
https://theses.hal.science/tel-04223134

Submitted on 29 Sep 2023

THÈSE

En vue de l'obtention du

DOCTORAT DE L'UNIVERSITÉ DE TOULOUSE

Délivré par :

Institut National Polytechnique de Toulouse (INP Toulouse)

Discipline ou spécialité :

Dynamique des fluides

Présentée et soutenue par :

Mme SOLENE CHEVRIER
le mardi 11 juillet 2017

Titre :

Développement de modèle de sous-maille pour la simulation numérique d'un écoulement polydisperse réactif

---

Ecole doctorale :
Mécanique, Energétique, Génie civil, Procédés (MEGeP)

Unité de recherche :
Institut de Mécanique des Fluides de Toulouse (I.M.F.T.)

Directeur(s) de Thèse :
M. OLIVIER SIMONIN
M. PASCAL FEDE

Rapporteurs :
M. JURAY DE WILDE, UNIVERSITE CATHOLIQUE DE LOUVAIN
M. SIMON SCHNEIDERBAUER, JOHANNES KEPLER UNIVERSITAT

Membre(s) du jury :
M. LOUIS JESTIN, UNIVERSITY OF CAPE TOWN, Président
Mme RIM BRAHEM, IFPEN, Membre
M. OLIVIER SIMONIN, INP TOULOUSE, Membre
M. PASCAL FEDE, UNIVERSITE TOULOUSE 3, Membre

Acknowledgements

Ce travail de thèse a été réalisée au sein de l'Institut de Mécanique des Fluides de Toulouse, dans le groupe Particule, Spray et Combustion et rendue possible grâce au financement du projet europén du projet NANOSIM. Je souhaite adresser mes remerciements aux nombreuses personnes qui ont contribuées directement ou indirectement à la réalisation de cette thèse.

Je tiens à remercier tout d'abord Olivier Simonin pour les discussions scientifiques passionnantes et très instructives que nous avons pu avoir ensemble. J'adresse aussi mes remerciements à Pascal Fede pour toute l'aide donnée sur les simulations, le post-traitement, ainsi que toutes les corrections et et conseils, qui m'ont permis de progresser.

Je souhaite remercier les membres du jury, Simon Schneuderbauer, Juray De Wilde, Shahriar Amini, Rim Brahem et Louis Jestin, d'avoir accepté d'évaluer mon travail ainsi que pour les discussions très intéressantes qui s'en sont suivies.

J'adresse aussi mes remerciements à Herve Neau, pour son soutien, ses dicussions et ses conseils avisés. Je souhaite remercier Enrica Masi pour tout le temps qu'elle a consacré à m'expliquer le filtrage.

Je souhaite ǵalement citer la contribution non négligeable des différents services techniques et administratifs de l'IMFT. Ici, je remercie tout particulièrement notre gestionnaire de groupe, Florence Colombiès.

Cette thèse m'a également permis de profiter de la bonne ambiance du groupe PSC, et je souhaite remercier l'ensemble des doctorants, post doctorants et stagiaires.
Je remercie les personnes avec lesquelles j'ai partagé le bureau : Blaise Delmotte, Adama Creppy, Lucas Baldo, Nicolas Reuge, Corentin Lapeyre, pour la relecture et les conseils, Salvatore Lovecchio, pour tes superbes expressions, Azeddine Rachih (Tchik-Tchik), pour les discussions philosophiques, Ivan Alt, Ainur Nigmetova et Asmaa Aissaoui, pour les blagues, les gateaux, les discussions multi-culturelles.
Je tiens aussi à remercier Amine Chadil, Christian Kraus, Diane Dherbecourt, Duc Le Hong, Ibrahima Thiam, Guiqan Wang, Jeanot , Lokman Bennani, Nicolas Morolin, Maxence Brebion, Quentin Douasbin, Valentin Gosselin, Thomas Kaiser, Bastien Polizzi pour les conseils de derniéres minutes, Abdulla Ghani, Emanuelle Tinon, Gorkem Oztarlik, Oliver Scorsim, Wenchao Yu, Mostafa Sulaiman, Princesse Praline (Pradip Xavier) pour ta

bonne humeur contagieuse. Je souhaite remercier mes camarades de thèse , Ziad Hammidouche et Framboise (François Audard), fier représentant de la gastronomie du sud-ouest et organisateur hors-pair de repas et barbecues. Merci pour les bons moments, les doutes et les succès partagés qui ont rythmés cette thèse et qui resteront dans ma mémoire.

Je tiens aussi à remercier ma famille et à mes amis, Amandine (soirées raviolis!!), Fanny, Geoffrey (un petit café plus tard), MC (vive le jardin des plantes), Elaine (pour ton accueil, et ton sourire).

Pour conclure ces remerciements, je tiens à remercier Vincent, qui m'a soutenu durant toute cette thése et qui m'a beaucoup apporté (y compris des pancakes pendant la rédaction).

Abstract

Keywords: *chemical looping combustion, fluidized beds, subgrid models, drag force, collision.*

Detailed sensitivity numerical studies have shown that the mesh cell-size may have a drastic effect on the modelling of circulating fluidized bed with small particles. Typically, the cell-size must be of the order of few particle diameters to predict accurately the dynamical behaviour of a fluidized bed. Hence, the Euler-Euler numerical simulations of industrial processes are generally performed with grids too coarse to allow the prediction of the local segregation effects. Appropriate modelling, which takes into account the influence of unresolved structures, have been already proposed for monodisperse simulations. In this work, the influence of unresolved structures on a binary mixture of particles is investigated and models are proposed to account for those effect on bidisperse simulations of bidisperse gas-solid fluidized bed. To achieve this goal, Euler-Euler reference simulations are performed with grid refinement up to reach a mesh independent solution. Such kind of numerical simulation is very expensive and is restricted to very simple configurations. In this work, the configuration consists of a 3D periodical circulating fluidized bed, that could represent the established zone of an industrial circulating fluidized bed. In parallel, a filtered approach is developed where the unknown terms, called sub-grid contributions, appear. They correspond to the difference between filtered terms, which are calculated with the reference results then filtered, and resolved contributions, calculated with the filtered fields. Then spatial filters can be applied to reference simulation results to measure each sub-grid contribution appearing in the theoretical filtered approach. A budget analysis is carried out to understand and model the sub-grid term. The analysis of the filtered momentum equation shows that the resolved fluid-particle drag and inter-particle collision are overestimating the momentum transfer effects. The analysis of the budget of the filtered random kinetic energy shows that the resolved production by the mean shear and by the mean particle relative motion are underestimating the filtered ones. Functional models are proposed for the subgrid contributions of the drag and the inter-particle collision.

Résumé

Mots-clé : *lit fluidisé circulant, modèle de sous mailles, force de traînée, collision.*

Des études numériques ont montré que la taille de la cellule de maillage peut avoir un effet drastique sur la modélisation du lit fluidisé circulant avec des petites particules. En effet, la taille de la cellule doit être de l'ordre de quelques diamètres de particules pour prédire avec précision le comportement dynamique d' un lit fluidisé. En conséquence, les simulations numériques d' Euler-Euler des processus industriels sont généralement effectuées avec des grilles trop grossières pour permettre la prédiction des effets de ségrégation locale. La modélisation appropriée, qui prend en compte l'influence des structures non résolues, a déjà été proposée pour les simulations monodisperses. Dans ce travail, l'influence des structures non résolues sur un mélange binaire de particules est analysée et on propose des modèles pour tenir compte de cet effet dans des simulations de lit fluidisé polydispersés. Pour atteindre cet objectif, des simulations Euler-Euler de références sont réalisées avec un raffinement du maillage aboutissant à une solution indépendante de la taille de la cellule. Ce type de simulation numérique est très coûteux et se limite à des configurations très simples. Dans ce travail, la configuration se consiste en un lit circulant périodique 3D, qui représente la région établie dún lit circulant. Parallèlement, une approche filtrée est développée où les termes inconnus, appelés contributions de sous-maille, doivent être modélisés. Les filtres spatiaux peuvent être appliqués aux résultats de simulation de référence afin de mesurer chaque contribution de sous-maille apparaissant dans l'approche théorique filtrée. Une analyse est réalisée afin de comprendre et de modéliser l'effet de la contribution des termes de sous-maille. L'opération de filtrage fait apparaître de nouveaux termes, les termes de sous-maille. Un terme filtré est la somme d'un terme résolu, obtenus à partir des champs filtrés, et d' un terme de sous-maille. L'analyse de l'équation filtrée de quantité de mouvement montre que les contributions résolues de la traînée des particules fluides et la collision entre particules surestiment les effets de transferts de quantité de mouvement filtrés. L'analyse de l'équation filtrée de l'énergie cinétique des particules montre que la production résolue par le cisaillement moyen et par le mouvement relatif moyen des particules sous-estime contribution filtrée. Des modèles fonctionnels sont proposés pour les contributions de sous-maille de la traînée et des collisions inter-particule.

Contents

Nomenclature

Roman letters

C_D	Drag coefficient	$[\,-\,]$
d_p	Particle diameter	$[\,\mathrm{m}\,]$
e_c	Restitution coefficient	$[\,-\,]$
$I_{f\rightarrow p,i}$	Gas-Particle momentum transfer	$[\,\mathrm{kg}\cdot\mathrm{m}^{-2}\cdot\mathrm{s}^{-2}\,]$
$I_{q\rightarrow p,i}$	Inter-particle momentum exchange	$[\,\mathrm{kg}\cdot\mathrm{m}^{-2}\cdot\mathrm{s}^{-2}\,]$
f_s	Probability density function	$[\,-\,]$
g_i	Gravity field	$[\,\mathrm{m}\cdot\mathrm{s}^{-2}\,]$
g_0	Radial function	$[\,-\,]$
m_p	Particle mass	$[\,\mathrm{kg}\,]$
Nu_p	Nusselt number	$[\,-\,]$
n_p	Particle number density	$[\,\mathrm{m}^{-3}\,]$
P_g	Mean gas pressure	$[\,\mathrm{Pa}\,]$
q_p^2	Particle kinetic energy	$[\,\mathrm{m}^2\cdot\mathrm{s}^{-2}\,]$
q_{fp}	Fluid-particle velocity correlations	$[\,\mathrm{m}^2\cdot\mathrm{s}^{-2}\,]$
Re_p	Particulate Reynolds number	$[\,-\,]$
$U_{k,i}$	Mean velocity of the phase k	$[\,\mathrm{m}\cdot\mathrm{s}^{-1}\,]$
U_{mf}	Minimun fluidization velocity	$[\,\mathrm{m}\cdot^{-1}\,]$
$U_{\sigma,i}$	Mean interface velocity	$[\,\mathrm{m}\cdot^{-1}\,]$
$u_{k,i}$	Instantaneous velocity of the phase k	$[\,\mathrm{m}\cdot^{-1}\,]$
$V_{fp,i}$	Mean relative velocity	$[\,\mathrm{m}\cdot^{-1}\,]$

Greek letters

α_k	Volume fraction of the phase k	$[\,-\,]$
δij	Kronecker symbol	$[\,-\,]$
Δ	Cell size	$[\,\mathrm{m}\,]$
Δ_f	Filter size	$[\,\mathrm{m}\,]$
Δ_G	Test-filter size	$[\,\mathrm{m}\,]$
ϕ	particle diamter ratio d_q/d_p	$[\,-\,]$
Φ	solid volume faction ratio $\alpha_q/(\alpha_p+\alpha_q)$	$[\,-\,]$
$\Theta_{f,ij}$	Viscous stress tensor	$[\,\mathrm{kg}\cdot\mathrm{m}^{-1}\cdots^{-2}\,]$
$\Theta_{p,ij}$	Collisional stress tensor	$[\,\mathrm{kg}\cdot\mathrm{m}^{-1}\cdots^{-2}\,]$

μ_k	Dynamic viscosity of the phase k	$[\,\mathrm{Pa}\cdot\mathrm{s}\,]$
ν_k	Kinematic viscosity of the phase k	$[\,\mathrm{m}^2\cdot\mathrm{s}^{-1}\,]$
ρ_k	Mean mass density of the phase k	$[\,\mathrm{kg}\cdot\mathrm{m}^{-3}\,]$
$\Sigma_{k,ij}$	Effective stress tensor of phase k	$[\,\mathrm{kg}\cdot\mathrm{m}^{-1}\cdot\mathrm{s}^{-2}\,]$
τ_p^{St}	Stokes characteristic time	$[\,\mathrm{s}\,]$
τ_f^t	Turbulence characteristic time	$[\,\mathrm{s}\,]$
τ_{fp}^F	Mean particle dynamic relaxation time	$[\,\mathrm{s}\,]$
τ_p^c	Inter-particle collision time	$[\,\mathrm{s}\,]$
τ_{fp}^t	Eddy-particle interaction time	$[\,\mathrm{s}\,]$
$\{\psi_k\}_k$	Average of any k-phase property ψ_k	[units of ψ_k]
$\langle\psi_k\rangle_k$	Density-weighted average of any k-phase property	[units of ψ_k]
ψ_k''	Fluctuating component of the variable ψ_k	[units of ψ_k]
	variable $g = ab$	

Notation

g	
$\tilde{g}$	Filtered variable $\tilde{g} = \widetilde{ab}$
g^{res}	Resolved variable $g^{res} = \tilde{a}\tilde{b}$
g^{sgs}	Subgrid variable $g^{sgs} = \tilde{g} - g^{res}$

Indices

f	fluid
p, q	particles

Chapter 1

Introduction

Fluidization consists in transforming solid particles into liquid-like state trough suspension in gas or liquid flow. Depending on the fluid velocity, various flow patterns can be observed. At low velocity, the fluid goes through the space between particles without disturbing them. Such a regime of fluidization is called fixed or packed regime. As the fluid velocity increases, a critical velocity value, called the minimum fluidization velocity, is reached and particles become agitated. Such pattern corresponds to bubbling or turbulent regime. At higher flow rate, particles are transported upwards and have to be reintroduced in the reactor. Such velocity is used in Circulating Fluidzed Bed (CFB) process, which implies the return of particles by a looping process. CFBs are widely used in industrial processes such Fluid Catalytic Cracking, Circulating Fluidized bed Combustion (CFBC) and Chemical Looping Combustion (CLC). A typical configuration of CLC consists usually in a dual CFB. A solid material, called oxygen-carrier, circulates between two reactors. In a fuel reactor, such a material provides the oxygen needed for fuel combustion and in an air reactor, the material is regenerated by air. The main advantage of this process is to avoid direct contact between fuel and air. Hence, the flue gases are composed of steam and carbon dioxide, which can be easily separated by condensation. Due to global warming and increase in energy demand, this process has been widely studied in the last years.

Experimental studies, focusing on various aspects as the configuration of the process, has been conducted. Numerical investigations have also been performed aiming to improve the design and the scale-up of the CLC and the understanding of the hydrodynamic behaviour. European projects, such as SUCESS or NANOSIM, deal with this process and combine experimental and numerical studies.Two approaches can be distinguished. In Euler-Lagrange approach, the fluid phase is assumed continuum and the trajectory of each particle is solved. This approach is computationally expensive and limited to simulations with a small number of particles. On the other hand, the Euler-Euler approach consists in treating both the gas and the solid phases as interpenetrating continua. Such an approach is computationally cost effective for simulations with significant particle volume fractions and useful for cases where the interactions between phases have an important role. In Euler-Euler approach, closure laws are needed to describe the inter-particle and the particle/wall interactions. In this study, simulations are performed using the Two-Fluid Model (TFM), closed by the Kinetic Theory of Granular Flows (KTGF). Such modelling is well established [11, 48, 95] and many types of research enabled to validate the Eulerian models by comparison with experimental data [94, 93, 14]. However providing accurate results with small particles, type A according to Geldart's classification [41], remains a challenge. For instance, in simulations of bubbling fluidized beds, the bed height is overestimated [101]. The mesh size appears to have a significant role in simulations with small particles, especially in CFB simulations [97, 128]. Such dependency is due to clusters and streamers, observed in dilute gas-particle flows as in the riser. Their size is of the order of 10-100 particle diameters and they are not taken in coarse mesh simulations [2]. One solution is to develop subgrid models for representing the small scale structures [97, 103]

Subgrid drag models have been developed for monodisperse dense fluidized beds and CLC. However, flows encountered in practical applications are polydisperse. In simulations of such flows, the drag force is not the only term that needs subgrid models, as the mesh refinement appears to affect also the inter-particle momentum exchange [100]. The present work deals with the development of sub-grid models in polydisperse flows. Chapter (2) describes the CLC process, especially the fuel reactor. In chapter (3), the equations of the TFM and simulations of CFB using this approach are presented. Chapter (4) is dedicated to filtered equations, where the local instantaneous variables are split in resolved and subgrid contributions. In Chapter (4), some of the subgrid models, which have been extensively studied in the last years, are presented for monodisperse and polydisperse simulations. In chapter (5), the filtered equations are applied to polydisperse mesh-refined simulations to determine which subgrid contributions need to be modelled. Development of the subgrid drag model is explained in chapter (6). Similarly, the subgrid contribution of the inter-particle momentum exchange needs to be modelled. Chapter 7 reported a study of this model and the subgrid contribution of the production of particle kinetic agitation by velocity gradient.

Chapter 2

Chemical Looping

Contents

2.1 Introduction

A great majority of the world's climate scientists and governments agree on the occurring of the climate change. The principal cause seems to be human activity, in particular the emission of the GreenHouse Gases (GHG). The main gases impacting climate change are H_2O, CO_2, N_2O,$CFC's$ and SF_6. In 1997, the Kyoto protocol, was adopted by the the United Nations Framework Convention on Climate Change (UNFCCC) to fight global warming. After ratification, 37 countries and the European Community committed themselves to reduce to an average of 5% the emissions of GHG over the period $2008 - 2012$ compared to 1990s levels. In 2001, 191 states have signed and ratified the protocol. Many of them committed themselves to decrease the emission of greenhouse gases by 18% (compared to the 1990 levels) in the period from 2013 to 2020.

CO_2 represents the 75% of GHG emissions produced by humans. In addition, CO_2 has a lifetime of 300 years, plus 25% which least forever [7]. The carbon dioxide levels have increased critically since the beginning of the industrial era: estimated at 280 ppm during the pre-industrial era and they reached 390 ppm in 2010 [1]. This increase is directly linked to the global energy consumption. According to the predictions of International Energy Agency (IEA), British Petroleum (BP) and US Energy Information Administration (EIA) this trend is expected to continue [61, 18, 31]. Emissions of CO_2 contributes to global warming, from which results an increase of sea levels due to melting of the polar ice cap and a rise of occurrence of sever weather events. That is why, it appears necessary to reduce the emissions of GHG, especially CO_2.

Up to now, the solutions to reduce the net CO_2 emissions in the atmosphere have focused on:

- reducing energy consumption,
- switching to less carbon intensive fuels,
- increasing the use of renewable energy sources (biofuels, solar thermic,...),
- sequestering CO_2 by enhancing biological absorption capacity in forests and soil.

Regrettably, none of these solutions will enable to reach the safe limitation [1]. Most CO_2 produced comes from combustion processes and several technologies have been developed to capture it when it is produced. Capturing and storing CO_2, chemically or physically, is an additional option to fulfil the environmental promises of the next few years. Several technologies have been developed concerning the Carbon Capture and Storage (CCS). Three main approaches have been developed pre-combustion, post-combustion and oxy-fuel combustion, as shown in Figure 2.1. They do not avoid to produce the CO_2 however they reduce the emissions in atmosphere.

For the post-combustion capture, the gas is burned with air in conventional power plants. Then the CO_2 is separated from the flue gases, using chemical absorption with monoethanolamine or a sterically hindered amine. This technology does not imply major transformation of the process[130].

For the pre-combustion capture, named also fuel decarbonation, the technology is usually coupled with an Integrated Gasification Combined Cycle (IGCC) power plant and becomes a process called IGCC-CCS. A coal gasification is used to get a gas(syngas) containing CO, CO_2, and H_2. The CO is converted into CO_2 and can then be separated from the remaining hydrogen which is burned in a gas turbine. The main drawback of this technology is the cost of building and the complexity of IGCC compared to suspension-fired burners [130].

The oxy-fuel combustion consists in eliminating the nitrogen to obtain flue gases containing only CO_2 and water, which can be easily separated. This technology usually involves important modification of the power plant compared to the post-combustion. The main disadvantage of oxy-fuel combustion is the use of pure oxygen. Indeed the available large-scale technology for air separation is based on cryogenic distillation and consumes a large amount of energy [130].

Although most of these technologies can decrease CO_2 emissions, they also have a high energy penalty, which leads to a decrease of energy efficiency of the processes. Hence, several studies have been carried out to develop new low-cost CCS technologies. Amongst them, the Chemical Looping Combustion (CLC) process appears as one of the best alter-

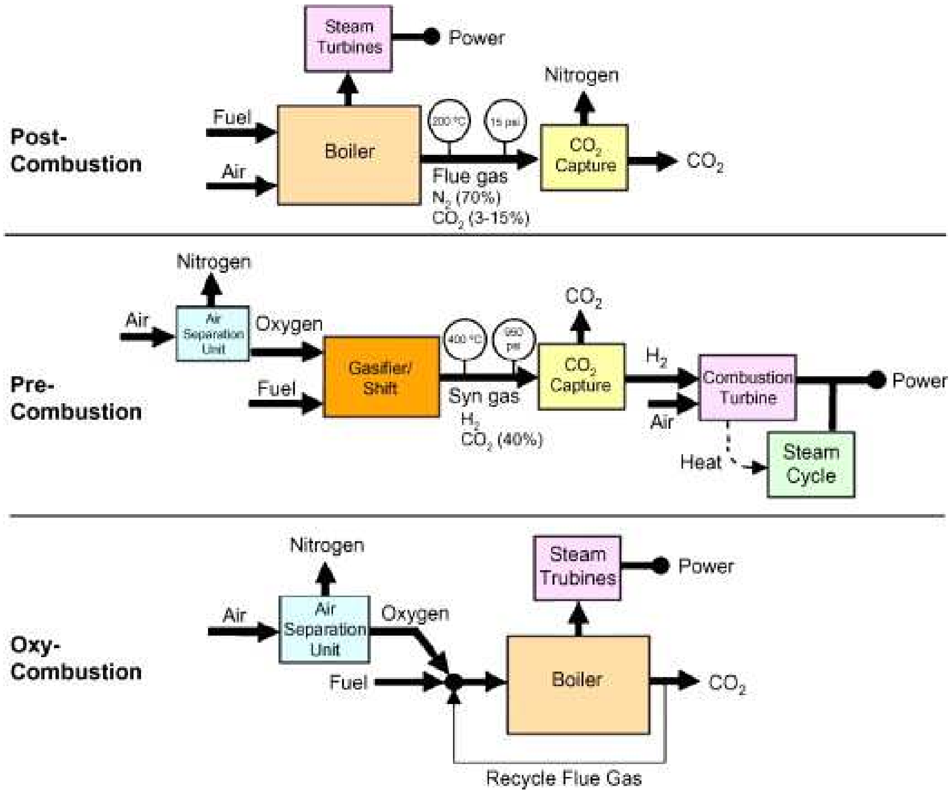

FIG. 2.1: Schematic of the three primary processes for carbon capture [38]

natives to reduce the cost of CO_2 capture [52]. This process involves an oxygen carrier which transports oxygen and avoid using air, which contains nitrogen. Such a process is presented in the following section.

2.2 Chemical Looping Combustion

2.2.1 Presentation of the process

The term Chemical-Looping refers to a cycling process where the oxygen needed for the conversion of the fuel is transported by a solid material, named oxygen-carrier. This permits to avoid direct contact between air and fuel, hence there is no emission of NO_x and decrease the cost of CO_2 separation. Indeed the flue gases included only CO_2 and steam. The two species can be easily separated from each other by condensation.

Initially it was developed in 1954 by Gilliland and Lewis [30], who patented a new way to produce pure carbon dioxide in two interconnected fluidized beds using solid oxidized copper as oxygen-carrier. Later, Richter et al. [111] and Ishida et al. [67] developed a new combustion process to effectively use the fuel energy. Then, Ishida and Jin [64, 65, 66] suggested CLC as a process for CO_2 capture. Since then, the CLC process has been extensively studied in order to develop and improve the efficiency of this technology [82, 113, 26].

Currently, the system is made of two interconnected reactors, an air and a fuel reactor (as shown in Figure 2.2) exchanging solid particles as the oxygen-carrier. The oxygen-carrier is oxidized in the air reactor at high temperature. This reaction is exothermic. Then the oxygen-carrier is transferred to the fuel reactor, where it is reduced. The oxygen-carrier

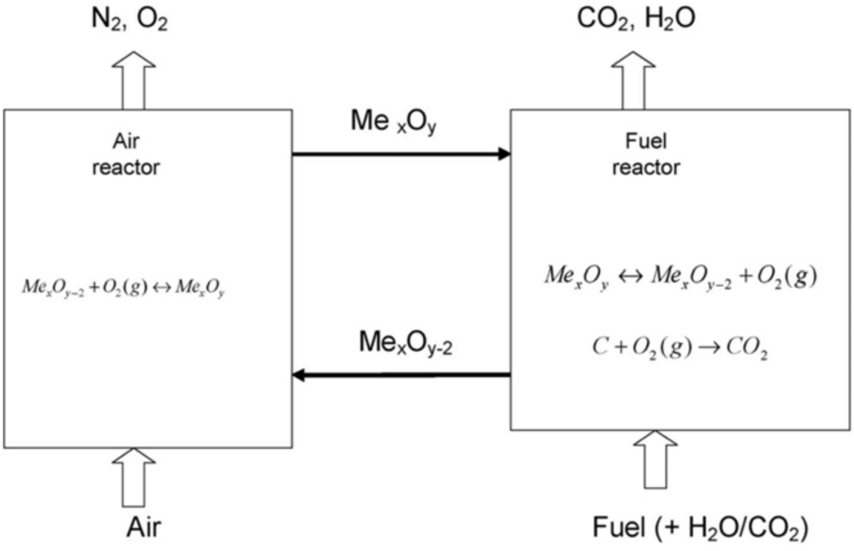

FIG. 2.2: General scheme of a Chemical Looping [87]

reduction can be exothermic or endothermic, depending on the oxygen-carrier and the fuel. To close the loop, the oxygen-carrier must be re-oxidized before beginning a new cycle. The gases leaving the air reactor include unreacted O_2 and N_2 and the flue gases from fuel reactor include steam and CO_2 [1, 81, 74].There is no contact between air and fuel, so no NO_x can be produced by this way. The main advantage of this system is to separate the CO_2 and H_2O from others flue gas components (for instance unused O_2 and N_2) without gas separation equipment and energy consumption. In addition, the steam and CO_2 can be used to produce additional power. The Chemical Looping Process can be used for combustion or hydrogen production and in both cases separation of the CO_2 occurs.

CLC processes can use gaseous or solid fuels. The CLC employing gaseous fuels, such as natural gas or refinery gas, are characterized by a direct reaction between the oxygen-carrier and the fuel. The CLC using the solid fuel (e.g. biomass, charcoal) present the benefit of rich resources of solid fuels (e.g. biomass, petroleum coke or coal) and the lower cost compared to natural gases. Using a solid fuel offers several possibilities, as illustrated in Figure 2.3. The reaction involved in the conversion of the solid fuel affects the design of the CLC process and the choice of the oxygen-carrier [1]. Indeed, three main options can be considered for the solid fuel processing in CLC:

- Syngas-CLC process: the solid fuel is converted into carbon monoxide, hydrogen and carbon dioxide (syngas) in a gasifier and then the oxygen-carrier comes into contact with the syngas.
- In-situ Gasification CLC (iG-CLC): the oxygen-carrier and the solid fuel can be mixed in the same reactor. The solid fuel generated gasification inside the fuel reactor and these products react with the oxygen-carrier [16, 1].
- Chemical-Looping with Oxygen Uncoupling (CLOU) : the oxygen-carrier releases oxygen needed for the combustion [87].

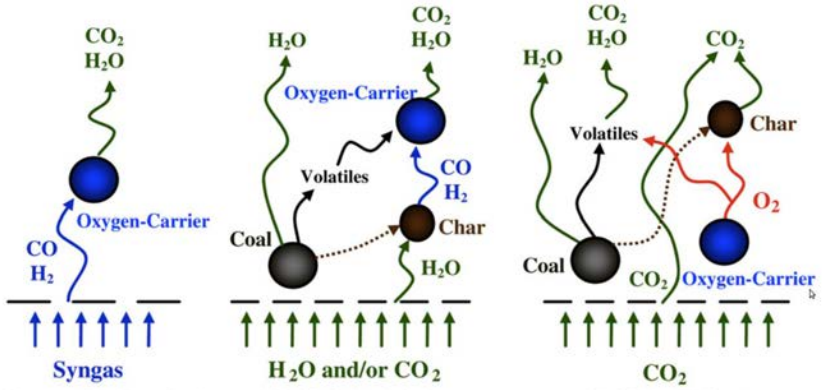

Syngas-CLC (gas fuel) iG-CLC (solid fuel) CLOU (solid fuel)

FIG. 2.3: Main processes involved in fuel-reactor for the three different options available for solid fuel processing in a CLC system [1]

Using solid fuel affects the design of the fuel reactor. Several characteristics for the design and the oxygen-carrier properties have been identified concerning CLC using solid fuels:

- Ash removal brings about losses of oxygen-carrier. This implies that the oxygen-carriers should be affordable. Luckily, most of the oxygen-carriers are highly reactive toward syngas released by gasification.
- Gasification is a slow process. Residence time must therefore be sufficient to avoid char particles going into the air reactor. Another possibility is to have an efficient separation system of ash from oxygen-carrier.
- To achieve high conversion of volatiles, the fuel inlet into the reactor should enable good contact between oxygen-carrier and volatiles.

The way the solid fuel is converted will also affect the design of the CLC process and the choice of the oxygen-carrier [1].

2.2.2 Oxygen-carrier materials for CLC of solid fuels

The main criteria for the choice of an oxygen-carrier are:

- sufficient oxygen transfer capacity,
- high reactivity for reactions in the air and fuel reactors,
- ability to convert fully the fuel to CO_2 and H_2O,
- High temperature of agglomeration, low fragmentation and resistance to attrition,
- negligible carbon deposition,
- low cost,
- environmental friendly characteristics[1].

The first two characteristics are linked with species involved in the reduction-oxidation reactions. The cost and the environmental characteristics depend on the type of oxygen-carrier used. The other characteristics are evaluated experimentally for each material. Oxygen-carriers are usually made of metal oxide [1].

However, using only a pure metal oxide does not appear suitable because their reaction rates decrease dramatically during cycles [27]. To prevent this phenomena, a solution is to employ a porous support. It supplies a higher surface area for reaction and increases the mechanical strength and attrition resistance.
Several methods can be used to prepare the materials. The powders of metal oxide and support can be mixed (mechanical mixing and extrusion, freeze granulation, spray drying, spin flash...). Another method consists in using a solution of metal oxide and support in order to obtain solid compounds by precipitation (co-precipitation, dissolution, sol-gel ...).

There is also the impregnation method, a solution containing the metal oxide is deposited on a resistant and porous support.

Several metal oxides have been studied, for example Ni, Fe, Mn and Cu. Metal oxides can also be added together. The first method is to use "combined oxides" to obtain a new oxygen-carrier with new properties. For instance, Mn can be combined with Ca, Fe, Si, Mg in order to form a new material able to release oxygen. Another method, named "mixed oxides", does not imply the creation of compound but is based on synergies of mixing oxygen-carriers with different properties. For example, limestone is added to ilmenite to improve charcoal particles conversion [1].

2.3 Gas-solid fluidization

Fluidization consists in dynamic fluid-like behaviour of a static solid granular material. This is realized through the suspension of solid particles in a fluid (gas or liquid). When the fluid has a slow velocity, it will get through the porosity of the bed. As the fluid velocity increases, so does relative velocity between particle and fluid, leading to an increase of the upward drag force exerted by the fluid on the solid particles. When the sum of the buoyancy and the drag force is equal to gravitational forces, the minimum fluidization velocity is reached and solid particles become suspended in the gas.

Fluidized beds have several advantages. First, a fluidized bed can be handled like a fluid, permitting continuous feeding and removal, a significant advantage when compared to packed beds. In addition, the mass and heat transfers are improved because of the intense mixing.

However, several issues can be encountered in fluidized beds: the production of solid fines particles, clusters and bubbles formation. As explained in the next section, the formation of clusters raises several questions about the simulations of CFB.

2.3.1 Classification of powders

To determine the force exerted on particles, particle size and shape must be characterized. A sieve analysis (or gradation test) evaluates the particle size, their shape and their surface texture. However, the solid phase is difficult to describe due to measurement issues (often intrusive), sampling and distribution.

2.3.1.1 Gedart's classification

The behaviour of fluidized bed depends on the characteristics of the fluidized particles. In 1973, Geldart [41] proposed to classify powders into four groups (Groups A,B,C and D), characterized by the density difference between liquid and solid and by the particle size [146]. Geldart's classification of powders is shown by Figure 2.4. A brief description of the different groups is given below:

- Goup A: dense phase expansion after minimum fluidization and prior to the begin-

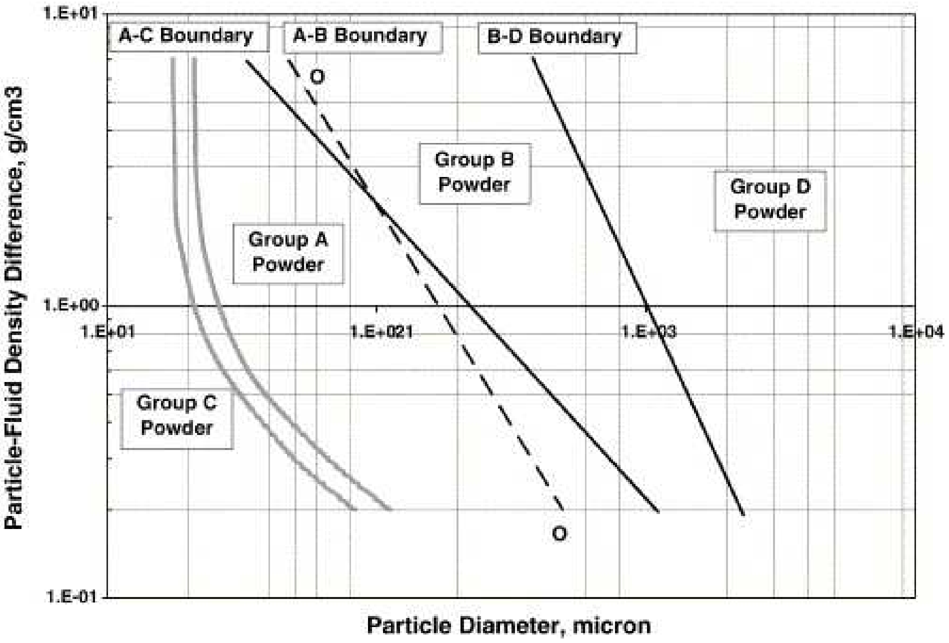

FIG. 2.4: The original Geldart's classification of powders [146]

ning of bubbling,

- Goup B: bubble at the minimum fluidization velocity,
- Goup C: difficult to fluidize,
- Goup D: large size and/or density and spout readily.

In fluidized beds, clusters are mainly encountered with the particles type A. Those fine particles enable to improve the mass transfer and maintain a low pressure drop [145]. To develop this classification, Geldart [41] used fluidization data obtained only at ambient temperature and pressure with air as fluidization gas. However, industrial processes imply high temperatures and pressures as well as a fluidization gas differing from air. Yang [146] adapted the chart for elevated temperatures and pressures and/or for various fluidization gases.

2.3.1.2 Classification of Kunii [71]

The behaviour of each Geldart group depends on the fluidization velocity. Particles can form a fixed, smooth, or bubbling fluidized bed. In 1991, Kunii and Levenspiel [71] proposed a classification taking into account the particle properties and fluidization velocity. This classification is presented in Figure 2.5.

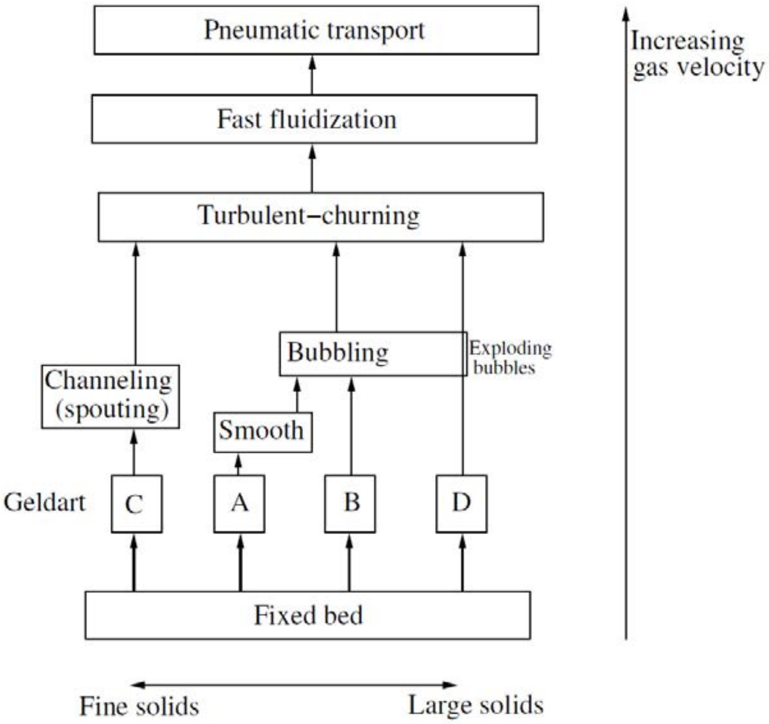

FIG. 2.5: Fluidization flow regimes according to Geldart's goups proposed by Kunii and Levenspiel [95]

2.3.2 Characterization of the solid phases in CLC

The solid fuel and the oxygen-carrier can have very different properties as shown in Table 2.1. Taking two different materials, with various diameter and density, will affect their velocities and therefore induce polydisperse effects. The size given in the table could evolve due to fragmentation or attrition effects.

	Coal	Ilmenite $FeTiO_3$
Particle density ρ_p ($\mathrm{kg/m^3}$)	100	4600
Particle diameter d_p (μm)	< 50	160
Settling velocity V_s ($\mathrm{m/s}$)	< 0.14	1.7

TAB. 2.1: Solid fuel properties from Nouyrigat [95]

Ingeneral manner, the particle phases have a Particle Size Distrbution (PSD). Due to the diversity of powders (shape, diameter), the particles, instead of being characterized individually, can be classified in several groups. PSD has a strong effect on the dynamical and kinetic behaviour of the CLC. For this reason, it is important to characterize accurately the PSD.

In industrial processes, PSD can have many different shapes. For instance, the log-normal

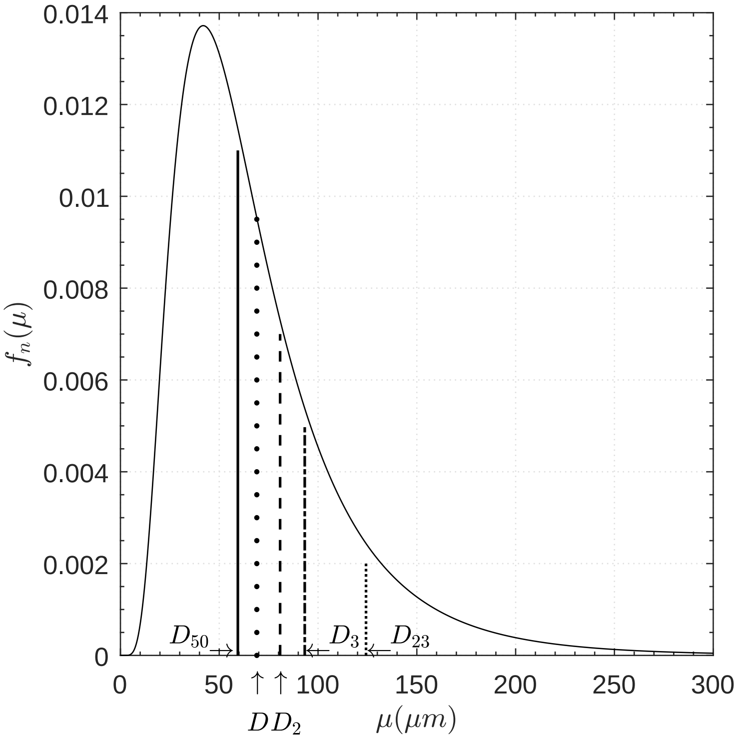

FIG. 2.6: Log-normal frequency distribution

distribution is commonly used in aerosol studies [127, 3]. This distribution is expressed as:

$$f_n(\mu) = \frac{1}{\sqrt{2\pi}\sigma} exp\left[-\frac{1}{2}\left(\frac{ln\mu - D}{\sqrt{2}\sigma}\right)^2\right]\frac{1}{\mu} \tag{2.1}$$

An example of this distribution is given in Figure 2.6. Integrating the PSD enables to define the cumulative distribution:

$$F_n(d) = \int_0^d f_n(\mu)d\mu \tag{2.2}$$

The log-normal cumulative distribution is depicted in Figure 2.7.

D is the mean diameter and is calculated by:

$$D = \int_0^\infty \mu f_n(\mu)d\mu \tag{2.3}$$

Several statistical parameters can be defined to characterize the distribution function. For instance, the variance is defined by:

$$\sigma^2 = \int_0^\infty (\mu - D)^2 f_n(\mu)d\mu \tag{2.4}$$

There are others definitions of mean diameter, for instance:

- the average surface diameter $D_2 = (\int_0^\infty \mu^2 f_n(\mu)d\mu)^{1/2}$

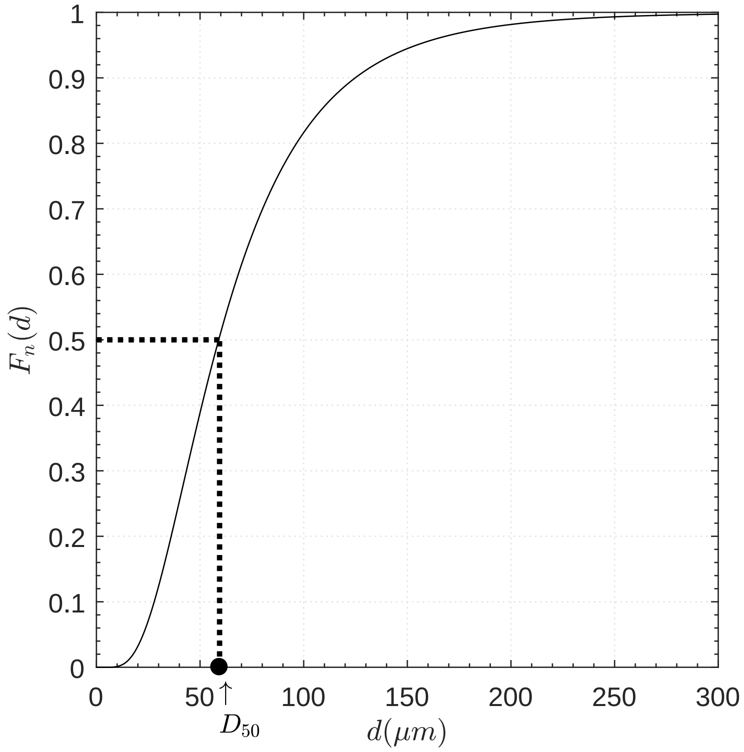

FIG. 2.7: log-normal cumulative distribution and d_{50}

- the average volume diameter $D_3 = (\int_0^\infty \mu^3 f_n(\mu) d\mu)^{1/3}$

- the Sauter diameter corresponds to the ratio of the particle volume to surface area in a distribution. This diameter is frequently used for spray and atomization calculations:

$$D_{32} = \frac{\int_0^\infty \mu^3 f_n(\mu) d\mu}{\int_0^\infty \mu^2 f_n(\mu) d\mu} = \frac{D_3^3}{D_2^2} \tag{2.5}$$

- The median diameter D_{50} corresponds to the diameter for which the cumulative distribution is 50%.The median diameter D_{50} is given in Figure 2.7.

Many scientist used the relative span, $\frac{D_{90}-D_{10}}{D_{50}}$, to characterize the distribution width. D_{90} and D_{10} represents respectively to the diameters for which the cumulative distribution is 90% and 10%. The quartile ratio, corresponding to $\frac{D_{75}}{D_{25}}$, can also be used to characterize the polydispersity. Another possibility is the coefficient of variation (COV), which is the standard deviation divided by the mean diameter D.

2.4 Description of the air reactor

A circulating fluidized bed (CFB) consists of a specific geometry where all particles are transported by the flow in the bed and then return to the bed by a loop. CFBs are used

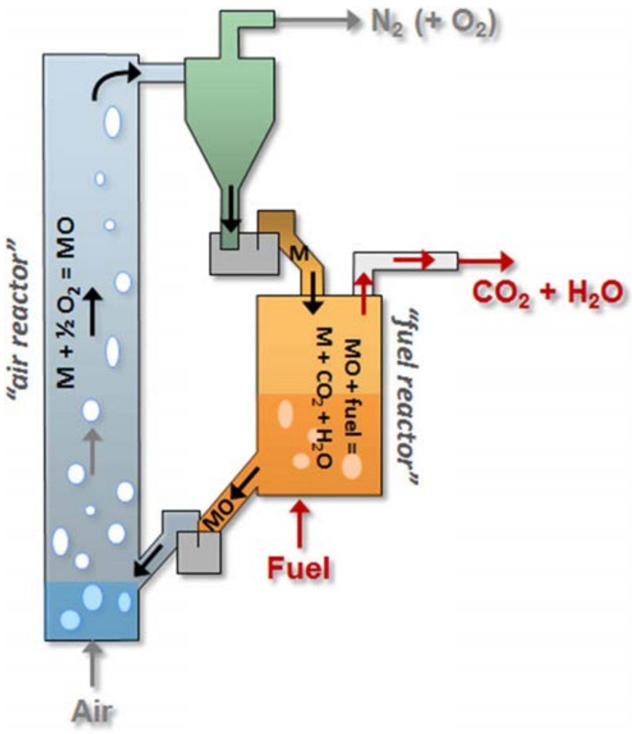

FIG. 2.8: Schematic of a chemical looping process [17]

in many industrial processes such as Fluid Catalytic Cracking (FCC) units, Circulating Fluidized bed Combustion (CFBC) and Chemical looping combustion (CLC). A typical scheme of a circulating fluidized bed with a simple recycle loop composed of a cyclone, a fuel reactor, a return seal and an air reactor is presented in Figure 2.8. The riser of a CFB, corresponding to the air reactor of a CLC, will be the focus of our thesis. The riser and its hydrodynamical behaviour are described below.

2.4.1 Evolution of the solid volume fraction and pressure

At the bottom of the riser, there is an acceleration zone where a momentum transfer from the gas phase, to the solid phase occurs. This zone corresponds to a large pressure drop due to a significant number of particles. The pressure drop measured in this zone can represent 40% of the total pressure drop in the riser [107]. Several interactions have to be taken into account, such as gas-particle, particle-particle and the wall-particle interactions. The height of this dense zone is linked to the operating point and the particle type. The particles usually go downwards near the wall and up in the center. Several studies report this as the “core-annulus regime” [144, 100, 110].

The pressure gradient and the solid volume concentration decrease as the height inside the riser increases. If the riser is high enough, a stationary state is reached in the upper part of the riser. In this zone, the pressure gradient and the solid volume fraction have very low fluctuations. The zone between the dense and the stationary regions, where the solid volume fraction decreases, is called the intermediate zone [112, 145].

The solid volume fraction changes with the height inside the riser but also with the radial position. The core annulus flow is usually found in the riser. This radial flow structure consists of a segregation of particles between a dense region close to the wall and a dilute region in the core. This segregation results from the force balance between the weight of particles, the wall friction and the collisional force. Mathiesen et al. [85] conducted an experimental study on a multiphase flow in a riser. It appears that the relative velocity between small and large particles is greater in the center and goes down near the wall. The turbulent velocity remains almost unchanged in the center.

Inside the riser, there are clusters of particles which are continuously formed and broken [2, 20, 120]. They are quite large, with sizes of the order of $10 - 100$ particle diameters [2]. They arise from the instability due to the relative motion between gas and particles, and from the dissipation of fluctuating energy of particles by both relative motion between particles and viscous damping [2].
The dispersion of the solid phase is not uniform and the particles form unstable clusters. Hence, the momentum transfer between gas and particles is less easy and the acceleration of the flow at the bottom of riser takes more time than with an uniform dispersion of the solid phase. The probability of cluster occurrence varies with the radial position. The influence of the operating conditions and of the particle type is more significant in the upper region of the riser. Indeed, the cluster density there tends to decrease as the gas velocity increases.

2.4.2 Mixing and segregation

2.4.2.1 Vertical segregation and mixing

For a wide distribution of particles, increasing the gas velocity through the bed of solid leads to the fluidization of the small particles while the large particles remain stationary. Indeed the small particles can slip into the void space between the large particles. The movement of the small particles counters the settling of the large particles. A partial fluidization occurs conducting to an intermediate pressure gradient. If the gas velocity increases further then all the particles are fluidized and the mixing process is predominant [71]. For a binary mixture of particles, it has been shown that the segregation occurs when the gas velocity is below the minimum fluidization velocity of the large particles [21, 71].

2.4.2.2 Horizontal/radial segregation and mixing

A radial segregation of particles has been reported by several studies [55, 85, 24]. The experimental data shows a significant difference between the mean diameter in the center and near the walls. This difference goes up as the height inside the riser increases. The horizontal segregation increases as the solid volume fraction decreases. By increasing the gas velocity, the difference between the core and the wall regions tends to decrease,

indicating that there is more mixing and less horizontal segregation.
This phenomenon can be due to the decrease of the gas velocity. This velocity can continue to fluidize the small particles but is not high enough to fluidize the large particles. This leads to the horizontal segregation. The largest and/or heaviest particles tend to go down near the wall. In the center, there is an upward flux of small particles easier to fluidize [55].

2.4.3 Effect of polydispersion on the hydrodynamics of CFB

An issue to model the CFB is the polydispersity of the solid phase. Indeed, the solid phase in industrial processes usually consists of a non-uniform distribution of particle diameters. The polydispersity of the solid phase can be an advantage, for instance it can improve the reactor performance and operation. Squires et al. [126] and Yates and Newton [147] showed that adding small particles in a monodisperse fluidized bed improves uniform fluidization. To better understand the effect of the particle diameter, most of the studies focus on binary mixtures.

2.4.4 Effect of the polydispersity on solid volume fraction

As shown by Batrack et al. [10], taking into account polydispersity of the solid phase enables to improve the prediction of the solid volume fraction at the bottom of the riser. Batrack's thesis focuses on 3D unsteady polydisperse Euler-Euler simulations of a circulating fluidized bed [11]. By comparing two cases with the reference case calculated with the Sauter mean diameter, it appears that taking into account the polydispersity improves the prediction of the pressure profiles and the radial description of the solid volume fraction. Indeed, the two simulations show similar pressure profiles in the upper part of the riser but the pressure tends to be underestimated by the monodisperse simulation at the bottom of the riser. It could be directly linked to the underestimation of the total solid volume fraction at the bottom of the riser. However, even if the polydispersity of the solid phase is taken into account, the solid concentration at the bottom of riser appears to still be underestimated compared to the experimental results [141]. In addition, Mathiesen et al. [85] and Nouyrigat [95] show that the largest/heaviest particles tend to accumulate along the walls. Bidisperse simulations conducted by Mathiesen et al. [85] show that core annulus flow can be observed experimentally and numerically for velocities and the solid volume fraction. However the mean diameter close to the walls appears to be underestimated compared to the experimental data. This may be due to the underestimation of the turbulence at the bottom of the riser or others forces, which were no taken into account.

2.4.5 Effect of collision between classes

Collision effects should also be investigated, as Batrak et al. [10] showed that the collisions between the different classes play a significant role in the fluidization of particles. Taking into account the collision between classes leads to decreasing the mean slip velocity between particles. The comparison between the influence of the mean slip velocity and the mean kinetic agitation of particles shows that the slip velocity is dominant when the effects of collisions between classes are neglected. On the contrary, the kinetic agitation of particles is dominant when the collisions are taken into account. Taking into account accurately the collisions between particles appears fundamental to predict the behaviour of the solid phases.

Nouyrigat [95] highlighted also the significant effect of collision on the hydrodynamic behaviour of bidisperse riser. The comparison between experimental and numerical results shows that the circulation of large particle tend to be underestimated by numerical simulations. Numerically, increasing the number of small particles decreases the maximum volume fraction in the riser. When the small particle ratio increases, the gas mass flux does not change but the mass flow of the large particles increases significantly. Adding small particles in the bed cause collisions with the bigger particles, which improves the large particle circulation and limits the circulation of the small particles. To reach the steady state and have a refined mesh, simulation are conducted on a part of the riser, represented by a periodic box. The bidisperse experiments performed by Fabre [33], with two classes with similar density and different diameters, has been compared the simulation of a periodic box initialized with the solid volume fraction and the fluidization gas velocity. The collisions between particles reduce the velocity of small particle and speed up the large particles. The repartition and the solid mass flux of each classes predicted by the simulation are in good agreement with the experimental results. In the simulation conducted by Mathiesen et al. [85] the velocity of particles depicts a core-annulus behaviour similarly to the experiment. Increasing the gas superficial velocity decreases slightly the relative velocity between particles with different diameter. This could be due to an increase of collision between particles and of the agitation of flow. At higher solid loading and higher velocities, the velocity radial becomes less symmetrical. However between the two solid phases seems overestimated compared to the experimental results. The authors assumed that it is due to the simplified geometry chosen for the simulations and the chose of the distribution of particles. In this study also, the role of the collisions appears significant and has to be accurately taken into account.

Summary

Gas–solid CFB are used in many industrial processes such as fluid catalytic cracking (FCC) in petroleum refineries, and biomass pyrolysis or fossil combustion in power plants. In the riser of a CFB, several zones are observed a dense zone at the bottom. As the height increases the solid volume fraction decreases and in the upper zone of the riser a stationary state is reached. In this region, core-annulus flow is observed with low particle volume fraction in the centre and high volume fraction in the near-wall region. The numerical simulations should predict accurately the radial and axial segregation in the riser. The polydispersity appears to have significant effect in the fluidization. Indeed, adding a small amount of small particles improves significantly the fluidization of large particle. However in the numerical simulations, taking into account the polydispersity of the solid phases requires to give careful consideration to the inter-particles collisions. Now the focus will be given on the model, including the collisions terms, used to perform the numerical simulations of the riser of the CFB.

Chapter 3

Mathematical Modelling

Contents

3.1 Introduction

The modelling method is based on an Euler-Euler approach, in which gas and solid phases are treated as continuous inter-penetrated media. To take into account, the presence of all phases, a variable is introduced: the volume fraction α_k for the phase k. This variable corresponds to the volume occupied by the phase k divided by the sum of the volumes of all phases. The mass, the momentum and the energy transport equations are solved for each phase and coupled by inter-phase transfer terms. For the fluid, the Navier-Stokes equations provide averaged transport equations for the velocities and the volume fraction. For the solid phase, the models presented are derivatived by the Kinetic Theory of Granular Flow (KTGF), an extension of the Kinetic theory of dense gases presented by Chapman and Cowling [19]. The transport equations are derived from the kinetic approach founded on a joint fluid-particle Probability Density Function (PDF). The set of PDF's moment transport equations is obtained by derivating a Boltzmann-like kinetic equation of the PDF [121]. The obtained mass, momentum and particle agitation transport equations need closure models. Hence, various approaches have been developed for the inter-particle collisions and the interaction between particle and turbulence.

In the framework of KTGF, models were first developed for monodisperse flows by Gidaspow [44], Balzer et al. [8], Sangani et al. [115], Tsao and Koch [131]. The KTGF has been extended from monodisperse systems to binary mixtures in vacuum by Jenkins and Mancini [68]. Only the transport equation of mass is solved for each solid species with a diffusion model. For the transport equations of the momentum and of the kinetic agitation, there is no distinction between each solid species and the mixture of particles is taken into account. Similar models, with mixture momentum and particle kinetic agitation equations, were developed by Van Wachem et. al [134] and van Sint Annaland et al. [132]. However, experiments conducted by Zhang et al. [148] show that the granular temperature varies with the particle diameter. Therefore, extension of the KTGF models to binary mixture with mean velocity and particle kinetic energy for each solid species has been studied by several authors, e.g. Gidaspow et al. [45], Fan and Fox [34], Manger [83], Mathiesen [86] and Rahaman et al.[108]. In those models, equations of momentum, and kinetic energy are soled for each solid phases. In the model developed by Huilin et al. [60], the determination of the pressure of the solid phase is based on an equation of state and the coupling between solid species is taken into account by the particle pressure, the radial distribution functions, the viscosities, the particle collision dissipation and the conductivities.

In this chapter, the transport equations and the closure models used in the NEPTUNE_CFD software are presented. They are based on the several studies dealing with the collisional transfer, the kinetic and collisional contribution of the particulate stress tensor.

- Gourdel et al. [50] focus on dilute binary mixtures of settling particles in homogeneous and isotropic gas turbulent flow. The transport equations of momentum and kinetic energy are solved for each solid species. Models were developped for the collisional transfer in the momentum and particle kinetic energy equation.
- Lathouwers and Bellan [72] focus on binary mixtures in dense fluidized beds. They

developed the transport equations of the velocity, $\mathbf{U_p}$ and $\mathbf{U_q}$, and of particle kinetic energy, q_p^2 and q_q^2. The kinetic part of the particulate stress tensor is neglected and only the collisional part is modelled.

- Fede et al. [35] focus on anisotropic and binary mixture and used two Gradś expansions instead of using two Maxwellian equilibrium distributions [50, 72]. He developed a model for the collisional flux, which takes into account the kinetic effects. Such a model is suitable for dense and dilute mixture. The transfer by collision in binary mixture was extended in the frame of kinetic stress transport model approach. Based on this work, a viscosity model developed and applied for polydisperse fluidized bed simulations conducted by Batrak [10], Patino [104], Konan et al. [69], Ciais et al. [22] and Fede et al. [36].

In the present work, the fluid is treated as laminar without effect of pseudo-turbulence due to particle motion and the inter-particle-collision model is written assuming no correlation effect between the colliding particles [124, 40]. Therefore, the focus will be given on the modelling of the solid phase in this chapter.

3.2 Solid phase model

3.2.1 Statistical description

Andresen [4], Morioka and Nakajima [90], Zaichik and Vinberg [150], Reeks [109] and Simonin [122] define $f_p(\mathbf{c}_p, \mathbf{x}, t)d\mathbf{c}_p d\mathbf{x}$ as the probable number of particles, whose center of mass at time t is located in the volume $[\mathbf{x}, \mathbf{x} + d\mathbf{x}]$, with velocities included in $[\mathbf{c}_p, \mathbf{c}_p + d\mathbf{c}_p]$. The mean number of particles per unit volume, n_p, can be defined as:

$$n_p(\mathbf{x}, t) = \int f_p(\mathbf{c}_p, \mathbf{x}, t)d\mathbf{c}_p \ .$$

The mean value of a physical property $g(\mathbf{u}_p(t), \mathbf{x}_p(t))$ of p-particle is defined as:

$$\langle g \rangle_p = \frac{1}{n_p} \int \psi(\mathbf{c}_p, \mathbf{x}, t) f_p(\mathbf{c}_p, \mathbf{x}, t)d\mathbf{c}_p \ .$$

where

$$\psi(\mathbf{c}_p, \mathbf{x}, t) = \langle g(\mathbf{u}_p(t), \mathbf{x}_p(t)) | \mathbf{u}_p = \mathbf{c}_p, \mathbf{x}_p = \mathbf{x} \rangle. \tag{3.1}$$

The mean particle volume fraction α_p and the density ρ_p are linked to the n_p and the particle mass, m_p:

$$\alpha_p \rho_p = n_p m_p.$$

The mean particle velocity at the position $\mathbf{x}$ is calculated using:

$$\mathbf{U}_p(\mathbf{x}, t) = \frac{1}{n_p} \int \mathbf{c}_p f_p(\mathbf{c}_p, \mathbf{x}, t)d\mathbf{c}_p \ .$$

The fluctuating velocity of the particle $u'_{p,i}(x_i, t)$ can be defined and enables the calculation of the the second order moment of velocity fluctuation:

$$\langle u'_{p,i} u'_{p,j} \rangle_p \quad = \quad \frac{1}{n_p} \int (c_{p,i} - U_{p,i})(c_{p,j} - U_{p,j}) f_p(\mathbf{c}_p, \mathbf{x}, t)d\mathbf{c}_p \ .$$

The particle kinetic agitation q_p^2 is defined as:

$$q_p^2 = \frac{1}{2}\langle u^{'}_{p,i} u^{'}_{p,i}\rangle_p \ .$$

The transport equation of the probability density function f_p can be obtained by derivation of the PDF. The collisions are assumed instantaneous, their time scale is small compared to the mean free time between collisions. Such an equation is written as:

$$\frac{\partial f_p}{\partial t} + \frac{\partial}{\partial \mathbf{x}}\left[\mathbf{c}_p f_p\right] = -\frac{\partial}{\partial \mathbf{c}_p}\left[\langle \frac{\mathbf{F}}{m}|\mathbf{c}_p\rangle f_p\right] + \left(\frac{\partial f_p}{\partial t}\right)_{coll} . \tag{3.2}$$

On the right-hand side of Eq. (3.2), the first term, corresponds to the contribution of external forces (gravity, drag force, buoyancy force, added mass force). The last term corresponds to the rate of change of the f_p due to particle-particle interactions, for instance collisions. Eq. (3.2) is multiplied by the property ψ then integrated over the whole domain, with the averaged values, to obtain the general form of the transport equation for the mean $\langle\psi\rangle_p$:

$$\frac{\partial \alpha_p \rho_p \langle\psi\rangle_p}{\partial t} + \frac{\partial}{\partial x_i}(\alpha_p\rho_p\langle c_{p,i}\psi\rangle_p) = \alpha_p\rho_p\langle\frac{F_i}{m}\frac{\partial\psi}{\partial c_{p,i}}\rangle_p + \mathbb{C}(\psi)$$

with $\mathbb{C}(\psi) = \int \psi \left(\frac{\partial f_p}{\partial t}\right)_{coll} d\mathbf{c_p}$ corresponding the mean change rate of the property ψ transported by the inter-particle collisions. This term is defined as an integral over all the potential binary collisions. According to Dahler and Sather [23], this term can be decomposed as the sum of a collisional source term, $\chi(\psi)$, and a collisional flux, $\frac{\partial}{\partial x_i}\theta_i(\psi)$, caused by the transport of ψ due to the collision between particles.

$$\mathbb{C}(\psi) = \chi(\psi) - \frac{\partial}{\partial x_i}\theta_i(\psi) \tag{3.3}$$

3.2.2 Mass balance equation

The mass transport equation reads:

$$\frac{\partial \alpha_p\rho_p}{\partial t} + \frac{\partial}{\partial x_i}(\alpha_p\rho_p U_{p,i}) = 0 \tag{3.4}$$

The right-hand side of the equation should account for the mass transfer between classes. In this work, such a term is null.

3.2.3 Momentum balance equation

The equation the momentum transport equation of the particle type p is obtained. Considering no change of class of particle due to collision (no coalescence nor dislocation), the equation of momentum transport can be written:

$$\begin{aligned}\frac{\partial \alpha_p\rho_p U_{p,i}}{\partial t} + \frac{\partial \alpha_p\rho_p U_{p,j} U_{p,i}}{\partial x_j} &= -\frac{\partial \Sigma_{p,ij}}{\partial x_j} + \alpha_p\rho_p g_i \\ &+ \varphi_{p,i} + I_{f\to p,i} + \sum_q I_{q\to p,i}\end{aligned} \tag{3.5}$$

On the right-hand side of the equation, $\Sigma_{p,ij}$ is the stress tensor, which need to be modelled. The second term on the right-hand side of Eq. (3.5) consists in the gravity acting on the particles, the third term represents the effect of the mean pressure gradient of the gas phase (Archimedes force). It is written as:

$$\varphi_{p,i} = -\alpha_p \frac{\partial P_f}{\partial x_i}$$

The fourth term on the right-hand side, $I_{f\to p,i}$, refers to the drag froce. The last term in Eq (3.5), $\sum_q I_{q\to p,i}$, is collisional source term by the collisions between particles of different classes. $\sum_q$ corresponds to the summation over all classes of particles and $I_{p\to q,i}$ is the momentum transfer from the particles class q to the particles class p.

Effective particulate stress tensor

The effective stress tensor $\Sigma_{p,ij}$ is written as:

$$\Sigma_{p,ij} \;=\; \left[P_p - \lambda_p \frac{\partial U_{p,m}}{\partial x_m}\right]\delta_{ij} - \mu_p\left[\frac{\partial U_{p,i}}{\partial x_j} + \frac{\partial U_{p,j}}{\partial x_i} - \frac{2}{3}\frac{\partial U_{p,m}}{\partial x_m}\delta_{ij}\right]$$

where the granular pressure P_p is deduced from the approach developed by Lathouwers and Bellan [72] by neglecting the effects of the relative mean and fluctuating velocity between solid species:

$$P_p = \alpha_p \rho_p \frac{2}{3} q_p^2 \left[1 + 2\alpha_p^* g_0 (1 + e_c)\right]$$

and the bulk viscosity λ_p is defined by:

$$\lambda_p = \frac{4}{3}\alpha_p \rho_p \alpha_p^* \hat{d}_p g_0 (1 + e_c)\sqrt{\frac{2}{3}\frac{q_p^2}{\pi}},$$

The effective volume fraction is written as:

$$\alpha_p^* = \sum_q \alpha_q \frac{2m_q}{m_p + m_q}\frac{d_{pq}^3}{d_q^3} \tag{3.6}$$

with d_{pq} the distance between particle centers when the collision takes place $d_{pq} = (d_p + d_q)/2$. $\hat{d}_p$ is defined as:

$$\hat{d}_p = \frac{1}{\alpha_p^*}\sum_q \alpha_q \frac{d_{pq}^4}{d_q^3}\frac{2m_q}{m_p + m_q}. \tag{3.7}$$

The solid viscosity μ_p is given by

$$\mu_p = \alpha_p \rho_p (\nu_p^{kin} + \nu_p^{coll})$$

By analogy with kinetic viscosity derivation in the monodisperse approach developed by Balzer et al. [8] and the dispersion coefficient in binary mixture of Gourdel et al. [50]

which takes into account the competition between drag and collisions in the estimation of the mean free path, the kinematic viscosity is written as:

$$\nu_p^{kin} = \left[\frac{1}{2}\tau_{fp}^F \frac{2}{3} q_p^2 (1 + \alpha_p^* g_0 \phi_c)\right] / \left[1 + \frac{\sigma_c}{2}\frac{\tau_{fp}^F}{\hat{\tau}_p^c}\right].$$

where

$$\frac{1}{\hat{\tau}_p^c} = \sum_q \frac{2m_q}{m_p + m_q}\frac{1}{\tau_{pq}^c} \tag{3.8}$$

Using α_p^*, $\hat{d}_p$ and $\hat{\tau}_p^c$ enables to account the presence of the others particle species. We can notce that in monodisperse flows, $\alpha_p^* = \alpha_p$ and $\hat{d}_p = d_p$. The collisional viscosity is given by:

$$\nu_p^{coll} = \frac{4}{5}\alpha_p^* g_0 (1 + e_c)\left(\nu_p^{kin} + \hat{d}_p\sqrt{\frac{2}{3}\frac{q_p^2}{\pi}}\right)$$

where $\sigma_c = \frac{1}{5}(1 + e_c)(3 - e_c)$ and $\phi_c = \frac{2}{5}(1 + e_c)(3e_c - 1)$.

Drag force

In the momentum equation of solid species, the drag force trm is written:

$$I_{f\rightarrow p,i} = -\alpha_p \langle\frac{F_i}{m_p}\rangle_p$$

The drag force is written:

$$I_{f\rightarrow p,i} = -\alpha_p \rho_p \frac{1}{\tau_{fp}^F} V_{r,i}^{(p)} \tag{3.9}$$

where $V_{r,i}^{(p)}$ is the mean relative velocity between $p-$particle and local undisturbed gas velocity, defined by $V_{r,i}^{(p)} = U_{p,i} - U_{f,i}$.
The mean $p-$particle relaxation time τ_{fp}^F is written as follows

$$\tau_{fp}^F = \frac{4}{3}\frac{\rho_p}{\rho_f}\frac{d_p}{C_D\langle|\mathbf{v}_r^{(p)}|\rangle}$$

where the drag coefficient C_D using various correlation (see Appendix A) and $\langle|\mathbf{v}_r^{(p)}|\rangle = \sqrt{(\mathbf{v}_r^{(p)})^2 + 2q_p^2}$. For instance the semi-empirical correlations given by Wen and Yu [139] is used:

$$C_D = \frac{24}{Re_p^*}[1 + 0.15 Re_p^{*0.687}]\alpha_f^{-1.7}$$

and

$$Re_p^* = \frac{\alpha_f d_p \langle|\mathbf{v}_r^{(p)}|\rangle}{\nu_f}$$

Particle-particle momentum exchange

According to Gourdel et al. [50], the particle-particle momentum transfer term is written as:

$$I_{q\rightarrow p,i} = -\frac{m_p m_q}{m_p + m_q} \frac{1+e_c}{2} \frac{n_p}{\tau^c_{pq}} H_1(z)\left(U_{p,i} - U_{q,i}\right) \tag{3.10}$$

where m_p and m_q are the masses of particles p and q, e_c the normal restitution coefficient of collision. This term considers binary collisions between rigid spherical particles and only translation movement is taken into account. τ^c_{pq} is the characteristic time scale between two collisions of any p-particle with all q-particles. Such a time scale is written as:

$$\frac{1}{\tau^c_{pq}} = g_0 n_q 4\pi d^2_{pq} \sqrt{\frac{1}{3\pi}(q^2_q + q^2_p)} H_0(z)$$

g_0 the radial pair distribution function is calculated using [80],

$$g_0 = \left[1 - \frac{\alpha_s}{\alpha_{max}}\right]^{-2.5\alpha_{max}}$$

with α_s the total solid volume fraction and $\alpha_{max} = 0.64$.
$H_0(z)$ and $H_1(z)$ are function of z, which characterize the competition between relative slip velocity between solid species and the relative inter-particle fluctuating motion:

$$z = \frac{|\mathbf{U}_p - \mathbf{U}_q|^2}{\frac{8}{3}q^2_r}$$

q_r is the mean relative agitation of particles and $q^2_r = \frac{1}{2}(q^2_p + q^2_q)$. The two function $H_0(z)$ and $H_1(z)$ can by calculated analytically [48, 151].

$$H_0(z) = \frac{\exp(-z)}{2} \frac{\sqrt{\pi z}}{2} erf\left(\sqrt{z}\right)\left(1 + \frac{1}{2z}\right) \tag{3.11}$$

$H_1(z)$ is a function dealing with the change from a regime of collision controlled by the slip between particles to a regime controlled by the relative agitation and is written as:

$$H_1(z) = \frac{\left[\frac{\exp(-z)}{\sqrt{\pi z}}\left(1 + \frac{1}{2z}\right) + erf\left(\sqrt{z}\right)\left(1 + \frac{1}{z} - \frac{1}{4z^2}\right)\right]}{\frac{2}{\sqrt{\pi z}} H_0(z)} \tag{3.12}$$

For $z \rightarrow 0$ the inter-species collisions are driven by the relative agitation and for $z \rightarrow +\infty$ the collisions are controlled by the mean particle-particle relative velocity. Partino and Simonin [105] proposed the following approximation:

$$H_0(z) = \sqrt{1 + \frac{\pi z}{4}} \qquad\qquad H_1(z) = \frac{4 + 2z}{3 + 2z}$$

The characteristic time scale, τ^c_{pq}, is then written:

$$\frac{1}{\tau^c_{pq}} = g_0 n_q \pi d^2_{pq} g_r$$

with g_r the mean relative velocity of impact of particles of different types, written as:

$$g_r = \sqrt{\frac{16}{\pi}\frac{2}{3}q^2_r + |\mathbf{U}_p - \mathbf{U}_q|^2}$$

3.2.4 Random particle kinetic energy equation

Changing ψ into $\frac{1}{2}c_{p,j}c_{p,i}$ allows to derive the transport equation of the fluctuating kinetic energy of p-particles $q_p^2 = \frac{1}{2}\langle u'_{p,j}u'_{p,j}\rangle_p$ is obtained. Considering no mass exchange, no transfer of particles between classes, this equation is written as:

$$\begin{aligned}\frac{\partial \alpha_p\rho_p q_p^2}{\partial t} + \frac{\partial}{\partial x_j}\left(\alpha_p\rho_p U_{p,j} q_p^2\right) &= \frac{\partial D_{p,j}}{\partial x_j} \\ &+ \Pi_p - \epsilon_{fp} \\ &+ \sum_q \epsilon_c + \sum_q P_{pq} + \sum_q T_{pq}\end{aligned} \tag{3.13}$$

On the right-hand side of the equation, the first term corresponds to the effective diffusivity and is written as:

$$D_{p,j} = \alpha_p\rho_p\langle\frac{1}{2}u'_{p,i}u'_{p,i}u'_{p,j}\rangle_p + \Theta_{p,j}(q_p^2)$$

where $\alpha_p\rho_p\langle\frac{1}{2}u'_{p,i}u'_{p,i}u'_{p,j}\rangle_p$ is the transport by velocity fluctuations and $\Theta_{p,j}(q_p^2)$ is the collisional flux. These terms need to be modelled.

On the right-hand side of the Eq. (3.14), the second term represents the production of kinetic energy by mean velocity gradient.

$$\Pi_p = -\Sigma_{p,ij}\frac{\partial U_{p,j}}{\partial x_i}$$

The third term takes into account the dissipation by drag and is expressed as:

$$\epsilon_{fp} = \frac{\alpha_p\rho_p}{\tau_{fp}^F}\left[2q_p^2\right]$$

The fourth term represents the dissipation by inelastic collision. The fifth term corresponds to the production of particle kinetic agitation by mean slip velocity of particles. The last term takes into account the transfer of agitation between particle species.

Effective diffusivity

The effective diffusivity $\alpha_p\rho_p\langle u'_{p,i}u'_{p,i}u'_{p,j}\rangle + \Theta_{p,j}$ have been decomposed by Balzer et al. [8] into the kinematic and collisional part.

$$\alpha_p\rho_p\frac{1}{2}\langle u'_{p,i}u'_{p,i}u'_{p,j}\rangle + \Theta_{p,j} = -\alpha_p\rho_p(K_p^{kin} + K_p^{coll})\frac{\partial q_p^2}{\partial x_j}$$

In the polydisperse approach, the kinematic diffusivity is given by:

$$K_p^{kin} = \left[\frac{5}{9}\tau_{fp}^F\frac{2}{3}q_p^2(1+\alpha_p^* g_0\varphi_c)\right] / \left[1 + \frac{5}{9}\xi_c\frac{\tau_{fp}^F}{\hat{\tau}_p^c}\right]$$

and the collisional diffusivity:

$$K_p^{coll} = \alpha_p^* g_0(1+e_c)\left(\frac{6}{5}K_p^{kin} + \frac{4}{3}\hat{d}_p\sqrt{\frac{2}{3}\frac{q_p^2}{\pi}}\right)$$

with $\xi_c = \frac{1}{100}(1+e_c)(49-33e_c)$ and $\varphi_c = \frac{3}{5}(1+e_c)^2$.

Dissipation of kinetic agitation by inelastic collisions

The formulation given by Gourdel et al. [49] of the collisional source term in the random particle kinetic energy equation takes into account the dissipation by inelastic collisions, the transfer between solid species and the production by mean slip velocity .The dissipation of kinetic energy q_p^2 due to inelastic collision is written as:

$$\epsilon_{pq} = -m_p \left(\frac{2m_q}{m_p + m_q} \right)^2 \frac{1-e_c^2}{4} \frac{n_p}{\tau_{pq}^c} \frac{2}{3} (q_p^2 + q_q^2)$$

Production and exchange of kinetic agitation between particle species

According to Gourdel et al. [49], the production by mean slip velocity is written as:

$$P_{pq} = \frac{m_p m_q^2}{(m_p + m_q)^2} \frac{(1+e_c)^2}{4} \frac{n_p}{\tau_{pq}^c} |\mathbf{U}_p - \mathbf{U}_q|^2 H_1(z),$$

and the exchange of kinetic agitation between particle species is written as:

$$T_{pq} = -\frac{m_p m_q}{m_p + m_q} \frac{1+e_c}{2} \frac{n_p}{\tau_{pq}^c} \left[\frac{8}{3} \frac{m_p q_p^2 - m_q q_q^2}{m_p + m_q} \right].$$

3.3 Numerical simulation of CFB

Modelling of gas-particle flows, using the Two-Fluid Model (TFM) approach closed by the Kinetic Theory of Granular Flows (KTGF) is well established [11, 48]. Indeed, several studies have been performed to validate the Eulerian models by making comparison with experimental data [94, 93, 95]. Nieuwland et al. [94] analysed the 2D simulations of CFB with sand and air. Even if the lateral segregation is not accurately predicted by numerical simulations, the experimental and numerical results are in good agreement. Such an inconsistency may be due to the interaction between the solid and the gas phase. Neri and Gidaspow [93] studied a transient 2D simulation. The aim was to compare numerical simulations and experiments by Miller and Gidaspow [89]. The numerical simulation results are in good agreement with the experiments for the main characteristics of the flow, in particular for the core-annulus flow and for the formation of clusters. Benyahia et al. [14] focused also on 2D simulations of CFB riser. The experimental and numerical results agreed reasonably well. However the study highlights the significant time required for time-averaging.

Thanks to the improvement of computational resources, several 3D simulations of CFB riser have been performed [70, 2, 152, 154, 6, 5, 106]. Petit [106] focused on monodisperse simulations of CFB with small particles. In simulations, the vertical mean pressure profiles obtained numerically and experimentally are very similar. On the contrary, the radial solid mass flux provided by the simulations are not consistent with the experimental results. For instance, recirculation of solid phase is shown experimentally in the near-wall region and is not observed by numerical simulation. Such an inconsistency could be due to the fact that clusters are observed in flows with particles type A according to Geldart classification. To take into account the clusters, an equivalent diameter was defined. However, using those diameter does not improve the accuracy of the simulations and no downwards solid mass flux is obtained near the walls. Then, the mesh dependence has been analysed. The hydrodynamic of the flow appears to be significantly influenced by the mesh refinement. In coarse mesh simulations, accumulation of particle is observed at the bottom of the riser and there is almost no particle in the upper part of the riser. On the contrary, with refined mesh, the solid phase is not concentrated at the bottom of the riser and more heterogeneous distribution in the upper part of the riser. However, the mesh refinement does not improve the results in the near-wall regions. The influence of mesh size has also been identified as a key parameter in CFB simulations with small particles by Ozel et al. [97] and Parmentier [101]. In the monodisperse simulations performed by Andreux et al. [5], the vertical mean pressure gradient is accurately predicted but no down-flow in the near-wall region is predicted in the near-wall region, similarly to the simulations analysed by Petit [106]. The mesh refinement, in particular in the near-wall region, could explain such a difference. Other studies shows that Eulerian approach does not succeed to predict the hydrodynamic characteristics of industrial applications in particular cases, especially for CFB with small particles [128, 135]. The study performed by Sundaresan [128] shows that mesh size could significantly affect the accuracy of the prediction. The mesh refined simulations performed by Zhang et VanderHeyden [152], even if the two-phase flow model used was very simple and does not take into account any effect of particle interaction, describes reasonably well the main characteristics the main with the experimental data.

The studies show that the mesh-refined simulations agreed reasonably well with experimental data. Hence, the existence of meso-scale structures, such as streamers and clusters, have dramatic effects on the overall dynamic behaviours and they are not taken into account by filtered n-fluid model simulations.

Summary

A lot of studies have been conducted to investigate the monodisperse gas-solid two-phase flow in CFB [125, 97, 25, 143, 59]. For industrial applications with small particles, Eulerian-Eulerian simulations with refined meshes are too expensive and only coarse meshes simulations are suitable for industrial cases. These simulations do not enable to take into account mesoscale structures. In the riser, these structures affect profoundly the hydrodynamics of the flow. In order to better understand the hydrodynamics of the flow in CFB, clarifying the solid phases behaviour appears as a key parameter. Several solutions have been developed to solve this issue and will be presented in the next chapter.

Chapter 4

Filtered approach for gas-particle flows

Contents

4.1 Introduction

Modelling of gas-particle flows, using the Two-Fluid Model (TFM) approach closed by the Kinetic Theory of Granular Flows (KTGF) is well established [11, 48, 95]. However, for A-type particles according to Geldart's classification, the numerical simulations with coarse grids fail to predict the behaviour of the solid phase due to the inaccurate prediction of the solid clusters [2, 99, 102]. To solve this issue, subgrid models can be developed to take into account the effect of subgrid structures and used to improve the accuracy of coarse grid simulation results. The modelling strategy consists in splitting the local instantaneous variables in resolved and subgrid contributions. The corresponding governing equations are obtained by filtering the particle kinetic moment transport equations leading to unknown subgrid terms which need to be modelled in terms of the computed resolved variables. The first step is the evaluation of the resolved and subgrid contributions of each term of the equations. This step highlights which term(s) need(s) to be modelled, leading to the subgrid modelling step to account accurately for the effect of the subgrid scale structures in the filtered equations. This chapter focuses on the filtering equations and the literature dealing with subgrid models and effect of mesh refinement for mono and polydisperse flows.

4.2 Filtered Two-Fluid Model

First, a spatial filter is applied to the momentum and particle kinetic energy equations. Then the aim of the budget analysis will be to examine the contribution of subgrid terms of those filtered equations. Several filter widths Δ_f are required to conduct this analysis. The spatial filter applied is defined as:

$$G(\mathbf{x}-\mathbf{r}) = \begin{cases} \frac{1}{\Delta_f^3} & \text{if } \mid x_i - r_i \mid \leq \frac{\Delta_f}{2} \\ 0 & \text{otherwise} \end{cases} \tag{4.1}$$

where G satisfies $\int\int\int \; G(\mathbf{r})d\mathbf{r} \;=\; 1$. Such a filter, whose size is independent of the direction, will be applied on simulations with cartesian grid. The filtered phase volume fraction is defined as,

$$\tilde{\alpha}_k(\mathbf{x},t) = \iiint \alpha_k(\mathbf{r},t)G(\mathbf{x}-\mathbf{r})d\mathbf{r} \tag{4.2}$$

Filtered phase velocities are defined according to,

$$\tilde{U}_k(\mathbf{x},t) = \frac{1}{\tilde{\alpha}_k} \iiint G(\mathbf{x}-\mathbf{r})\alpha_k(\mathbf{r},t)U_k(\mathbf{r},t)d\mathbf{r} \tag{4.3}$$

The filter is applied to the TFM equations. Due to the filtering process, new terms, named the subgrid terms, arise.

Considering f as the product of a and b (for instance the volume fraction and the velocity), the subgrid term, f^{sgs}, is the difference between the filtered term, $\tilde{f} = \widetilde{ab}$, and the resolved term, $f^{res} = \tilde{a}\tilde{b}$. Considering a size of filter Δ_f, the resolved part of a physical contribution of the equation (i.e pressure gradient) represents the value obtained thanks to a simulation with a mesh cell size of Δ_f. The subgrid term f^{sgs} represents the effect of the subgrid scales and needs to be modelled.

4.2.1 Momentum equation

After filtering operation, the momentum equation of the particles of class p becomes:

$$\begin{aligned}\tilde{\alpha}_p\rho_p\frac{\partial\tilde{U}_{p,i}}{\partial t}+\tilde{\alpha}_p\rho_p\tilde{U}_{p,j}\frac{\partial\tilde{U}_{p,i}}{\partial x_j}=&-\frac{\partial}{\partial x_j}\Sigma^{res}_{p,ij}-\frac{\partial}{\partial x_j}\Sigma^{sgs}_{p,ij}\\&+\tilde{\alpha}_p\rho_p g_i-\tilde{\varphi}^{res}_{p,i}-\varphi^{sgs}_{p,i}\\&+I^{res}_{f\rightarrow p,i}+I^{sgs}_{f\rightarrow p,i}\\&+\sum_q I^{res.}_{q\rightarrow p,i}+\sum_q I^{sgs}_{q\rightarrow p,i}\\&-\frac{\partial}{\partial x_j}\rho_p\sigma^{sgs}_{p,ij}\end{aligned}\tag{4.4}$$

The subgrid contributions of the particle kinetic stress, $\Sigma^{sgs}_{p,ij}$, the gas-particle momentum transfer,$I^{sgs}_{f\rightarrow p,i}$, and particle-particle momentum transfer, $I^{sgs}_{q\rightarrow p,i}$, are calculated similarly.

For instance, the filtered drag is expressed as:

$$\tilde{I}_{f\rightarrow p,i}=-\widetilde{\frac{\alpha_p\rho_p}{\tau^F_{fp}}\left(U_{p,i}-U_{f,i}\right)}$$

The resolved gas-particle drag is written as:

$$I^{res}_{f\rightarrow p,i}=-\frac{\tilde{\alpha}_p\rho_p}{\tau^{F,res}_{fp}}\left(\tilde{U}_{p,i}-\tilde{U}_{f,i}\right)$$

and the subgrid contribution is defined as:

$$I^{sgs}_{f\rightarrow p,i}=\tilde{I}_{f\rightarrow p,i}-I^{res}_{f\rightarrow p,i}$$

A Reynolds stress-like contribution coming from the gas or particle phase velocity fluctuations, $\sigma^{sgs}_{p,ij}$, is defined by the following equation:

$$\sigma^{sgs}_{p,ij}=\widetilde{\alpha_p U_{p,i}U_{p,j}}-\tilde{\alpha}_p\tilde{U}_{p,i}\tilde{U}_{p,j}\tag{4.5}$$

4.2.2 Particle random kinetic energy equation

The filtering process is applied to the random kinetic energy equation, Eq. (3.14), to separate the resolved and the subgrid contributions. The filtered energy balance can be written as:

$$\begin{aligned}\tilde{\alpha}_p\rho_p\frac{\partial \tilde{q}_p^2}{\partial t} + \tilde{\alpha}_p\rho_p\tilde{U}_{p,j}\frac{\partial \tilde{q}_p^2}{\partial x_j} = {} & \frac{\partial}{\partial x_j}D^{res}_{p,j} + \frac{\partial}{\partial x_j}D^{sgs}_{p,j} \\ & + \Pi_p^{res} + \Pi_p^{sgs} \\ & - \epsilon_{fp}^{res} - \epsilon_{fp}^{sgs} \\ & + \sum_q \epsilon_c^{res} + \sum_q \epsilon_c^{sgs} \\ & + \sum_q P_{pq}^{res} + \sum_q P_{pq}^{sgs} \\ & + \sum_q T_p^{res} + \sum_q T_p^{sgs} \\ & - \frac{\partial}{\partial x_j}\rho_p Q_j^{sgs}\end{aligned} \tag{4.6}$$

Similarly to the filtered momentum equation, new terms need to be calculated. The last term is written:

$$Q^{sgs} = \widetilde{\alpha_p q_p^2 U_p} - \tilde{\alpha}_p\tilde{q}_p^2\tilde{U}_p \tag{4.7}$$

The other subgrid terms are written in Annexe B.

4.3 Subgrid models

4.3.1 Monodisperse flows

4.3.1.1 Mesh refinement

Clusters and streamers are observed in dilute gas-particle flows as in the riser and their size is of the order of 10-100 particle diameters. These structures result from two instability mechanisms, an instability due to dissipation of the fluctuating motion of particle by interstitial fluid, collisions between particles and nonlinearity of momentum coupling between phases [2]. Several simulations of a fuel reactor have been carried out [96, 101, 15]. Their first aim was to study the effect of the mesh size. Indeed coarse grid simulations of gas-solid flows are commonly used in order to quickly obtain results but they do not take into account the small structures. Simulations with mesh sufficiently fine, to capture the clusters and streamers [2], are conducted. Those mesh-independent results are used to study the effect of the small structures on the prediction of the hydrodynamics of the bed.

Several authors [96, 101, 142, 2, 153] studied the effect of the mesh refinement on the terms of the particle momentum equation. The drag force term appears to be overestimated due to the subgrid scales [96, 101, 2, 153] for various configurations. For fluidized bed with group A and group B particles, the unresolved part of the drag has the most significant effect in the prediction of the bed expansion [101]. For Circulating Fluidized Beds, the effect of the subgrid scale on the drag force has also been shown. Zhang [153] showed that for volume fraction below 20% the drag force tends to be overestimated with large mesh cell size. In addition, Ozel [96] studied a periodical fluidized bed representing the upper zone of the fuel reactor where the flow is assumed to be established. It appears that the averaged solid mass flux over space and time increases with increasing the mesh size. The solid mass in the riser is not well predicted with coarse grid simulations. It seems also that the solid volume fraction goes up at the center of the riser with increasing mesh size. The mesh size has also an effect on gas velocity. With moderate mesh resolution, positive vertical gas velocities are obtained and with higher mesh resolution, gas velocity are negative close to the walls. It appears that the resolved drag contribution increases significantly with the filter size. It means that the drag force tend to be overestimate when the small structures are not taken into account. Igci et al. focus on two ranges of particle volume fractions, below 0.30 ([62]) and above 0.30 ([63]). For both cases, with increasing filter size, the filtered drag coefficient decreases. The effect of the mesh refinement on the filtered drag coefficient is more significant for low solid volume fraction ($\alpha_p < 0.30$) and becomes less significant when the solid volume fraction goes up. For high volume fraction ($\alpha_p > 0.59$) the effect of mesh size can be neglected.

Recently, several studies focus also on the effects of the mesh refinement on the effective stresses [62, 88]. The drag force has a more significant magnitude than the particulate stresses. However, the unresolved contribution of the particulate stresses appears to affect the prediction and closure are needed for the particulate stresses and the drag force in monodisperse simulations. Recently, scientists have developed several approach, such as Energy-minimization multi-scale[76] or CD-Lab[118], to improve the accuracy of coarse mesh simulations with particle type A according to Geldartś classification.

4.3.1.2 Subgrid drag modification

All the studies conducted on mesh-independent results show that the drag force tends to be overestimated with coarse mesh simulations. Hence various approaches have been developed to represent the effect of the unresolved scales on the drag correlation when TFM is applied with coarse grid. To model such a subgrid contribution, the functional or the structural strategies can be used. On the one hand, the functional strategy consists in taking into account the effect of the subgrid term on the transported scalar, instead of considering the subgrid term itself. On the other hand, the aim of the structural strategy is to determine the best local approximation of the subgrid contribution based on the structures of the subgrid scales.

Structural models

In LES, structural modelling relies on the mathematical properties of the filter and not on assumption on the nature of the subgrid transfer. Two structural models have been developed by Parmentier [101], the Gradient and the scale-similarity model. In both models, the sugrid contribution is approximated similarly. The subgrid contribution represents:

$$I^{sgs}_{f\to p,i} = \tilde{I}_{f\to p,i} - \frac{\tilde{\alpha}_p \rho_p}{\tau^{F,res}_{fk}} \left(\tilde{U}_{f,i} - \tilde{U}_{p,i}\right). \tag{4.8}$$

Following Parmentier [101] and Ozel [96], the filtered contribution, $\tilde{I}_{f\rightarrow p,i}$, can be approximated by:

$$\begin{aligned}\tilde{I}_{f\rightarrow p,i} &= \widetilde{\frac{\alpha_p \rho_p}{\tau_{fp}^{F}}\left(U_{f,i} - U_{p,i}\right)} \\ &\approx \frac{\tilde{\alpha}_p \rho_p}{\tau_{fp}^{F,res}}\left(\tilde{U}_{f,i} - \tilde{U}_{p,i} + V_{d,i}^{(p)}\right) \qquad (4.9)\end{aligned}$$

with $\tilde{\alpha}_p V_{d,i}^{(p)} = \widetilde{\alpha_p U_{f,i}} - \tilde{\alpha}_p \tilde{U}_{f,i}$. $V_{d,i}^{(p)}$ is the subgrid drift velocity due to correlation between subgrid fluid velocity and particle distribution.

The Gradient model is obtained by expanding a Taylor series for the solid volume fraction, α_p, and the gas velocity $U_{f,i}$. By limiting the Taylor expansion to the second order, the model is written as:

$$\tilde{\alpha}_p V_{d,i}^{(p)} = C_1 \Delta_G^2 \frac{\partial \tilde{\alpha}_p}{\partial x_j} \frac{\partial \tilde{U}_{f,i}}{\partial x_j}$$

where C_1 is a constant, which depends on the ratio between the characteristic length of the implicit filter and the grid size chosen, Δ_G. For a grid size, which is twice the implicit filter, C_1 is equal to $1/3$.

A second Gradient model has been developped based on the fact that:

$$\frac{\partial \tilde{\alpha}_p}{\partial x_j} \frac{\partial \tilde{U}_{f,i}}{\partial x_j} = \frac{1}{2}\left(\Delta(\tilde{\alpha}_p \tilde{U}_{f,i}) - \tilde{\alpha}_p \Delta(\tilde{U}_{f,i}) - \tilde{U}_{f,i} \Delta(\tilde{\alpha}_p)\right)$$

where Δ is the Laplacian operator. A second order scheme is used to determine the laplacian operator:

$$\delta^2 \theta = \sum_i \frac{(\theta(\mathbf{x} + \Delta_G \mathbf{e_i}) - 2\theta(\mathbf{x}) + \theta(\mathbf{x} - \Delta_G \mathbf{e_i}))}{\Delta_G^2}$$

and the model becomes:

$$\tilde{\alpha}_p V_{d,i}^{(p)} = C_2 \frac{\Delta_G^2}{2}\left(\delta(\tilde{\alpha}_p \tilde{U}_{f,i}) - \tilde{\alpha}_p \delta(\tilde{U}_{f,i}) - \tilde{U}_{f,i} \delta(\tilde{\alpha}_p)\right)$$

where C_2 is a constant.

Those models tend to underestimate the subgrid contribution according to the a priori analysis conducted by Parmentier [101]. However, the second version of the model tends to be more accurate than the first one in a priori and a posteriori analysis.

In the scale similarity model, the subgrid contribution can be determined using the Germano decomposition [42]. Such decomposition consists in:

$$\widetilde{\alpha_p U_{f,i}} - \tilde{\alpha}_p \tilde{U}_{f,i} = L_i + C_i + R_i$$

where

$$\begin{aligned} L_i &= \widetilde{\tilde{\alpha}_p \tilde{U}_{f,i}} - \tilde{\tilde{\alpha}}_p \tilde{\tilde{U}}_{f,i} \\ C_i &= \widetilde{\tilde{\alpha}_p U''_{f,i}} - \tilde{\tilde{\alpha}}_p \tilde{U}''_{f,i} + \widetilde{\alpha'_p \tilde{U}_{f,i}} - \tilde{\alpha}'_p \tilde{\tilde{U}}_{f,i} \\ R_i &= \widetilde{\alpha'_p U''_{f,i}} - \tilde{\alpha}'_p \tilde{U}''_{f,i} \end{aligned}$$

where $\alpha'_p = \alpha_p - \tilde{\alpha}_p$ and $U''_{f,i} = U_{f,i} - \tilde{U}_{f,i}$ Following Bardina et al. [9], the subgrid contribution is modeled as:

$$\alpha_p \tilde{U}_{f,i} - \tilde{\alpha}_p \tilde{U}_{f,i} \approx \widetilde{\tilde{\alpha}_p \tilde{U}_{f,i}} - \tilde{\tilde{\alpha}}_p \tilde{\tilde{U}}_{f,i}$$

Such a model has been generalized for different fitler than the implicit filter [77]:

$$\tilde{\alpha}_p V^{(p)}_{d,i} \approx C_s \widehat{\tilde{\alpha}_p \tilde{U}_{f,i}} - \hat{\tilde{\alpha}}_p \hat{\tilde{U}}_{f,i}$$

where C_s is a positive constant and $\hat{\cdot}$ respresents the test fitler, which has a characteristic length-scale larger than the implicit filter. Such model tend to underestimate the subgrid contribution.

Functional models

The functional modelling consists in modelling the effect of the subgrid scales on the resolved slip velocity. Such an approach requires knowing the interaction between scales. Using this strategy, the effective filtered drag force is modelled by:

$$I^{sgs}_{f \to p,i} = (H_d - 1)\, I^{res}_{f \to p,i} \tag{4.10}$$

with $I^{res}_{f \to k,i} = \tilde{\beta}(\tilde{U}_{f,i} - \tilde{U}_{p,i})$, where $\tilde{\beta}$ is the homogeneous drag correlation calculated based on resolved variables. The correlation of Wen and Yu provides accurate results for bubbling fluidized so, it will be used as homogeneous drag correlation. H_d is a function taking into account the unresolved scales.

In 1994, Li and Kwauk presented the Energy-Minimization Multi-Scale (EMMS) method. Their aim was to describe the stationary state of fluidization. In this model, it is assumed that the heterogeneity inside the fluidized bed is due to the formation of local clusters. The particle distribution is considered homogeneous inside and outside a cluster. The system is divided into dense and dilute phase which corresponds to inside and outside the clusters [76]. In the following, the subscript d and c refer respectively to the dilute and the dense (cluster) phases. Eight variables are needed in the EMMS model to describe the system, the velocity of gas and solid phase, the solid volume fraction in the dense and dilute phase, the volume fraction of dense phase and the cluster diameter. It gives a set of constraint conditions presented in Figure 4.1. In the EMMS, six hydrodynamic equations are solved:

- Pressure balance between cluster and dilute phase
- Force balance equation for particles in the dense phase

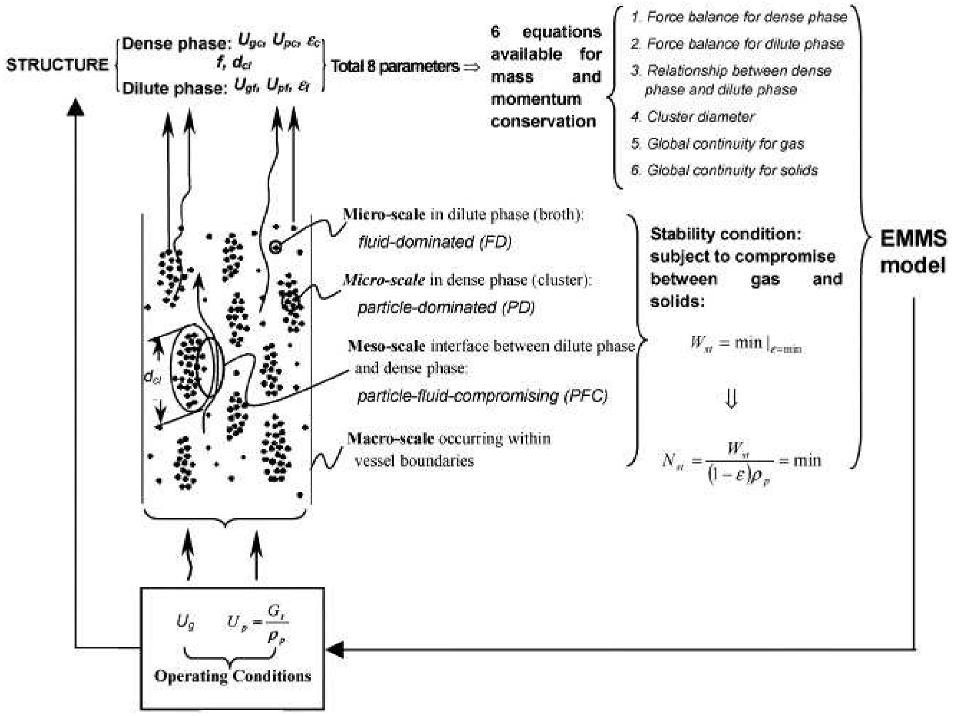

FIG. 4.1: Physical basis of the EMMS model [76]

- Force balance equation for particles in the dilute phase
- Mass balance for the particles
- Mass balance for the fluid
- Cluster diameter

The 6 equations for mass and momentum conservation are not sufficient to resolved the 8 parameters. The stability condition has to be set. The stability condition was first described as the minimum energy consumption for suspending and transporting solids.
Finally the cost function is introduced and represents the energy consumed by the suspension and the transport of particles. For a fluidize bed, such a function is minimized to close the set of equations.
This approach is a non-linear problem, hence using it with coarse grid simulation can be very inefficient. A solution is to connect the optimization problem with functions of the Reynolds number and the mean voidage value. Hence, H_d can be expressed as below [78]:

$$H_d = a(Re + b)^c \tag{4.11}$$

with a, b, and c functions of the mean voidage. Results provided by such an approach have already been compared to experimental results and mesh-refined simulations [137, 136, 138].

Considering also dense and dilute phase, Kuipers' Group proposed another model. Wang et al. [138] worked on bubbling and slugging beds of Geldart B particles. The volume fraction inside the bubble is very low compared to Geldart A particles. Hence, the drag force on particles inside bubbles can be neglected. In the emulsion phase, the particle distribution is considered homogeneous. The homogeneous drag correlation for homogeneous fluidization can be used in this approach. The drag force can be expressed as:

$$\mathbf{F}_K = \alpha^d \beta_{WY}(\alpha_f^c, Re_p^d c)\mathbf{U}_{pg}^c \tag{4.12}$$

$\mathbf{U}_{pg}^c$ and α_f^c are respectively the gas velocity and the the voidage in the dense phase. α^c represents the part of the cell occupied by the dense phase. The Reynolds number in the dense phase, Re_p^c is expressed by as fucntion of the particle diameter. Assuming that the solid fraction in the bubble phase disappears, the mean voidage can be simplified and the drag coefficient can be expressed as:

$$\beta_K = \beta_{WY}(\alpha_f^c, Re_p^{de})\frac{\alpha_p}{\alpha_f^c}\frac{u_{pg}^c}{|\mathbf{U}_f - \mathbf{U}_p|} \tag{4.13}$$

Experimental correlations are used to close the equation of drag coefficient and the correlation of Werther and Wein [140] is used to calculated ϵ_g^c. This empirical correlation can only be used for a small range of process and system parameters. Knowing ϵ_s^c, the Richardson and Zaki correlation enables to calculate the velocity $|u_{sg}^c|$. This approach has been validated for only two particular cases.

Schneiderbauer et al. [119] worked on a new closure, which will be named here CD-Lab approach, for the heterogeneity index H_d, which is used to take account the subgrid structures. As compared with EMMS, the structures are divided into unresolved and resolved clusters. Another assumption is that the solid volume fraction inside dilute phase is low and can be neglected. It means the mass conservation for the fluid written in the EMMS can be simplified. This assumption means also that the drag force per unit volume on the particles in the dilute phase can be neglected compared to the drag force on the particle in the dense phase and the one from the interactions between the dilute and the dense phase.

Another approach, developped by Princeton Group, consists in using highly resolved TFM simulations of solid-gas flow of particles type A according to Geldart's classification in periodic domain were filtered to obtain correlations. The filtered drag coefficient is written:

$$\beta_{IS} = \beta_{WY}(1 - f_{IS}(Fr)h_{IS}(\tilde{\alpha}_p)g(\tilde{\alpha}_p)) \tag{4.14}$$

With

$$f_{IS}(Fr) = \frac{Fr^{-1.6}}{Fr^{-1.6} + 0.4} \tag{4.15}$$

The Froude number Fr is based on the filter length and is equal to: $Fr^{-1} = \frac{g\Delta_f}{u_t^2}$ with u_t the terminal settling velocity of a particle. $h_{IS}(\tilde{\alpha}_p)$ and $g(\tilde{\alpha}_p)$ are written as functions of the filtered volume fraction. Igci and Sundaresan observed that the closures for their filtered drag coefficient are determined by particle volume fraction, filter length and by distance from the wall.

In a riser, the filtered drag near walls decreases dramatically. [63] worked also on a correlation for the drag coefficient near wall and obtained the expression below:

$$\beta_{IS}^{W} = \beta_{IS}\frac{1}{1+6e^{-a(\theta)x_d}} \tag{4.16}$$

With $x_d = gx/u_t^2$ the normalized distance from the wall. $a(\theta)$ depending on θ, which represents the fraction of collisions transferring tangential momentum to the wall. Their wall corrections appear independent of the filter length and of the mean particle volume fraction. Igci and al observed a significant contribution to the filtered particle stress results from the subfiltered scale Reynolds-stress-like velocity fluctuations. This contribution was much larger than the particle stress from kinetic theory. Hence, they neglected the filtered kinetic theory stresses. It increases the computational efficiency of their model.

Similarly to the one of Princeton group, Parmentier et al. [103] developed a filtered drag force as:

$$\mathbf{F}_P = \beta_P(\mathbf{U}_f - \mathbf{U}_p) \tag{4.17}$$

With

$$\beta_P = \beta_{WY}(1 + Kf_P(\Delta^*)h_P(\tilde{\alpha}_p)) \tag{4.18}$$

K is a constant which is dynamically adapted.
$f_P(\Delta^*)$ describes the scaling with filter length.

$$f_P(\Delta^*) = \frac{\Delta^{*2}}{a^2 + \Delta^{*2}} \tag{4.19}$$

With $a \approx 0.0613$ and $\Delta^* = \frac{\Delta_f/\tau_p^{St}}{\sqrt{gD_h}}$, with D_h the hydraulic diameter. τ_p^{St} is the Stokes relaxation time of an isolated particle and Δ_f is the filter length. h_p is deduced from fine grid simulations:

$$h_P(\tilde{\alpha}_p) = -\sqrt{\frac{\tilde{\alpha}_p}{0.64}}\left(1 - \frac{\tilde{\alpha}_p}{0.64}\right)^2\left(1 - 1.88\frac{\tilde{\alpha}_p}{0.64} + 5.16\left(\frac{\tilde{\alpha}_p}{0.64}\right)^2\right) \tag{4.20}$$

Another model have been developped by Ozel [96] using a 3D periodic box and particles type A according to Geldart's classification. The functions obtained are slightly different:

$$f_O(Fr) = \frac{Fr^{-1,6}}{0.3 + Fr^{-1,6}} \tag{4.21}$$

$$h_O(\tilde{\alpha}_p) = -\tanh\left(\frac{\tilde{\alpha}_p}{0.1}\right)\sqrt{\frac{\tilde{\alpha}_p}{0.64}}\left(1 - \frac{\tilde{\alpha}_p}{0.64}\right)^2\left(1 - 1.88\frac{\tilde{\alpha}_p}{0.64} + 5.16\left(\frac{\tilde{\alpha}_p}{0.64}\right)^2\right) \tag{4.22}$$

Such an appraoch is equivalent to model $V_{d,i}^{(p)}$ as:

$$V_{d,i}^{(p)} = Kf(\Delta^*)h(\tilde{\alpha}_p)(U_{q,z} - U_{p,z}).$$

Parmentier and al.[103] and Ozel [96] used the methodology of Germano et al. [43] and Lilly [75] to adjust dynamically the constant K. Test-level filtered of a function f, noted $\hat{\tilde{f}}$, is defined with Δ_G the test filter width. Applying the test-filter on Eq. (7.8) and assuming that K is independent of the filter width, the subgrid contribution of the drag force, is written as:

$$\begin{aligned}\widehat{\tilde{\alpha}_p V_{d,z}^{(p)}} &= \widehat{\widetilde{\alpha_p(U_{f,z} - U_{p,z})}} - \tilde{\alpha}_p(\widehat{\tilde{U}_{f,z} - \tilde{U}_{p,z}}) \\ &\approx K\widehat{f(\Delta^*)h(\tilde{\alpha}_s)\tilde{\alpha}_p(\tilde{U}_{f,z} - \tilde{U}_{p,z})} \end{aligned} \tag{4.23}$$

The subgrid contribution of the drag force, at the test-scale level, is written as:

$$\begin{aligned}\widehat{\tilde{\alpha}_p V_{d,z}^{(p)}} &= \widehat{\widetilde{\alpha_p(U_{f,z} - U_{p,z})}} - \hat{\tilde{\alpha}}_p(\hat{\tilde{U}}_{f,z} - \hat{\tilde{U}}_{p,z}) \\ &\approx Kf(\hat{\Delta}^*)h(\hat{\tilde{\alpha}}_s)\hat{\tilde{\alpha}}_p(\hat{\tilde{U}}_{f,z} - \hat{\tilde{U}}_{p,z}) \end{aligned} \tag{4.24}$$

Combining Eq. (7.10) and (4.24), K can be expresses as:

$$K = \frac{L_z}{M_z} \tag{4.25}$$

with

$$\begin{aligned} L_z &= \tilde{\alpha}_p(\widehat{\tilde{U}_{f,z} - \tilde{U}_{p,z}}) - \hat{\tilde{\alpha}}_p(\hat{\tilde{U}}_{f,z} - \hat{\tilde{U}}_{p,z}) \\ M_z &= \widehat{f(\Delta^*)}h(\hat{\tilde{\alpha}}_s)\hat{\tilde{\alpha}}_p(\hat{\tilde{U}}_{f,z} - \hat{\tilde{U}}_{p,z}) - \widehat{f(\Delta^*)h(\tilde{\alpha}_s)\tilde{\alpha}_p(\tilde{U}_{f,z} - \tilde{U}_{p,z})} \end{aligned}$$

In order to avoid numerically unstable value, the domain average coefficient may be calculated as follow:

$$K = \frac{\langle L_z M_z \rangle}{\langle M_z M_z \rangle} \tag{4.26}$$

Comparison of subgrid drag models

Schneiderbauer et al. [118] compared different subgrid drag models. They plotted the heterogeneity index $H_d^i = \beta_i/\beta_{WY}$ as a function of the mean voidage. Various slip velocity and grid spacing were tested. For the CD-lab approach, $H_d^{CL} \ll 1$ at high voidages, it means that the effective drag β_{CL} is lower than the Wen and Yu correlation β_{WY} at high voidages with large unresolved clusters. H_d^{CL} sightly goes up for when the slip velocity increases. The same trend is observed with the EMMS approach β_E. On the contrary, the drag Model of Kuipers' Group β_K decreases when the slip velocity increases. Any effect of the slip velocity on the heterogeneity index is observed for the approach of Princeton Group and the approach of Simonin's Group.

The effect of the grid size on the heterogeneity index was also studied. The diameter of the unresolved structures is expected to increase as the grid size becomes larger. When the grid size increases, H_d^{CL}, H_d^{IS} and H_d^P decrease. The EMMS approach does not distinguish the resolved and the unresolved structures, hence the H_d^E is lower than the H_d^{CL} at low voidage, where the clusters may be resolved by the grid. H_d^E decreases again when the solid volume fraction reaches the maximum packing. For refined mesh, the homogeneous drag coefficient (Wen and Yu) and the subgrid drag models should be equal. For the CD Lab approach, the Princeton approach and the Simonin's Groups approach it is obtained. However, for the EMMS approach and for the Kuiper's Group approach, the value of the heterogeneity index are not 1. Indeed, the approach does not take into account the resolved and the unresolved parts. Schneiderbauer and al. [118] observed that the heterogeneity index H_d^{IS} and H_d^P are the same for $150\mu m$ particles.

Comparison with fine-grid simulations

Schneiderbauer et al. [118] worked on the sub grid drag models in the bubbling /slugging regime. They used Gelart type B particles and the geometry presented in Figure 4.2. In their article, two cases with different gas inlet velocities, W_g^{in} are studied.

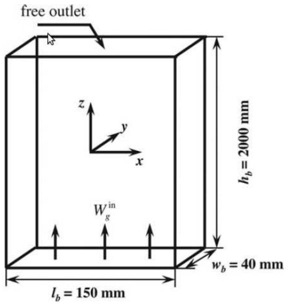

FIG. 4.2: Sketch of the bubbling fluidized bed geometry

With low superficial gas velocity ($W_g^{in} = 0.21m/s$), a mesh independent simulation is conducted. Then several drag correlations are used with coarse-grid simulations. Each subgrid drag correlation provides bed expansion with an error of $\pm 10\%$. However, the simulations with correlations of Parmentier et al., Wang et al. and EMMS model underestimate the mean voidage at the center of the bed. The others correlations provide particle distributions similar to the one given by fine-grid particle distributions. The bubble number and size predicted with the subgrid drag models are similar to the results provided by the fine-grid simulations. The subgrid models enable to obtain accurate predictions with coarse grid simulations and to decrease the computational time by two order compared to the fine grid simulations.

The same study is conducted for a high superficial gas velocity ($W_g^{in} = 0.63m/s$). The drag correlation of Wen and Yu overestimates the bed expansion. As in the study with $W_g^{in} = 0.21m/s$, the correlation of Parmentier overestimates the bed expansion and the EMMS model predicts a lower bed height than the high resolved simulation. The correlation of Princeton Group and the one of the CD Lab model provides acceptable bed height. All correlations enable to obtain good measurements of bubble number density. In this case, the bubble shape corresponds to a long vertical slug.

To sum up, the coarse mesh simulations with small particles fail to predict hydrodynamics. To take into account the effect of the subgrid scale on the prediction of the gas-particle momentum transfer, several subgrid drag correlations have been developed for monodisperse non-reactive flows. However, gas-solid flow encountered in industrial processes are often polydisperse. The next section will deal with those flows.

4.3.2 Polydisperse flows

4.3.2.1 Mesh refinement

In the flows with several classes of particles, the inter-particles contributions like inter-particle momentum transfer, dissipation and production of particle kinetic agitation by collisions have to be taken into account. The effect of the mesh refinement on the contributions of the momentum and particle kinetic agitation equations have also been studied for polydisperse flows [95, 100] focus on poly-solid simulations of CFB.

Simulations with small particles belonging to class B according to Geldart classification and the large ones are type D were conducted by Nouyrigat [95]. As the mesh size decreases, the inventory of the small particles decreases and the predicted circulation of large particles goes up. A 3D periodical box corresponding to the upper zone of the riser is studied to show the effects of the interclass collision. It appears that the interclass collisions improve the radial segregation between species and the circulating mass flux in the core of the bed. They also increase the dissipation of particle agitation for large diameters and the production of agitation for the small particles. Taking into account interclass collision leads to decrease significantly the drag contribution in the momentum equation for large particles and increase slightly this contribution on the small particles.

The effect of the mesh refinement on the term related to collisions in the momentum and kinetic energy equations have been analysed by Ozel et al. [100] for a binary mixture of particles. For both particulate species, the subgrid contibutions of the drag and the inter-particle momentum transfer have similar trends. The particle phase agitation of both classes decreases significantly as the mesh sizes increases. The filtered contribution of drag force decreases for both phases as the filter size goes down. It means that the drag force is overestimated in coarse grid simulations if no subgrid model is applied. The same trend was observed for monodisperse flows but it is more significant for the bidisperse case. As for monodisperse flows, subgrid models are needed to predict accurately polydisperse flows with small particles.

4.3.2.2 Subgrid models for polydisperse flows

Various methods have been developed to take into account the unresolved structures and to predict accurately the inter-phase drag force. Few studies have dealt with binary systems [56, 57]. Holloway and Sundaresan [57] used a microscopic multi-fluid model to perform fine grid simulations to evaluate the filter dependence of the filtered fluid-particle drag, inter-particle momentum exchange and particle phase pressure. The study shows that subgrid models are needed for all those terms. In bidisperse flows, the parameters are not limited to the total solid volume fraction and the filter size, there are also the diameter ratio and the volume fraction ratio. The filtered inter-particle momentum exchange coefficient decreases significantly as the particle size ratio increases and is almost independent of the volume fraction ratio. The computed particle phase pressure and particle phase viscosity of the smaller particle are also affected by the filter size but slightly depend on the particle size ratio and volume fraction ratio. The authors also showed that the viscosity of larger particle can be neglected in their filtered model approach. The subgrid behaviour of the polydisperse fluid-particle drag coefficient appears to be similar to the monodisperse one. However, the monodisperse fluid-particle drag coefficient decreases more slowly with the solid volume fraction. This term appears to depend strongly on the total solid volume fraction.

Other studies focus on a wide particle diameter distribution [13, 141, 79]. Chen et al. Benyahia and Lu et al. [13, 79] applied EMMS drag model to simulate polydisperse flows even if this model has been developed for monodisperse systems. The EMMS drag in the hydrodynamic model causes the formation of heterogeneous flow structures. They restrict the circulation of particles. Hence, adding this model improve the accuracy of the prediction of the circulation rate of particles. Chen et al. [141] combine the PBM(Population Balance Model) with the TFM-EMMS method. The PBM is employed to characterize the spatiotemporal variation of particle properties in the domain. Their algorithm uses TFM to characterize the hydrodynamics of fluidized bed and provides the gas and particles velocities and these values are used to solve the PBM. This model is used to get the Sauter mean diameter for each cell, which will be employed in the EMMS drag model. The effective drag coefficient calculated affects,in turn, the TFM. All the models derive advantages from each other in this coupled algorithm. The simulations results provided by the coupled approach, especially the axial volume fraction and segregation and mixing characteristics, are in good agreement with the experimental results for various superficial gas velocities.

Summary

In this chapter, the spatial filter has been defined and applied on the particles momentum and kinetic energy equations. The filtered terms have been defined as the sum of two contributions the resolved and the subgrid contributions. That last contribution takes into account the subgrid scales. The effect of the mesh refinement on monodisperse simulations shows that the drag force tends to be overestimated as the mesh size increases. It leads to poor prediction of the hydrodynamics of flows in fluidized and circulating fluidized beds with coarse meshes. In literature, several models can be found to predict the effect of the subgrid scales on the drag force. For polydisperse flows, the mesh refinement affects the transfer of momentum between classes of particles and the drag force as in monodisperse cases. Subgrid drag models have been adapted from monodisperse to polydisperse cases. Some studies show that the exchange of momentum between classes strongly dependent on the total solid volume fraction, the particle size ratio.

Chapter 5

Budget analysis

Contents

5.1 Introduction

Detailed sensitivity numerical studies have shown that the cell-size may have a drastic effect on the modelling of circulating fluidized beds. Typically the cell-size must be of the order of few particle diameters to predict accurately the dynamical behaviour of a fluidized bed. However, Euler-Euler numerical simulations of industrial processes are generally performed with grids too coarse to allow accurate prediction of local segregation effects. Those effects may be accounted for using the modelling using filtered approaches. A filtered approach is developed where the unknown terms, called sub-grid contributions, have to be modelled. Highly resolved simulations are used to develop the model. Those simulations based on Euler-Euler approach, are performed with grid refinement small enough to reach the mesh independence. Then spatial filters can be applied in order to quantify each sub-grid contribution appearing in the theoretical filtered approach. Such numerical simulations are very expensive and are restricted to very simple configurations. In the present study, highly resolved simulations are carried out in order to investigate the sub-grid contributions in case of binary particle mixtures in a periodic circulating gas-solid fluidized bed. A budget analysis is conducted to understand and model the effect of sub-grid contributions on the hydrodynamic of polydisperse gas-solid circulating fluidized bed.

5.2 Numerical simulation overview

Using the TFM, several simulations of reactive polydisperse flows have already been performed [69, 37]. Ozel et al. [99] highlighted effects of small structures on polydisperse simulations. The budget analysis shows how the mesh refinement affects the terms of momentum and particle kinetic agitation equations. In this study, gas-particle flows are simulated in a 3D periodical Circulating Fluidized Bed (CFB). The theoretical configuration consists of the upper part of the riser where stationary state is reached. The geometry, previously used by Ozel et al. [98], has a squared-section of 0.0275 m and a length of 0.22 m. A sketch of such configuration is shown in Figure 5.1. Agrawal et al. [2] studied three

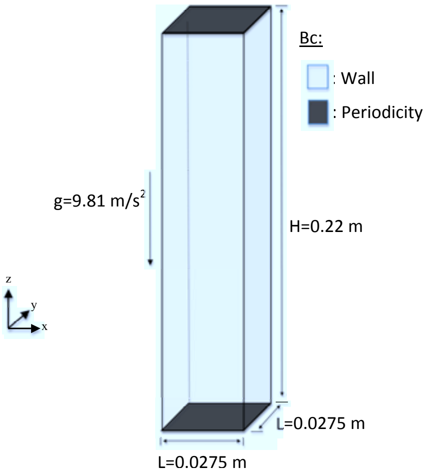

FIG. 5.1: Sketch of the computational domain [96]

different boundary conditions for the solid phase which are free-slip, partial-slip which requires a particle-wall restitution coefficient and no-slip conditions. Meso-scale structures were observed in all cases. In the case here studied, no-slip condition for the gas and free-slip condition for the particulate phase, at the wall, are retained. The velocity fields are initially set to zero for all phases. Due to the imposed pressure gradient, the movement of the fluid is opposite to the gravity.

To ensure periodicity of simulations, it is necessary to maintain momentum in the whole domain at each time step. Hence, a term, F_i, representing a source term, is added in momentum equation of gas and particle phases. Considering the periodicity and F_i independence from the filter width, integration of the momentum equation Eq. (3.5) over the whole domain V leads to:

$$\begin{aligned} \int \frac{D\alpha_k \rho_k U_{k,z}}{Dt} dV &= -\int \alpha_k \rho_k g_z dV + \int \frac{\partial \Sigma_{k,zj}}{\partial x_j} dV \\ &+ \int I_{f\to k} dV + \int \sum_q I_{q\to k} dV + \int \alpha_k F_z dV, \end{aligned} \tag{5.1}$$

and

$$\int \frac{\partial \Sigma_{k,zj}}{\partial x_j} dV = \int_S \Sigma_{k,zj} n_j dS = \int_{S_{in}} \Sigma_{k,zj} n_j dS + \int_{S_{out}} \Sigma_{k,zj} n_j dS + \int_{S_{wall}} \Sigma_{k,zj} n_j dS$$

According to the periodic boundary condition, $\int_{S_{in}} \Sigma_{k,zj} n_j dS = \int_{S_{out}} \Sigma_{k,zj} n_j dS$ and the term $\int_{S_{wall}} \Sigma_{k,zj} n_j dS$ corresponds to the wall friction effect. Considering the free-slip condition for the particles, such a term is null for the solid phase. For the fluid, as no-slip boundary condition is applied ledaing to a global wall effort, $H_{w\to g}$. The sum of the Eq. (5.2) for each phase gives the total momentum in the domain, as:

$$\frac{DQ}{Dt} = -\sum_k m_k g_z + F_z V + H_{w\to g}, \tag{5.2}$$

where Q is defined by $\sum \langle \alpha_k \rho_k U_{k,z} \rangle$ and m_k is the total mass of phase k, which remains unchanged. Indiscrete form, this equation is written:

$$\frac{Q^n - Q^{n-1}}{\Delta t} = -\sum_k m_k g_z + F_z^n V + H_{w\to g}^n. \tag{5.3}$$

where m_k is a constant.

According to the given momentum condition, the term on the left-hand side of the equation (5.3) should satisfy: $Q^n = Q^0$. Therefore,the source term for the next time step is chosen in order to insure the given momentum condition:

$$F_z^{n+1} = F_z^n + \Delta F_z^n \tag{5.4}$$

$$\Delta F_z^n = \frac{Q^0 - Q^n}{\Delta t V} \tag{5.5}$$

For $n = 1$, we impose $F_z^1 = \sum_k m_k g_z$ and $Q^0 = 0$.

For the cases studied, materials properties are given in the Tab. 5.1 and Tab. 5.2 for bidisperse and monodisperse simulations. $\alpha_{p,ini}$ represents the initial solid volume fraction in the periodic circulating fluidized bed. W_{wall} corresponds to the velocity of the wall, which affects the fluid velocity. For all cases, the fluid is treated as laminar and the drag force is modelled by the correlation developed by Wen and Yu[139]. Case B1 and case B2 enable to investigate the effect of the solid volume fraction ratio on the budget analysis. Whereas case B1 and case B3 focus on the effect of the diameter ratio. The properties of the fluid phase, $\rho_f = 1.186\,kg/m^3$ and $\mu_f = 1.8 \cdot 10^{-5}\,Pa \cdot s$.

TAB. 5.1: Particles properties for bidisperse cases

Cases		B1	B2	B3	B4
Particle p	$\rho_p\,[kg/m^3]$	1500	1500	1500	1500
	$d_p\,[\mu m]$	75	75	75	75
	$\alpha_p\,[\%]$	5	9	5	8
Particle q	$\rho_q\,[kg/m^3]$	1500	1500	1500	1500
	$d_q\,[\mu m]$	150	150	112.5	112.5
	$\alpha_q\,[\%]$	5	1	5	2

TAB. 5.2: Particle properties for monodisperse cases

Cases	M1	M2	M3	M4	M5	M6	M7
$\rho_p\,[kg/m^3]$	1500	1500	1500	1500	1500	3000	6000
$W_{wall}\,[m/s]$	0	0	0	5	10	0	0
$d_p\,[\mu m]$	75	112	150	75	75	75	75
$\alpha_{p,ini}\,[m^3/m^3]$	0.05	0.05	0.05	0.05	0.05	0.05	0.05

Three-dimensional numerical simulations of the fluidized bed have been carried out using an Eulerian n-fluid modeling approach for gas-particle turbulent polydisperse flows developed and implemented by IMFT (Institut de Mécanique des Fluides de Toulouse). NEPTUNE_CFD is a multiphase flow software developed in the framework of the NEPTUNE project, financially supported by CEA (Commissariat à l'Energie Atomique), EDF (Electricité de France), IRSN (Institut de Radioprotection et de Sureté Nucléaire) and AREVA_NP. The numerical solver has been developed for High Performance Computing [92, 91].

In a monodisperse case with $d_p = 75\mu m$, Ozel [96] investigated the effect of the mesh refinement on the average gas-particle velocity, the total mass flux and the random kinetic energy of solid phase. The mesh refinement was expressed in term of the Froude number, which is written as:

$$Fr_\Delta^{-1} = \frac{(\Delta_x \Delta_y \Delta_z)^{\frac{1}{3}}}{(\tau_p^{St})^2 |g|} \tag{5.6}$$

If Froude number Fr_{Δ}^{-1} is below 0.1, then the average gas-particle velocity, the total mass flux and the random kinetic energy change slightly. They tend to constant values. In the present work, three meshes have been studied and the finest mesh involved around $7.1 \cdot 10^{6}$ cells, each having a size of $2.9 \cdot 10^{-4}$ m, and Froude number equal to $Fr_{\Delta}^{-1} = 0.043$. This cell-size corresponds mesh-independent simulations for the smallest particles of the bidisperse case studied. Hence, this mesh will be used for the budget analysis. The budget analysis has already been conducted on monodiserse simulations [99, 102]. Hence, in the following section, only budget analysis of bidisperse simulations will be presented.

5.3 Budget analysis for bidisperse case

Mesh independent results are used for the budget analysis of the filtered particle momentum and agitation equations. The aim of the analysis is to assess the contribution of sub-grid terms obtained by filtering equations. To reach this goal, different filter widths, Δ_f, have been applied to the results. The domain studied is restricted to the interior of the periodic box and regions near the wall are not accounted for. such a domain ensure that the temporally and spatially averaged values of the filtered variables $\tilde{\alpha}_k$, $\tilde{\alpha}_k \tilde{U}_{k,i}$, $\tilde{\alpha}_k \tilde{q}_k^2$, as averaged value of the filtered contributions, are indepedent of the filter width. The distance between the wall and the domain studied is set to $\delta = 0.1L$, where L is the square section of the periodic box. Depending of the filter width, Δ_f, the domain studied can also varies. Thus, the domain is restricted to the one studied with the largest filter size.

5.3.1 Particle momentum budget

After filtering (Eq. (4.4)) and averaging each term over space, $\langle f \rangle$, and time, $\bar{f}$, the momentum equation of the particles of class p becomes:

$$\begin{aligned}
\overline{\langle \tilde{\alpha}_p \rho_p \tilde{U}_{p,j} \frac{\partial \tilde{U}_{p,i}}{\partial x_j} \rangle} = & - \overline{\langle \frac{\partial}{\partial x_j} \Sigma_{p,ij}^{res} \rangle} - \overline{\langle \frac{\partial}{\partial x_j} \Sigma_{p,ij}^{sgs} \rangle} \\
& + \overline{\langle \tilde{\alpha}_p \rho_p g_i \rangle} - \overline{\langle \tilde{\varphi}_{p,i}^{res} \rangle} - \overline{\langle \varphi_{p,i}^{sgs} \rangle} \\
& + \overline{\langle I_{f \to p,i}^{res} \rangle} + \overline{\langle I_{f \to p,i}^{sgs} \rangle} \\
& + \overline{\langle \sum_q I_{q \to p,i}^{res.} \rangle} + \overline{\langle \sum_q I_{q \to p,i}^{sgs} \rangle} \\
& - \overline{\langle \frac{\partial}{\partial x_j} \rho_p \tilde{\alpha}_p \sigma_{p,ij}^{sgs} \rangle}
\end{aligned} \tag{5.7}$$

In the momentum equation, subgrid contributions of the particle kinetic stress, $\Sigma_{p,ij}^{sgs}$, the gas-particle momentum transfer, $I_{f \to p,i}^{sgs}$, and particle-particle momentum transfer, $I_{q \to p,i}^{sgs}$, are similarly computed. The resolved and subgrid contributions of the gas-particle momentum transfer, the particle-particle momentum transfer and the pressure gradient are normalized by the gravity term. Those contributions are depicted for the case B1 in Figures 5.2 and 5.3 for small and large particles respectively.

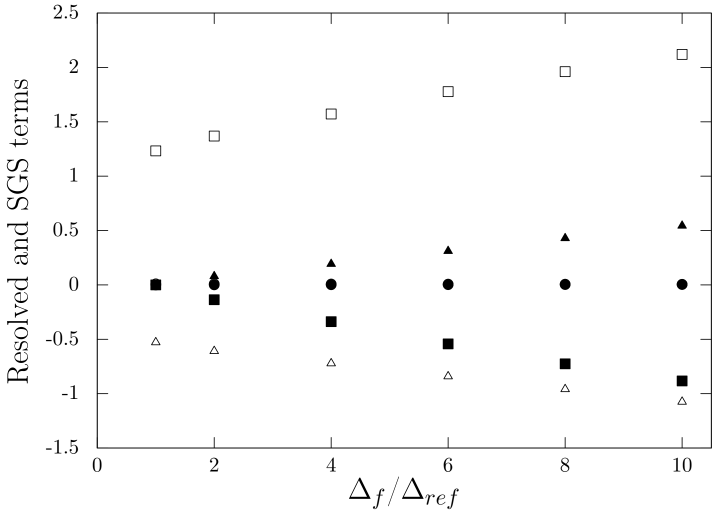

FIG. 5.2: Resolved and sub-grid contributions (normalized by $\tilde{\alpha}_p\rho_p g_z$) in the particle momentum filtered transport equation for $d_p = 75\mu m$ for various filter widths Δ_f for case B1. The symbols represent □: $I^{res}_{f\rightarrow p,i}$, ■: $I^{sgs}_{f\rightarrow p,i}$, ○: $\varphi^{res}_{p,i}$, ●: $\varphi^{sgs}_{p,i}$, △: $I^{res}_{q\rightarrow p,i}$ and ▲: $I^{sgs}_{q\rightarrow p,i}$

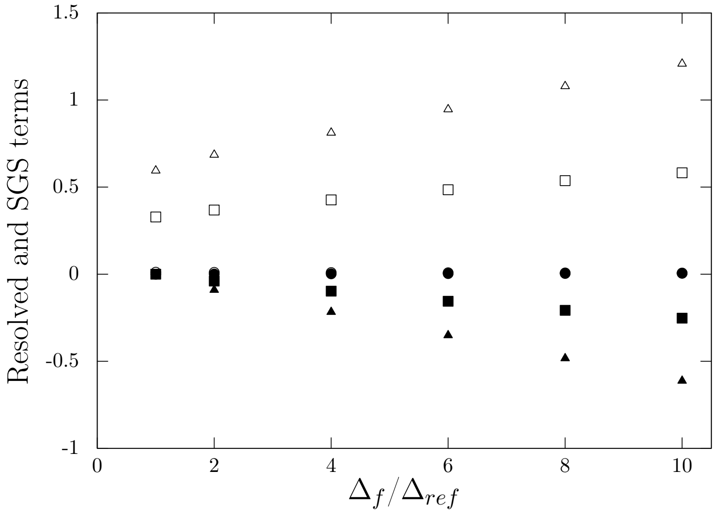

FIG. 5.3: Resolved and sub-grid contributions (normalized by $\tilde{\alpha}_q\rho_q g_z$) in the particle momentum filtered transport equation for $d_q = 150\mu m$ for various filter widths Δ_f for case B1. The symbols represent □: $I^{res}_{f\rightarrow q,i}$, ■: $I^{sgs}_{f\rightarrow q,i}$, ○: $\varphi^{res}_{q,i}$, ●: $\varphi^{sgs}_{q,i}$, △: $I^{res}_{p\rightarrow q,i}$ and ▲: $I^{sgs}_{p\rightarrow q,i}$

For both particle species, the resolved and sub-grid contributions of the pressure gradient can be neglected in comparison to the others contributions. As for the pressure gradient, the sub-grid contributions of the kinetic stress and the particle phase velocity fluctuations are negligible for both the particle species. For small particles, the main contribution is the drag force. Whereas for large particles, this is the inter-particle momentum transfer.

Furthermore, the sub-grid gas-particle momentum transfer increases with the filter width, in agreement with the work of Ozel et al. [99]. For both particles species, the filtered gas-momentum transfer is overestimated by the resolved contribution and the subgrid contribution must be accounted for to correct this effect. The trend is similar for the particle-particle momentum transfer with an overestimation of the inter-species momentum transfer effect by the resolved contributions. Hence, such an effect should be accounted for by developing a model for the subgrid contribution of the particle-particle momentum transfer. Such an overestimation might appear to be in contradiction with coarse mesh simulation of bidisperse gas-solid fluidized beds [11] where the inter-particle momentum transfer effects are underestimated. The probable explanation of this inconsistency is that the resolved collision frequency, and the corresponding momentum transfer, are underestimated due to a drastic undervaluation of the resolved random particle kinetic energy in coarse mesh simulations. As a consequence, it is crucial to analyse the corresponding filtered equation to identify the missing contribution that should be accounted for to better predict the random particle kinetic energy.

Budget analysis has also been performed for the case B2 ($\alpha_{p,ini} = 9\%$ and $\alpha_{q,ini} = 1\%$). Figures 5.4 shows the subgrid and the resolved contributions of the pressure gradient, the drag force and the particle-particle momentum transfer normalized by the gravity contribution for the small particles. The gas-particle momentum transfer and the particle-particle momentum transfer appear overestimated by the resolved contribution. Those overestimation are similar to the case B1. However, the resolved contributions of the particle-particle momentum transfer for small particles is significantly lower in case B2 than in case B1. Such a difference can probably be explained by a lower amount of particle q in case B2 with respect to case B1. This leads to a less significant transfer of momentum with class q in case B2. Contrary to the particle-particle momentum transfer, the gas-particle transfer remains in the same order of magnitude. Hence, decreasing the large particles volume fraction increases significantly the contribution of the gas-particle momentum transfer in the momentum equation for small particles. Such a result is consistent with the study of binary particle mixtures with large particle diameter ratio performed by Nouyrigat [95]. For large particles, Figure 5.5 shows that the resolved contributions drag and the particle-particle momentum transfer increases with the filter size, which is similar to case B1. Unlike contributions in the case of small particles, the particle-particle momentum transfer is more significant than the gas-particle momentum transfer.

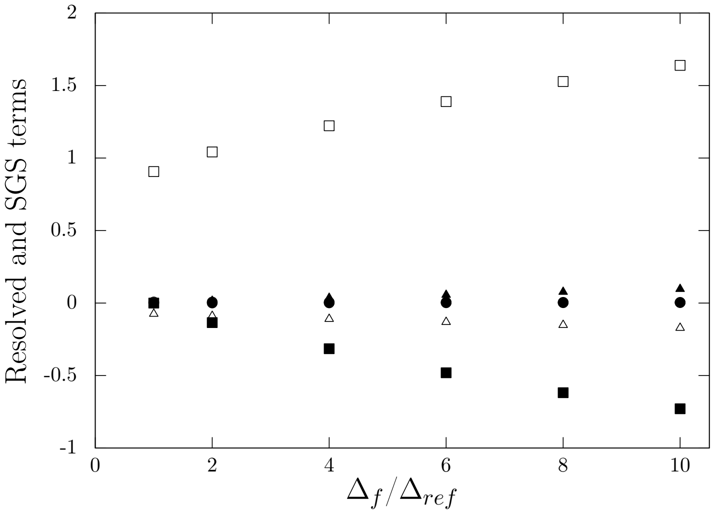

FIG. 5.4: Resolved and sub-grid contributions (normalized by $\tilde{\alpha}_p\rho_p g_z$) in the particle momentum filtered transport equation for $d_p = 75\mu m$ for various filter widths Δ_f for case B2. The symbols represent □: $I^{res}_{f\rightarrow p,i}$, ■: $I^{sgs}_{f\rightarrow p,i}$, ○: $\varphi^{res}_{p,i}$, ●: $\varphi^{sgs}_{p,i}$, △: $I^{res}_{q\rightarrow p,i}$ and ▲: $I^{sgs}_{q\rightarrow p,i}$

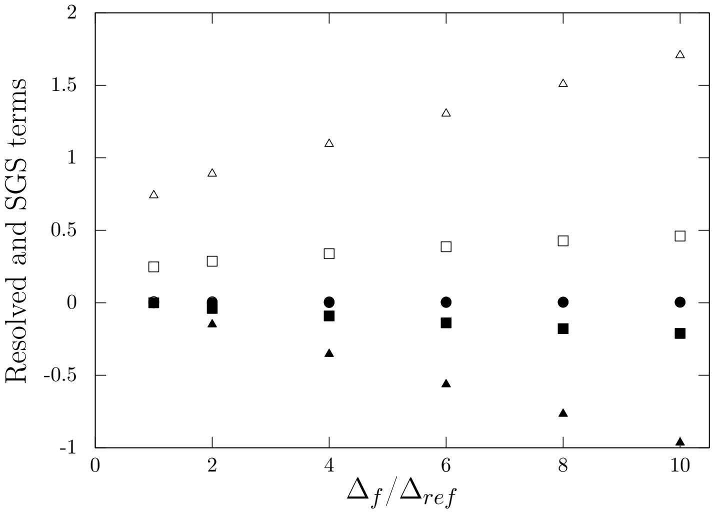

FIG. 5.5: Resolved and sub-grid contributions (normalized by $\tilde{\alpha}_q\rho_q g_z$) in the particle momentum filtered transport equation for $d_q = 150\mu m$ for various filter widths Δ_f for case B2. The symbols represent □: $I^{res}_{f\rightarrow q,i}$, ■: $I^{sgs}_{f\rightarrow q,i}$, ○: $\varphi^{res}_{q,i}$, ●: $\varphi^{sgs}_{q,i}$, △: $I^{res}_{p\rightarrow q,i}$ and ▲: $I^{sgs}_{p\rightarrow q,i}$

5.3.2 Particle random kinetic energy budget

After the time and spatial averaging, the filtered energy balance can be written as:

$$\begin{aligned}
\overline{\langle \tilde{\alpha}_p \rho_p \tilde{U}_{k,j} \frac{\partial \tilde{q}_p^2}{\partial x_j} \rangle} =& \overline{\langle \frac{\partial}{\partial x_j} D_j^{res} \rangle} + \overline{\langle \frac{\partial}{\partial x_j} D_j^{sgs} \rangle} \\
&+ \overline{\langle \Pi_p^{res} \rangle} + \overline{\langle \Pi_p^{sgs} \rangle} \\
&- \overline{\langle \epsilon_{fp}^{res} \rangle} - \overline{\langle \epsilon_{fp}^{sgs} \rangle} \\
&+ \overline{\langle \sum_q \epsilon_c^{res} \rangle} + \overline{\langle \sum_q \epsilon_c^{sgs} \rangle} \\
&+ \overline{\langle \sum_q P_{pq}^{res} \rangle} + \overline{\langle \sum_q P_{pq}^{sgs} \rangle} \\
&+ \overline{\langle \sum_q T_p^{res} \rangle} + \overline{\langle \sum_q T_p^{sgs} \rangle} \\
&- \overline{\langle \frac{\partial}{\partial x_j} \alpha_p \rho_p Q_j^{sgs} \rangle}
\end{aligned} \tag{5.8}$$

In the following figures, the resolved and the subgrid contributions are normalized by $\tilde{\alpha}_p \rho_p V_{p,St}^2 / \tau_{p,St}$, with $\tau_{p,St} = \frac{\rho_p}{\rho_f} \frac{d_p^2}{18 \nu_f}$ and $V_{p,St} = \tau_{p,St} |\mathbf{g}|$. The mean velocity and diffusive transport and the sub-grid particle kinetic energy flux are negligible compared to the others contributions. Figures 5.6 and 5.7 depict resolved and subgrid contributions of the production by gradient, the dissipation by friction with the gas phase and the sum of all the collisions terms according to the filter size. For the small particles, Figure 5.6 shows that the production by the mean velocity gradient is mostly in equilibrium with the dissipation by the fluid-particle drag and, secondarily, by inter-particle collision effects. For large particles, the filtered random kinetic energy equation is dominated by the equilibrium between mean velocity production and dissipation by collision effects. However the dissipation by friction can be considered as negligible in respect with the others terms.
The resolved production by velocity gradient underestimates the filtered production for both particle species. Hence, the resolved production should be completed by a subgrid contribution. The subgrid contribution of the dissipation by friction with gas phase is negligible. In contrast, the resolved contribution of the sum of the collision terms underestimates the filtered sum of collision terms for small particles. For large particles, the collision effect is overestimated by the resolved contribution. Hence, the contributions of each collision term in Eq. (5.8) should be quantified.

Figures 5.8 and 5.9 show the dissipation by inelastic collision, the production by relative velocity, the transfer by collisions as functions of the filter width for small and large particles respectively. For small particles, the filtered production by the mean relative velocity between particle species is overestimated by the resolved production. Thus, the subgrid effect must be accounted for in the filtered modelling approach. In contrast, the resolved kinetic energy transfer between particle species and the inelastic dissipation rate are nearly independent from the mesh size implying negligible subgrid contributions. For large particles, the subgrid effect are mostly observed for the transfer by collision in Figure 5.7. For both particle species, the production by the mean relative particle motion, is the smallest

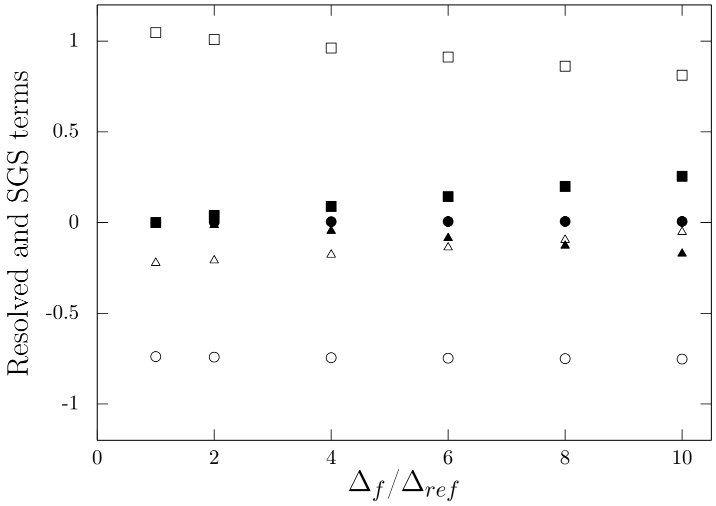

FIG. 5.6: Resolved and sub-grid contributions (normalized by $\tilde{\alpha}_p \rho_p V_{p,St}^2/\tau_{p,St}$) in the random particle kinetic energy filtered transport equation for $d_p = 75\mu m$ for various filter widths Δ_f for case B1. The symbols represent □: Π_p^{res}, ■: Π_p^{sgs}, ○: ϵ_{fp}^{res}, ●: ϵ_{fp}^{sgs}, △: $coll^{res}$ and ▲: $coll^{sgs}$

.

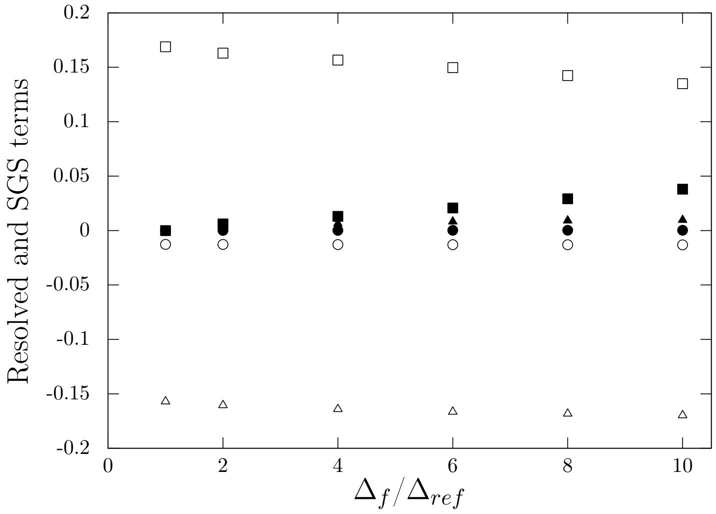

FIG. 5.7: Resolved and sub-grid contributions (normalized by $\tilde{\alpha}_q \rho_q V_{q,St}^2/\tau_{q,St}$) in the random particle kinetic energy filtered transport equation for $d_q = 150\mu m$ for various filter widths Δ_f for case B1. The symbols represent □: Π_q^{res}, ■: Π_q^{sgs}, ○: ϵ_{fq}^{res}, ●: ϵ_{fq}^{sgs}, △: $coll^{res}$ and ▲: $coll^{sgs}$.

contribution of all collision terms. Such a result is consistent with the values of z, which are mostly below 0.1. Such values mean that the inter-species collisions are driven by the relative agitation and not by the relative motion between particles.

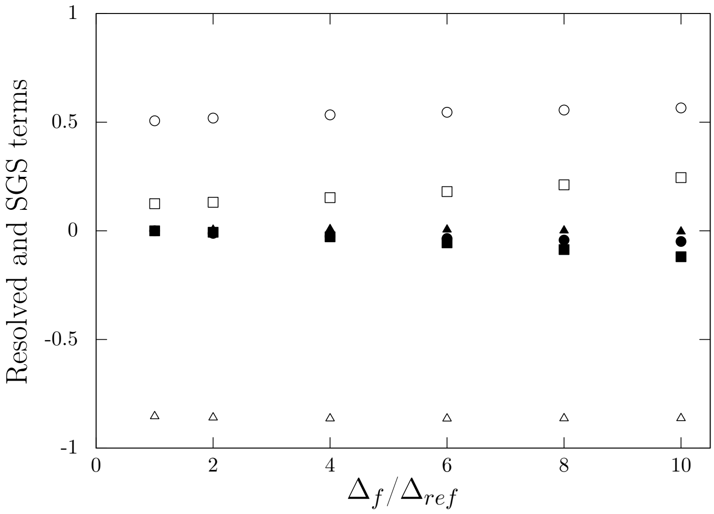

FIG. 5.8: Resolved and sub-grid collision contributions (normalized by $\tilde{\alpha}_p\rho_p V^2_{p,St}/\tau_{p,St}$) in the random particle kinetic energy filtered transport equation for $d_p = 75\mu m$ for various filter widths Δ_f for case B1. The symbols represent □: Π^{res}_{pq}, ■: Π^{sgs}_{pq}, ○: T^{res}_{pq}, ●: T^{sgs}_{pq}, △: $\sum_q \epsilon^{res}_{pq}$ and ▲: $\sum_q \epsilon^{sgs}_{pq}$.

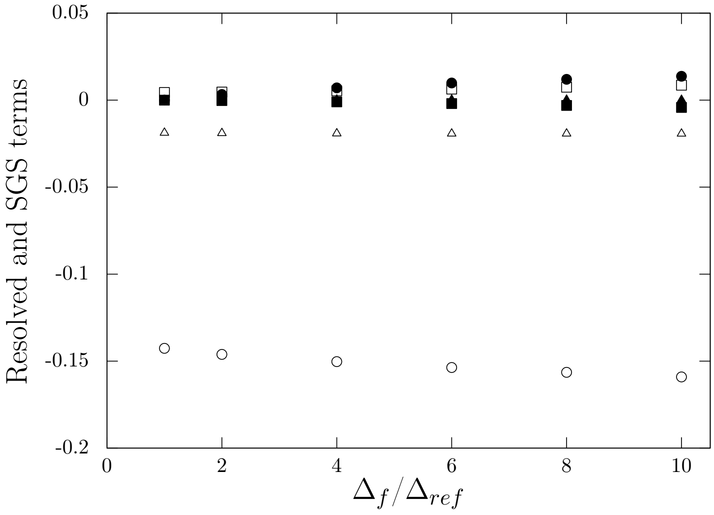

FIG. 5.9: Resolved and sub-grid collision term contributions (normalized by $\tilde{\alpha}_q\rho_q V^2_{q,St}/\tau_{q,St}$) in the random particle kinetic energy filtered transport equation for $d_q = 150\mu m$ for various filter widths Δ_f for case B1. The symbols represent □: Π^{res}_{qp}, ■: Π^{sgs}_{qp}, ○: T^{res}_{qp}, ●: T^{sgs}_{qp}, △: $\sum_q \epsilon^{res}_{qp}$ and ▲: $\sum_q \epsilon^{sgs}_{qp}$.

Figures 5.10 and 5.11 show the resolved and subgrid contribution of the production by velocity gradient, the dissipation by friction with the gas phase and the sum of all the collisions terms in the case B2 for small and large particles respectively. Similarly to the case B1, the resolved production tends to be underestimated for large filter size for both particle diameters. For small particles, the dissipation with the gas phase and the sum of the effects of collision have the same order of magnitude. The effect of collision takes into account the collision between two particles with the same diameter and with two different diameters. The number of particles is larger for this case than for the case B1. This difference could explain why the effects of collisions is more significant for the case B2 than for the case B1. For the large particles, Figure 5.11 shows that the production by velocity gradient is mostly in equilibrium with the sum of the effects of collisions. Such a result is similar to the case B1.

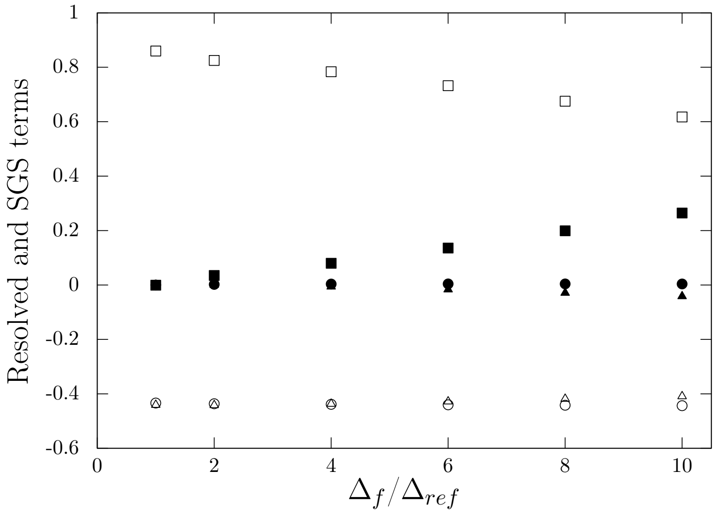

FIG. 5.10: Resolved and sub-grid contributions (normalized by $\tilde{\alpha}_p\rho_p V_{p,St}^2/\tau_{p,St}$) in the random particle kinetic energy filtered transport equation for $d_p = 75\mu m$ for various filter widths Δ_f for case 2. The symbols represent □: Π_p^{res}, ■: Π_p^{sgs}, ○: ϵ_{fp}^{res}, ●: ϵ_{fp}^{sgs}, △: $coll^{res}$ and ▲: $coll^{sgs}$.

Figures 5.12 and 5.13 show the dissipation by inelastic collision, the production by relative velocity, the transfer by collisions as functions of the filter width in the case B2 for small and large particles respectively. For small particles, the filtered production by the mean relative velocity between particle species is overestimated by the resolved production similarly to the case B1. The subgrid contributions of the transfer by collision and dissipation by collision increase similarly to the subgrid contribution of the production by velocity gradient. Those subgrid contributions are more significant in the case B2 than in the case B1 with respect to the subgrid contribution of the production by relative velocity. It could be explained by the fact that the highest amount of small particles in case B2 leads to velocity of large particles closer to the velocity of small particles. Hence the relative velocity is less important the case B2 than in the case B1. For large particles, the subgrid effect are mostly observed for the transfer by collision in Figure 5.11. For both particle species, the production by the mean relative particle motion is the smallest contribution of all collision terms. Such a result is similar to the case B1.

Figures 5.14 and 5.15 depict the resolved and subgrid contributions of the dissipation of

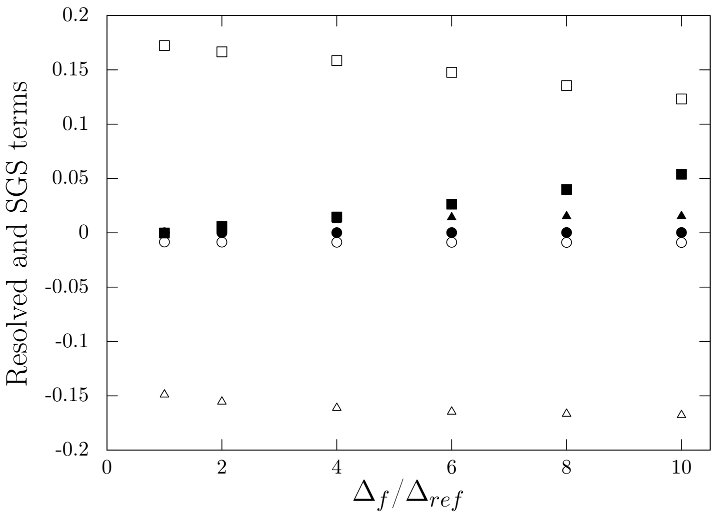

FIG. 5.11: Resolved and sub-grid contributions (normalized by $\tilde{\alpha}_q \rho_q V^2_{q,St}/\tau_{q,St}$) in the random particle kinetic energy filtered transport equation for $d_p = 150\mu m$ for various filter widths Δ_f for case B2. The symbols represent □: Π_q^{res}, ■: Π_q^{sgs}, ○: ϵ_{fp}^{res}, ●: ϵ_{fp}^{sgs}, △: $coll^{res}$ and ▲: $coll^{sgs}$.

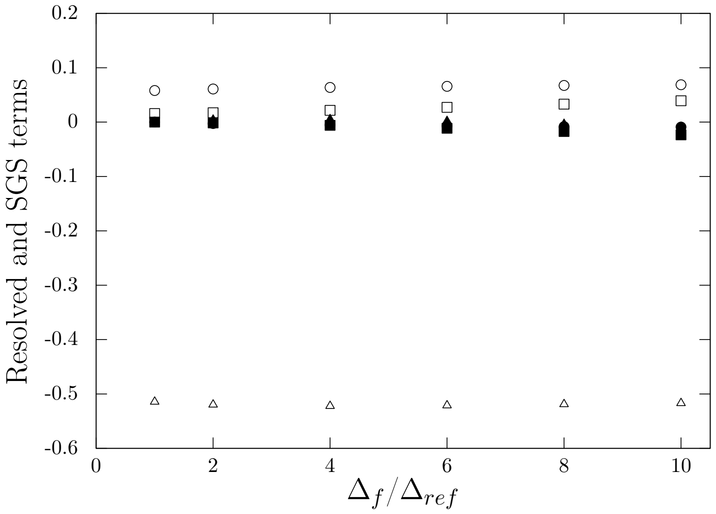

FIG. 5.12: Resolved and sub-grid collision term contributions (normalized by $\tilde{\alpha}_p \rho_p V^2_{p,St}/\tau_{p,St}$) in the random particle kinetic energy filtered transport equation for $d_p = 75\mu m$ for various filter widths Δ_f for case B2. The symbols represent □: Π_{pq}^{res}, ■: Π_{pq}^{sgs}, ○: T_{pq}^{res}, ●: T_{pq}^{sgs}, △: $\sum_q \epsilon_{pq}^{res}$ and ▲: $\sum_q \epsilon_{pq}^{sgs}$.

kinetic energy between particles of the same class, ϵ_{pp} or ϵ_{qq}, and dissipation due to collision of particles of different classes, ϵ_{pq} or ϵ_{qp}, for the small and large particles respectively for case B2. For the small particles, the dissipation collisions is mainly due to collision of particles of the same class. On the contrary, the dissipation by collision for large particles

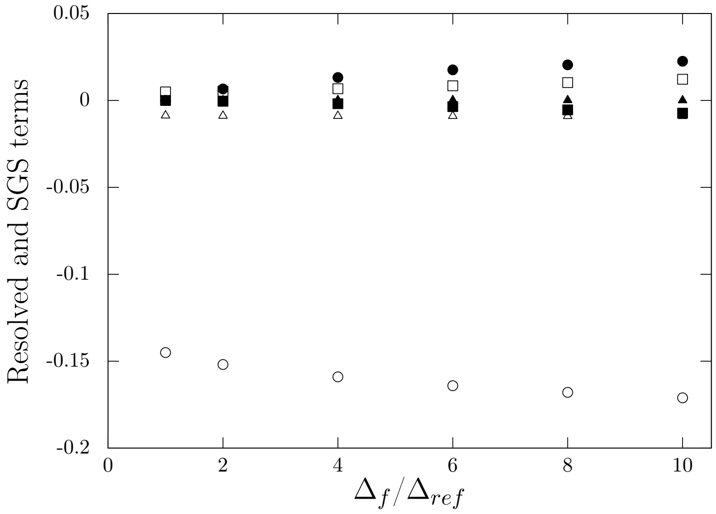

FIG. 5.13: Resolved and sub-grid collision term contributions (normalized by $\tilde{\alpha}_q\rho_q V_{q,St}^2/\tau_{q,St}$) in the random particle kinetic energy filtered transport equation for $d_p = 150\mu m$ for various filter widths Δ_f for case B2. The symbols represent □: Π_{qp}^{res}, ■: Π_{qp}^{sgs}, ○: T_{qp}^{res}, ●: T_{qp}^{sgs}, △: $\sum_q \epsilon_{qp}^{res}$ and ▲: $\sum_q \epsilon_{qp}^{sgs}$.

is driven by particles of different class. For both class of particles, the subgrid contributions can be neglected. Such results are also showed for the case B1. Figures 5.16 and

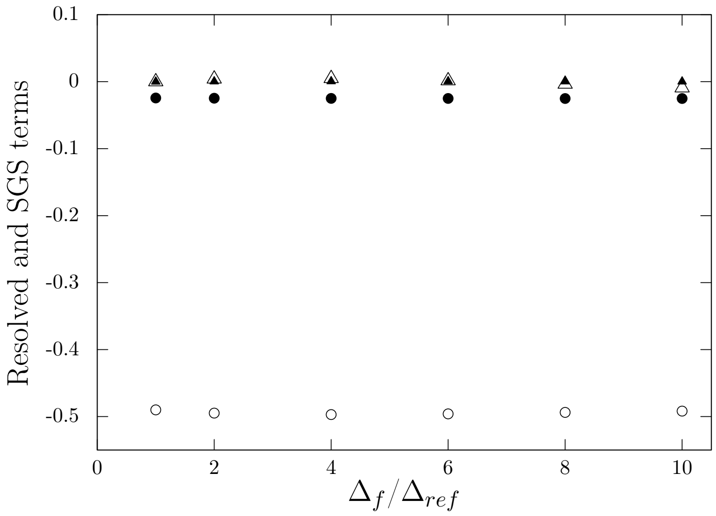

FIG. 5.14: Sub-grid contributions of ϵ_{pq} and ϵ_{pp} (normalized by $\tilde{\alpha}_p\rho_p V_{p,St}^2/\tau_{p,St}$) in the random particle kinetic energy filtered transport equation for the small particles, $d_p = 75\mu m$ for various filter widths Δ_f for case B2. The symbols represent ○: ϵ_{pp}^{res}, ●: ϵ_{pp}^{sgs}, △: ϵ_{pq}^{res} and ▲: ϵ_{pq}^{sgs}.

5.17 depict the subgrid contributions of the transfer by collision, the dissipation of inelastic

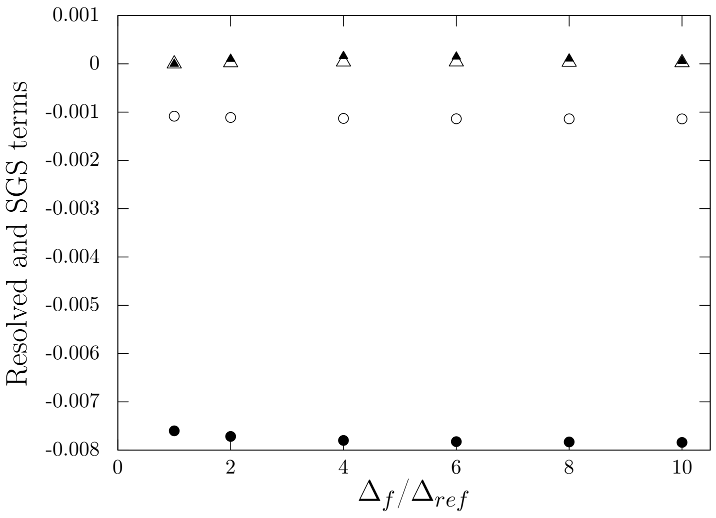

FIG. 5.15: Sub-grid contributions of ϵ_{pq} and ϵ_{qq} (normalized by $\tilde{\alpha}_q \rho_q V_{q,St}^2/\tau_{q,St}$) in the random particle kinetic energy filtered transport equation for the large particles, $d_p = 150\mu m$ for various filter widths Δ_f for case B2. The symbols represent ○: ϵ_{qq}^{res}, ●: ϵ_{qq}^{sgs}, △: ϵ_{qp}^{res} and ▲: ϵ_{qp}^{sgs}.

collision between particles of the same class ϵ_p and of the particles of different classes ϵ_{pq} for the case B1 and the case B2 respectively. The transfer by collision appear to be the main subgrid contribution in the case B1. However, all subgrid contributions are of the same order of magnitude in the case B2.

The same budget analysis has been carried out for Case B3 and trends similar to Case B1 are obtained. Hence, the solid volume fraction ratio does not affect the comparison of the different subgrid term and the main subgrid contributions, which needs to be modelled, remain the gas-particle and particle-particle momentum transfer and the production of particle agitation by velocity gradient. The subgrid contributions of transfer of kinetic agitation by collision, T_p, and the dissipation by collision, $\sum_q \epsilon_{pq}$, should also be investigated.

5.4 A priori analysis

5.4.1 Subgrid gas-particle momentum transfer term

The budget analysis shows that one of the main contribution of the particle momentum equation is the gas-particle momentum transfer. The filtered contribution of such term corresponds to, $\tilde{I}_{f\to k,i} = \widetilde{-\frac{\rho_k}{\tau_{fk}^F}\alpha_k V_{r,i}^{(p)}}$. Such a term tends to be be overestimated in coarse mesh simulations, and subgrid model has to be developed. A priori analysis are carried out in order to know which part of the drag force is the most affected by the mesh refinement and needs to be modelled. Correlations between filtered contributions and terms,

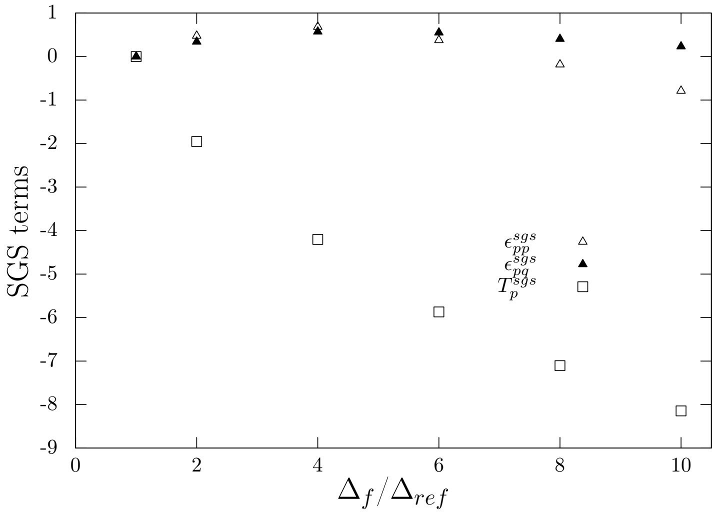

FIG. 5.16: Sub-grid contributions of kinetic energy transfer between particle species, T_p^{sgs}, and of the dissipation by collision, $\epsilon_{pq}^{s}gs$ and ϵ_{pp}^{sgs}, in the random particle kinetic energy filtered transport equation for case B1.

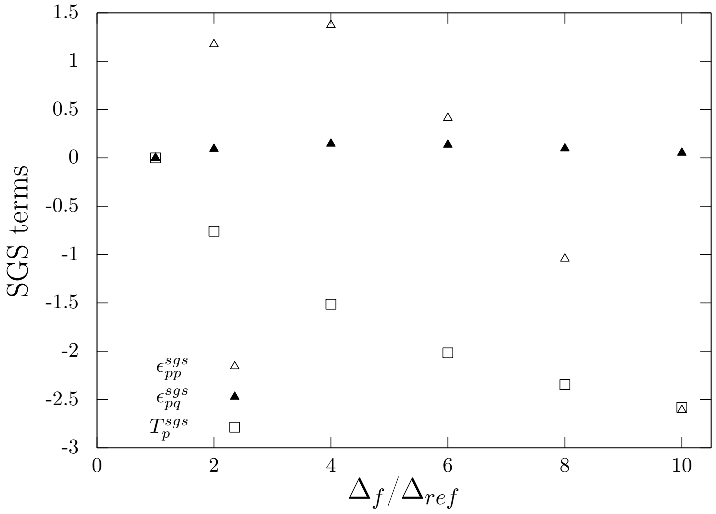

FIG. 5.17: Sub-grid contributions of kinetic energy transfer between particle species, T_p^{sgs}, and of the dissipation by collision, $\epsilon_{pq}^{s}gs$ and ϵ_{pp}^{sgs}, in the random particle kinetic energy filtered transport equation for case B2.

which include resolved and filtered terms, are analysed. Figure 5.18 depicts the correlation coefficients between the filtered contribution of gas-particle momentum transfer, $\tilde{I}_{f\rightarrow k,i}$, and the corresponding resolved contribution, $I_{f\rightarrow k,i}^{res}$, and also a term, which includes resolved and filtered terms. Such term, mixing filtered and resolved part, is noted with the

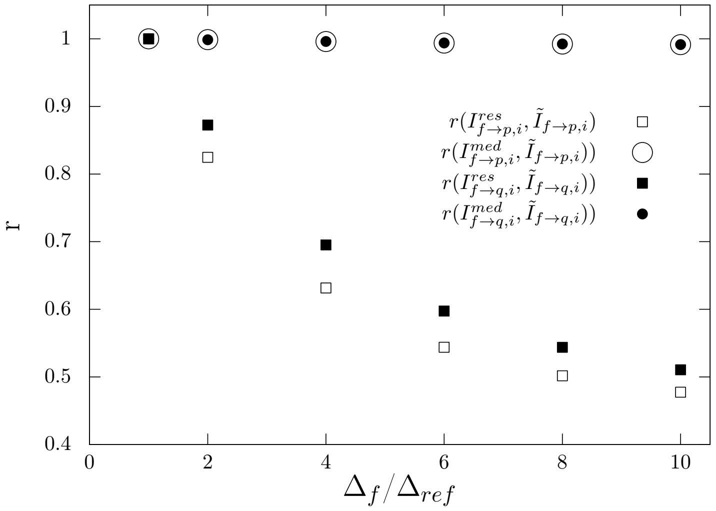

FIG. 5.18: Correlation coefficients for case B1with $I^{med}_{f\to p,i}$ given in Eq. (5.9) for the small particles, and $I^{med}_{f\to q,i}$ given in Eq. (5.9) for the large particles.

superscript med and is written as:

$$I^{med}_{f\to k,i} = -\frac{\rho_k}{\tau^{F,res}_{fk}} \widetilde{\alpha_k (U_{k,i} - U_{f,i})} \tag{5.9}$$

Considering two fields A and B, the Pearson correlation coefficient is defined as:

$$r = \frac{\langle AB\rangle - \langle A\rangle\langle B\rangle}{(\langle A^2\rangle - \langle A\rangle^2)(\langle B^2\rangle - \langle B\rangle^2)}$$

Figure 5.18 shows that if the correlation between resolved and filtered contribution decreases significantly as the filter size increase and reaches 0.5 for $\Delta_f/\Delta_{ref} = 10$ for both classes of particles. Such a decrease highlights the need of model for subgrid contribution. The correlation is significantly improved for both classes of particles when the expression given in Eq. (5.9) is used. Figure 5.19 indicates that the filtered drag force can be approximated by:

$$\tilde{I}_{f\to k,i} \approx -\frac{\rho_k}{\tau^{F,res}_{fk}} \widetilde{\alpha_p (U_{k,i} - U_{f,i})} \tag{5.10}$$

According to previous studies [101, 96], the drag force is decomposed as the difference between filtered velocities of solid and gas phases and the subgrid drift velocity. The filtered drag force is then modelled as:

$$\tilde{I}_{f\to k,i} = \frac{\tilde{\alpha}_k \rho_k}{\tau^{F,res}_{fk}} \left(\tilde{U}_{f,i} - \tilde{U}_{k,i} + V^{(k)}_{d,i}\right) \tag{5.11}$$

with

$$\alpha_k V^{(k)}_{d,i} = \widetilde{\alpha_k U_{f,j}} - \tilde{\alpha}_k \tilde{U}_{f,j} \tag{5.12}$$

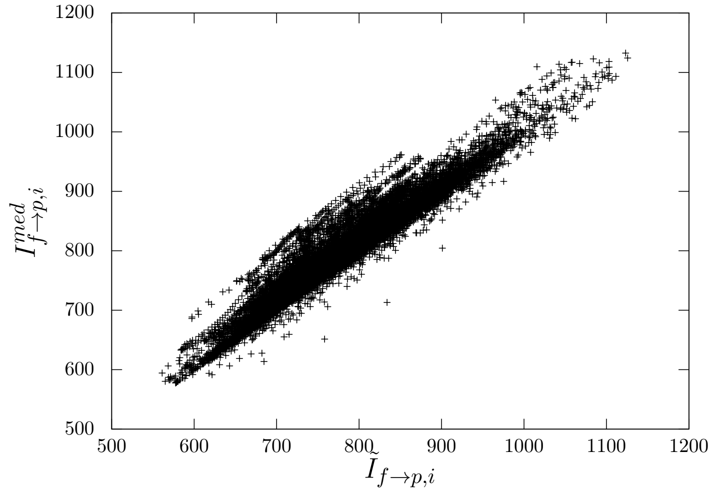

FIG. 5.19: Scattering plot of the expression given in Eq. (5.9) versus the filtered contribution for case B1.

Hence, the subgrid contribution of the drag force is written as:

$$I^{sgs}_{f\to k,i} \approx \frac{\rho_k}{\tau^{F,res}_{fk}} \tilde{\alpha}_k V^{(k)}_{d,i} \tag{5.13}$$

To model the subgrid contribution of the drag force, the focus will be given on $V^{(k)}_{d,i}$.

5.4.2 Subgrid inter-particle momentum transfer term

The inter-particle momentum transfer is one of the main contribution of the momentum equation. Figure 5.20 shows that the correlation between resolved and filtered contributions decreases significantly as the filter size increases. The subgrid contribution of the inter-particle momentum exchange term needs to be modelled . Using Eq. (3.2.3) and (3.10), the fitlered contribution of the particle-particle momentum transfer term is expressed as:

$$\tilde{I}_{q\to p,i} = -\widetilde{\frac{m_p m_q}{m_p + m_q}\frac{1+e_c}{2} n_p n_q g_r g_0 \pi d^2_{pq} H_1(z)\left(U_{p,i} - U_{q,i}\right)} \tag{5.14}$$

Similarly to the gas-particle momentum transfer force, correlation analysis is carried out to determine which part of the term is the most influenced by the cell-size. Several terms, calculated with resolved and filtered have been analysed. Figure 5.20 depicts correlation between filtered contribution and A_{qp} written as :

$$I^{med}_{q\to p,i} = -\frac{m_p m_q}{m_p + m_q}\frac{1+e_c}{2} \widetilde{n_p n_q (U_{p,i} - U_{q,i})} g^{res}_r g^{res}_0 \pi d^2_{pq} H_1(z^{res}) \tag{5.15}$$

In Figure 5.20, the correlation increases significantly when the expression Eq. (5.15) is considered. Figure 5.21 shows the filtered inter-particle collision term is approximated

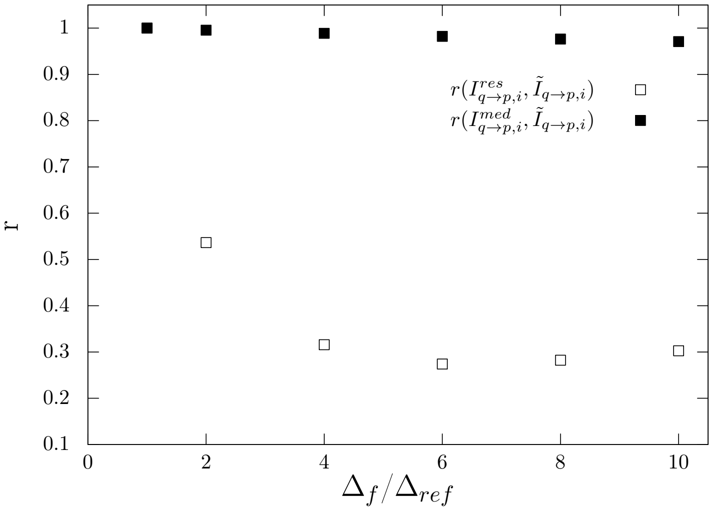

FIG. 5.20: Correlation coefficients for case B1 with A_{qp} given in Eq (5.15).

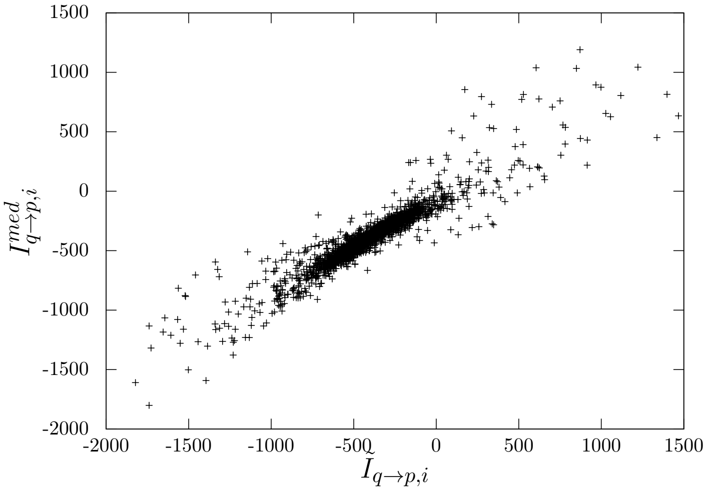

FIG. 5.21: Scattering plot of the expression given in Eq. (5.15) versus the filtered contribution for case B1.

by:

$$\tilde{I}_{q\to p,i} \approx -\frac{m_p m_q}{m_p+m_q}\frac{1+e_c}{2} g_r^{res} g_0^{res} \pi d_{pq}^2 H_1(z^{res}) \widetilde{n_p n_q \left(U_{p,i}-U_{q,i}\right)} \tag{5.16}$$

Similarly to the drag force, the filtered particle-particle drag force is written by using a subgrid velocity as follow:

$$\tilde{I}_{q\to p,i} \approx -\frac{m_p m_q}{m_p+m_q}\frac{1+e_c}{2}\tilde{n}_p\tilde{n}_q g_r^{res} g_0^{res} \pi d_{pq}^2 H_1(z^{res}) \left(\tilde{U}_{p,i}-\tilde{U}_{q,i}+V_{pq,i}\right)$$

Where $V_{pq,i}$ is the subgrid slip velocity, $\tilde{g}_r$, $\tilde{g}_0$ and z the resolved contributions of g_r, g_0 and z. Since mass and density of particles are independent of the filtering, then the filtered number of particle satisfies:

$$\tilde{n}_p m_p = \tilde{\alpha}_p \rho_p \tag{5.17}$$

Therefore, to model the subgrid contribution of the inter-particle momentum transfer, the focus can be given on $\alpha_p\alpha_q\left(U_{p,i}-U_{q,i}\right)$ instead of $n_p n_q\left(U_{p,i}-U_{q,i}\right)$. Hence, the subgrid particle relative flux can be expressed as:

$$V_{pq,i} = \frac{\widetilde{\alpha_p\alpha_q\left(U_{p,i}-U_{q,i}\right)}}{\tilde{\alpha}_p\tilde{\alpha}_q} - \left(\tilde{U}_{p,i}-\tilde{U}_{q,i}\right) \tag{5.18}$$

Then, the subgrid contribution of inter-particle momentum transfer is written as:

$$I^{sgs}_{p\rightarrow q,i} = -\frac{m_p m_q}{m_p+m_q}\frac{1+e_c}{2}\tilde{n}_p\tilde{n}_q g_r^{res} g_0^{res}\pi d_{pq}^2 H_1(z^{res})V_{pq,i} \tag{5.19}$$

5.4.3 Transfer by collision

The transfer of kinetic energy between particles particles species reads:

$$T_p = -\frac{m_p m_q}{m_p+m_q}\frac{1+e_c}{2}\frac{8}{3}g_0\pi\frac{d_p+d_q}{2}g_r n_p n_q\frac{m_p q_p^2 - m_q q_q^2}{m_p+m_q} \tag{5.20}$$

Figure 5.22 depicts the correlation coefficients between the filtered and the resolved contributions of the transfer between species, between filtered contribution and a term including resolved and filtering part:

$$T_p^{med} = -\frac{m_p m_q}{m_p+m_q}\frac{1+e_c}{2}\frac{8}{3}g_0\pi\frac{d_p+d_q}{2}g_r^{res}\widetilde{n_p n_q\frac{m_p q_p^2 - m_q q_q^2}{m_p+m_q}} \tag{5.21}$$

The filtered and resolved contributions are significantly correlated. The correlation coefficient of the filtered and resolved contributions of the fluid-particle and particle-particle momentum transfer are lower than the correlation coefficient between filtered and resolve contribution of the transfer of kinetic energy between classes. The correlation coefficient can be increased by taking into account the subgrid effect on $n_p n_q\frac{m_p q_p^2 - m_q q_q^2}{m_p+m_q}$. Such an effect is due to the influence on the cell-size on $n_p n_q q_p^2$ and $n_p n_q q_q^2$. The term of dissipation by collision $\sum_q \epsilon_{pq}$ should also be affected by this subgrid effect. The transfer between species is computed with the difference between $n_p n_q m_p q_p^2$ and $n_p n_q m_q q_q^2$ and the dissipation corresponds to the total $n_p n_q q_p^2$ and $n_p n_q q_q^2$. It could explain why one term is more affected by the subgrid effect than the other.

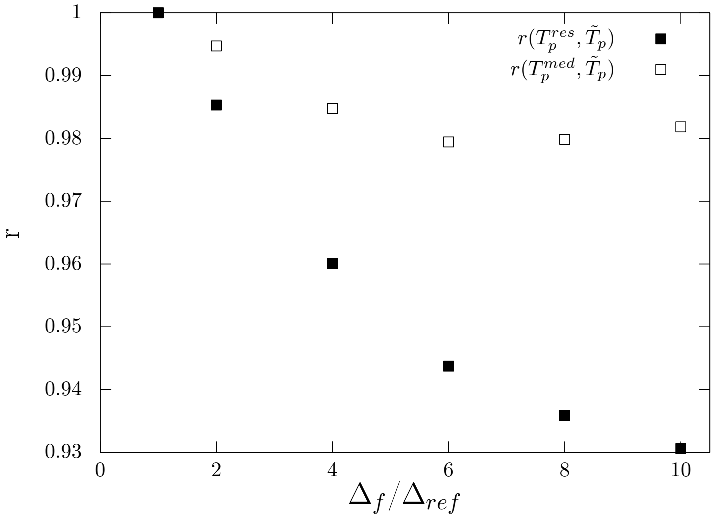

FIG. 5.22: Correlation for case B1with T_p^{med} given by Eq. (5.21)

Summary

Meso-scale structures, formed in the CFB , can be resolved in the frame of Euler-Euler approach, based on kinetic theory of polydisperse granular flows if highly-refined mesh are used. However, such simulations are expensive and coarse mesh simulations cannot account for these structures accurately, which may lead to very poor predictions of bed hydrodynamics for very small particle to mesh size ratio. For monodisperse gas-solid flows, Parmentier et al.[103] and Ozel et al. [99] analyse the influence of the small structures on the simulations for dense fluidised beds and CFB, respectively. In this chapter, the effects of unresolved structures on resolved field for bidisperse gas-solid flows have been investigated. First, mesh-independent results of gas-solid in a 3D periodic circulating fluidized bed have been obtained. A filtering procedure was performed on particulate momentum and kinetic agitation equations. Additional resolved and subgrid terms, arising with the filtering procedure, are studied by budget analysis in order to identify the main subgrid contributions. In the filtered momentum equation, the resolved fluid-particle drag and inter-particle collision are overestimating the momentum transfer effects. Hence, subgrid modelled contributions must be developed to predict accurately those two momentum transfer in coarse mesh simulations. The analysis of the budget of the filtered random kinetic energy indicates that the resolved production by the mean shear and production by relative motion are overestimated their resolved contributions. So new subgrid models have to be developed for these terms. Considering that the production by relative motion is significantly smaller than the production by the mean shear, the focus will be given on the subgrid contribution by the mean shear should be investigated first.

Chapter 6

Subgrid drag model

Contents

6.1 Introduction

The subgrid drift flux needs to be modelled in order to avoid an overestimation of the resolved gas-particle momentum exchange in coarse mesh simulations. An analogy can be drawn between the subgrid contribution of the gas-particle momentum transfer and the one of a scalar flux in single phase and turbulent flows. A widely-used functional model, taking into account the effect of the subgrid scale on the transported scalar, is the Smagorinsky model. Such a model relies on the eddy viscosity concept and is function of the rate-of-strain tensor and the scalar gradient:

$$T_i = -C_s \Delta^2 |S_{ij}| \frac{\partial \bar{\theta}}{\partial x_i} \quad \text{with} \quad S_{ij} = \frac{1}{2}\left(\frac{\partial \tilde{U}_{f,i}}{\partial x_j} + \frac{\partial \tilde{U}_{f,j}}{\partial x_i}\right)$$

Δ is the implicit filter width, $\tilde{U}_i$ corresponds to the Favre averaged velocity and $\bar{\theta}$ represents the averaged scalar. The smagorinsky coefficient, C_s, is determined by a constant. Dynamical model have been developed for the coefficient, C_s, instead of using a constant [43, 75].

Others approaches, such as the scale similarity model and the ones relying on Taylor series expansion, have been developed to model the subgrid drift flux. The filtered fields can be expressed as Taylor series in the filter width. This approach provides a good local approximation of the subgrid scalar flux in a priori studies. However, the main drawback of this approach is the instability resulting from inaccurate prediction of the dissipation. In scale similarity models, the full structures below the scale Δ are assumed similar to the ones above Δ. Those models require a second filter, whose width is higher or equal to Δ. Bardina et al. were the first to developed such a model with a filter width similar to the implicit filter width.

$$T_i = C_{ss}(\widehat{\bar{\theta}\tilde{U}_i} - \hat{\bar{\theta}}\hat{\tilde{U}}_i)$$

with $\hat{\cdot}$ representing the second filter. Then, Horiuti [58] and Layton et al. [73] suggested to use the filtered Bardina model, in which the filtering operation is applied to the modelled term. Then Liu et al. [77] extended the Bardina's Model to two different filters.

Other models combining functional and structural approaches have been developed. The gradient model combines the eddy viscosity model which the consists in expressing the subgrid scalar flux as a function of the gradient of the filtered scalar and of the filtered velocity. The coefficient can be dynamically adjusted. A mixed model combining scale similarity approach and Smagorinsky's model has been developed by Bardina et al. [9].

The subgrid drift velocity will be here developed following a priori analysis. Mesh independent results of monodisperse and polydisperse simulations enable to compute subgrid and filtered contributions similarly to the filtering operation applied to perform the budget analysis. The model obtained with the resolved contributions are compared to the subgrid values.

6.2 Monodisperse cases

6.2.1 Case description

Characteristics of the monodisperse simulations are described in Table 5.2. Such mesh-independent monodisperse simulations are used to determine the model of the subgrid velocity and analyse the effects of several characteristics of particle and gas velocities. Indeed, the budget analysis highlights the need for subgrid drag model. Similarly to the previous studies conducted by conducted by Ozel et al. and Parmentier et al. [99, 103], the correlation analysis shows that the filtered drag force can be approximated by:

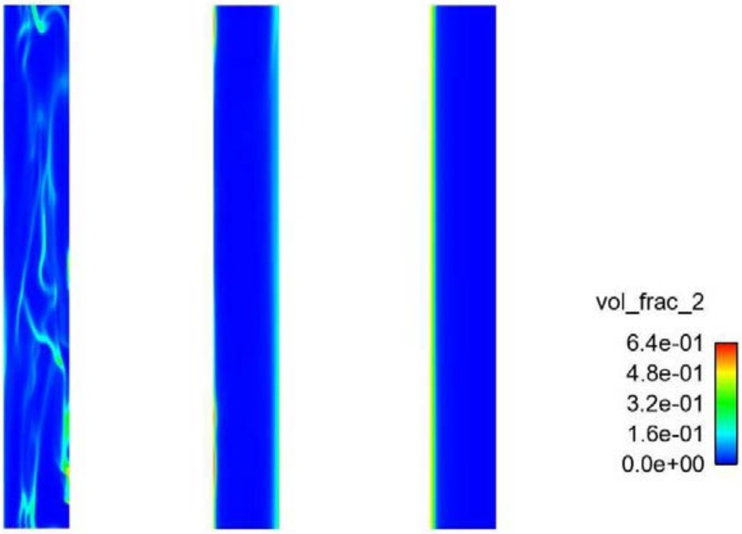

(a) (b) (c)

FIG. 6.1: Instantaneous fields of the solid volume fraction for several cases (a):M1, (b):M2, (c):M3

$$\tilde{I}_{f\to p,i} = \frac{\tilde{\alpha}_p \rho_p}{\tau_{fp}^{F,res}} \left(\tilde{U}_{f,i} - \tilde{U}_{p,i} + V_{d,i}^{(p)} \right) \tag{6.1}$$

with

$$\tilde{\alpha}_p V_{d,i}^{(p)} = \widetilde{\alpha_p U_{f,i}} - \tilde{\alpha}_p \tilde{U}_{f,i}. \tag{6.2}$$

Figure 6.2 shows the dependence of the subgrid velocity, $\tilde{\alpha}_p V_{d,i}^{(p)}$, on the resolved slip velocity, $\tilde{\alpha}_p(\tilde{U}_{f,j} - \tilde{U}_{p,j})$, with different filter widths. Such a dependency requires to model the subgrid drift flux as function of the resolved slip velocity. In addition, the subgrid contribution is assumed to be affected by the filter size and the solid phase amount in the cell, represented by the filtered solid volume fraction. Hence, the sugrid contribution is assumed being modelled by a form proposed by Ozel et al. [99] and Parmentier [103]:

$$V_{d,z}^{(p)} = g(\Delta_f, \alpha_p) K_{zz} \left(\tilde{U}_{f,z} - \tilde{U}_{p,z} \right) \tag{6.3}$$

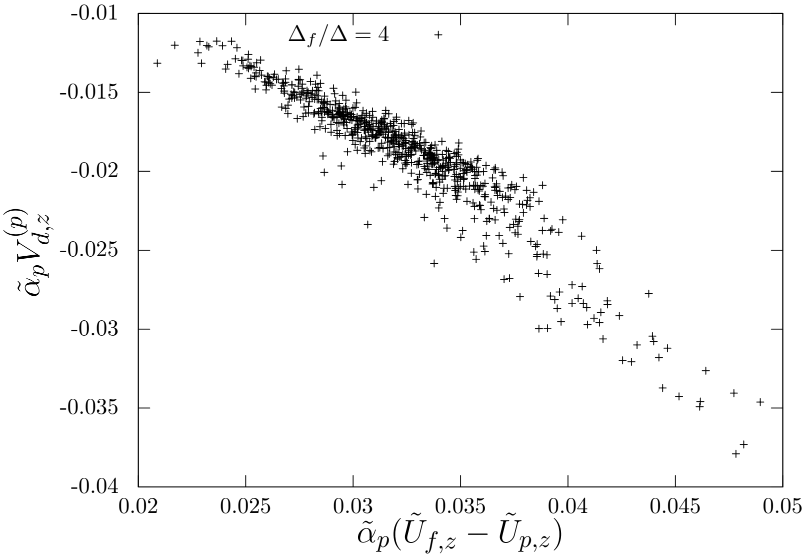

FIG. 6.2: Scattering plot of $\tilde{\alpha}_p V_{d,z}^{(p)}$ versus $\tilde{\alpha}_p(\tilde{U}_{f,z} - \tilde{U}_{p,z})$ for case B2

K_{zz} is the model constant and g is a function of the filtered particle volume fraction and a filter size. The constant is assumed to be diagonal. The function g will be determined using the refined simulations results and the constant K_{zz} will be dynamically adjusted following a method adapted from Germano et al. [43] and Lilly [75].

The first step to develop the model is a better understanding of the flow behaviour and the effects of the different diameters, densities and gas velocities. To achieve this goal, statistic quantities are averaged over the domain and in time after reaching the steady state. A domain averaged quantity of statistic value $Q_k(x,t)$ is noted $\langle Q_k \rangle$ and the corresponding temporal averaged value $\bar{Q_k}$ is given by:

$$\bar{Q_k} = \frac{\sum_{k=1}^{k=N_{time}} \alpha_k(\mathbf{x},t) Q_k(x,t)}{\sum_{k=1}^{k=N_{time}} \alpha_k(\mathbf{x},t)} \tag{6.4}$$

where N_{time} corresponds to the number of realization.

The domain averaged quantity is computed as:

$$\bar{Q}(\mathbf{x}) = \frac{\sum_{x=1}^{x=N_{cell}} \alpha(\mathbf{x},t) Q(\mathbf{x},t)}{\sum_{x=1}^{x=N_{cell}} \alpha(\mathbf{x},t)} \tag{6.5}$$

where N_{cell} is the time instant.

6.2.1.1 Particle diameter

First, the focus will be given on the particle diameter. Three different diameters, $75\,\mu m$, $112\,\mu m$ and $150\,\mu m$, which correspond respectively to cases M1, M2 and M3are retained.

Table 6.1 gives the domain and time averaged values for different characteristics of the flow. Cases M2 and M3 appear to have similar gas and particle velocities and case M1 has lower gas and particle velocities in absolute values. This could be due to the fact that, as shown in Figure 6.1 more clusters are formed for case M1 than for cases M2 and M3. The fluid entrains more particles for case M1 and the fluid velocity tends to decreases. The mean kinetic agitation increases with the particle diameter.

TAB. 6.1: Particles and gas temporal and spatial averaged properties for monodisperse cases M1, M2 and M3.

Case	M1	M2	M3
$\overline{\langle U_{f,z}\rangle}\,[m/s]$	0.68	2.7	2.8
$\overline{\langle U_{p,z}\rangle}\,[m,s]$	$-1.05\cdot10^{-2}$	$-4.3\cdot10^{-2}$	$-4.3\cdot10^{-2}$
$\overline{\langle \alpha_p\rangle}\,[-]$	$5.0\cdot10^{-2}$	$4.9\cdot10^{-2}$	$4.9\cdot10^{-2}$
$\overline{\langle q_p^2\rangle}\,[m^2/s^2]$	$1.26\cdot10^{-2}$	$7.5\cdot10^{-2}$	$9.1\cdot10^{-2}$

For this study the temporal average used is presented in Table 6.2. The Stokes's relaxation time τ_p^{St} corresponding to $\frac{\rho_p}{\rho_g}\frac{d_p^2}{18\nu_g}$.

TAB. 6.2: Characteristic time scales for monodisperse cases with various diameters

Case	M1	M2	M3
$\tau_{p,St}\,[s]$	$2.20\cdot10^{-2}$	$4.50\cdot10^{-2}$	$8.79\cdot10^{-2}$
n_{time}	200	195	191
$time\,[s]$	4	3.85	3.03
$time/\tau_{p,St}$	182	78	34

Figure 6.3 shows the profiles of average in time appear independent of the heights. Hence, the profiles averaged over two sectional plans will be presented to study the behaviour of the flows. The time averaged radial profiles of solid volume fractions, velocities and particle kinetic agitation are presented in Figures 6.4, 6.5, 6.6 and 6.7. The radial profiles of solid volume fractions exhibit a core-annulus flow structure in the riser, with an accumulation of particles in the near-wall regions, for the three cases studied. However, profiles for case M1 are significantly different from case M2 and M3. In those cases, particles tend to accumulate more near the walls and less in the center of the riser. The influence of particle diameter is also observed on the profile of gas and particle velocities. The gas velocity is more significant and remains positive for cases M2 and M3. On the contrary, the radial profile of gas velocity for case M1 shows that, near the walls, the mean gas velocity tends to decrease and becomes negative. This is consistent with the spatial averaged velocities presented in Table 6.2. Figure 6.6 shows that the solid velocity, in the near-wall region, decreases as the particle diameter goes up. Such a velocity is positive for case M3, slightly negative for case M2 and negative and more significant in absolute value for case M1. The small particles, which tend to go down near the walls, drag down the gas phase with them.

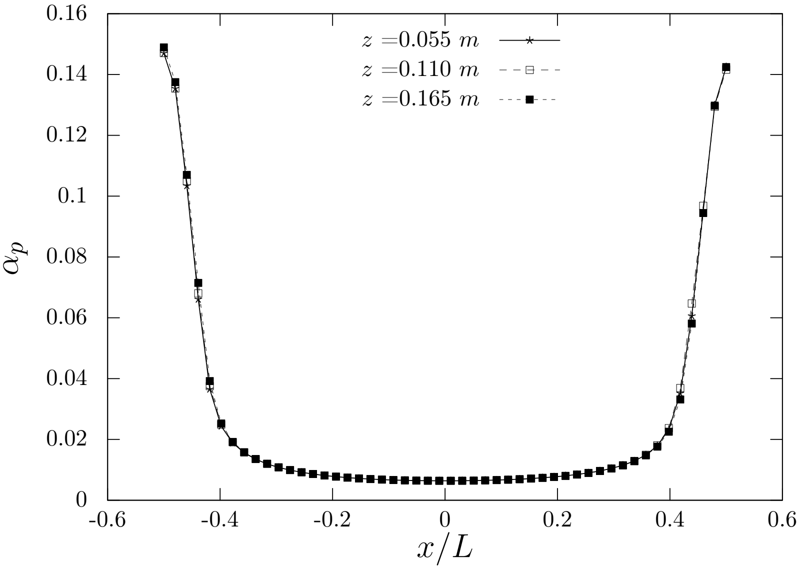

FIG. 6.3: profiles of solid volume fractions averaged in time for several heights for case M3.

The solid volume fraction in the center of the riser is most significant for case M1. The particle kinetic agitation appears more significant for the large and medium particle than for the small particles. The asymmetry observed in the radial profiles is due to the twisted movement of the solid phase during the time, as illustrated in Figure 6.8.

The Probability Density Functions (PDF) of the solid volume fraction of the three cases. The peak corresponds to higher values for case M1 than for cases M2 and M2. One explanation could be that the number of cells occupied by the center of the riser is more important than the one of the near-wall region and in the center of the riser, the solid volume fraction is more significant for case M1 than for cases M2 and M3.

6.2.1.2 Particle density

The influence of the particle density is also studied by cases M1, M6 and M7 corresponding respectively to $\rho_p = \rho_{p,ref}$, $\rho_p = 2\rho_{p,ref}$ and $\rho_p = 4\rho_{p,ref}$, with $\rho_{p,ref} = 1500\,kg/m^3$. The domain and time averaged values for the solid volume fraction, velocities and the kinetic agitation are given in Table 6.3. The averaged gas velocity and particle kinetic agitation increase with density. The mean particle velocity is slightly density dependent. On the contrary, the mean particle kinetic agitation and the mean gas velocity increase significantly with density.

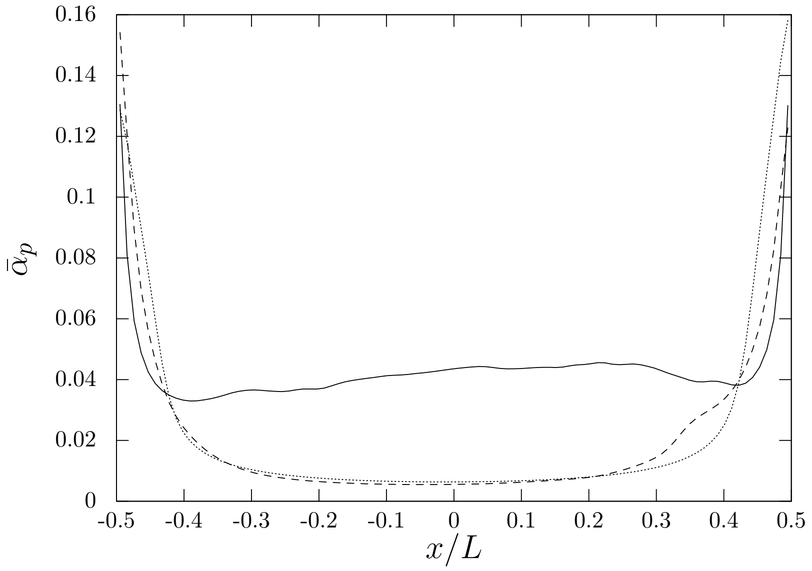

FIG. 6.4: Radial profiles of the mean solid volume fraction solid volume fraction. The lines corresponds to case M1(——), case M2(- - -) and case M3(········) .

TAB. 6.3: Particles and gas temporal and spatial averaged properties for monodisperse cases M1, M6 and M7 .

Case	M1	M6	M7
$\overline{\langle U_{f,z}\rangle}\,[m/s]$	0.68	1.3	3.1
$\overline{\langle U_{p,z}\rangle}\,[m,s]$	$-1.05\cdot10^{-2}$	$-1.03\cdot10^{-2}$	$-1.2\cdot10^{-2}$
$\overline{\langle\alpha_p\rangle}\,[-]$	$5.0\cdot10^{-2}$	$5.0\cdot10^{-2}$	$4.9\cdot10^{-2}$
$\overline{\langle q_p^2\rangle}\,[m^2/s^2]$	$1.26\cdot10^{-2}$	$2.7\cdot10^{-2}$	$5.65\cdot10^{-2}$

In the cases studied, the time average used is presented in Table 6.4.

TAB. 6.4: Characteristic time scales for monodisperse cases with various densities

Case	M1	M6	M7
$\tau_{p,St}\,[s]$	$2.20\cdot10^{-2}$	$4.40\cdot10^{-2}$	$8.8\cdot10^{-2}$
n_{time}	200	161	164
$time\,[s]$	4	3.3	3.2
$time/\tau_{p,St}$	182	75	36

Figures 6.10, 6.11, 6.12 and 6.13 show respectively the time averaged radial profiles of solid volume fraction, gas and particle axial velocities and particle kinetic energy agitation. The radial profiles of solid volume fractions exhibit a core-annulus flow regime in the riser for the three densities. The cases M1 and M6 appear to have very similar solid volume

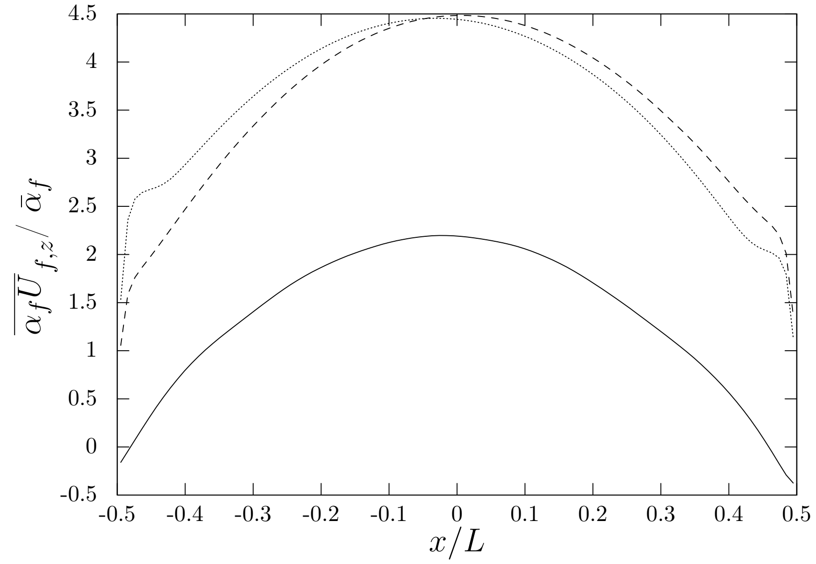

FIG. 6.5: Radial profiles of the mean gas velocity. The lines corresponds to case M1(——), case M2(- - -) and case M3(········).

fraction distribution. However, such a quantity is significantly lower in the case M7 than for case M1 and M6, in the center of the riser. The density also affects the profiles of gas and particle velocities. The mean gas velocity tends to increase with the density. In the near-wall regions, the gas velocity is negative for case M1 and positive for the two other cases. The Stokes characteristic time of cases M6 and M7 are very close to the ones of case M2 and M3 respectively. Figures 6.5 and 6.11 illustrates similar behaviour of the mean gas velocity. Hence, the radial profile of the mean gas velocity depends on the Stokes characteristic times. However, the profiles of averaged mean particle velocity do not depict such dependency and no clear link appears between the averaged particle velocities and the density. The mean kinetic agitation increases with the density. Figure 6.13 shows similar shape for cases M1 and M6 as for the solid volume fraction. For case M7, the particle kinetic agitation is significantly higher in the center of the riser and the shape of the profile differs significantly from the ones obtained for case M1 and M6.

Figure 6.14 illustrates that most of the solid volume fractions tend to decrease as the density increases, which is in good agreement with the observation about the solid volume fraction profiles.

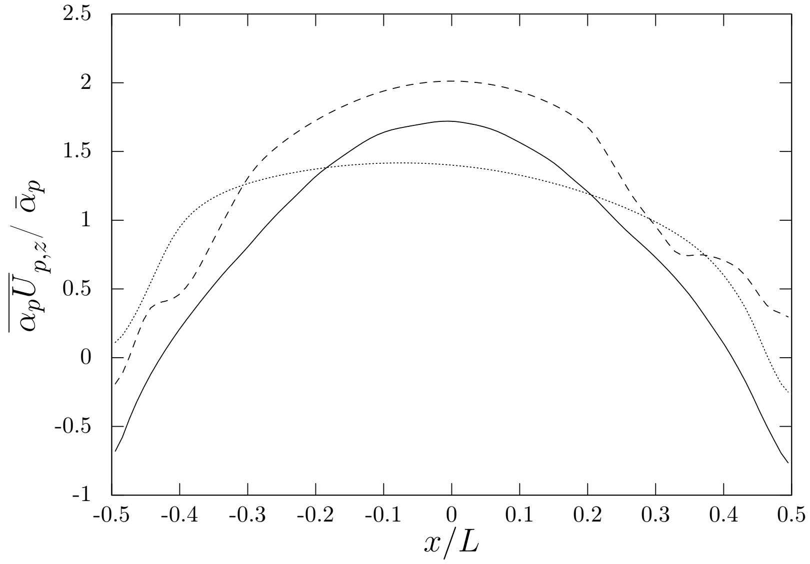

FIG. 6.6: Radial profiles of the mean particle velocity. The lines corresponds to case M1(——), case M2(– – –) and case M3(········).

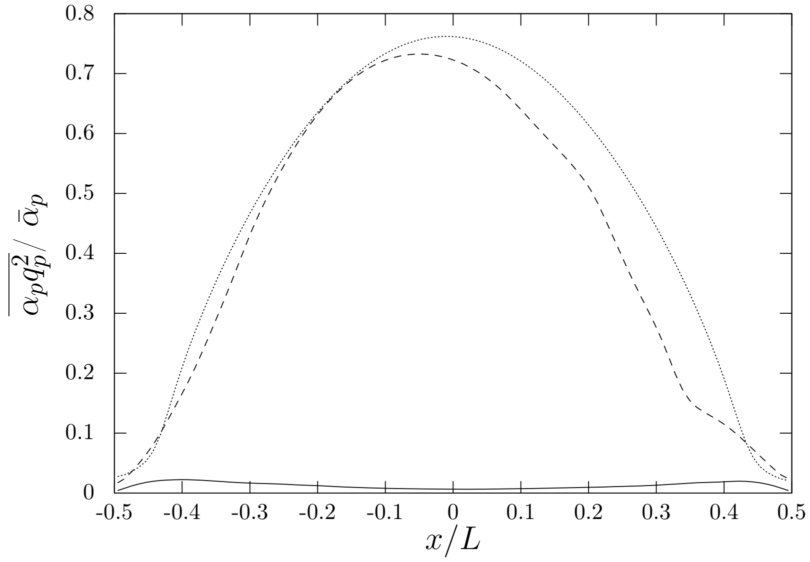

FIG. 6.7: Radial profiles of the mean particle kinetic agitation. The lines corresponds to case M1(——), case M2(– – –) and case M3(········).

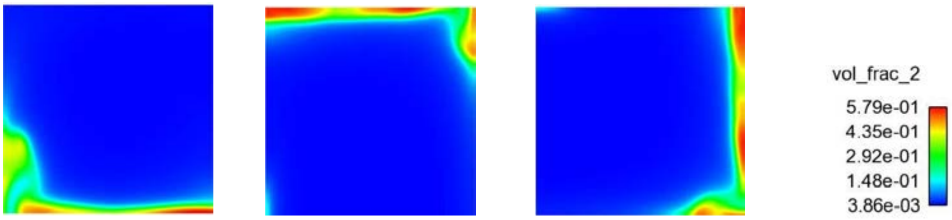

(a) (b) (c)

FIG. 6.8: Instantaneous fields of the solid volume fraction in plan z for several time instants with (a): $t = 7.6\,s$, (b): $t = 8.1\,s$ and (c): $t = 9.6\,s$ for case M1.

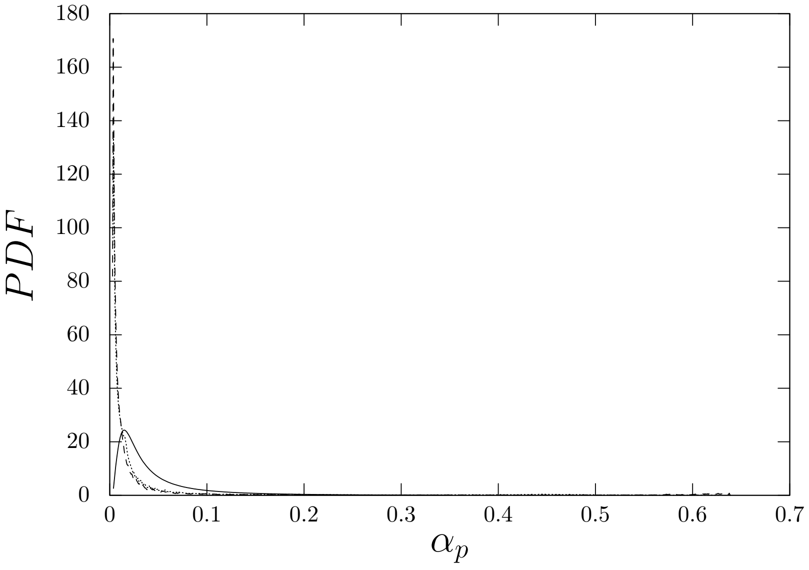

FIG. 6.9: PDF of the solid volume fraction α_p. The lines corresponds to case M1(——), case M2(- - -) and case M3(········).

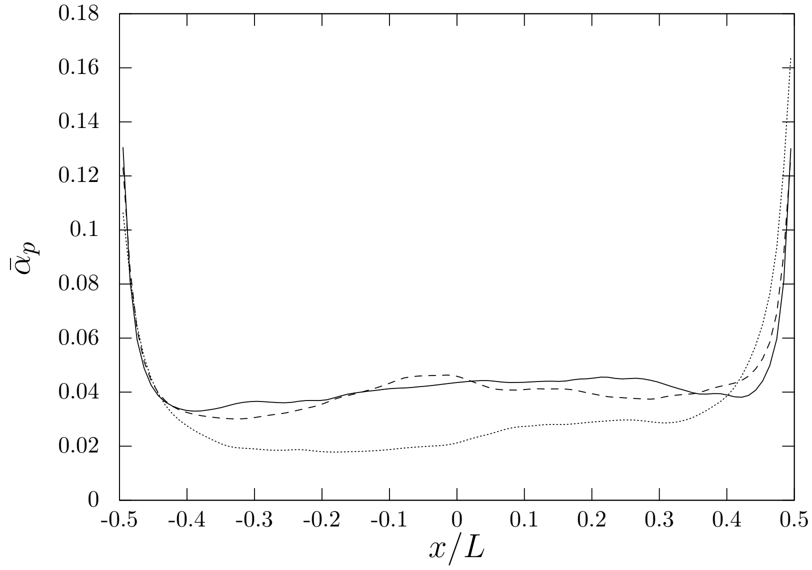

FIG. 6.10: Radial profiles of the mean solid volume fraction solid volume fraction. The lines corresponds to case M1(——), case M6(- - -) and case M7(········).

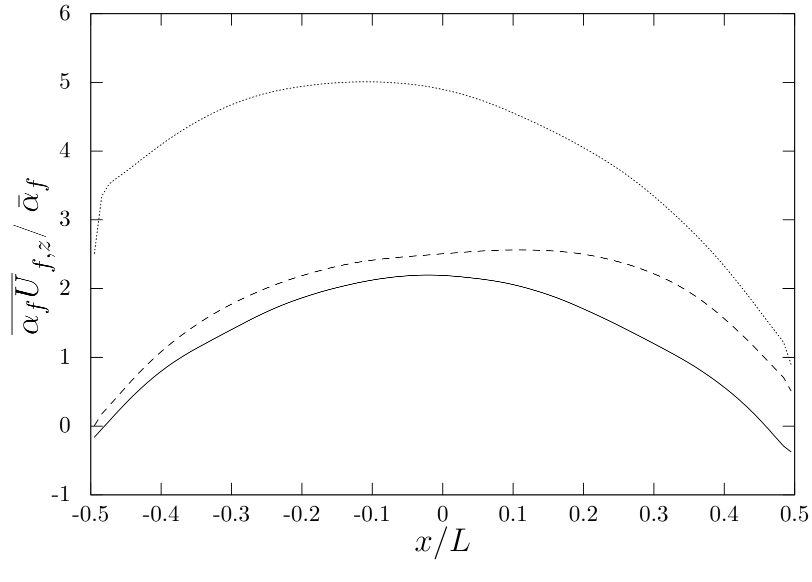

FIG. 6.11: Radial profiles of the mean gas velocity. The lines corresponds to case M1(——), case M6(- - -) and case M7(········).

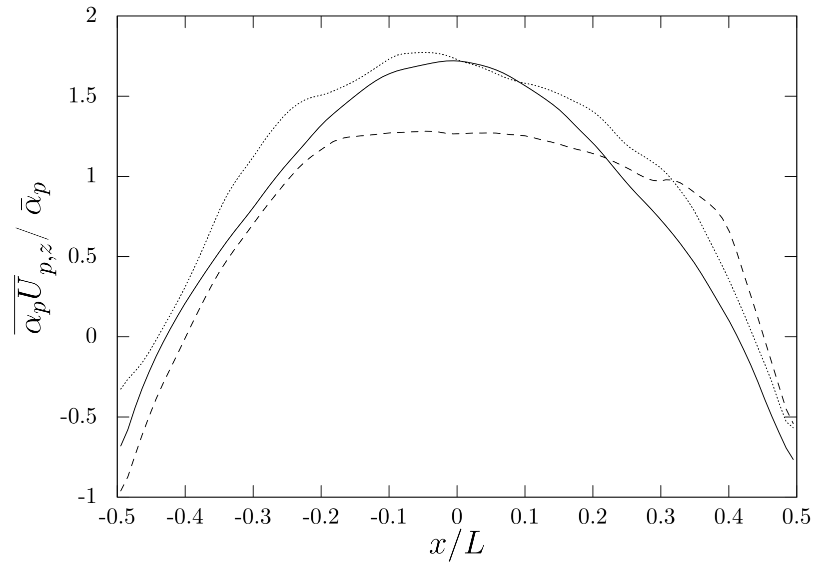

FIG. 6.12: Radial profiles of the mean particle velocity. The lines corresponds to case M1(——), case M6(– – –) and case M7(········).

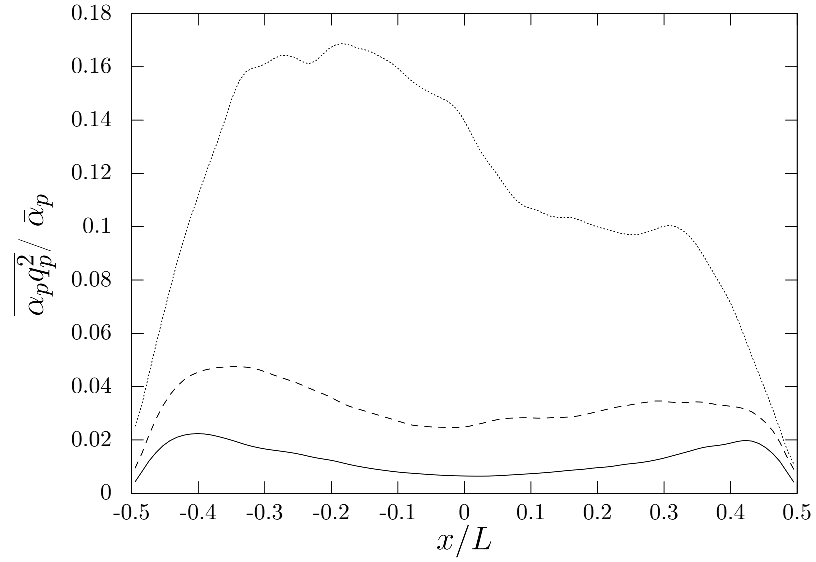

FIG. 6.13: Radial profiles of the mean particle kinetic agitation. The lines corresponds to case M1(——), case M6(– – –) and case M7(········).

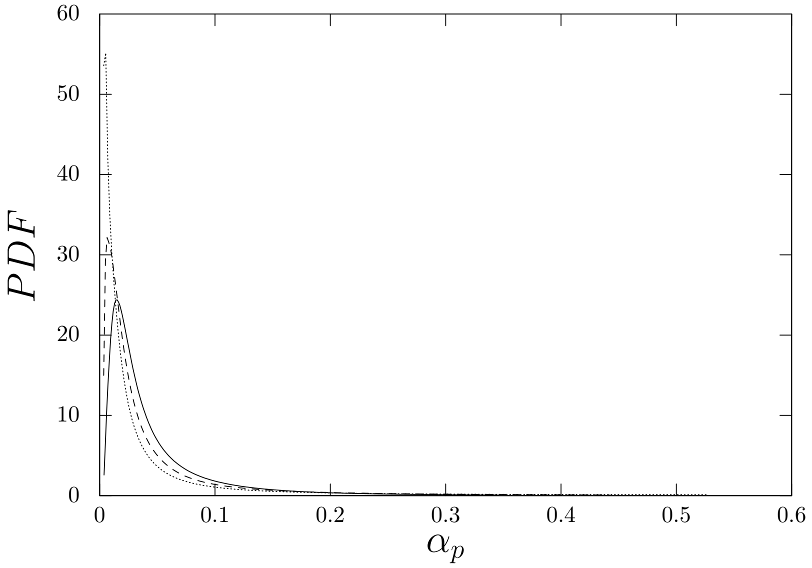

FIG. 6.14: PDF of the solid volume fraction α_p. The lines corresponds to case M1(——), case M6(- - -) and case M7(·······).

6.2.1.3 Wall velocity

Wall velocity changes the velocity of the fluid due to the no-slip condition for the fluid phase. Three cases are considered, M1, M4 and M5 corresponding respectively to $W_{wall} = 0\,m/s$, $W_{wall} = 5\,m/s$ and $W_{wall} = 10\,m/s$. The domain and time averaged values for the solid volume fraction, the velocities and the kinetic agitation are summarized in Table 6.5. The difference between averaged values due to wall velocity remains small compared to the ones related to the particle diameter and density. When the wall velocity goes up, the mean fluid and particle velocities decreases slightly and the particle kinetic agitation tends to increase.

TAB. 6.5: Particles and gas temporal and spatial averaged properties for monodisperse cases M1 M4 and M5 .

Case	M1	M4	M5
$W_{wall}\,[m/s]$	0	5	10
$\overline{\langle U_{f,z}\rangle}\,[m/s]$	0.68	0.64	0.51
$\overline{\langle U_{p,z}\rangle}\,[m,s]$	$-1.05\cdot10^{-2}$	$-9.93\cdot10^{-3}$	$-8.04\cdot10^{-3}$
$\overline{\langle \alpha_p\rangle}\,[-]$	$5.0\cdot10^{-2}$	$4.99\cdot10^{-2}$	$4.9\cdot10^{-2}$
$\overline{\langle q_p^2\rangle}\,[m^2/s^2]$	$1.26\cdot10^{-2}$	$1.57\cdot10^{-2}$	$1.67\cdot10^{-2}$

For this study the time average used is around 200 instants for the three cases corresponding a physical time of $4\,s$. In Figures 6.15, 6.16, 6.17 and 6.18, the time averaged radial profiles of solid volume fraction, gas and particle vertical velocities and particle kinetic energy agitation are presented. Figures 6.15 shows a core-annulus flow regime for the three cases studied. The averaged solid volume fraction has similar values in the center of the riser for all the cases. However, the number of particles in the near-wall regions decreases as the wall velocity goes up. The probable explanation is that the fluid velocity near the wall tends to pull the particle away. Shapes of the particle velocity profiles and kinetic agitation profiles are very similar for the three cases.

The PDFs of the solid volume fraction distributions is presented in Figure 6.19. Such a Figure points also out the similarity between cases. Hence, the effect of the fluid velocity can be neglected compared to the effect of the diameter and density.

In the next section, the model development will be investigated. The aim is to define a model which predict accurately the subgrid drift flux in all monodisperse cases. Considering the similarities between cases with different wall velocities, cases M4 and M5 do not need to be analysed for the development of such a model.

6.2.2 Study on the whole domain

In this section the whole domain, illustrated in Figure 5.1, is taken into account. First the constant K_{zz} is assumed equal to M1 and the focus is given to the function g which

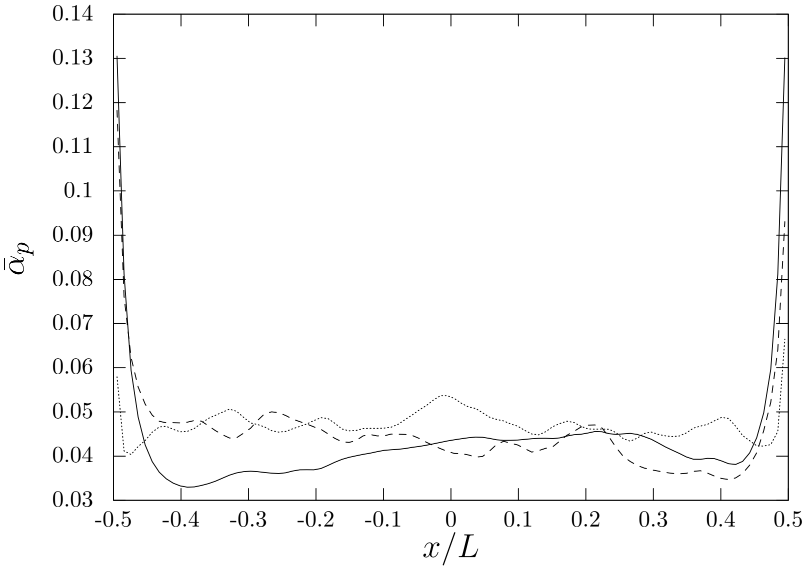

FIG. 6.15: Radial profiles of the mean solid volume fraction solid volume fraction. The lines corresponds to case M1(——), case M4(- - -) and case M5(········).

depends on the solid volume fraction and the filter size. Hence, the sub-grid contribution of the drag force will be taken into account by modelling $\tilde{\alpha}_p V_{d,z}^{(p)}$ as:

$$V_{d,z}^{(p)} = g(\Delta_f, \tilde{\alpha}_s)(\tilde{U}_{f,z} - \tilde{U}_{p,z}) \tag{6.6}$$

with g the drag correction tensor and Δ_f the filter size. Using results of the refined mesh simulations, the function g can be calculated by the following expression:

$$g(\Delta_f, \tilde{\alpha}_p) = \frac{\overline{\langle V_{d,z}^{(p)} | \tilde{\alpha}_s \rangle}}{\overline{\langle (\tilde{U}_{f,z} - \tilde{U}_{p,z}) | \tilde{\alpha}_s \rangle}} \tag{6.7}$$

the $\tilde{V}_{d,z}^{(p)}$ and $\tilde{U}_{f,z} - \tilde{U}_{p,z}$ are conditionally averaged by the solid volume fraction then averaged in time.

6.2.2.1 Effect of the particle diameter

First, the effect of the particle diameter is studied by comparing results of three monodisperse simulations with various diameters. Figure 6.20 shows the function g for the three monodisperse simulations, along the mean flow direction, for a minimum value of statistical points equal to 1000. The functions g with different diameters and various filter sizes appear to have the same shape, especially for cases M1 and M2. However, the number of statistical points appears to decrease significantly as the solid volume fraction increases. Such a result is consistent with values of solid volume, which are mostly fraction were below 0.05. This could lead to inconsistent values of the function g for high volume fraction.

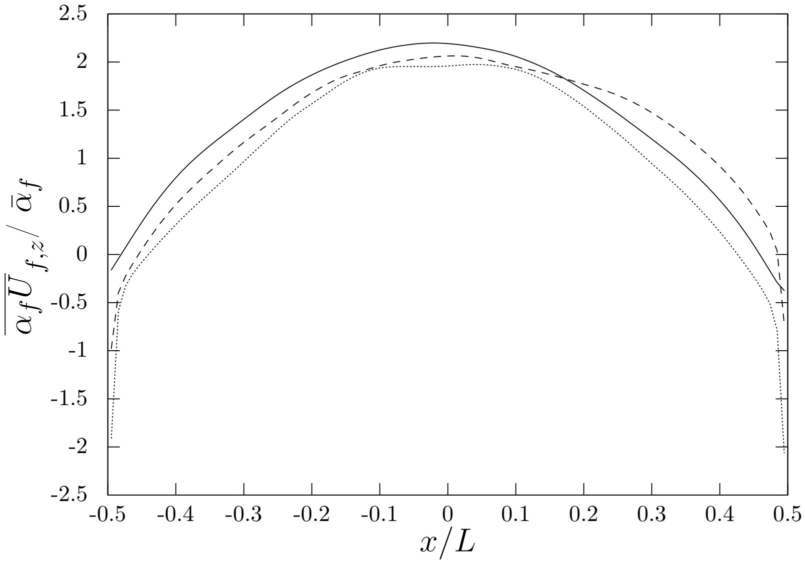

FIG. 6.16: Radial profiles of the mean gas velocity for the diameters. The lines corresponds to case M1(——), case M4(– – –) and case M5(·········).

Therefore, the study will focus on solid volume fraction below 0.3. Figure 6.21 depicts the function g below solid volume fraction below 0.3. The Figure suggests that the shape of the function g does not depend on the filter size. Considering such similarities between shapes of the function g, such a quantity is assumed to be the product of a function h, which takes into account the effects of the volume fractions, and a function f corresponding to influence of the filter size. The function is expressed as:

$$g(\tilde{\alpha}_s, \Delta_f) = h(\tilde{\alpha}_s) f(\Delta_f) \tag{6.8}$$

Considering the range limitations, the function h can be calculated by normalizing the function g by its integral, and then:

$$h(\tilde{\alpha}_s) = \frac{g(\tilde{\alpha}_s, \Delta_f)}{\int_{0.0}^{0.3} g(\tilde{\alpha}_s, \Delta_f)} \tag{6.9}$$

Such a function is shown in Figure 6.22. The function h, obtained for each particle diameter, overlay and the model developed by Ozel for small particle $d_p = 75\,\mu m$ [96] fits well the values of function h computed in the three cases.

$$\begin{aligned} h_O &= -tanh\left(\frac{2\tilde{\alpha}_s}{0.2}\right)\sqrt{\frac{\tilde{\alpha}_s}{\alpha_{p,max}}}\left(1-\frac{\tilde{\alpha}_s}{\alpha_{p,max}}\right)^2 \\ & \left(1-1.88\frac{\tilde{\alpha}_s}{\alpha_{p,max}}+5.16\left(\frac{\tilde{\alpha}_s}{\alpha_{p,max}}\right)^2\right) \end{aligned} \tag{6.10}$$

The function f is computed by integrating the function g. Figure 6.23 presents values obtained for each filter width. The function f appears to vary linearly with the filter widths.

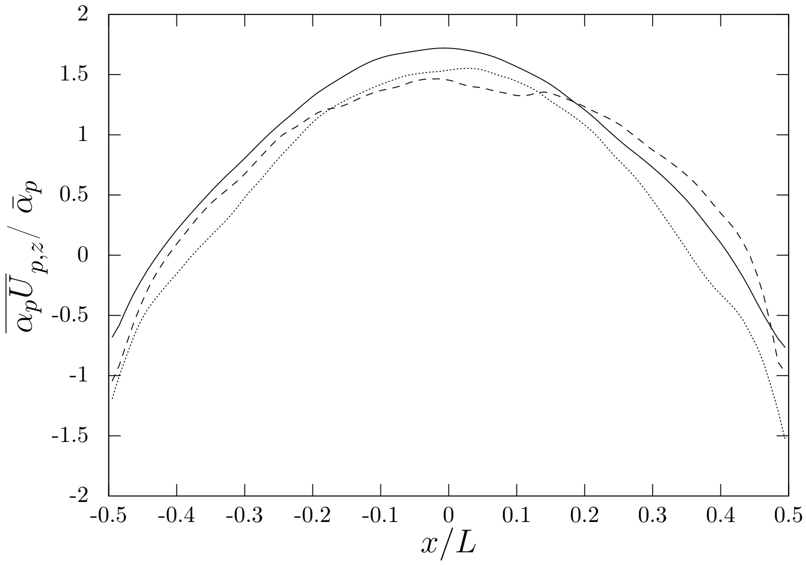

FIG. 6.17: Radial profiles of the mean particle velocity. The lines corresponds to case M1(——), case M4(- - -) and case M5(········).

Instead of using the filter size Δ_f, the function f can be computed with a dimensionless subgrid length scale Δ^* [96, 101]. Such a parameter could take into account some characteristics, such as the particle density and diameter. To obtain the dimensionless parameter, combinations between the filter and cell size ratio and the particle diameter with various power values were tested. Some of them are depicted in Figure 6.24. The aim is to overlay the values of f computed in the three cases on the same curve. None of the combinations reaches this goal.

6.2.2.2 Effect of the density

Similarly to the study performed on cases M1, M2 and M3, the function g is computed for cases M6 and M7, in order to analyse the effect of the density. Figure 6.25 depicts the function g obtained for cases M1, M6 and M7 for a minimum number of statistical points of 1000. The g values tend to decrease in absolute value when the density increases. As for the cases with various diameters, the shape of g is independent of the filter width. However, the function g of case M7, whose Stokes characteristic time is almost equal to that of case M3, has a shape more similar to case M1 than the function g of case M3. Such a difference could be explained by a larger amount of particles in the case M7. Indeed the solid volume fraction remains constant for all monodisperse cases and increasing the diameter decreases the number of particles in the box. As for the study of cases M1, M2 and M3, most of the volume fractions studied are below 0.3. In Figure 6.26, values of function g are reported for this range of solid volume fractions. The function h is computed and illustrated in Figure 6.27 for cases M1, M6 and M7. The expression of h defined by Eq. 6.10 fits very well the computed values of h. The function f is given in in Figure 6.28. The function f decreases linearly as the filter size goes up for each case.

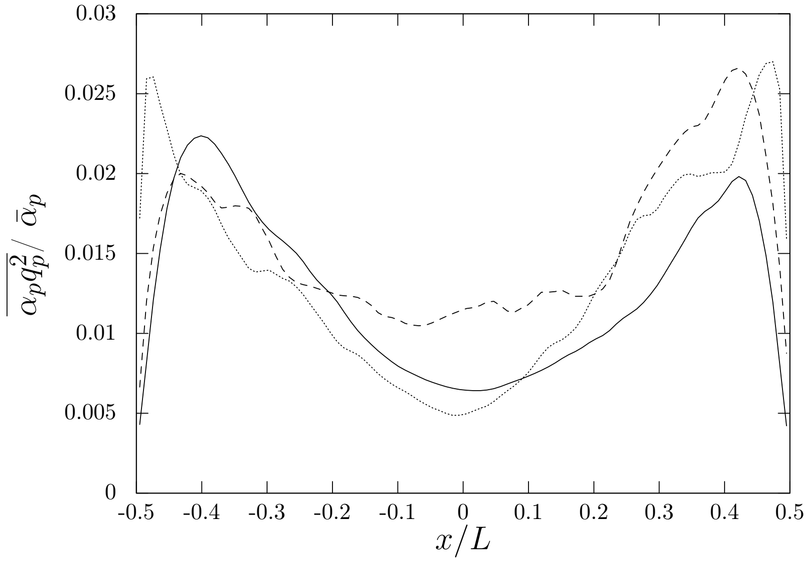

FIG. 6.18: Radial profiles of the mean particle kinetic agitation. The lines corresponds to case M1(——), case M4(– – –) and case M5(········).

6.2.3 Study on a restricted domain

The focus will be given on the effect of the near-wall region. All cases have been studied with the whole domain. Now the restricted domain, without the near-wall regions, is taken into account for cases M1, M2 and M3. Figure 6.29 depicts the function g for the three cases. The function g for $d_p = 75\,\mu m$ and $d_p = 112.5\,\mu m$ are similar but for $d_p = 150\,\mu m$, the values tend to differ α_s above 0.01. One explanation could be that the solid tend to accumulate near the walls. In Figure 6.30, the function h, as expressed in Eq. 6.10, is in good agreement with the function h computed by taking into account the restricted domain. The domain studied does not change the trend, however due to the number of particles in the near-wall regions, taking into account the whole domain enables to have more statistical points. Hence, the next analysis will be performed on the whole domain.

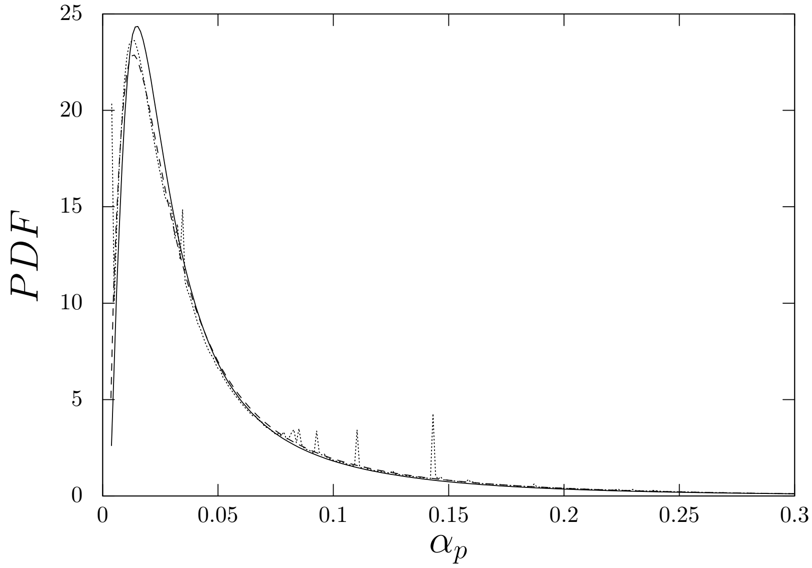

FIG. 6.19: PDF of the solid volume fraction α_p. The lines corresponds to case M1(——), case M4(- - -) and case M5(········).

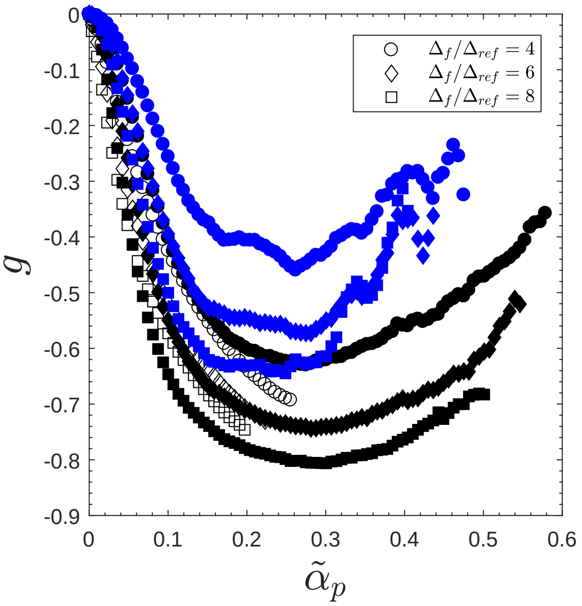

FIG. 6.20: The function g for various filter size ratio for cases M1, M2 and M3 for a minimum value of statistical points equal to 1000. The open symbols correspond to the case M1, the black filled symbols are the case M2 and the blue filled symbols refer to the case M3.

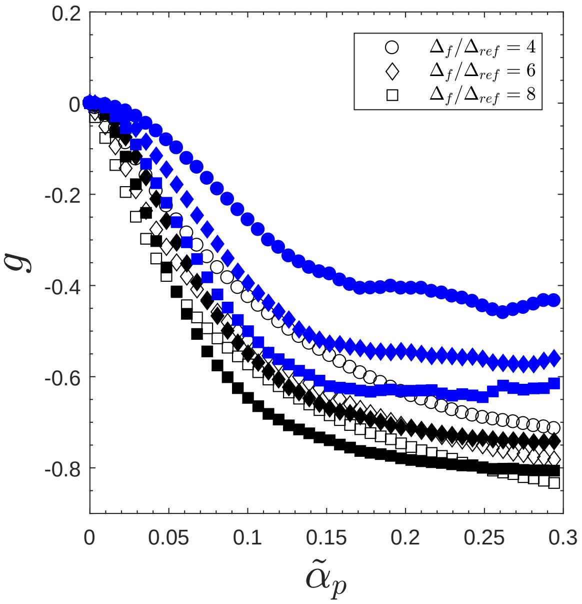

FIG. 6.21: The function g for various filter size ratio for cases M1,M2 and M3. The open symbols correspond to the case M1, the black filled symbols are the case M2 and the blue filled symbols refer to the case M3.

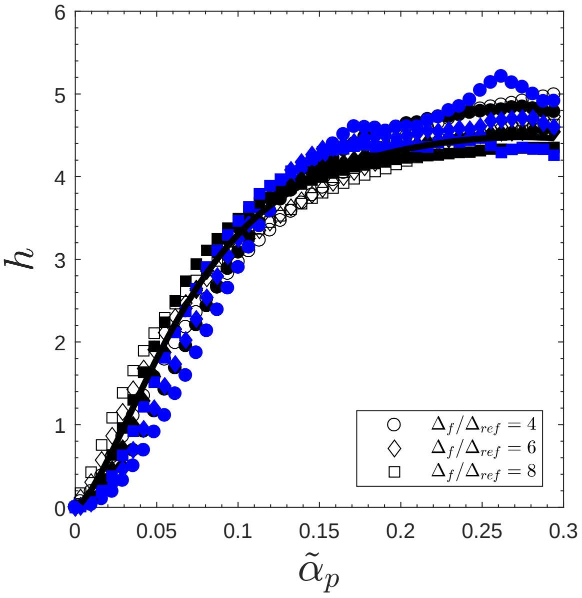

FIG. 6.22: The function h for various filter size ratio for cases M1, M2 and M3. The open symbols correspond to the case M1, the black filled symbols are the case M2 the blue filled symbols refer to the case M3 and the line(▬) is h_O.

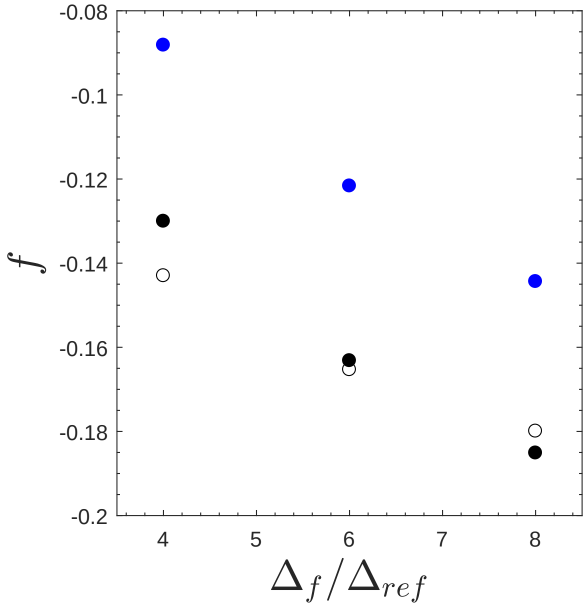

FIG. 6.23: The function f for various filter size ratio for cases M1, M2 and M3. The open symbols correspond to the case M1, the black filled symbols are the case M2 and the blue filled symbols refer to the case M3.

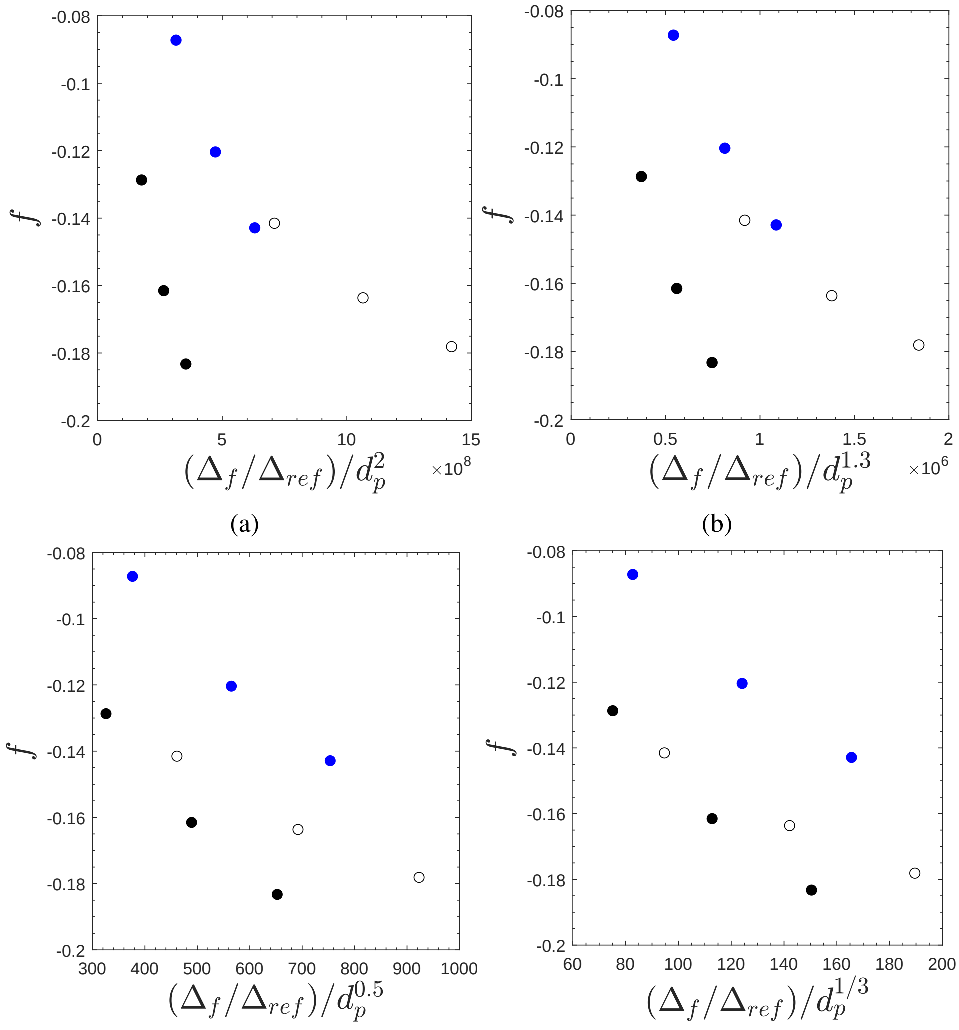

(a) (b)

(c) (d)

FIG. 6.24: Values of f as function of combinations between Δ_f and d_p^n with (a): $n = 2$, (b): $n = 1.3$, (c): $n = 0.5$ and (d): $n = \frac{1}{3}$. The open symbols correspond to the case M1, the black filled symbols are the case M2 and the blue filled symbols refer to the case M3.

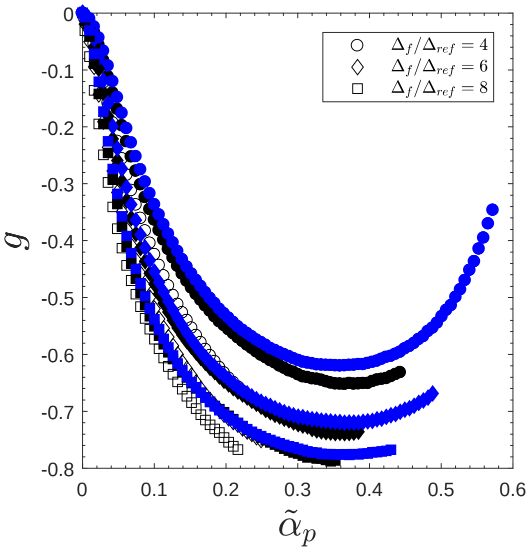

FIG. 6.25: The function g for various filter size ratio for a minimum of points N=1000. The open symbols correspond to the case M1, the black filled symbols are the case M6 and the blue filled symbols refer to the case M7.

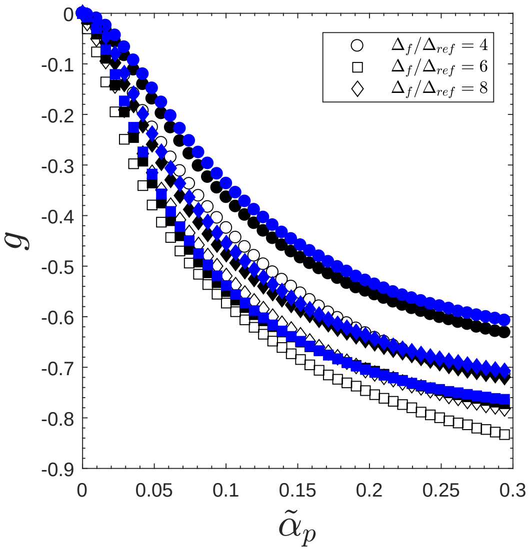

FIG. 6.26: The function g for various filter size ratio. The open symbols correspond to the case M1, the black filled symbols are the case M6 and the blue filled symbols refer to the case M7.

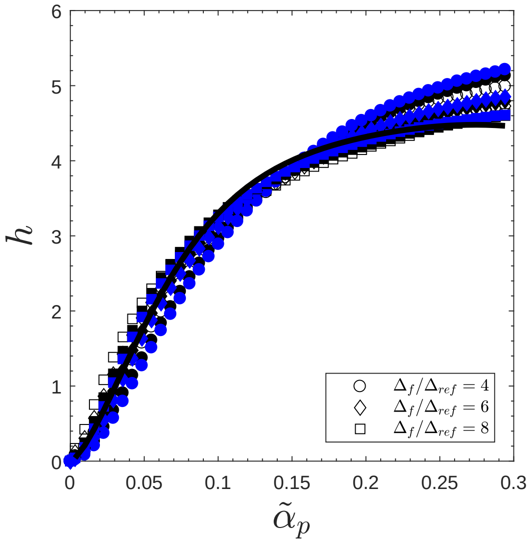

FIG. 6.27: The function h for various filter size ratio. The open symbols correspond to the case M1, the black filled symbols are the case M6, the blue filled symbols refer to the case M7 and the line(▬) is h_O.

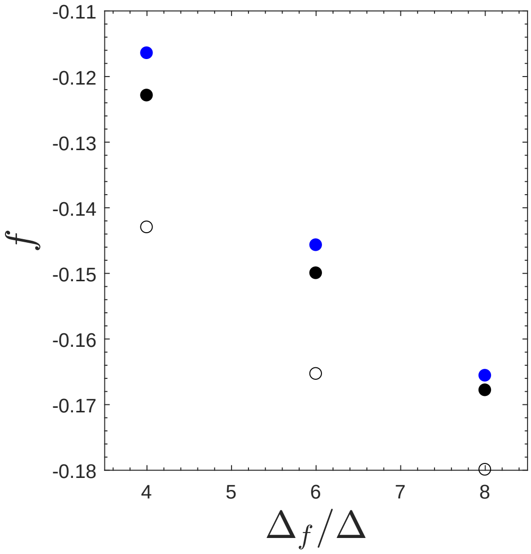

FIG. 6.28: The function g for various filter size ratio. The open symbols correspond to the case M1, the black filled symbols are the case M6 and the blue filled symbols refer to the case M7.

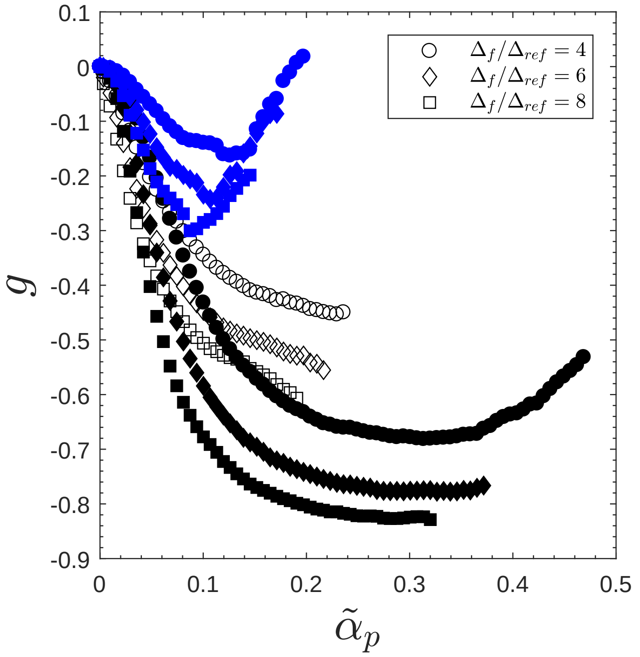

FIG. 6.29: The function g for various filter for cases and for $d_p = 112.5\,\mu m$ and $d_p = 150\,\mu m$. The open symbols correspond to the case M1, the black filled symbols are the case M2 and the blue filled symbols refer to the case M3.

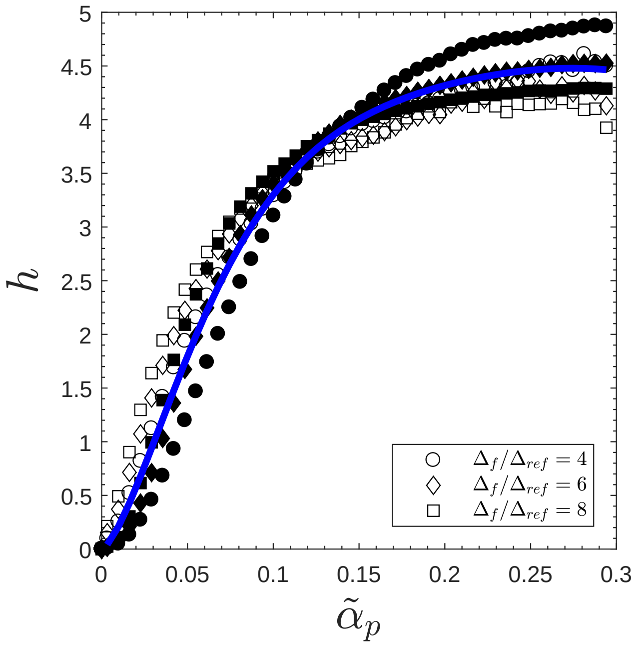

FIG. 6.30: The function h for various filter for cases M1 and M2. The open symbols correspond to the case M1, the black filled symbols are the case M2, the blue filled symbols refer to the case M3 and the line(——) is h_O .

6.3 Polydisperse cases

6.3.1 Cases description

Various cases are studied in order to analyse the effect of the particle volume fraction ratio and diameter ratio in polydisperse cases. The flow properties are summarized in Table 5.1. Comparisons between cases B1 and B2 and between cases B3 and B4 enable to determine the effect of the solid volume fraction ratio. The analysis of the influence of the diameter ratio is studied using cases B1 and B3. Table 6.6 summarizes the spatial and temporal averaged values of gas and particle velocities and particle kinetic energy.

TAB. 6.6: Particles and gas temporal and spatial averaged properties properties for polydisperse cases

Cases	B1	B2	B3	B4
$\overline{U_{f,z}}\,[m/s]$	0.88	2.7	2.8	0.75
$\overline{U_{p,z}}\,[m,s]$	$7.86 \cdot 10^{-2}$	$-4.3 \cdot 10^{-2}$	$-4.3 \cdot 10^{-2}$	$1.23 \cdot 10^{-2}$
$\overline{\alpha_p}\,[-]$	$5.0 \cdot 10^{-2}$	$4.9 \cdot 10^{-2}$	$4.9 \cdot 10^{-2}$	$8.0 \cdot 10^{-2}$
$\overline{q_p^2}\,[m^2/s^2]$	$1.99 \cdot 10^{-2}$	$7.5 \cdot 10^{-2}$	$9.1 \cdot 10^{-2}$	$1.1 \cdot 10^{-2}$
$\overline{U_{q,z}}\,[m,s]$	$-9.29 \cdot 10^{-2}$	$-4.3 \cdot 10^{-2}$	$-4.3 \cdot 10^{-2}$	$-7.8 \cdot 10^{-2}$
$\overline{\alpha_q}\,[-]$	$5.0 \cdot 10^{-2}$	$4.9 \cdot 10^{-2}$	$4.9 \cdot 10^{-2}$	$2.0 \cdot 10^{-2}$
$\overline{q_q^2}\,[m^2/s^2]$	$5.39 \cdot 10^{-3}$	$7.5 \cdot 10^{-2}$	$4.9 \cdot 10^{-2}$	$4.5 \cdot 10^{-2}$

Figures 6.31, 6.32, 6.33 and 6.34 show the PDF of the solid volume fractions of cases B1, B2, B3 and B4 respectively. The PDF of the largest particle and small particles are similar for cases B1 and B3. Such results differ from the PDF of monodisperse cases, where the solid volume fraction of the largest particles are mostly lower than the volume fraction of small particles. This difference between monodisperse and polydisperse cases is probably due to an entrainment of large particles by the small particles, which leads to a more uniform distribution of large particles.

Figures 6.35 and 6.36 depict the radial profiles of both particles volume fractions. Figures show a core annulus flows for all types of particles and all cases. The large particles tend to accumulate more in the near-wall region than the small particles. This is in good agreement with the horizontal segregation observed in experiments and numerical simulation results [55, 85]. However, the solid volume fraction in the center of the riser is higher in the bidisperse cases than in the monodisperse cases. Such an observation is consistent with the improvement of the fluidization of large particles showed by the PDF.

The radial profiles of mean gas velocity are presented in Figures 6.37 and 6.38. For all cases, the values are of the same order of magnitude. However the profile for case B2 appears less flat in the center of the riser than case B1. This is not observed for cases B3 and B4.

In Figures 6.39 and 6.40, the profile of the small particles appears to be similar to that the large particle for all cases. There is a difference between the profiles of case B1 and B2. Such a difference is not observed for case B3 and B4, therefore, the effect solid volume fraction ratio on velocity cannot be determined clearly.

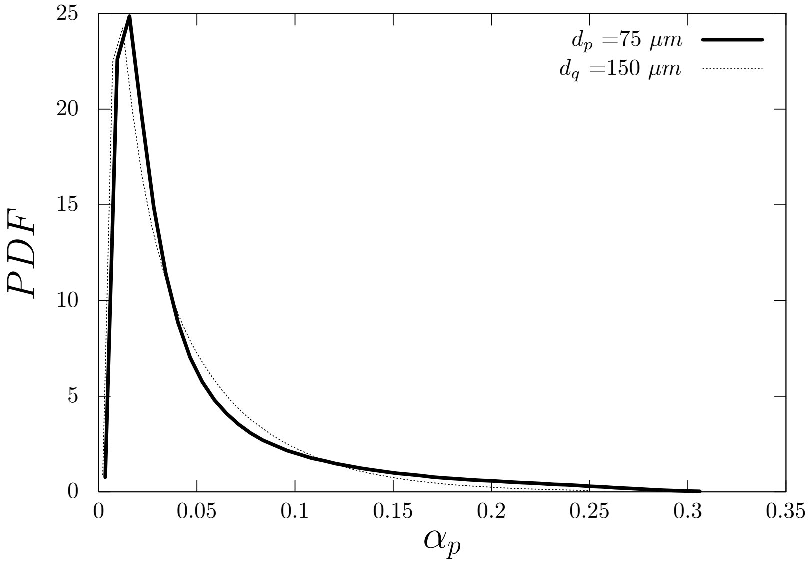

FIG. 6.31: The pdf of particle volume fractions for case B1.

Figures 6.41 and 6.42 depict the radial profiles of particle kinetic agitation. The maximum value of particle kinetic energy tends to increase as the particle diameter decreases and as the solid volume fraction of large particle increases.

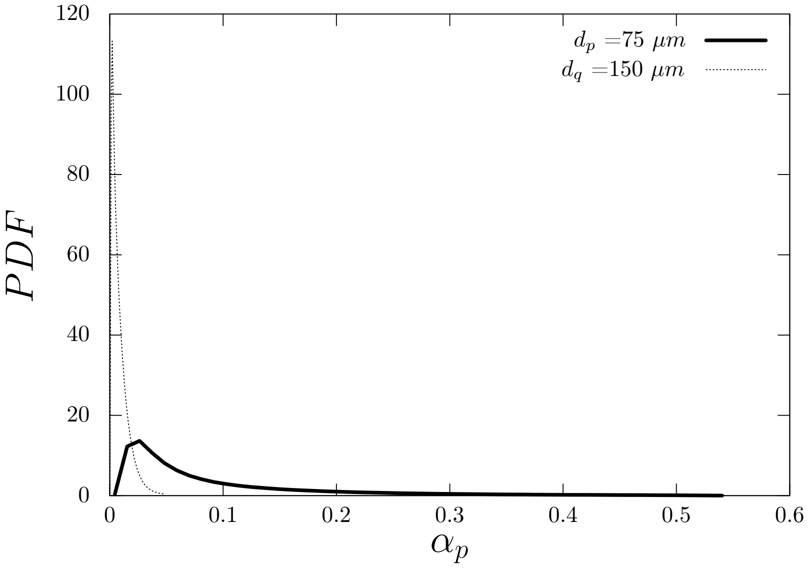

FIG. 6.32: The pdf of particle volume fractions for case B2.

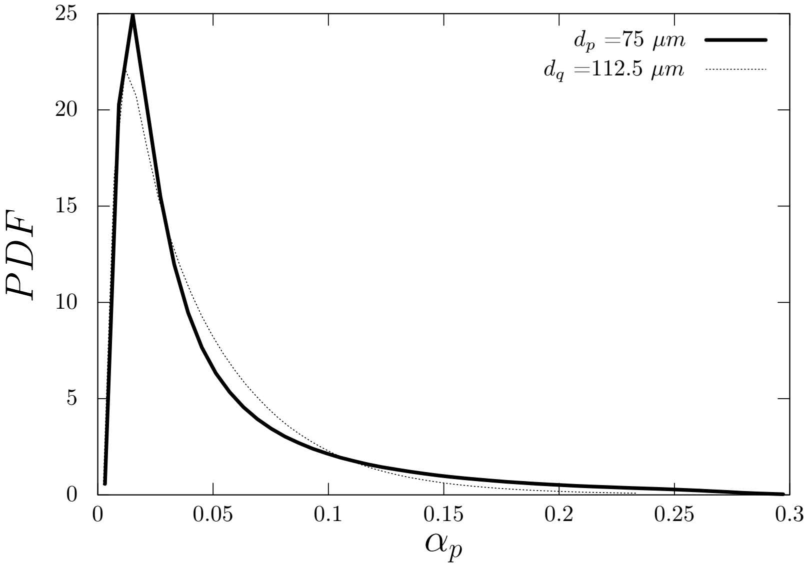

FIG. 6.33: The pdf of particle volume fractions for case B3.

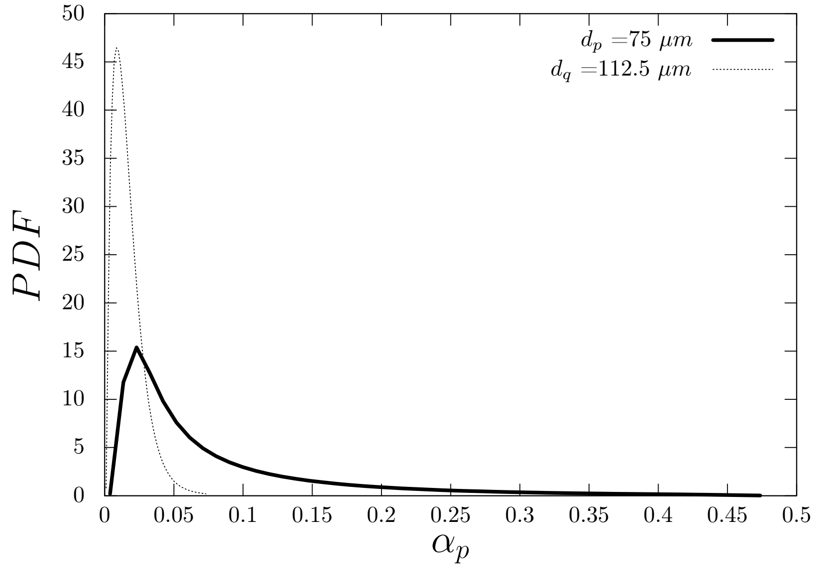

FIG. 6.34: The pdf of particle volume fractions for case B4.

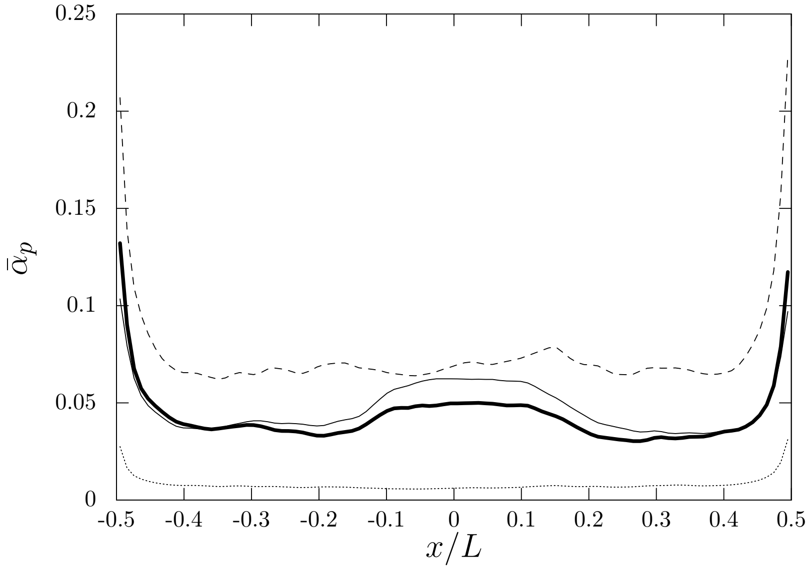

FIG. 6.35: Radial profiles of the mean solid volume fraction solid volume fraction. The line are: ——: B1 $d_p = 75\mu m$, ▬▬: B1 $d_q = 150\mu m$, - - -: B2 $d_p = 75\mu m$ and ········: B2 $d_q = 150\mu m$.

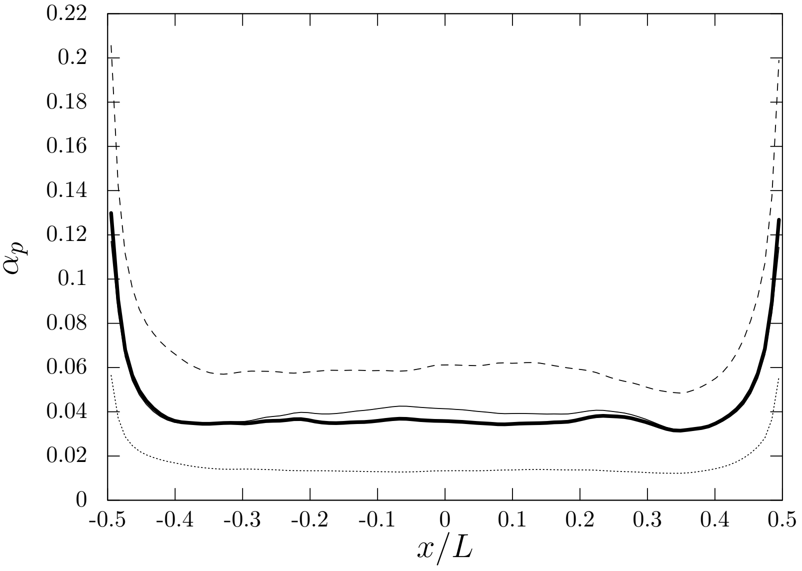

FIG. 6.36: Radial profiles of the mean solid volume fraction solid volume fraction. The symbols are: ——: B3 $d_p = 75\mu m$, ━━: B3 $d_q = 112.5\mu m$, - - -: B4 $d_p = 75\mu m$ and ········: B4 $d_q = 112.5\mu m$.

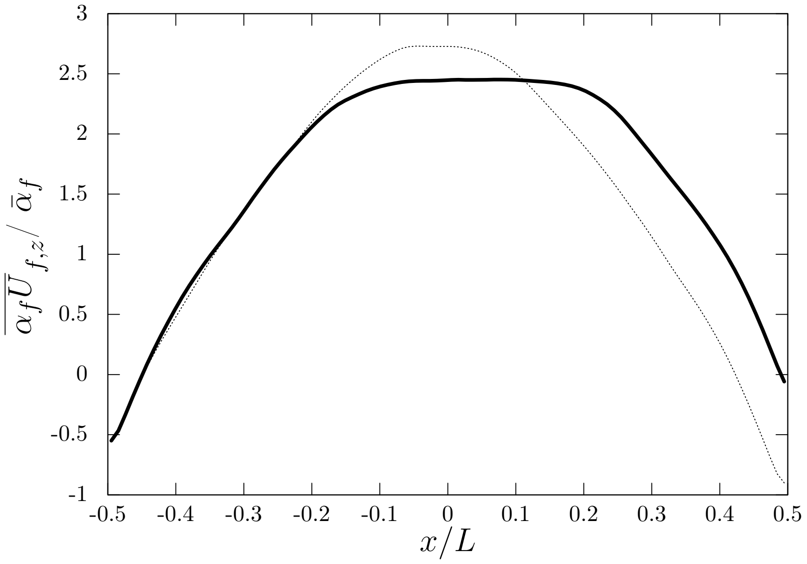

FIG. 6.37: Radial profiles of the mean gas velocity. The symbols are: ━━: B1 and ········: B2 .

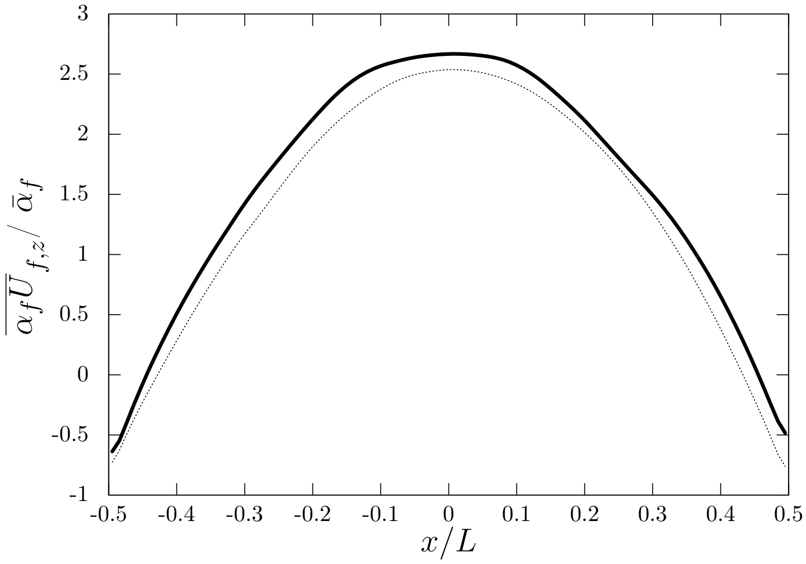

FIG. 6.38: Radial profiles of the mean gas velocity. The symbols are: ▬: B3 and ········: B4 .

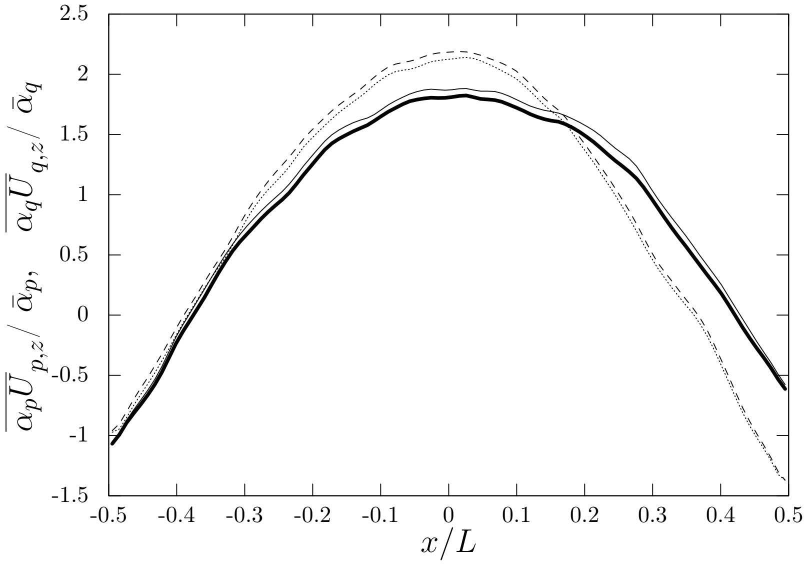

FIG. 6.39: Radial profiles of the mean particle velocity. The symbols are: —: B1 $d_p = 75\mu m$, ▬: B1 $d_q = 150\mu m$, - - -: B2 $d_p = 75\mu m$ and ········: B2 $d_q = 150\mu m$.

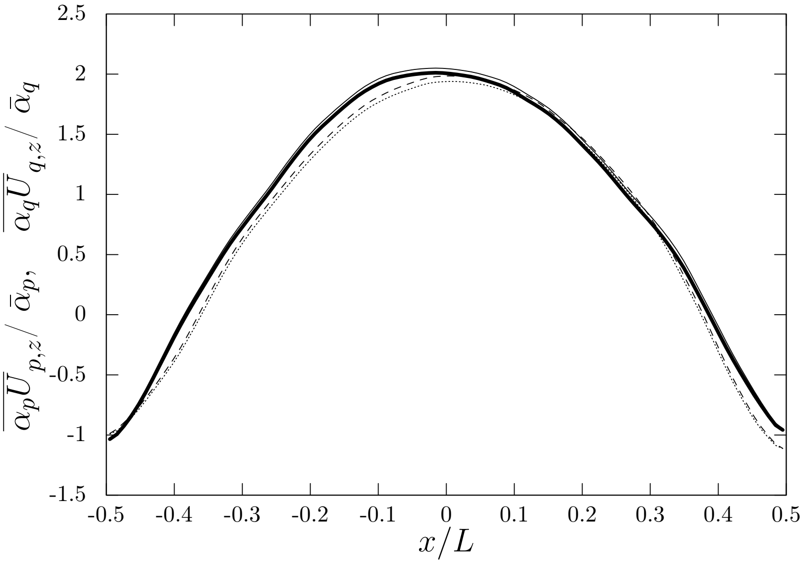

FIG. 6.40: Radial profiles of the mean particle velocity. The symbols are: ——: B3 $d_p = 75\mu m$, ▬: B3 $d_q = 112.5\mu m$, - - -: B4 $d_p = 75\mu m$ and ········: B4 $d_q = 112.5\mu m$.

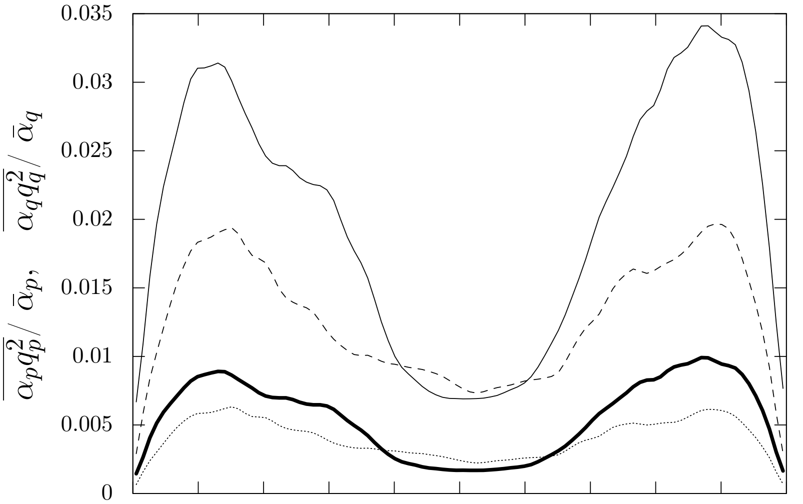

FIG. 6.41: Radial profiles of the mean particle kinetic agitation. The symbols are: ——: B1 $d_p = 75\mu m$, ▬: B1 $d_q = 150\mu m$, - - -: B2 $d_p = 75\mu m$ and ········: B2 $d_q = 150\mu m$.

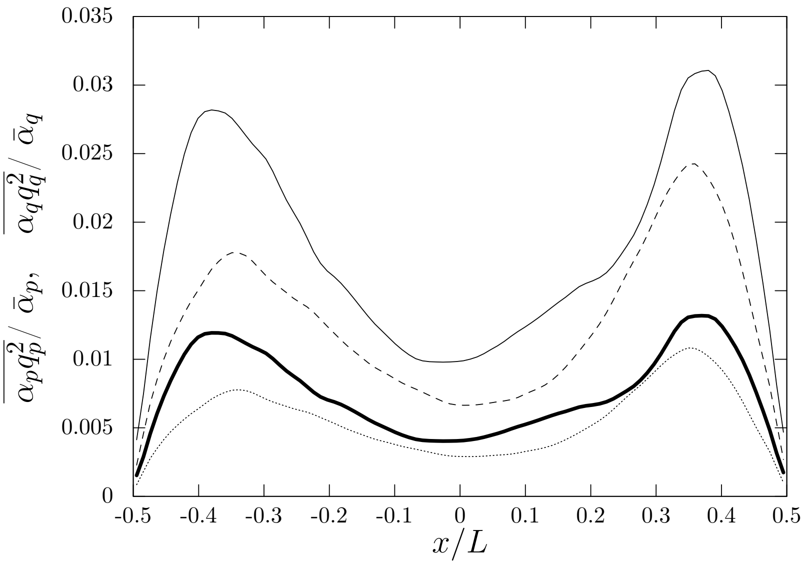

FIG. 6.42: Radial profiles of the mean particle kinetic agitation. The symbols are: ——: B3 $d_p = 75\mu m$, ━━: B3 $d_q = 112.5\mu m$, - - - : B4 $d_p = 75\mu m$ and ········ : B4 $d_q = 112.5\mu m$.

6.3.2 Study on the whole domain

Similarly to the study of monodisperse cases, the constant, K_{zz}, is firstly assumed equal to unity and the focus is given on the determination of function g. Considering the comparison of domain studied with and without the near-wall region for monodisperse cases, the development of the model will be performed by using the whole domain. The same approach will be applied to find the function g. However, the total filtered solid volume fraction, α_s, will be considered instead of the filtered volume fraction of the particle p or q. Indeed, the volume fractions of the two types of particles appear very correlated as shown in Figure 6.43 for the case B1. For the sake of clarity, data presented in such figure, were randomly plotted. Figures 6.44 and 6.45 present the function g conditionally averaged by the total filtered solid fraction, $\tilde{\alpha}_s$, for the small particles in all cases. From those Figures, it can be seen that the shape of the function g is similar for all cases and the number of statistical points remains significant even for high solid volume fraction. Figures 6.46 and 6.47 depict the function g for the two classes of particles for cases B2 and B4. For case B2, the function g appears independent of the particle diameter. For case B4, the shapes of function g computed for the two types of particles slightly differ for the largest filter widths.

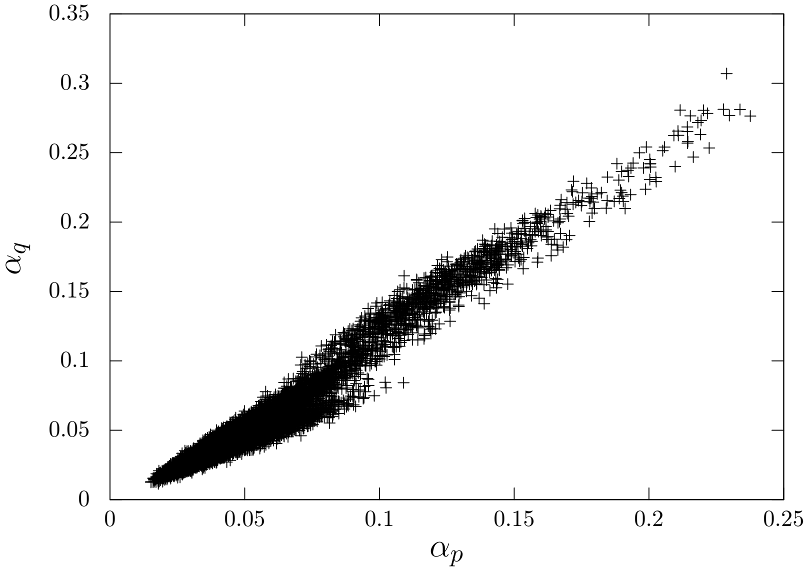

FIG. 6.43: Scattering plot of time averaged sα_q versus α_p in case B1.

In Figure 6.48,the effect of the particle diameter ratio is analysed by comparing case B1 and B2. The functions g of the small particles for the cases B1 and B3 appears to be similar. The particle diameter ratio has no effect on the value of the function g.
Figures 6.44, 6.45, 6.46 and 6.47 show that the function g is more affected by the particle volume fraction ratio than by the particle diameter. Similarly to the monodisperse cases, the function h, which depends on $\tilde{\alpha}_s$, is defined for solid volume fractions below 0.3 and is presented in Figures 6.49, 7.3. The shape of h appears similar for all cases. The function developed for the monodisperse cases, given in Eq. 6.10, appears to fit well the computed

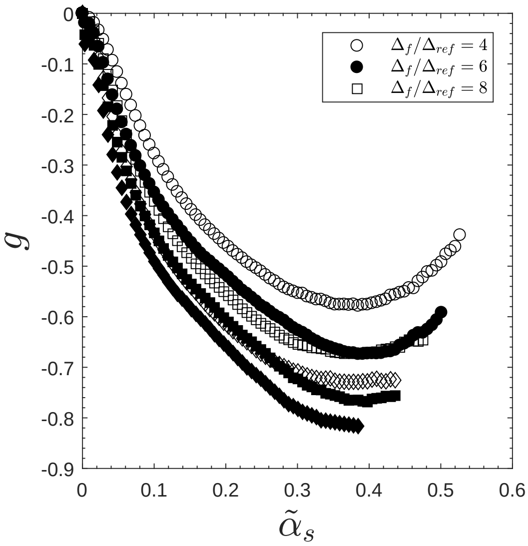

FIG. 6.44: The function g calculated with $d_p = 75\mu m$ in the bidisperse cases B1 and B2 and a minimum value of statistical points set to 1000. The open symbols correspond to the case B1 and the black filled symbols are the case B2.

values of h for volume fraction below 0.25 but tends to underestimate the value of h as the volume fraction increases. The flow studied consists mainly of small volume fraction as shown in PDFs of solid volume fractions. Hence, the function developed for the monodisperse cases appears to fit well most of the computed values of h. The function f is given in Figure 7.4. In all cases, the function tends to decreases linearly as the filter size increases similarly to the monodisperse cases. The function f appears to be more affected by the volume fraction ratio than by the types of particles chosen. Such a result is consistent with the comparison of the function g, which has been previously presented. The function f decreases linearly in all monodisperse and polydisperse cases. Yet, no dimensionless parameter appears to be valid for all cases. The model developed by Ozel [96] and Parmentier [101] are based on a dimensionless parameter, with the Froude number and the hydraulic diameter, respectively. Those models use a dynamic adjustment for the constant, K_{zz}, and they predict reasonably well the subgrid drift velocity. Considering the linearity of the function f, the difference and the similarity between the previous models, the function f is assumed being expressed as the cell size. The dynamical adjustment of the constant, K_{zz}, will take into account the characteristics of each case.

6.4 Dynamic adjustment of the constant

The study of monodisperse and polydisperse cases leads to write the filtered subgrid drag model as:

$$\begin{aligned} \tilde{\alpha}_p V_{d,z}^{(p)} &= \widetilde{\alpha_p (U_{f,z} - U_{p,z})} - \tilde{\alpha}_p (\tilde{U}_{f,z} - \tilde{U}_{p,z}) \\ &\approx K_{zz} \Delta_f h(\tilde{\alpha}_s) \tilde{\alpha}_p (\tilde{U}_{f,z} - \tilde{U}_{p,z}) \end{aligned} \tag{6.11}$$

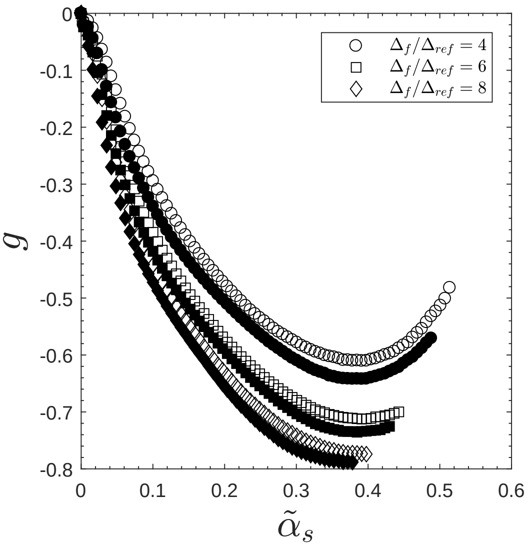

FIG. 6.45: The function g calculated with $d_p = 75\mu m$ in the bidisperse cases B4and B3 and a minimum value of statistical points set to 1000. The open symbols correspond to the case B3 and the black filled symbols are the case B4.

The model constant, K_{zz} can be dynamically adjusted by using a method adapted from Germano et al. [43] and Lilly [75]. A filter, named the test-filter, is applied on the resolved fields. Test-level filtered of a function f, noted $\hat{\tilde{f}}$, corresponds to an averaged base level function :

$$\begin{aligned}
\hat{\tilde{f}}(\mathbf{x},t) &= \frac{1}{7}(\tilde{f}(\mathbf{x},t) \\
&+ \tilde{f}(\mathbf{x}+\Delta_G\cdot\mathbf{e}_x,t)\tilde{f}(\mathbf{x}-\Delta_G\cdot\mathbf{e}_x,t) \\
&+ \tilde{f}(\mathbf{x}+\Delta_G\cdot\mathbf{e}_y,t)+\tilde{f}(\mathbf{x}-\Delta_G\cdot\mathbf{e}_y,t) \\
&+ \tilde{f}(\mathbf{x}+\Delta_G\cdot\mathbf{e}_z,t)+\tilde{f}(\mathbf{x}-\Delta_G\cdot\mathbf{e}_z,t))
\end{aligned} \quad (6.12)$$

where Δ_G the test fitler width.

In this study the mesh refined simulations enable to determine the real value of K_{zz}:

$$\frac{\langle \widetilde{\alpha_p(U_{f,z}-U_{p,z})} - \tilde{\alpha}_p(\tilde{U}_{f,z}-\tilde{U}_{p,z})\rangle}{\langle \Delta_f h(\tilde{\alpha}_s)\tilde{\alpha}_p(\tilde{U}_{f,z}-\tilde{U}_{p,z})\rangle} \quad (6.13)$$

Such constant will be evaluated in monodisperse and bidisperse cases. Then an priori analysis, comparing the modelled subgrid contribution and the real one, will be carried out.

6.4.1 Monodisperse cases

The average values of K_{zz} in Table 6.7 are in the same order or magnitude. However the constant tend to decreases as the test filter size increases. The effect is opposite for the

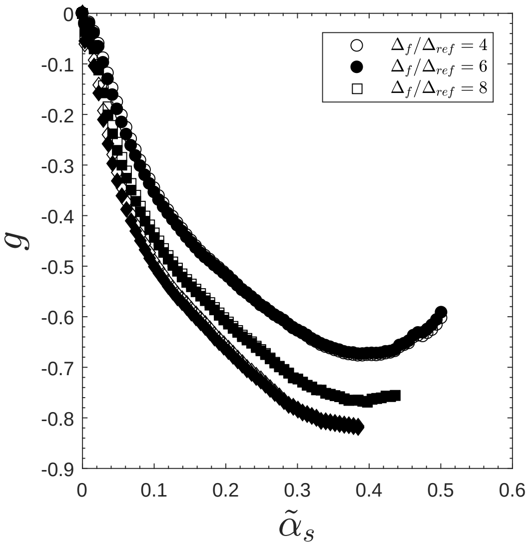

FIG. 6.46: The function g calculated for the two classes of particles ($d_p = 75\mu m$ and $d_q = 150\mu m$) bidisperse cases B1 and a minimum value of statistical points set to 1000. The open symbols correspond to particles p and the black filled symbols are for the particles q .

case with $4\rho_{p,ref}$. The correlation coefficients between modelled and subgrid contributions increase with Δ_f for all cases. They are significantly lower for cases M6 and M7. Given the average K_{zz} it is possible to find to determine the modelled subgrid drag force with $K_{zz}\Delta_f h(\tilde{\alpha}_s)\tilde{\alpha}_p(\tilde{U}_{f,z} - \tilde{U}_{p,z})$ and to compare the results with the real subgrid drag force $\widetilde{\alpha_p(U_{f,z} - U_{p,z})} - \tilde{\alpha}_p(\tilde{U}_{f,z} - \tilde{U}_{p,z})$. Figures 6.53 and 6.54 show the real subgrid contribution of gas-particle momentum transfer conditionally averaged by the modelled subgrid contribution. The Cumulative Density Function (CDF), resulting form the inegration of the PDF, presented in Figure 6.52, highlighted that most of the values are negative and close to 0. For the sake of clarity, the conditional averages are computed by taking into account the modelled subgrid contribution above 2% and below 98%. Most of the values appear well predicted by the model in the cases M1 and M2 independently of set of filter widths. However, the model overestimated the real subgrid contribution for the case M3.

6.4.2 Polydisperse cases

Tables 6.8 and 6.9 summarized respectively the constant, K_{zz}, computed for the small and the large particles and the correlation coefficient r between modelled and real subgrid contribution. The modelled and real values are in the same order or magnitude for small and large particles in all cases. The values appear to decrease as the filter size increases.

The averaged values can be computed by several ways, for the small particles. One way has been given in Table 6.8 and others are presented in Table 6.10. The values remains of the same order of magnitude, except one value with the larger filter size. The averaging procedure could not explain the difference found in Table 6.8.

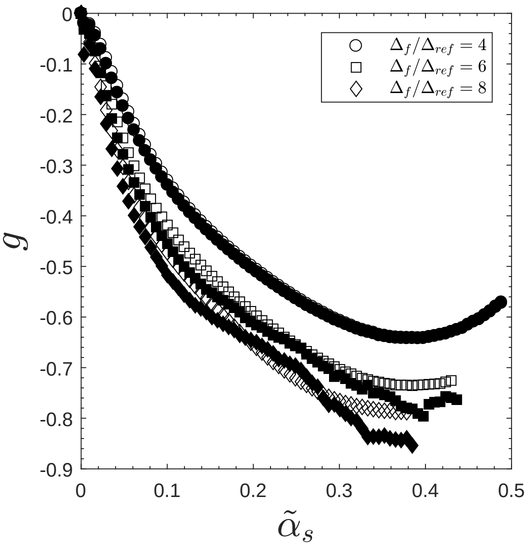

FIG. 6.47: The function g calculated for the two classes of particles ($d_p = 75\mu m$ and $d_q = 112.5\mu m$) in the bidisperse cases B4 and a minimum value of statistical points set to 1000. The open symbols correspond to particles p and the black filled symbols are for the particles q .

Figure 6.55 depicts the real subgrid contribution conditionally averaged by the modelled contribution for case B1 for the small particles. Considering the corresponding PDF presented in Figure 6.56, the modelled contributions and the real subgrid contributions appear to be in good agreement for most of the values as for the monodisperse cases. However, the subgrid contributions tend to be underestimated or overestimated by the model below and above the peak of the PDF. Figures 6.57 and 6.58 present the real subgrid contribution conditionally averaged by the modelled for cases B1, B2, B3 and B4 for $\Delta_f = 6\Delta_{ref}$ and $\Delta_G = 8\Delta_{ref}$ for the small and large particles respectively.For the small particles and ratio of solid volume fraction, the model appears to fit most of the values. However, the model appears to slightly overestimate the subgrid contribution or to predict positive values instead of negative ones for the large particle, especially for case B1. Such results could be related to the fact that the model does not predict accurately the subgrid contribution in the monodisperse case with $dp = 150\mu m$. It has to be noted that the sub-grid contribution of such large particles seems to be more accurately predicted in the polydisperse cases than in the monodisperse case. As it can be seen from Figure 6.39, the averaged velocity of both solid phase are similar. It can be assumed that the effect of the small particles on the velocity of the large particles leads to more accurate predictions of the subgrid contribution by the model.

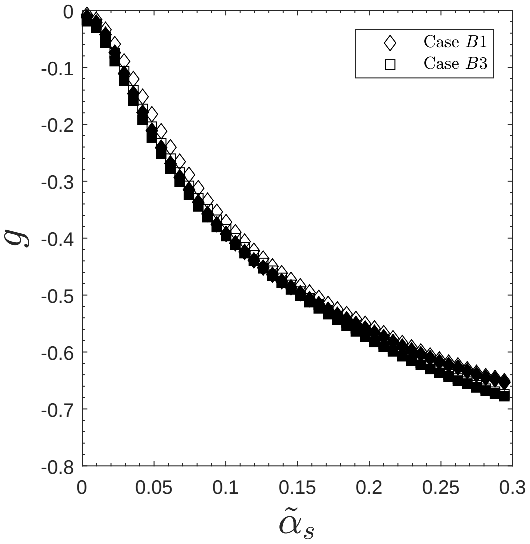

FIG. 6.48: The function g calculated for the two classes of particles for cases B1 and B3 and $\Delta_f/\Delta_{ref} = 6$. The open symbols correspond to particles p and the black filled symbols are for the particles q .

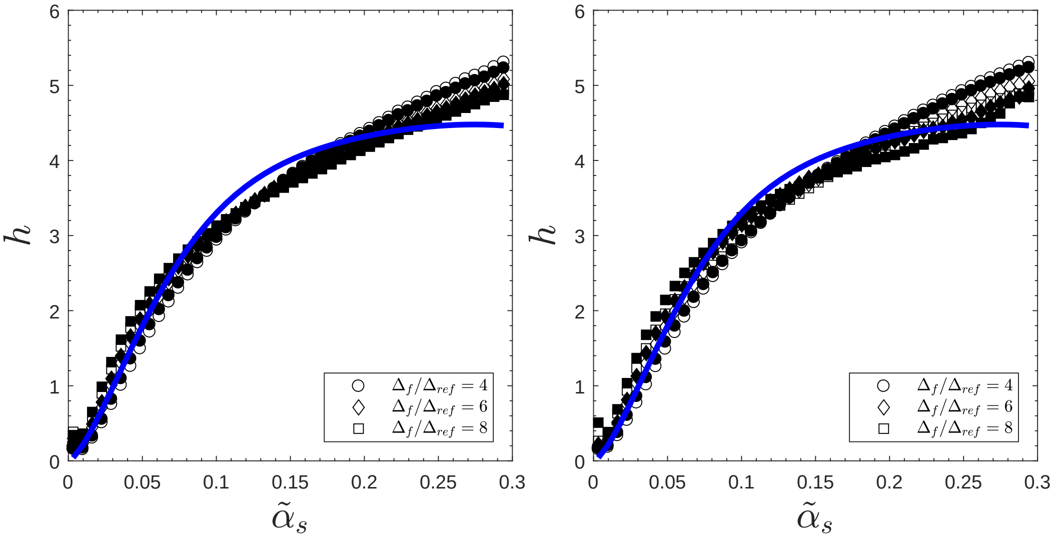

(a) (b)

FIG. 6.49: The function h computed for particle p and q particles in (a): B2, (b): B4. The open symbols correspond to particles p and the black filled symbols are for the particles q.

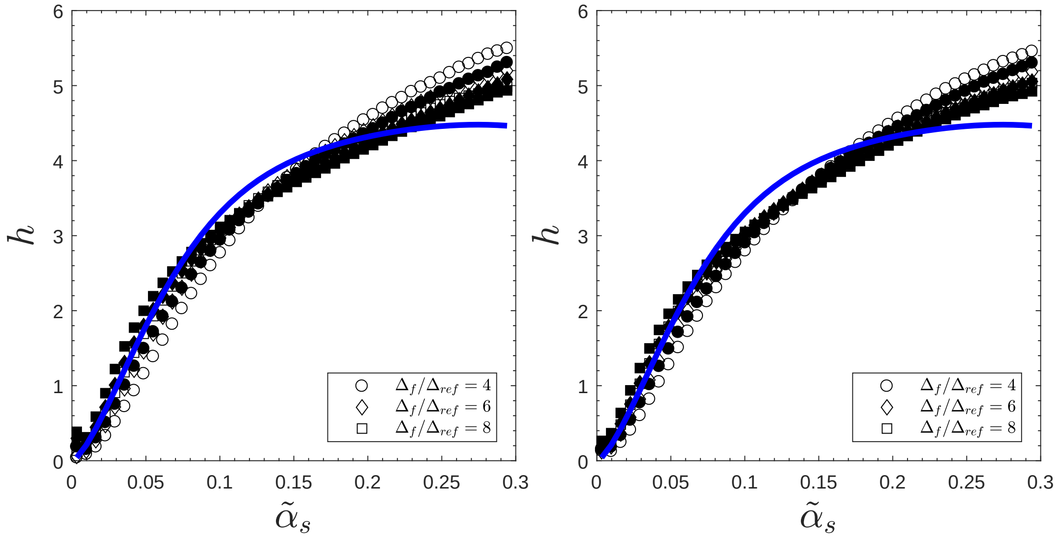

(a) (b)

FIG. 6.50: The function h computed for particle p particles ($d_q = 75\,\mu m$) in (a): B1 and B2, (b): B3 and B4. The open symbols correspond to cases with $\alpha_p = \alpha_q$(B1 and B3) and the black filled symbols are for the cases with $\alpha_p \neq \alpha_q$(B2 and B4).

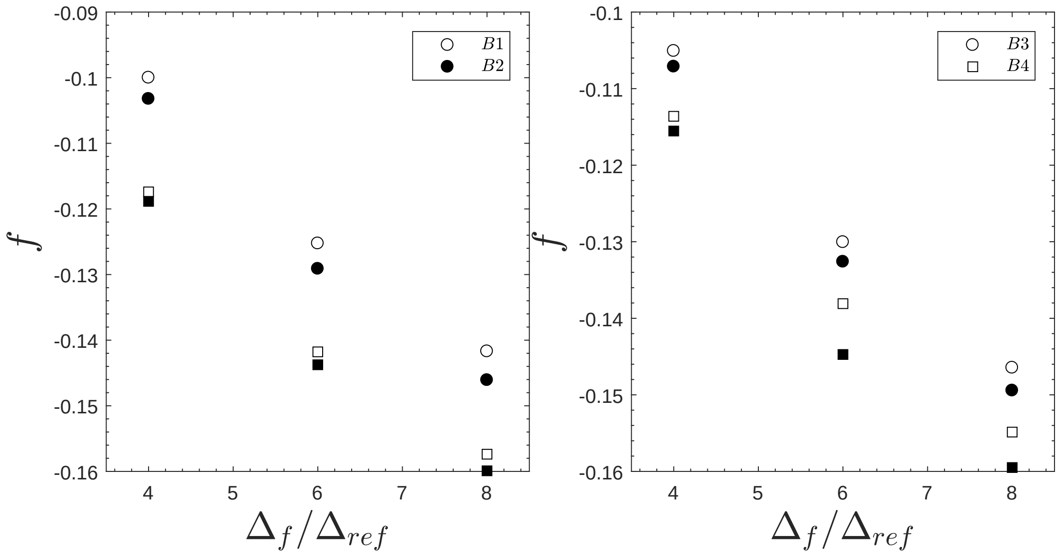

(a) (b)

FIG. 6.51: The function f computed for particle p and q in (a): B1 and B2, (b): B3 and B4. The open symbols correspond to particles p and the black filled symbols are for the particles q.

TAB. 6.7: Average K_{zz} for various test filters in monodisperse cases

Filters	Case	$\frac{\langle L_z M_z \rangle}{\langle M_z M_z \rangle}$	$\frac{\langle \widetilde{\alpha_p V_{r,z}^{(p)}} - \tilde{\alpha}_p V_{r,z}^{(p),res} \rangle}{\langle \Delta_f h(\tilde{\alpha}_s) \tilde{\alpha}_p V_{r,z}^{(p),res} \rangle}$	r
$\frac{\Delta_f}{\Delta_{ref}} = 4$, $\frac{\Delta_G}{\Delta_{ref}} = 6$	M1	$0.186 \cdot 10^4$	$0.212 \cdot 10^4$	0.82
	M2	$0.191 \cdot 10^4$	$0.208 \cdot 10^4$	0.97
	M3	$0.156 \cdot 10^4$	$0.113 \cdot 10^4$	0.90
	M6	$0.193 \cdot 10^4$	$0.198 \cdot 10^4$	0.78
	M7	$0.141 \cdot 10^4$	$0.116 \cdot 10^4$	0.77
$\frac{\Delta_f}{\Delta_{ref}} = 4$, $\frac{\Delta_G}{\Delta_{ref}} = 8$	M1	$0.142 \cdot 10^4$	$0.212 \cdot 10^4$	0.82
	M2	$0.152 \cdot 10^4$	$0.208 \cdot 10^4$	0.97
	M3	$0.123 \cdot 10^4$	$0.113 \cdot 10^4$	0.88
	M6	$0.193 \cdot 10^4$	$0.198 \cdot 10^4$	0.78
	M7	$0.108 \cdot 10^4$	$0.113 \cdot 10^4$	0.77
$\frac{\Delta_f}{\Delta_{ref}} = 6$, $\frac{\Delta_G}{\Delta_{ref}} = 8$	M1	$0.163 \cdot 10^4$	$0.188 \cdot 10^4$	0.85
	M2	$0.152 \cdot 10^4$	$0.191 \cdot 10^4$	0.98
	M3	$0.139 \cdot 10^4$	$0.118 \cdot 10^4$	0.93
	M6	$0.193 \cdot 10^4$	$0.198 \cdot 10^4$	0.84
	M7	$0.123 \cdot 10^4$	$0.108 \cdot 10^4$	0.85

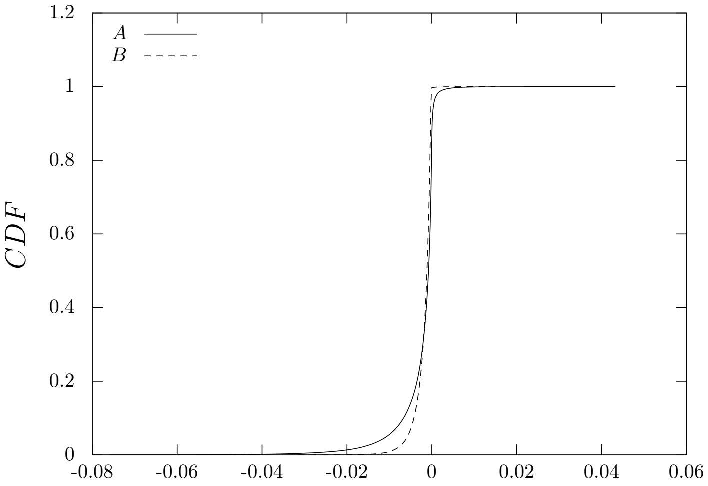

FIG. 6.52: CDF of $A = \tilde{\alpha}_p V_{d,z}^{(p)}$ and $B = K_{zz} \Delta_f h(\tilde{\alpha}_s) \tilde{\alpha}_p (\tilde{U}_{f,z} - \tilde{U}_{p,z})$ for case M1with $\Delta_f = 4\Delta_{ref}$ and $\Delta_G = 6\Delta_{ref}$

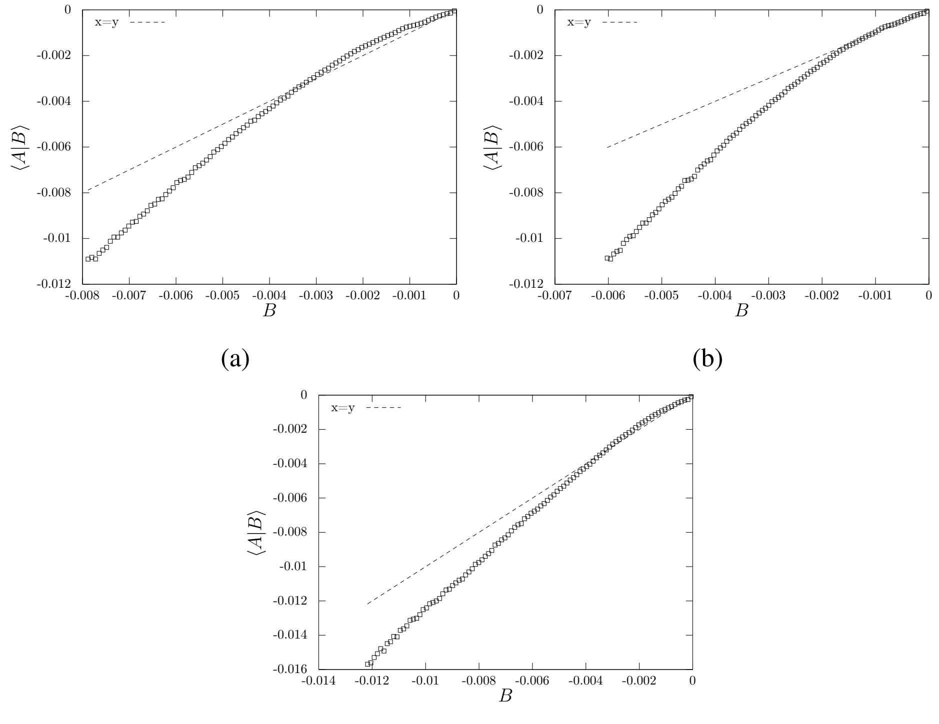

(a) (b)

(c)

FIG. 6.53: The conditional mean of the instantaneous real subgrid contribution by the instantaneous modelled subgrid contribution for case M1with $A = \tilde{\alpha}_p V_{d,z}^{(p)}$ and $B = K_{zz}\Delta_f h(\tilde{\alpha}_s)\tilde{\alpha}_p(\tilde{U}_{f,z} - \tilde{U}_{p,z})$, for several filter widths (a): $\Delta_f = 4\Delta_{ref}$ and $\Delta_G = 6\Delta_{ref}$, (b): $\Delta_f = 4\Delta_{ref}$ and $\Delta_G = 8\Delta_{ref}$, (c): $\Delta_f = 6\Delta_{ref}$ and $\Delta_G = 8\Delta_{ref}$

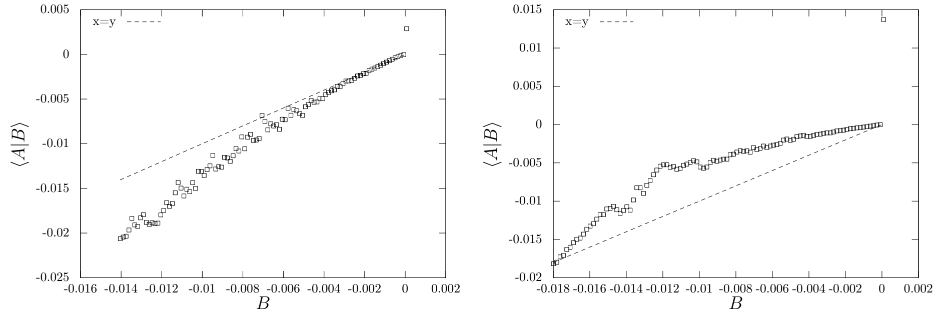

(a) (b)

FIG. 6.54: The conditional mean of the instantaneous real subgrid contribution by the instantaneous modelled subgrid contribution for $\Delta_f = 6\Delta_{ref}$ and $\Delta_G = 8\Delta_{ref}$ with $A = \tilde{\alpha}_p V_{d,z}^{(p)}$ and $B = K_{zz}\Delta_f h(\tilde{\alpha}_s)\tilde{\alpha}_p(\tilde{U}_{f,z} - \tilde{U}_{p,z})$, for two cases, (a): M2, (b): M3.

TAB. 6.8: Average K_{zz} for various test filters for the gas-particle momentum exchange ($d_p = 75\mu m$)

Filters	Case	$\frac{\langle L_z M_z \rangle}{\langle M_z M_z \rangle}$	$\frac{\langle \widetilde{\alpha_p V_{r,z}^{(p)}} - \tilde{\alpha}_p V_{r,z}^{(p),res} \rangle}{\langle \Delta_f h(\tilde{\alpha}_s) \tilde{\alpha}_p V_{r,z}^{(p),res} \rangle}$	r
$\frac{\Delta_f}{\Delta_{ref}} = 4$, $\frac{\Delta_G}{\Delta_{ref}} = 6$	B1	$0.140 \cdot 10^4$	$0.146 \cdot 10^4$	0.83
	B2	$0.156 \cdot 10^4$	$0.168 \cdot 10^4$	0.83
	B3	$0.151 \cdot 10^4$	$0.154 \cdot 10^4$	0.86
	B4	$0.156 \cdot 10^4$	$0.171 \cdot 10^4$	0.90
$\frac{\Delta_f}{\Delta_{ref}} = 4$, $\frac{\Delta_G}{\Delta_{ref}} = 8$	B1	$0.106 \cdot 10^4$	$0.146 \cdot 10^4$	0.83
	B2	$0.114 \cdot 10^4$	$0.169 \cdot 10^4$	0.83
	B3	$0.115 \cdot 10^4$	$0.154 \cdot 10^4$	0.85
	B4	$0.118 \cdot 10^4$	$0.171 \cdot 10^4$	0.87
$\frac{\Delta_f}{\Delta_{ref}} = 6$, $\frac{\Delta_G}{\Delta_{ref}} = 8$	B1	$0.117 \cdot 10^4$	$0.128 \cdot 10^4$	0.88
	B2	$0.125 \cdot 10^4$	$0.142 \cdot 10^4$	0.87
	B3	$0.127 \cdot 10^4$	$0.135 \cdot 10^4$	0.90
	B4	$0.129 \cdot 10^4$	$0.145 \cdot 10^4$	0.87

TAB. 6.9: Average K_{zz} for various test filters for the gas-particle momentum exchange ($d_p = 150\mu m$)

Filters	Case	$\frac{\langle L_z M_z \rangle}{\langle M_z M_z \rangle}$	$\frac{\langle \widetilde{\alpha_p V_{r,z}^{(p)}} - \tilde{\alpha}_p V_{r,z}^{(p),res} \rangle}{\langle \Delta_f h(\tilde{\alpha}_s) \tilde{\alpha}_p V_{r,z}^{(p),res} \rangle}$	r
$\frac{\Delta_f}{\Delta_{ref}} = 4$, $\frac{\Delta_G}{\Delta_{ref}} = 6$	B1	$0.162 \cdot 10^4$	$0.113 \cdot 10^4$	0.83
	B2	$0.176 \cdot 10^4$	$0.174 \cdot 10^4$	0.83
	B3	$0.169 \cdot 10^4$	$0.139 \cdot 10^4$	0.87
	B4	$0.167 \cdot 10^4$	$0.155 \cdot 10^4$	0.90
$\frac{\Delta_f}{\Delta_{ref}} = 4$, $\frac{\Delta_G}{\Delta_{ref}} = 8$	B1	$0.120 \cdot 10^4$	$0.113 \cdot 10^4$	0.82
	B2	$0.129 \cdot 10^4$	$0.130 \cdot 10^4$	0.82
	B3	$0.122 \cdot 10^4$	$0.139 \cdot 10^4$	0.86
	B4	$0.126 \cdot 10^4$	$0.155 \cdot 10^4$	0.87
$\frac{\Delta_f}{\Delta_{ref}} = 6$, $\frac{\Delta_G}{\Delta_{ref}} = 8$	B1	$0.134 \cdot 10^4$	$0.113 \cdot 10^4$	0.88
	B2	$0.143 \cdot 10^4$	$0.121 \cdot 10^4$	0.87
	B3	$0.134 \cdot 10^4$	$0.129 \cdot 10^4$	0.90
	B4	$0.138 \cdot 10^4$	$0.137 \cdot 10^4$	0.83

TAB. 6.10: Average K_{zz} for various test filters for the gas-particle momentum exchange for case B3

Filters	$\frac{\langle L_z \rangle}{\langle M_z \rangle}$	$\langle \frac{L_z}{M_z} \rangle$
$\frac{\Delta_f}{\Delta_{ref}} = 4$, $\frac{\Delta_G}{\Delta_{ref}} = 6$	$0.129 \cdot 10^4$	$0.147 \cdot 10^4$
$\frac{\Delta_f}{\Delta_{ref}} = 4$, $\frac{\Delta_G}{\Delta_{ref}} = 8$	$0.991 \cdot 10^3$	$0.837 \cdot 10^3$
$\frac{\Delta_f}{\Delta_{ref}} = 6$, $\frac{\Delta_G}{\Delta_{ref}} = 8$	$0.114 \cdot 10^4$	$0.304 \cdot 10^4$

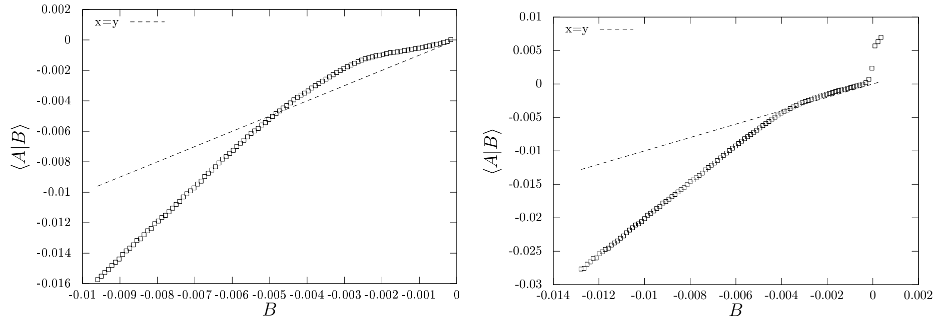

(a) (b)

FIG. 6.55: The conditional mean of the instantaneous real subgrid contribution by the modelled subgrid contribution for case B3 and the small particles with $A = \tilde{\alpha}_p V_{d,z}^{(p)}$ and $B = K_{zz}\Delta_f h(\tilde{\alpha}_s)\tilde{\alpha}_p(\tilde{U}_{f,z} - \tilde{U}_{p,z})$, for several filter widths (a): $\Delta_f = 4\Delta_{ref}$ and $\Delta_G = 6\Delta_{ref}$, (b): $\Delta_f = 6\Delta_{ref}$ and $\Delta_G = 8\Delta_{ref}$

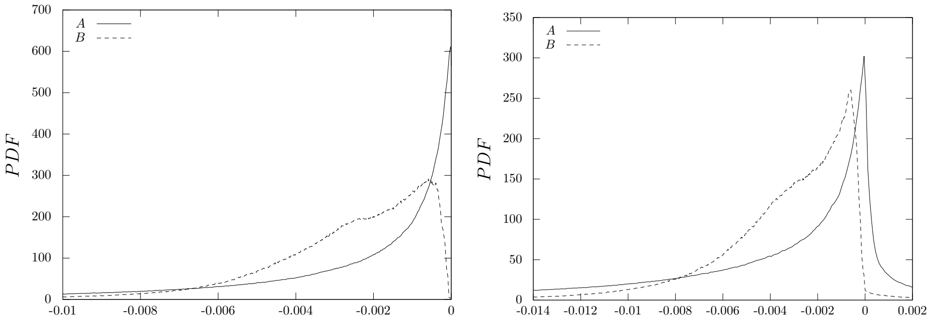

(a) (b)

FIG. 6.56: PDF of the instantaneous modelled subgrid contribution for B3 and the small particles with $A = \tilde{\alpha}_p V_{d,z}^{(p)}$ and $B = K_{zz}\Delta_f h(\tilde{\alpha}_s)\tilde{\alpha}_p(\tilde{U}_{f,z} - \tilde{U}_{p,z})$, for several filter widths (a): $\Delta_f = 4\Delta_{ref}$ and $\Delta_G = 6\Delta_{ref}$, (b): $\Delta_f = 6\Delta_{ref}$ and $\Delta_G = 8\Delta_{ref}$

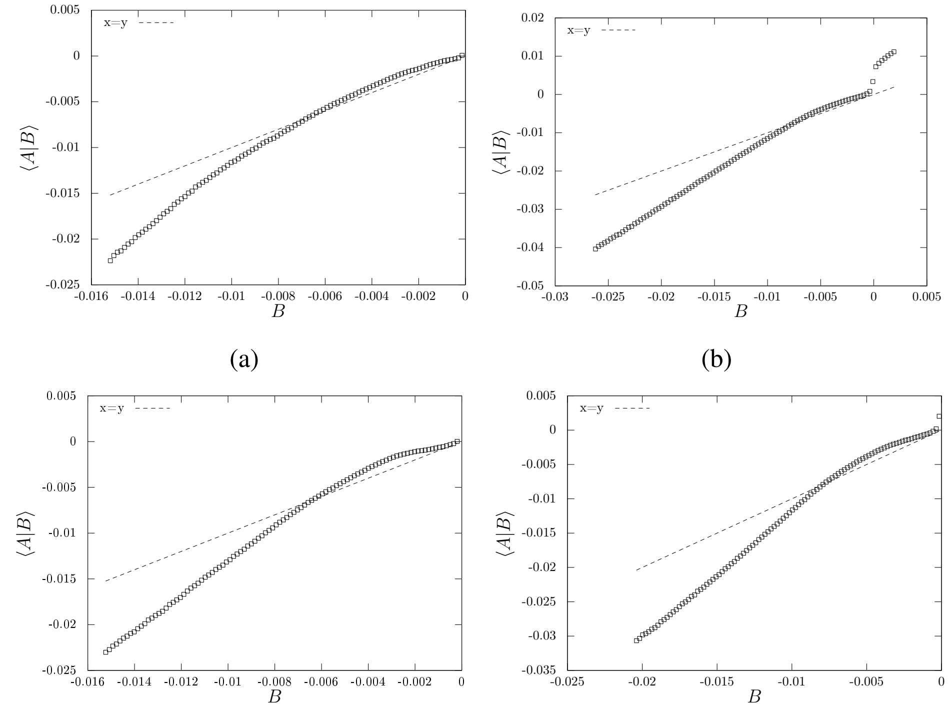

(a) (b)

(c) (d)

FIG. 6.57: The conditional mean of the instantaneous real subgrid contribution by the instantaneous modelled subgrid contribution for $\Delta_f = 4\Delta_{ref}$ and $\Delta_G = 8\Delta_{ref}$ with $A = \tilde{\alpha}_p V_{d,z}^{(p)}$ and $B = K_{zz}\Delta_f h(\tilde{\alpha}_s)\tilde{\alpha}_p(\tilde{U}_{f,z} - \tilde{U}_{p,z})$, for several cases (a): B1, (b): B2, (c): B3 and (d): B4.

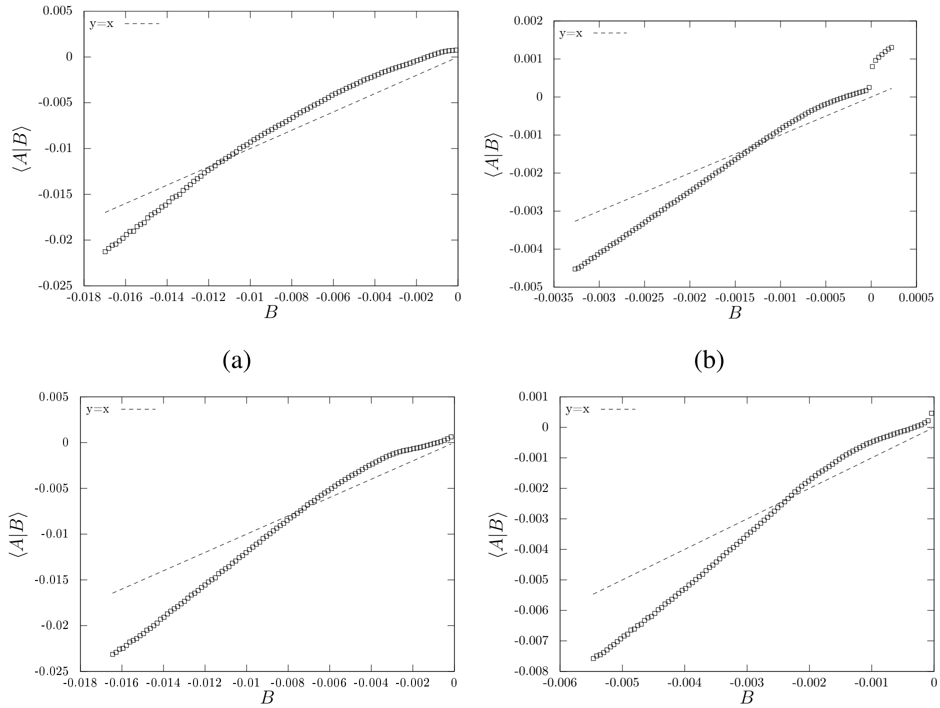

(a) (b)

(c) (d)

FIG. 6.58: The conditional mean of the instantaneous real subgrid contribution by the instantaneous modelled subgrid contribution for $\Delta_f = 4\Delta_{ref}$ and $\Delta_G = 8\Delta_{ref}$ with $A = \tilde{\alpha}_p V_{d,z}^{(p)}$ and $B = K_{zz}\Delta_f h(\tilde{\alpha}_s)\tilde{\alpha}_p(\tilde{U}_{f,z} - \tilde{U}_{p,z})$, for several cases (a): B1, (b): B2, (c): B3 and (d): B4.

Summary

The monodisperse and bidisperse mesh-refined simulations have been to perform budget analysis, which highlights the need of a subgrid model for gas-particle momentum transfer. To predict accurately such term, the subgrid drift flux, the slip velocity between gas and particle multiples by the solid volume fraction, has to be modelled. A functional model has been developed in keeping with work of Ozel et al. [98] and Parmentier et al. [103]. A function h considers the influence of the total solid volume fraction, $\tilde{\alpha}_s$. The shape of such a function was found to be in good agreement with the one obtained by Ozel et al. [98] in monodisperse simulation of CFB. Then the model includes the size of the filter and a constant, K_{zz}, which is dynamically adapted following a method adapted from Germano et al. [43] and Lilly [75]. A priori analysis shows that such model is adapted for monodisperse simulations with small particles, however, the model provides inaccurate predictions in the monodisperse case with the largest particles. In the bidisperse simulations, the model appears to predict accurately most of the subgrid contributions values. Such a difference between monodisperse and bidisperse simulations could be due to the effect of the small particles on the velocity of the large particles.

Chapter 7

Subgrid contribution of the inter-particle collision

Contents

7.1 Introduction

In the momentum equation, the subgrid contributions of drag and inter-particle momentum transfer need to be modelled in order to predict correctly the hydrodynamic behaviour of bidisperse flows with coarse mesh simulations. The collision between particles in bidisperse flows includes two mechanisms. On the one hand, the collisions are caused by the fluid turbulence. On the other hand, they are due to mean relative velocity between different particle species. Statistical models, which take into account both collision mechanism, were developed by Gourdel et al. [50] for bidisperse particle flows. Such a model, relying on the Maxwell velocity distribution, is not able to take into account the particle motion correlation and the fluctuating velocity anisotropy. Fede and Simonin [35] developed a model based on the Grad's approach to define the particle velocity distribution. Such a model considers the turbulent fluctuation anisotropy and the particle velocity correlation. However the relative drift between the particles of different species is not taken into account. In coarse mesh simulations, the inter-particle tends to be overestimated, which is consistent with the results obtained by Ozel et al. [99]. The prediction of such term may have a significant influence in simulations of bidisperse flows since the inter-particle momentum transfer by collision enables the entrainment of large particles by the small ones.

The expression of the inter-particle momentum transfer includes the collision frequency, which depends on the particle kinetic agitation. In the transport equation of particle kinetic agitation, the production by velocity gradient tends to be underestimated in coarse mesh simulations. Such an influence of the mesh-size has already been observed in monodisperse simulations [96, 2]. One explanation is that the non-uniformity of clusters decreases as the cell-size goes up. Such decrease leads to smaller velocity gradient.

In this chapter, a functional subgrid model for the inter-particle momentum transfer will be developed. The correlation analysis shows that the focus should be given to the relative velocity between particle species. Then, the subgrid contribution of production by velocity gradient will be studied with monodisperse simulations. A solution will be investigated to improve the production of q_p^2.

7.2 Subgrid model for the inter-particle momentum transfer

7.2.1 Model description

In polydisperse cases, the budget analysis shows that the subgrid contribution of inter-particle momentum transfer needs to be modelled. In this section, polydisperse simulations are analysed in order to develop such a subgrid model. The study will be performed on the whole domain, which provides more statistical points. As previously shown, the inter-particle momentum transfer can be approximated as:

$$\tilde{I}_{q\rightarrow p,z} \approx -\frac{m_p m_q}{m_p + m_q}\frac{1+e_c}{2} g_r^{res} g_0^{res} \pi d_{pq}^2 H_1(z^{res}) \widetilde{n_p n_q \left(U_{p,z} - U_{q,z}\right)} \qquad (7.1)$$

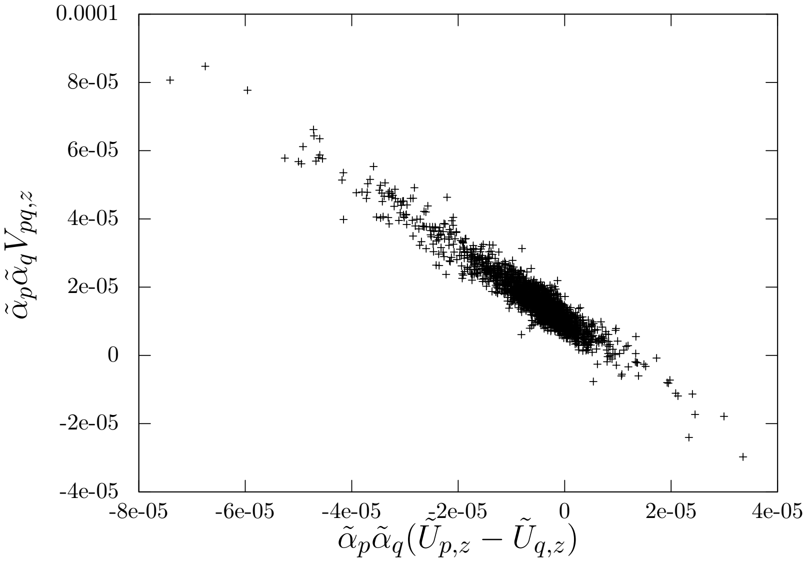

FIG. 7.1: Scattering plot of $\tilde{\alpha}_p\tilde{\alpha}_q V_{pq,z}$ versus $\tilde{\alpha}_p\tilde{\alpha}_q(\tilde{U}_{p,z}-\tilde{U}_{q,z})$ for case B2

Similarly to the gas-particle momentum exchange, the filtered inter-particle momentum transfer is expressed as:

$$\tilde{I}_{q\to p,z} = -\frac{m_p m_q}{m_p+m_q}\frac{1+e_c}{2} g_r^{res} g_0^{res} \pi d_{pq}^2 H_1(z^{res})\tilde{n}_p\tilde{n}_q \left(\tilde{U}_{p,z}-\tilde{U}_{q,z}+V_{pq,z}\right) \quad (7.2)$$

The diameter and the density are independent of the filter size, hence $V_{pq,z}$ is written as:

$$V_{pq,z} = \frac{\widetilde{\alpha_p\alpha_q\left(U_{p,z}-U_{q,z}\right)}}{\tilde{\alpha}_p\tilde{\alpha}_q} - \left(\tilde{U}_{p,z}-\tilde{U}_{q,z}\right). \quad (7.3)$$

Figure 7.1 shows the subgrid contribution and their respective resolved contribution for various filter widths. For the sake of clarity, data are randomly plotted. The subgrid contribution of the inter-particle momentum transfer appears highly correlated to the resolved contribution. High similarities can be observed between gas-particle and inter-particle momentum transfer, hence the model of $V_{pq,z}$ is assumed to be expressed as:

$$V_{pq,z} = g(\Delta_f,\tilde{\alpha}_s)(\tilde{U}_{p,z}-\tilde{U}_{q,z}) \quad (7.4)$$

with g the drag correction tensor, function of the length-scale Δ_f and the filtered particle volume fraction $\tilde{\alpha_s}$. The function g can computed using the mesh-independent data for a gas-solid flow simulations given in Table 5.1:

$$g(\Delta_f,\tilde{\alpha}_s) = \frac{\overline{\langle V_{pq,z}|\tilde{\alpha}_s\rangle}}{\overline{\langle(\tilde{U}_{p,z}-\tilde{U}_{q,z})|\tilde{\alpha}_s\rangle}} \quad (7.5)$$

with $V_{pq,z}$ and $(\tilde{U}_{p,z}-\tilde{U}_{q,z})$ conditionally averaged by the total solid volume fraction then averaged in time. Figure 7.2 shows that the shape of g is independent of the filter widths.

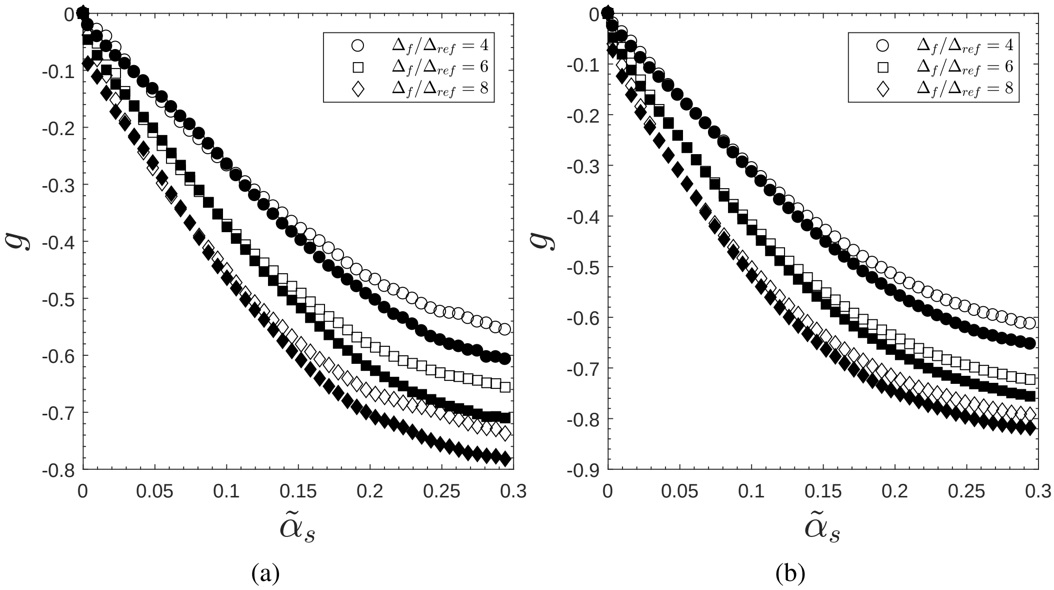

(a) (b)

FIG. 7.2: The function g computed in (a): B1 and B2, (b): B3 and B4. The open symbols correspond to cases with $\alpha_p = \alpha_q$((a):B1 and (b):B3) and the black filled symbols are for the cases with $\alpha_p \neq \alpha_q$((a):B2 and (b):B4).

The function g is only slightly affected by the volume fraction ratio. Cases B3 and B4 appears to be more independent of the solid volume fraction ratio than Case B1 and B2. This could be explained by the diameter of the larger particles, which is more significant for Case B1 and B2 and also by the fact that solid volume fraction ratio differs between Case B2 and B4. Considering the similarity of the shape of g, the function can be decomposed as a function of the filter solid volume fraction $\tilde{\alpha}_s$ and a function of Δ_f.

$$g(\Delta_f, \tilde{\alpha}_s) = h(\tilde{\alpha}_s) f(\Delta_f) \tag{7.6}$$

The aim is to determine the function h and f valid for all cases, the constant K_{zz} will be determined by dynamic adjustement. The function h can be deduced using the integration of the function g between 0 and 0.3. Figure 7.3 depicts the function h as function of the filtered solid volume fraction for different filter widths for each diameter. The function h can be expressed for all cases as:

$$h_{model}(\tilde{\alpha}_s) = (1 + 26.41u - 32.91u)u^{1/4} \tag{7.7}$$

with $u = \frac{\tilde{\alpha}_s}{0.64}$.

The function f is then computed and presented in Figure 7.4 for small and large particles in both cases. The function f appears to have a linear evolution for both types of particles in all cases.

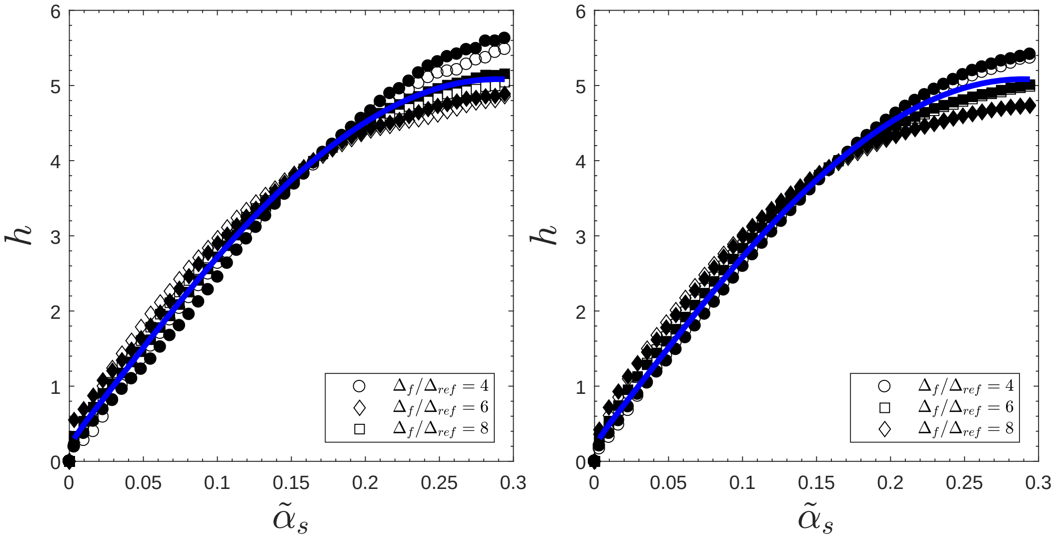

(a) (b)

FIG. 7.3: The function h computed in (a): Cases B1 and B2, (b): Cases B3 and B4. The open symbols correspond to cases with $\alpha_p = \alpha_q$((a):B1 and (b):B3), the black filled symbols are for the cases with $\alpha_p \neq \alpha_q$((a):B2 and (b):B4) and ▬ refers to h_{model}.

7.2.2 Dynamic adjustment

Similarly to the subgrid model of the gas-particle momentum exchange, the constant of the model can be adjusted dynamically by using a method adapted from Germano et al. and Lilly. The subgrid relative velocity can be expressed as:

$$\begin{aligned}\tilde{\alpha}_p\tilde{\alpha}_q V_{pq,z} &= \widetilde{\alpha_p\alpha_q(U_{q,z}-U_{p,z})} - \tilde{\alpha}_p\tilde{\alpha}_q(\tilde{U}_{q,z}-\tilde{U}_{p,z}) \\ &\approx K_{zz} f(\Delta_f) h(\tilde{\alpha}_s)\tilde{\alpha}_p\tilde{\alpha}_q(\tilde{U}_{q,z}-\tilde{U}_{p,z}) \end{aligned} \tag{7.8}$$

At the test-filter level, the relative velocity is expressed as:

$$\begin{aligned}\tilde{\alpha}_p\widehat{\tilde{\alpha}_q V}_{pq,z} &= \widehat{\widetilde{\alpha_p\alpha_q(U_{p,z}-U_{q,z})}} - \hat{\tilde{\alpha}}_p\hat{\tilde{\alpha}}_q(\hat{\tilde{U}}_{p,z}-\hat{\tilde{U}}_{q,z}) \\ &\approx \hat{\tilde{\alpha}}_p\hat{\tilde{\alpha}}_q(\hat{\tilde{U}}_{p,z}-\hat{\tilde{U}}_{q,z}) K_{zz} f(\Delta_G) h(\hat{\tilde{\alpha}}_s) \end{aligned} \tag{7.9}$$

Applying the test-filter on Eq. 7.8, the relative velocity is written as:

$$\tilde{\alpha}_p\widehat{\tilde{\alpha}_q V}_{pq,z} = \widehat{\widetilde{\alpha_p\alpha_q(U_{p,z}-U_{q,z})}} - \tilde{\alpha}_p\tilde{\alpha}_q(\widehat{\tilde{U}_{p,z}-\tilde{U}_{q,z}}) \tag{7.10}$$

Assuming that K_{zz} is independent of the filter width, Eq. 7.10 can be written:

$$\widehat{\widetilde{\alpha_p\alpha_q V_{pq,z}}} \approx K_{zz} f(\Delta_f) h(\tilde{\alpha}_s)\widehat{\tilde{\alpha}_p\tilde{\alpha}_q}(\tilde{U}_{p,z}-\tilde{U}_{q,z}) \tag{7.11}$$

Combining 7.9 and 7.11, K_{zz} can be expressed as:

$$K_{zz} = \frac{L_z}{M_z} \tag{7.12}$$

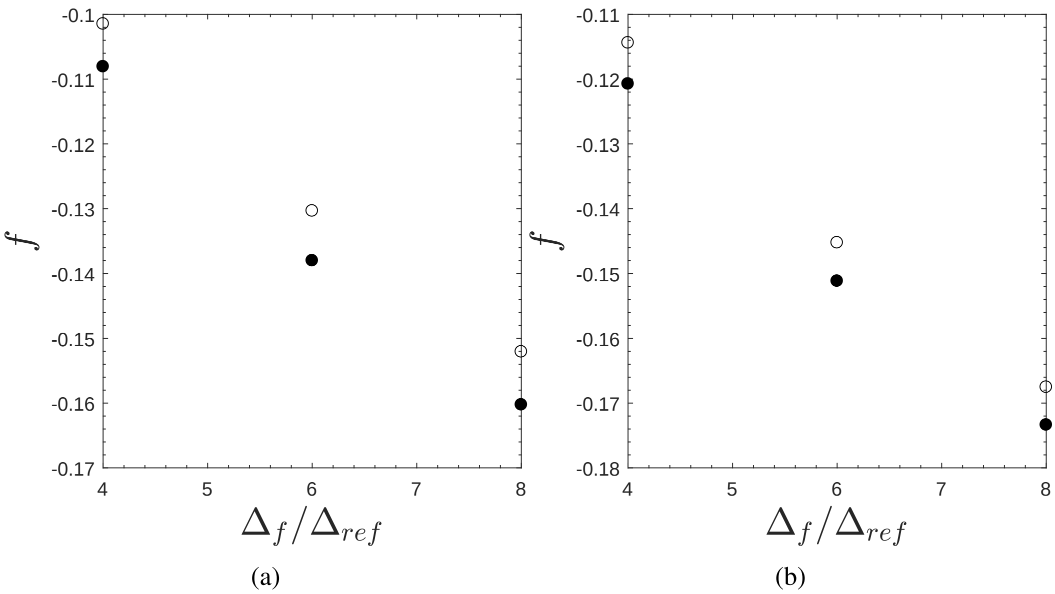

FIG. 7.4: The function f in (a): Cases B1 and B2, (b): Cases B3 and B4. The open symbols correspond to cases with $\alpha_p = \alpha_q$((a):B1 and (b):B3) and the black filled symbols are for the cases with $\alpha_p \neq \alpha_q$((a):B2 and (b):B4).

with $L_z = \tilde{\alpha}_p(\widehat{\tilde{U}_{p,z} - \tilde{U}_{q,z}}) - \hat{\tilde{\alpha}}_p(\hat{\tilde{U}}_{p,z} - \hat{\tilde{U}}_{q,z})$ and $M_\beta = f(\Delta_G)h(\hat{\tilde{\alpha}}_s)\hat{\tilde{\alpha}}_p(\hat{\tilde{U}}_{p,z} - \hat{\tilde{U}}_{q,z}) - f(\Delta_f)h(\tilde{\alpha}_s)\widehat{\tilde{\alpha}_p(\tilde{U}_{p,z}} - \tilde{U}_{q,z})$. In order to avoid numerically unstable value, the domain average coefficient along the mean flow is calculated:

$$K_z = \frac{\langle L_z M_z \rangle}{\langle M_z M_z \rangle} \tag{7.13}$$

Assuming that $f(\Delta_f) = \Delta_f$ the constant K_{zz} should be equal to:

$$\frac{\langle \widetilde{\alpha_p \alpha_q (U_{p,z} - U_{q,z})} - \tilde{\alpha}_p \tilde{\alpha}_q (\tilde{U}_{p,z} - \tilde{U}_{q,z}) \rangle}{\langle \Delta_f h(\tilde{\alpha}_s) \tilde{\alpha}_p \tilde{\alpha}_q (\tilde{U}_{p,z} - \tilde{U}_{q,z}) \rangle}. \tag{7.14}$$

Table 7.1 summarized the time averaged values of K_{zz}. The spatial averaged of the modelled and real coefficients are in good agreement for all cases and sets of filter widths. Figures 7.5 and 7.6 show the real subgrid contributions conditionally averaged by the modelled ones and its PDF. The modelled contributions appear to be able to predict accurately most of the subgrid values. However, the predictions are underestimated or overestimated outside the peak of the PDF. In Figure 7.7, the real subgrid contributions conditionally averaged by the modelled ones are shown for all bidisperse cases. Most subgrid contributions are accurately predicted by the model for all cases.

TAB. 7.1: Average K_{zz} for various test filters for the particle-particle momentum exchange for cases B1, B2, B3 and B4

Filters	Case	$\frac{\langle L_\beta M_\beta \rangle}{\langle M_\beta M_\beta \rangle}$	$\frac{\langle \widetilde{\alpha_p \alpha_q (U_{p,\beta} - U_{q,\beta})} - \tilde{\alpha}_p \tilde{\alpha}_q (\tilde{U}_{p,\beta} - \tilde{U}_{q,\beta}) \rangle}{\langle \Delta_f h(\tilde{\alpha}_s) \tilde{\alpha}_p \tilde{\alpha}_q (\tilde{U}_{p,\beta} - \tilde{U}_{q,\beta}) \rangle}$	r
$\Delta_f = 4$, $\Delta_G = 6$	B1	$-0.829 \cdot 10^2$	$-0.853 \cdot 10^2$	0.90
	B2	$-0.874 \cdot 10^2$	$-0.989 \cdot 10^2$	0.93
	B3	$-0.918 \cdot 10^2$	$-0.102 \cdot 10^3$	0.94
	B4	$-0.913 \cdot 10^2$	$-0.103 \cdot 10^3$	0.93
$\Delta_f = 4$, $\Delta_G = 8$	B1	$-0.628 \cdot 10^2$	$-0.853 \cdot 10^2$	0.90
	B2	$-0.667 \cdot 10^2$	$-0.989 \cdot 10^2$	0.93
	B3	$-0.708 \cdot 10^2$	$-0.102 \cdot 10^3$	0.93
	B4	$-0.708 \cdot 10^2$	$-0.103 \cdot 10^3$	0.94
$\Delta_f = 4$, $\Delta_G = 8$	B1	$-0.663 \cdot 10^2$	$-0.748 \cdot 10^2$	0.93
	B2	$-0.720 \cdot 10^2$	$-0.749 \cdot 10^2$	0.95
	B3	$-0.728 \cdot 10^2$	$-0.883 \cdot 10^2$	0.83
	B4	$-0.656 \cdot 10^2$	$-0.834 \cdot 10^2$	0.96

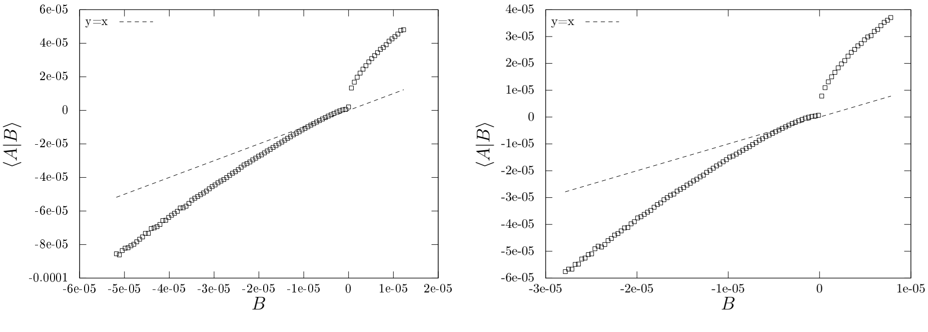

(a) (b)

FIG. 7.5: The conditional mean of the instantaneous real subgrid contribution by the instantaneous modelled subgrid contribution for Case B3 with $A = \tilde{\alpha}_p \tilde{\alpha}_q V_{pq,z}$ and $B = K_{zz} \Delta_f h(\tilde{\alpha}_s) \tilde{\alpha}_p \tilde{\alpha}_q (\tilde{U}_{p,z} - \tilde{U}_{q,z})$, for several filter widths (a): $\Delta_f = 4\Delta_{ref}$ and $\Delta_G = 6\Delta_{ref}$, (b): $\Delta_f = 6\Delta_{ref}$ and $\Delta_G = 8\Delta_{ref}$

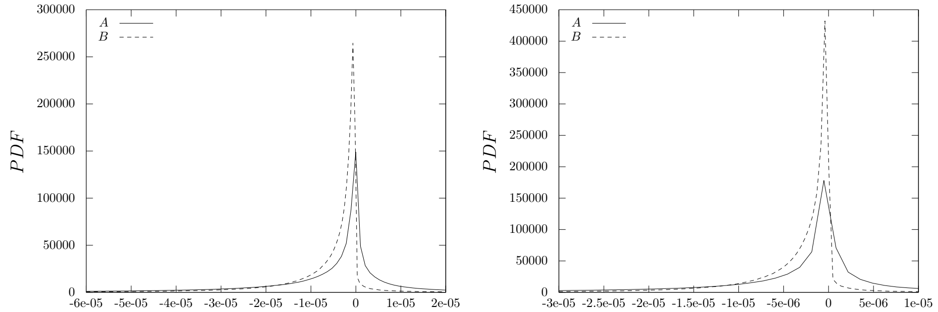

(a) (b)

FIG. 7.6: PDF of the instantaneous modelled subgrid contribution for Case B3 and the small particles with $A = \tilde{\alpha}_p\tilde{\alpha}_q V_{pq,z}$ and $B = K_{zz}\Delta_f h(\tilde{\alpha}_s)\tilde{\alpha}_p\tilde{\alpha}_q(\tilde{U}_{p,z} - \tilde{U}_{q,z})$, for several filter widths (a): $\Delta_f = 4\Delta_{ref}$ and $\Delta_G = 6\Delta_{ref}$, (b): $\Delta_f = 6\Delta_{ref}$ and $\Delta_G = 8\Delta_{ref}$

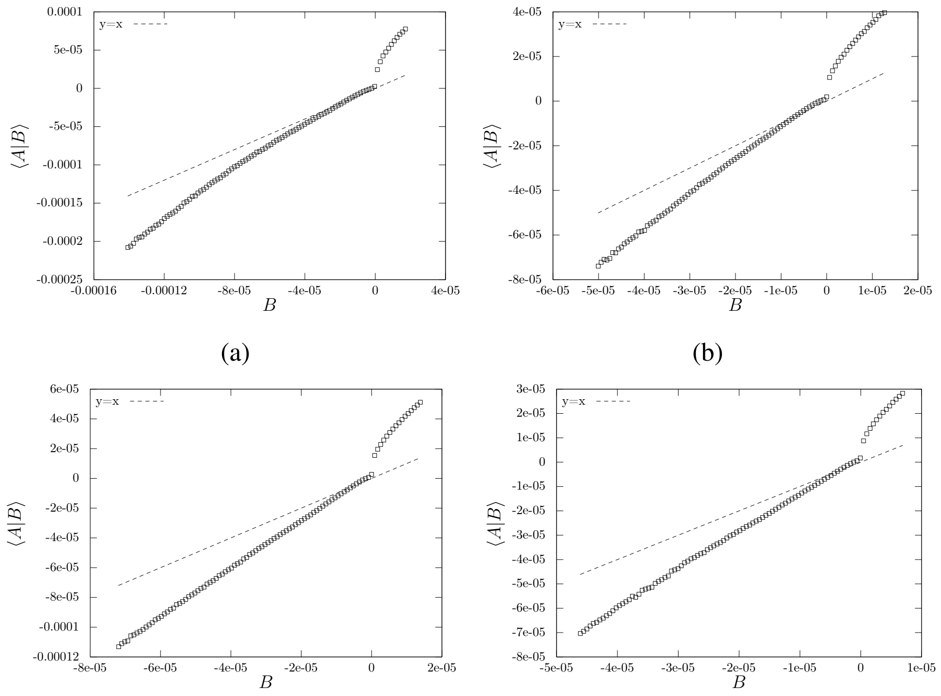

(a) (b)

(c) (d)

FIG. 7.7: PDF of the modelled subgrid contribution for Case B3 and the small particles with $A = \tilde{\alpha}_p\tilde{\alpha}_q V_{pq,z}$ and $B = K_{zz}\Delta_f h(\tilde{\alpha}_s)\tilde{\alpha}_p\tilde{\alpha}_q(\tilde{U}_{p,z} - \tilde{U}_{q,z})$ for several cases (a): B1, (b): B2, (c): B3 and (d): B4.

7.3 Subgrid model for the production by shear

The production of random particle kinetic energy, Π_p, is underestimated by the resolved contribution. In this section, a subgrid model is developed to take into account the subgrid structures in the production by shear. The resolved results obtained after applying the filter can be assimilated with the results obtained by coarse grid simulations. The test filter previously defined (Eq. (6.12)) is applied on the resolved term. By analogy with the subgrid term, the terms $\hat{P}$, $P^{r,h}$, $P^{sgs,h}$ are defined as:

$$\hat{P} = \widehat{\Sigma_{ij}^{res} \frac{\partial \tilde{U}_{p,i}}{\partial x_j}} \tag{7.15}$$

$$P^{r,h} = \Sigma_{ij}^{r,h} \frac{\partial \hat{\tilde{U}}_{p,i}}{\partial x_j} \tag{7.16}$$

$$P^{sgs,h} = \hat{P} - P^{r,h} \tag{7.17}$$

The subgrid contribution is modelled as:

$$\Pi_p^{SGS} = A P^{sgs,h} \tag{7.18}$$

with $A = \frac{1}{C_1}$.

In this study, the mesh-refined simulation results enable to know the subgrid contribution, Π_p^{SGS}. Hence, the value of the constant C_1 can be determined:

$$C_1 = \frac{\langle \Pi_p^{SGS} P^{sgs,h} \rangle}{\langle \Pi_p^{SGS} \Pi_p^{SGS} \rangle}.$$

Monodisperse cases are analysed in order to determine the constant C_1. The aim would be to determine a constant which can provide good approximation of the subgrid contribution of the production of particle kinetic agitation for all cases. The Table 7.2 summarized the temporal averaged C_1 for the monodisperse cases with various diameter. The value appears to vary significantly in time and no constant value can be determined.

TAB. 7.2: Average C_1 for various test filters for the gas-particle momentum exchange for monodisperse cases

Filters	Case	$\overline{C_1}$	variance C_1	$\overline{\langle \Pi_p^{SGS} P^{sgs,h} \rangle} / \overline{\langle \Pi_p^{SGS} \Pi_p^{SGS} \rangle}$
$\Delta_f = 4\Delta_{ref}$, $\Delta_G = 6\Delta_{ref}$	M1	0.5196	0.0142	0.47
	M2	0.8873	0.0484	0.42
	M3	0.8548	0.0182	0.90
$\Delta_f = 4\Delta_{ref}$, $\Delta_G = 8\Delta_{ref}$	M1	0.5403	0.0272	0.49
	M2	1.2948	0.2461	0.47
	M3	1.2602	0.2231	1.17
$\Delta_f = 6\Delta_{ref}$, $\Delta_G = 8\Delta_{ref}$	M1	0.3902	0.0133	0.37
	M2	0.8218	0.0854	0.40
	M3	0.7923	0.1325	0.735

Figure 7.8 shows the production the instantaneous and temporally averaged values of C_1 for two cases M1 and M2. This confirms us the variation in time of the constant. Figure 7.9 presents the temporal averaged values of the subgrid contribution at the test-scale conditionally averaged by the real subgrid contribution for one set of filter widths. Figure 7.10 depicts the PDF of the real subgrid contribution. They show that most of the values of the conditional mean of the temporal averaged value of C_1. Such a results let us think the subgrid contribution of the production by shear could be modelled as:

$$\Pi_p^{SGS} = AP^{sgs,h} \tag{7.19}$$

with A a constant. Such a constant should be function of the particle diameter. Other analysis have to be performed on monodisperse and bidisperse simulations to determine the constant.

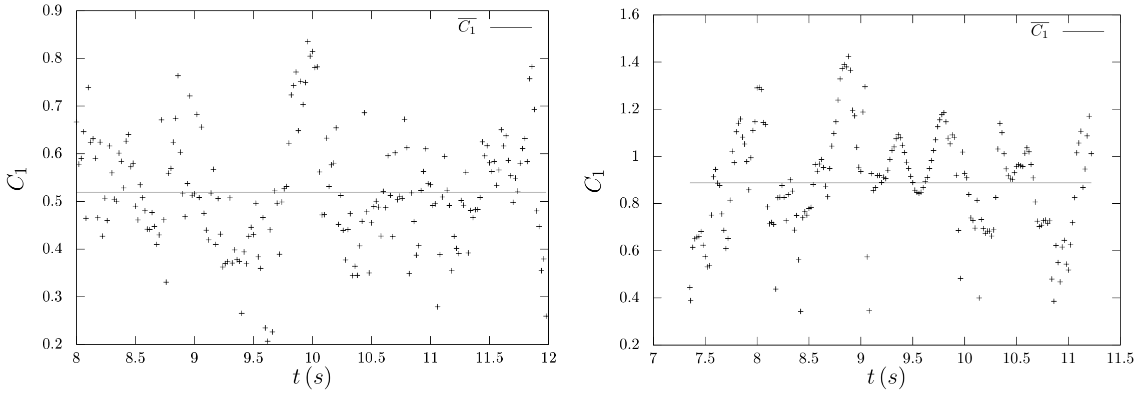

(a) (b)

FIG. 7.8: Instantaneous and time-averaged values of the constant C_1 with $\Delta_f = 4\Delta_{ref}$ and $\Delta_G = 6\Delta_{ref}$ in (a): M1 and (b): M2.

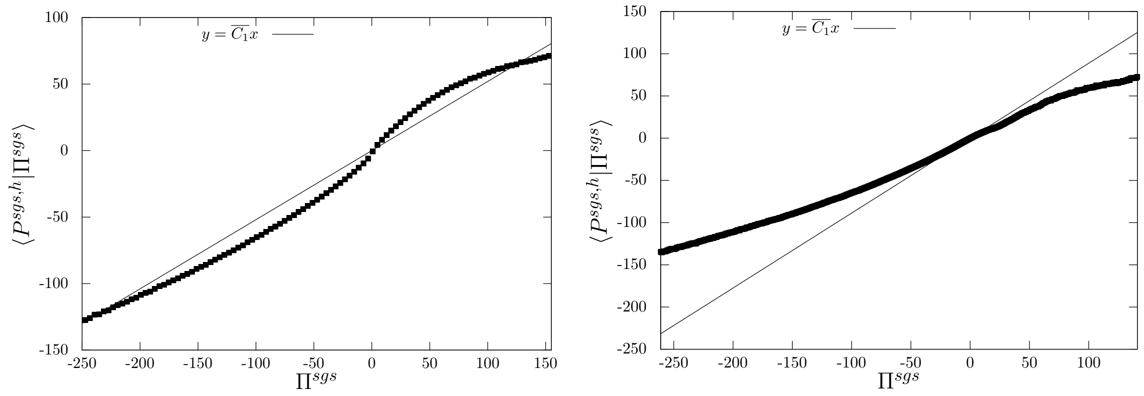

(a) (b)

FIG. 7.9: Temporal averaged conditional mean of the subgrid contribution at the test-scale by the real subgrid contribution with $\Delta_f = 4\Delta_{ref}$ and $\Delta_G = 6\Delta_{ref}$ in (a): M1 and (b): M2.

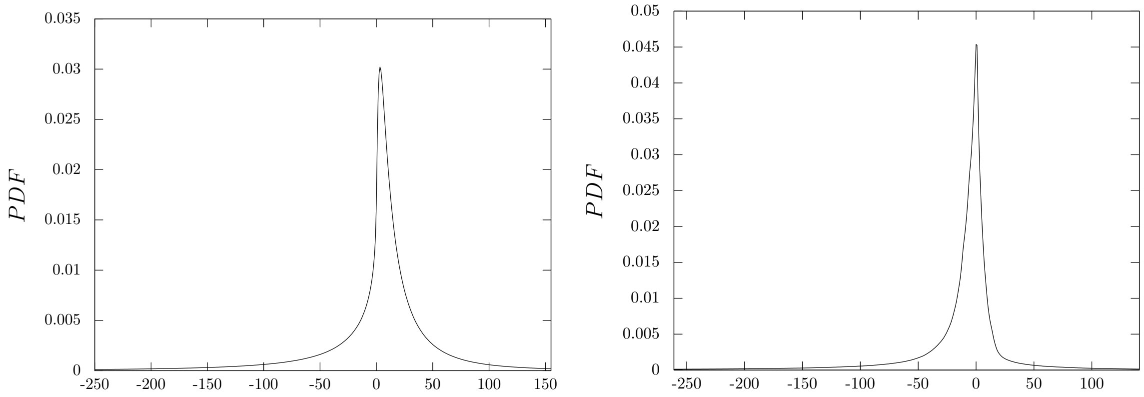

(a) (b)

FIG. 7.10: PDF of the real subgrid contribution with $\Delta_f = 4\Delta_{ref}$ and $\Delta_G = 6\Delta_{ref}$ in (a): M1 and (b): M2.

Summary

The bidisperse mesh-refined simulations have been to perform budget analysis, which highlights the need for subgrid models for inter-particle momentum transfer and the production of particle kinetic energy by shear. To predict accurately the subgrid contribution of inter-particle momentum transfer, the slip velocity between particle species multiplied by the solid volume fractions has to be modelled. A functional model has been developed similarly to the subgrid model for the gas-particle momentum transfer. A function h considers the influence of the total solid volume fraction, $\tilde{\alpha}_s$. Then, the model includes the size of the filter and a constant, K_{zz}, which is dynamically adapted following a method adapted from Germano et al. [43] and Lilly [75]. A priori analysis shows that the model predicts accurately most of the values of the subgrid contribution for the bidisperse case studied. Considering the subgrid contribution of the production by shear, the subgrid contribution appears to be very similar to the subgrid contribution at the test-scale. The constant appears to vary significantly in time and with the particle diameter. Such variation is an issue to determine a constant valid for all cases. Using time-averaged values, the constant enables to predict most of the real subgrid contribution. Hence, such an approach, linking the real subgrid contribution and the one at the test-scale, could predict the subgrid contribution of the production by shear. Further investigations have to be carried out to determine the constant.

Chapter 8

Conclusions

In CFBs with particle type A or A/B according to Geldart's classification, mesoscale structures are continuously formed. They can be resolved in Two-Fluid Model simulations with highly-resolved mesh. However, such simulations are computationally expensive. Hence, coarse meshes are used to simulate CFB with small particles. They are not able to take into account small structures, which leads top poor prediction of the overall hydrodynamic behaviour of CFB. This thesis focuses on the development of models to take into account the effect of the small structures on bidisperse gas-particle flows in CFB.

To develop such models, the first step is to obtain mesh-refined simulations of a 3D periodic box. The Two-Fluid Model is used to perform such simulations. This approach is presented in Chap 3. Then, a filter is applied on the momentum and particle kinetic energy equations. Additional terms, called the subgrid contributions, arise due to the filtering operation. Chap 4 summarizes those filtered equations. Using the highly resolved simulations, a budget analysis, presented in Chap 5, is carried out to understand the effects of subgrid contributions on the hydrodynamic of bidisperse flows. The influence of the filter size on the subgrid contributions is evaluated for each term. This study enables us to determine which subgrid contributions need to be modelled. In the momentum equation, the gas-particle and the inter-particle momentum transfer is overestimated by coarse-mesh simulations. The inter-particle momentum exchange is computed with the particle kinetic agitation. In the particle random kinetic energy equation, the production by velocity gradient tends to be underestimated as the filter size goes up. The correlation analysis shows that to predict accurately the gas-particle momentum transfer, the subgrid drift velocity, $V_{d,z}^{(p)}$, which corresponds to the correlation between subgrid fluid velocity and particle distribution, should be modelled. Based on correlation analysis, a model should be developed for the relative velocity between particle species multiplied by particle volume fractions to predict accurately inter-particle momentum transfer in coarse mesh simulations.

The development of the subgrid model for the gas-particle momentum transfer is presented in Chap 6. Monodisperse and bidisperse simulations are used to construct a functional model:

$$\tilde{\alpha}_p V_{d,z}^{(p)} = K_{zz} \Delta_f h(\tilde{\alpha}_s) \tilde{\alpha}_p (\tilde{U}_{f,z} - \tilde{U}_{p,z}) \tag{8.1}$$

with $h(\tilde{\alpha}_s)$ closed by using the data-base of mesh-refined simulations. The constant K_{zz} is dynamically adapted by using a method adapted from Germano et al. [43] and Lilly [75]. Such approach relies on the use of a second filter, called the test-filter. A priori analysis has been conducted to evaluate the model prediction.The model appears to fit well most of the data, however, the prediction of the subgrid contribution appears to be inaccurate in the monodisperse case with large particles $d_p = 150\mu m$.

Using the mesh-refined bidisperse simulations, the subgrid model for the inter-particle momentum transfer is developed and presented in Chap 7. Great similarities can be observed with the subgrid contribution of gas-particle momentum transfer. Hence, the methodology to build the models are very similar and the functional model is expressed as:

$$\tilde{\alpha}_p\tilde{\alpha}_q V_{pq,z} = \widetilde{\alpha_p\alpha_q\left(U_{p,z} - U_{q,z}\right)} - \tilde{\alpha}_p\tilde{\alpha}_q\left(\tilde{U}_{p,z} - \tilde{U}_{q,z}\right) = K_{zz} f(\Delta_f) h(\tilde{\alpha}_s)\tilde{\alpha}_p\tilde{\alpha}_q(\tilde{U}_{p,z} - \tilde{U}_{q,z}) \tag{8.2}$$

A priori analysis shows good agreement between the real subgrid contribution and the modelled one even if the subgrid contribution which values differ from the mean values are not accurately predicted.

The model for the subgrid contribution of the production by shear is also investigated using monodisperse highly resolved simulations. A significant correlation between subgrid contribution at the first filter scale and at the test-filter scale let us assume that the subgrid contribution could be expressed as:

$$\Pi_p^{SGS} = AP^{sgs,h} \tag{8.3}$$

with Π_p^{SGS} the subgrid contribution at the test-filter scale and A a constant. Knowing the real subgrid contribution, the constant can be evaluated for each monodisperse case and the result with a time-averaged constant provide reasonable predictions of the subgrid contribution. However the constant appears to depend on the case and can vary significantly in time. This work shows that the subgrid models for the gas-particle momentum transfer in monodisperse and bidisperse simulations have similar dependence in solid volume fraction. The volume fraction ratio and the particle diameter ratio have been investigated in bidisperse cases. Considering the significant difference between monodisperse flows with different density, analysing bidisperse flows with different density ratio would be interesting. Even if a good agreement were found between modelled and real subgrid contributions in two monodisperse cases, the predictions appear inaccurate as the particle diameter increases. Further work should be conducted to improve such subgrid model, for instance, a function including particle diameter. A posteriori analysis should be realized in order to test the models with coarse grid simulations. For the subgrid model of the production by shear, the constant appears to varies in time and depends on the cases studied and on the filter size. More cases should be analysed and a function including the filter size, a mean particle diameter or a diameter ratio should be investigated. One test-filter has been defined in this work, however, it appears interesting to study the influence of the test-filter on the prediction of the model.

This work focuses on a bidisperse simulation of a 3D periodic box, representing the upper part of the riser of the air reactor in CLC process. Such process appears very promising technology because the CO_2 can be easily separated from other flue gases and simulation of CLC implies modelling reaction. Hence, further study should be conducted with subgrid models in bidisperse reacting flows.

Appendix A

This work corresponds to the publication in the ICMF-2016-9th International Conference on Multiphase Flow, dealing with the drag models for monodisperse and polydisperse flows [123].

Modelling of momentum transfer into gas-particle flow

Let us define $F_{fp,i}$ the local average force exerted by the fluid on the particles of section p in polydisperse powder. In the frame of the Euler-Euler approach for gas-particle flows [121], such a force is usually written as the sum of two contributions: the drag force, $F^D_{fp,i}$ and the buoyancy force,

$$F_{fp,i} = F^D_{fp,i} - V_p \frac{\partial P_f}{\partial x_i} \tag{A.1}$$

where $\partial P_f / \partial x_i$ is the mean fluid pressure gradient, and $V_p = \pi d_p^3/6$ is the volume of the particle of diameter d_p. Then, the fluid momentum transport equation writes:

$$\begin{aligned}\alpha_f \rho_f \frac{\partial U_{f,i}}{\partial t} + \alpha_f \rho_f U_{f,j} \frac{\partial U_{f,i}}{\partial x_j} = & - \alpha_f \frac{\partial P_f}{\partial x_i} \\ & + \alpha_f \frac{\partial \Sigma_{f,ij}}{\partial x_j} \\ & + \alpha_f \rho_f g_i \\ & - \sum_q n_q F^D_{fq,i}\end{aligned} \tag{A.2}$$

where $\sum_q$ means that the summation is performed over all particulate diameter distribution. For steady flow through arrays of fixed particles, and without gravity, the equation becomes

$$- \alpha_f \frac{\partial P_f}{\partial x_i} - \sum_q n_q F^D_{fq,i} = 0 \tag{A.3}$$

Let us introducing the following quantities

$$x_p = \frac{\alpha_p}{\alpha_s} \qquad \text{and} \qquad y_p = \frac{d_p}{d_s}, \tag{A.4}$$

where α_s is the whole particle volume fraction ($\alpha_s = \sum_q \alpha_q$) and d_s the Sauter's diameter given by

$$d_s = \left[\sum_p \frac{x_p}{d_p} \right]^{-1} . \tag{A.5}$$

Then the total force measured in fully-resolved simulation can be related to the drag force by equating Eqn (A.3) & (A.4) as

$$F_{fp,i} = F^D_{fp,i} + \frac{\alpha_s}{\alpha_f} y_p^3 \sum_q \frac{x_q}{y_q^3} F^D_{fq,i} . \tag{A.6}$$

For the monodisperse case, $x_p = 1$ and $y_p = 1$, the expression becomes

$$F_{fp,i} = \frac{1}{\alpha_f} F^D_{fp,i} . \tag{A.7}$$

In Ref. [12, 28, 116] the mean force exerted by the fluid on the particle is measured from LBM simulations allowing to derive several fluid force correlatons. Finally, in the following, we will evaluate drag force correlations derived using various DNS approaches for dense suspension of monodisperse and polydisperse solid mixture.

Drag force in a fixed array of mono-sized spherical solid particles

The mean drag force in a fixed array of mono-sized solid spheres may be written,

$$F^D_{fp,i} = -\rho_f \frac{\pi d_p^2}{8} C_D |\mathbf{V}_{pf}| V^{(p)}_{r,i} \tag{A.8}$$

with d_p the particle diameter, ρ_f the fluid density, $\mathbf{V}^{(p)}_r = \mathbf{U}_p - \mathbf{U}_f$ the mean fluid-particle relative velocity and $C_D \equiv C_D(Re_p)$ the drag coefficient. The drag coefficient depends on the particle Reynolds number Re_p that is defined by

$$Re_p = \frac{|\mathbf{V}^{(p)}_r| d_p}{\nu_f} . \tag{A.9}$$

For a single particle ($\alpha_f = 1$) the drag force in the Stokes limit ($Re_p \ll 1$) is written,

$$F^D_{fp,i} = -3\pi \rho_f \nu_f d_p V^{(p)}_{r,i} . \tag{A.10}$$

Then the drag coefficient C_D in the Stokes regime is given by,

$$C_D = \frac{24}{Re_p} \tag{A.11}$$

Practical correlations of the drag coefficient may be found in the literature such as the one proposed by Schiller & Naumann [117] which is extensively used in gas-solid flow simulation.

TAB. A.1: Relations for the normalized drag force of a monodisperse system, as function of gas volume fraction and Reynolds number $Re_p^* = \alpha_f|\mathbf{V}_r^{(p)}|d_p/\nu_f$

Author	Drag force
Ergun 1952 [32]	$F_{Erg}^D = \frac{150}{18}\frac{1-\alpha_f}{\alpha_f^2} + \frac{7}{4}\frac{1}{18}\frac{Re_p^*}{\alpha_f^2}$
Wen and Yu 1965 [139]	$F_{WY}^D = (1 + 0.15 Re_p^{*0.687})\alpha_f^{-3.65}$
Gobin et al. 2003 [46]	$F_{Gob}^D = \begin{cases} F_{WY}^D & \text{if} \quad \alpha_p \leq 0.3 \\ min(F_{WY}^D, F_{Erg}^D) & \text{otherwise} \end{cases}$
Beetstra, Van der Hoef & Kuipers 2007 [12]	$F_{BVK}^D = 10\frac{1-\alpha_f}{\alpha_f^2} + \alpha_f^2(1 + 1.5\sqrt{1-\alpha_f})$ $+ \frac{0.413}{\alpha_f^2}\frac{Re_p^*}{24}\left[\frac{\alpha_f^{-1}+3\alpha_f(1-\alpha_f)+8.4Re_p^{*-0.343}}{1+10^{3(1-\alpha_f)}Re_p^{*-0.5-2(1-\alpha_f)}}\right]$
Tenneti et al. 2011 [129]	$F_{TGS}^D = F_{WY}^D(Re_p^*)\alpha_f^{1.65} + \alpha_f F_1(\alpha_f) + \alpha_f F_2(\alpha_f, Re_p^*)$ $F_1(\alpha_f) = \frac{5.81(1-\alpha_f)}{\alpha_f^3} + 0.48\frac{(1-\alpha_f)^{1/3}}{\alpha_f^4}$ $F_2(\alpha_f, Re_p^*) = (1-\alpha_f)^3 Re_p^* \left[0.95 + \frac{0.61(1-\alpha_f)^3}{\alpha_f^2}\right]$

By analogy with the form of a single particle drag force, Eqn (A.8), the drag force in dense particle laden flows is written as

$$F_{fp,i}^D = -\rho_f \frac{\pi d_p^2}{8} C_D^* |\mathbf{V}_r^{(p)}| V_{r,i}^{(p)} \tag{A.12}$$

where the drag coefficient $C_D^* \equiv C_D^*(Re_p^*, \alpha_f)$ is a given function of the particle Reynolds number Re_p^* and of α_f the fluid volume fraction.

$$Re_p^* = \frac{\alpha_f |\mathbf{V}_{pf}| d_p}{\nu_f} . \tag{A.13}$$

The semi-empirical popular correlations given by Ergun [32] and Wen & Yu [139] are evaluated in this section for mono-sized particles. Ding & Gidaspow [29] proposed a correlation with a transition from the Wen & Yu to the Ergun correlations for $\alpha_s > 0.2$. However this correlation leads to discontinuous transition and overestimation of the drag force for $\alpha_s > 0.2$ and for the particle Reynolds number > 100 encountered in gas phase olefin polymerization reactor. This leads to Gobin & al. [47] propose a continuous transition given in Table 1 according to the DNS results of Massol [84]. Recently, new forms for the monodisperse drag force correlation were derived from DNS results such as the ones proposed by Beetstra et al. [12] and Tenneti et al. [129], given in Tab. [1]. Table [1] shows the different correlation proposed by the different author in the literature. For all results presented the drag force are normalized by the Stokes drag force,

$$F^D(\alpha_f, Re_p^*) = \frac{|\mathbf{F}_{fp}^D|}{\alpha_f 3\pi\mu_f d_p |\mathbf{V}_r^{(p)}|} \tag{A.14}$$

Figure 1, shows the dimensionless drag force for low particle Reynolds number (Re_p^* =1) as a function of the solid volume fraction, the line represent the correlations given in Table [1] and the black symbols are the LBM numerical results from [53]. For volume fraction larger than 0.1, LBM results are found in good agreement with theoretical developments made by [51, 114], Gobin et al. correlation (ie. Wen & Yu and Ergun) leads to an underestimation of the drag force with respect to the LBM results of Hill et al. This theoretical developments are valid for fixed bed, in cubic arrays configuration (simple, body-centered and face-centered), Hill et al. [53, 54] shown this theory are valid for random array. In contrast when the particles are not frozen, the behaviour of flow could be changed, and the drag force acting on the particle are not strictly equivalent to a fixed bed.

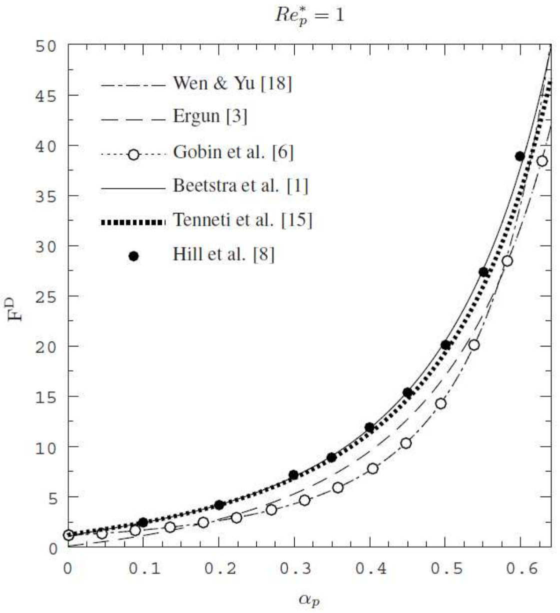

FIG. A.1: Comparison between the LBM and the different equations of dimensionless drag force apply in a fixed array of mono-sized spherical solid particles (see Tab. [1]) (without the pressure gradient) as a function of the particle volume fraction α_p for $Re_p^* = 1$.

Figure 2, shows the dependence of the dimensionless drag force on the solid volume fraction for several particle Reynolds numbers Re_p, comparing the predictions of the correlation functions given Table [1] and the DNS results with a body fitted mesh by Massol [84]. Results using Tenneti et al. correlation [129] and DNS results from Massol [84] are very closed. We can notice that Tenneti et al correlations are fitted from DNS results obtained using immersed boundary methods (IBM).

Gobin et al. [46] drag force correlation predictions, are really closed to the Massol DNS results for the whole range of particle Reynolds number and particle volume fraction shown. In particular, the proposed transition model from Wen & Yu to Ergun correlations allows to predict accurately the drag force in dense particle-laden flows for large particle Reynolds number values : $Re_p^* \geq 100$. Hence, to develop a correlation for polydisperse systems, a simple polydispersed correlation based Gobin et al. [46] mono-sized drag force

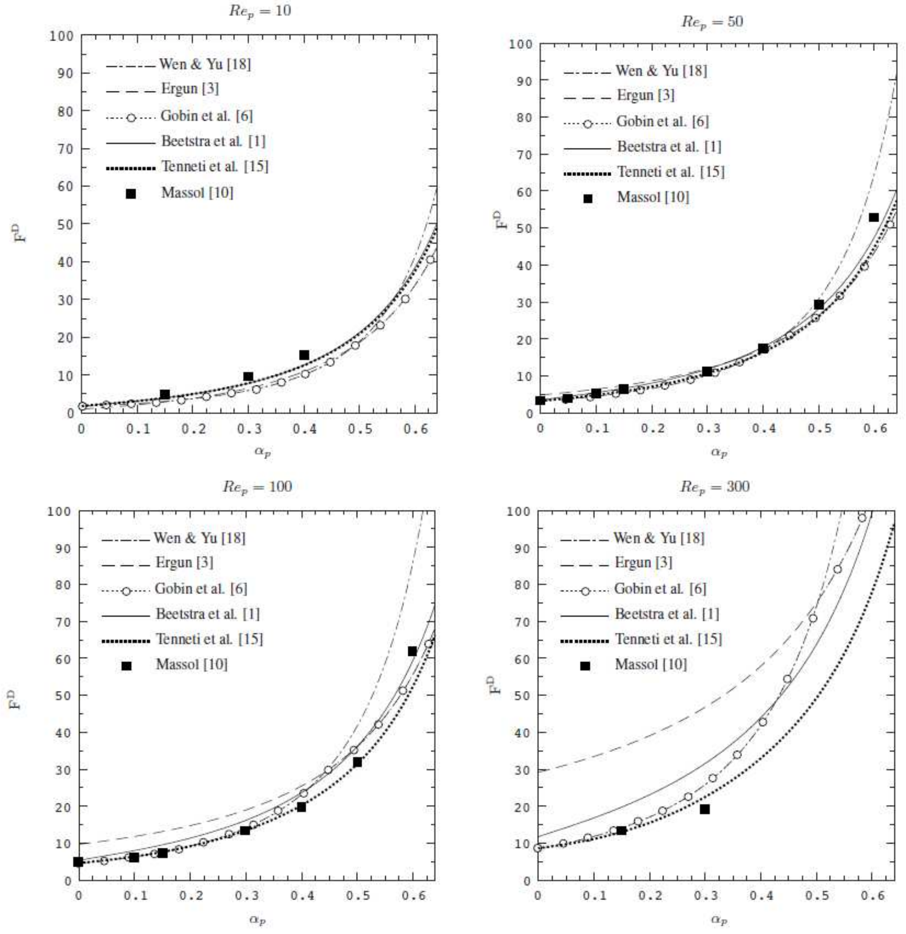

FIG. A.2: Comparison between the DNS and the different equations of dimensionless drag force (see Tab. [1]) (without the pressure gradient) as a function of of the gas volume fraction α_f for different Reynolds number Re_p apply in a fixed array of mono-sized spherical solid particles.

will be presented and evaluated.

Drag force in a fixed array of polydisperse spherical solid particles

Some authors, like Van der Hoef [28] and Yin and Sundaresan [149], developed polydisperse models using the monodisperse force applied to a mean diameter corrected by a function of the particle mixture properties. Van der Hoef et al. [28] propose the following form for the normalized by Stokes force drag force for particle type p,

$$F^D_{VBK,poly} = f_{poly}(\alpha_f, y_p) F_{BVK}(\alpha_f, Re^*_s) \tag{A.15}$$

with $f_{poly}(\alpha_f, y_p)$ written as,

$$f_{poly}(\alpha_f, y_p) = [\alpha_f y_p + (1-\alpha_f) y_p^2]$$

Re^*_s is the Reynolds number using the Sauter's diameter, written:

$$Re^*_s = \frac{\alpha_f |\mathbf{V}^{(p)}_r| d_s}{\nu_f}. \tag{A.16}$$

Yin and Sundaresan 2009[149] propose the following form,

$$F^D_{YS,poly} = C_1 + f_{poly}(\alpha_f, y_p) F^D_{VBK}(d_s, Re^*_s) \tag{A.17}$$

$$f_{poly}(\alpha_f, y_p) = [a y_p + (1-a) y_p^2]$$

$$a = 1 - 2.660(1-\alpha_f) + 9.096(1-\alpha_f)^2 - 11.338(1-\alpha_f)^3$$

$$C_1 = \frac{1}{\alpha_f} + \frac{1}{\alpha_f}[a y_p + (1-a) y_p^2]$$

The monosdiperse force F^D_{VBK} corresponds to the correlaiton developed by Van der Hoef et al. [28],

$$F^D_{VBK} = 10\frac{1-\alpha_f}{\alpha_f^2} + \alpha_f^2(1 + 1.5\sqrt{1-\alpha_f}) \tag{A.18}$$

The Gobin et al. drag force correlation was already used for Euler-Euler numerical simulation of laboratory and industrial scale gas-solid polydisperse fluidized bed [36, 39]. The corresponding dimensionless drag force takes the following form,

$$F^D_{Gob,poly} = y_p F^D_{Gob}(\alpha_f, y_p Re^*_s) \tag{A.19}$$

A second form more complex, accounting the separate dependance on the diameter ratio y_p and the gas volume fraction α_f is,

$$F^D_{2,Gob,poly} = f_{poly}(\alpha_f, y_p) F^D_{Gob}(\alpha_f, y_p Re^*_s) \tag{A.20}$$

The function is determined by a fitting with the LBM data using the least-squares methods,

$$f_{poly} = y_p + 0.1(y_p - 1)((y_p^{1.5} - 1) + \alpha_f(1.25 - 5\alpha_f)).$$

This correlation focus only on the range [0:100] of particle Reynolds number.

Figure 3, shows the normalized polydisperse drag force divided by the normalized monodisperse drag force. These monodisperse force for each case has been calculated with the Reynolds number depending on the Sauter's diameter Re_s^*. The Figure schows the dependance of the normalized polydisperse drag force coefficient on the particle diameter ratio y_p, for given values of the Reynolds number Re_s^* and of the gas volume fraction α_f. The different line corresponds to the correlations by the Eqn (A.15), (A.17), (A.19) & (A.20). The point represents the LBM numerical data given by these different authors [12, 116]. $F^D_{Gob,poly}$ and $F^D_{2,Gob,poly}$ represent the models given in Eqn (A.19) and (A.20). All correlation are equal to the monodisperse drag force when the diameter is equal to the Sauter 's diameter, $y_p = 1$. For low $Re_s^* = 1$, The simple Gobin et al. correlation corresponding to $F^D_{Gob,poly}$, shows a good agreement with the LBM data. In contrast, the results for higher Re_s^* shows an underestimation by this simple model. SECTION : Discussion

Summary

The drag force correlations developed from DNS results using Lattice Boltzmann Method (LBM) [12] and semi-empirical functions found in the literature (Ergun [32], Wen & Yu et al. [139], Gobin et al. [46], were compared for monodisperse flows. The correlation of Gobin et al.[46] provides satisfactory predictions and maximum discrepancies are measured for low Reynolds number values. For polydisperse flows several correlations may be found in the literature to take into account the dependence on the particle diameter ratio, the particle Reynolds number and the solid volume fraction, likes the ones of Van der Hoef [28] and of Yin and Sundaresan [149]. The different authors proposed for polydisperse drag force to multiply the monodisperse drag force calculated with the Sauter mean diameter by a function depending on particle size ratio y_p and gas volume fraction.

The results provided by a polydisperse applicaiton of the Gobin et al. [46] correlation tend to slightly underestimated the drag force compared to the LBM results of Beetstra [12] and to the others correlation developed for polydisperse flows [28, 149] for low Reynolds $Re_s^* \leq 10$. An overestimation of the drag force is observed for large Reynolds number value $Re_s^* = 100$.

However to take into account the higher Reynolds number regime a modification of this correlation is proposed in Eqn (A.20). LBM data represent frozen particle suspension in a steady gas flow, but the gas-solid suspensions are usually unstable.

The particle-particle relative motion and particle-turbulence interactions should modify the drag force correlation modelling. So, additional numerical studies using unsteady particle resolved simulation allowing separate particle motion [133] are needed to improve the drag force modelling accuracy in fluidized beds.

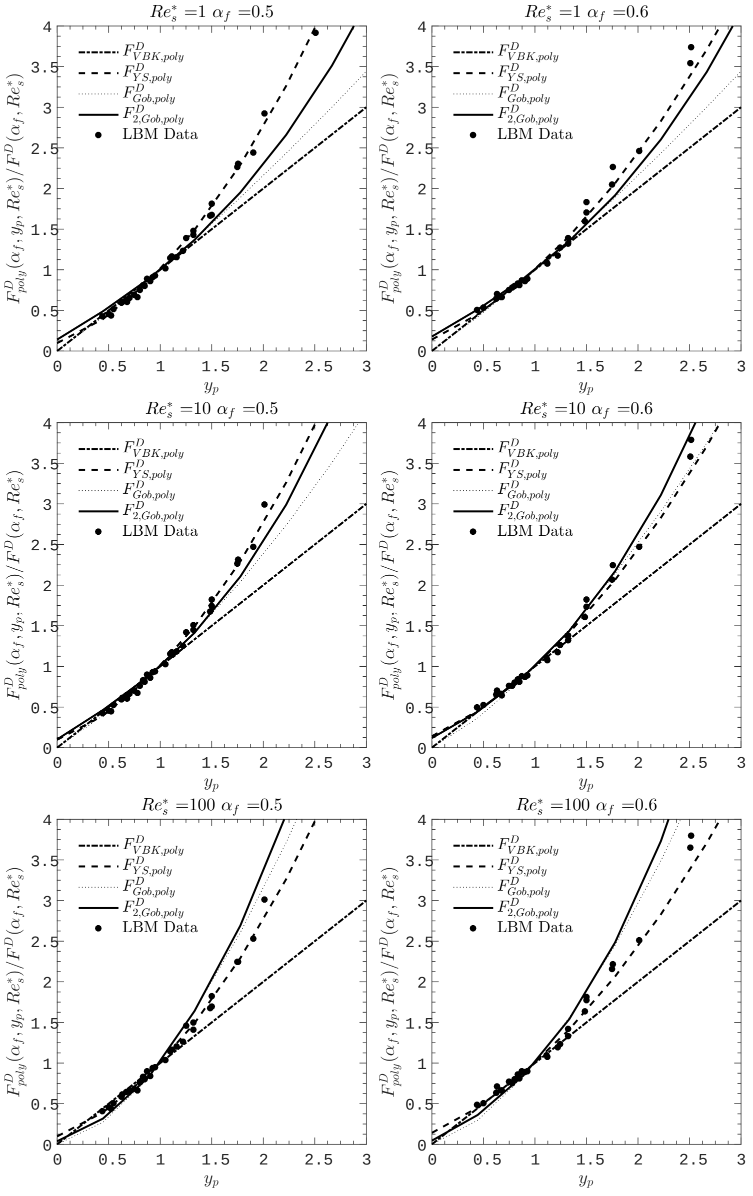

FIG. A.3: Comparison between LBM data [12] [116] and the correlations and the new correlation written in section 8. The vertical axis corresponds to the dimensionless drag force normalized by the dimensionless monodisperse drag force using the Reynolds number based on mean Sauter diameter Re_s^*; the horizontal axis is the dimensionless particle size ratio y_p.

Appendix B

This work corresponds to the publication in the ICMF-2016-9th International Conference on Multiphase Flow, dealing with the drag models for monodisperse and polydisperse flows [123].

Filtered particle momentum equation

The resolved inter-aprticle momentum exchange is expressed as:

$$I_{q\rightarrow p,i} = -\frac{m_p m_q}{m_p + m_q}\frac{1+e_c}{2}\frac{\tilde{n}_p}{\tau_{pq}^{c,\,res}} H_1(z^{res})(\tilde{U}_{p,i} - \tilde{U}_{q,i})$$

The terms, $\Sigma_{p,ij}^{res}$ and $\Sigma_{p,ij}^{sgs}$, are the resolved and subgrid contribution of the particle kinetic stress tensor. The resolved contribution of this term is written as:

$$\Sigma_{p,ij}^{res} = \left(P_p^{res} - \lambda_p^{res}\frac{\partial \tilde{U}_{p,m}}{\partial x_m}\right)\delta_{ij} - \mu_p^{res}\left(\frac{\partial \tilde{U}_{p,i}}{\partial x_j} + \frac{\partial \tilde{U}_{p,j}}{\partial x_i} - \frac{2}{3}\frac{\partial \tilde{U}_{p,m}}{\partial x_m}\delta_{ij}\right)$$

Filtered particle random kinetic energy equation

First the subgrid contribution to the turbulent transport, $\overline{\langle \frac{\partial}{\partial x_j} D_j^{sgs} \rangle}$, is the difference between filtered term, written:

$$\langle \frac{\partial}{\partial x_j} D_j^{sgs} \rangle = \widetilde{\frac{\partial}{\partial x_j}\alpha_p\rho_p(K_p^{kin} + K_p^{coll})\frac{\partial q_p^2}{\partial x_j}} - \frac{\partial}{\partial x_j}\tilde{\alpha}_p\rho_p(K_p^{kin,\,res} + K_p^{coll,\,res})\frac{\partial \tilde{q}_p^2}{\partial x_j}$$

where $\tilde{K}_p^{kin}$ and $\tilde{K}_p^{coll}$ are respectively the resolved contributions of the kinematic and collisional part of the diffusivity.

The subgrid production by velocity gradient is written:

$$\Pi^{sgs} = \widetilde{\Sigma_{p,ij}\frac{\partial U_{p,i}}{\partial x_j}} - \Sigma_{p,ij}^{res}\frac{\partial \tilde{U}_{p,i}}{\partial x_j}$$

where $\Sigma_{p,ij}^{res}$ corresponds to the resolved particle stress tensor.

For the dissipation by friction with the gas phase, the subgrid contribution is written:

$$\epsilon_{fp}^{sgs} = \frac{\widetilde{\alpha_p \rho_p}}{\tau_{fp}^F} 2q_p^2 - \frac{\tilde{\alpha}_p \rho_p}{\tau_{fp}^{F,res}} 2\tilde{q}_p^2$$

The subgrid contribution of the dissipation due to collision is:

$$\begin{aligned} \sum_q \epsilon_c^{sgs} &= \sum_{q=1}^{n} m_p \left(\frac{2m_q}{m_p + m_q}\right)^2 \frac{1-e_c^2}{4} \widetilde{\frac{n_p}{\tau_{pq}^c} \frac{2}{3} (q_p^2 + q_q^2)} \\ &- \sum_{q=1}^{n} m_p \left(\frac{2m_q}{m_p + m_q}\right)^2 \frac{1-e_c^2}{4} \frac{\tilde{n}_p}{\tau_{pq}^{c,res}} \frac{2}{3} (\tilde{q}_p^2 + \tilde{q}_q^2) \end{aligned}$$

where $\tau_{pq}^{c,res}$ is the resolved collision time scale.

The subgrid contributions of those terms are:

$$\begin{aligned} P_{pq}^{sgs} &= \frac{m_p m_q^2}{(m_p + m_q)^2} \frac{(1+e_c)^2}{4} \widetilde{\frac{n_p}{\tau_{pq}^c} (U_{p,i} - U_{q,i})^2 H_1(z)} \\ &- \frac{m_p m_q^2}{(m_p + m_q)^2} \frac{(1+e_c)^2}{4} \frac{\tilde{n}_p}{\tau_{pq}^{c,res}} (\tilde{U}_{p,i} - \tilde{U}_{q,i})^2 H_1(z^{res}) \end{aligned}$$

$$\begin{aligned} T_{pq}^{sgs} &= \frac{m_p m_q}{m_p + m_q} \frac{1+e_c}{2} \widetilde{\frac{n_p}{\tau_{pq}^c} \frac{8}{3} \frac{m_p q_p^2 - m_q q_q^2}{m_p + m_q}} \\ &- \frac{m_p m_q}{m_p + m_q} \frac{1+e_c}{2} \frac{\tilde{n}_p}{\tau_{pq}^{c,res}} \frac{8}{3} (\tilde{q}_p^2 + \tilde{q}_q^2) \end{aligned}$$

where $\tilde{\tau}_{pq}^c$ and $\tilde{z}$ corresponds to the resolved terms.

Appendix C

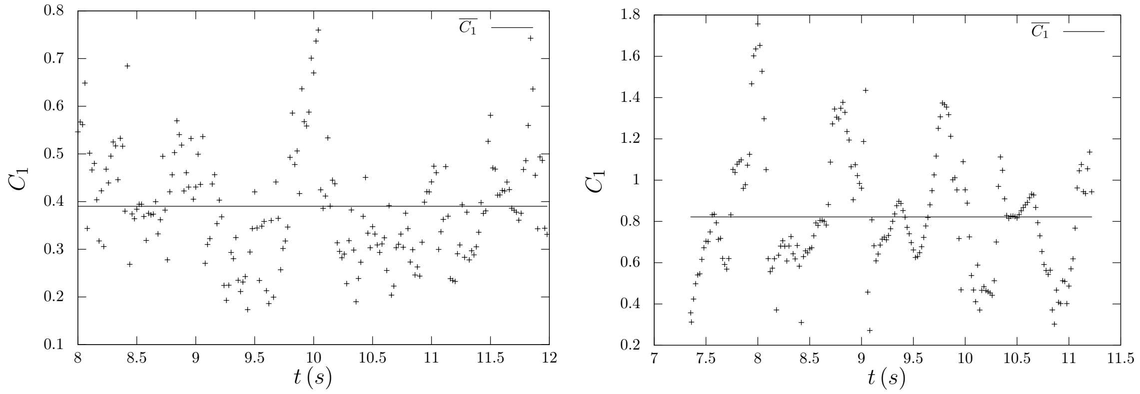

(a) (b)

FIG. C.1: Instantaneous and time-averaged values of the constant C_1 with $\Delta_f = 6\Delta_{ref}$ and $\Delta_G = 8\Delta_{ref}$ in (a): M1 and (b): M2.

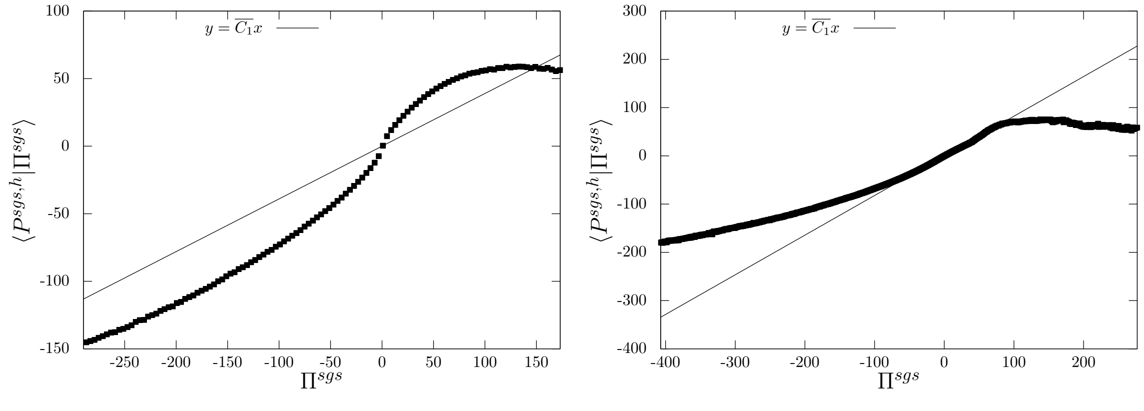

(a) (b)

FIG. C.2: Temporal averaged conditional mean of the subgrid contribution at the test-scale by the real subgrid contribution with $\Delta_f = 6\Delta_{ref}$ and $\Delta_G = 8\Delta_{ref}$ in (a): M1 and (b): M2.

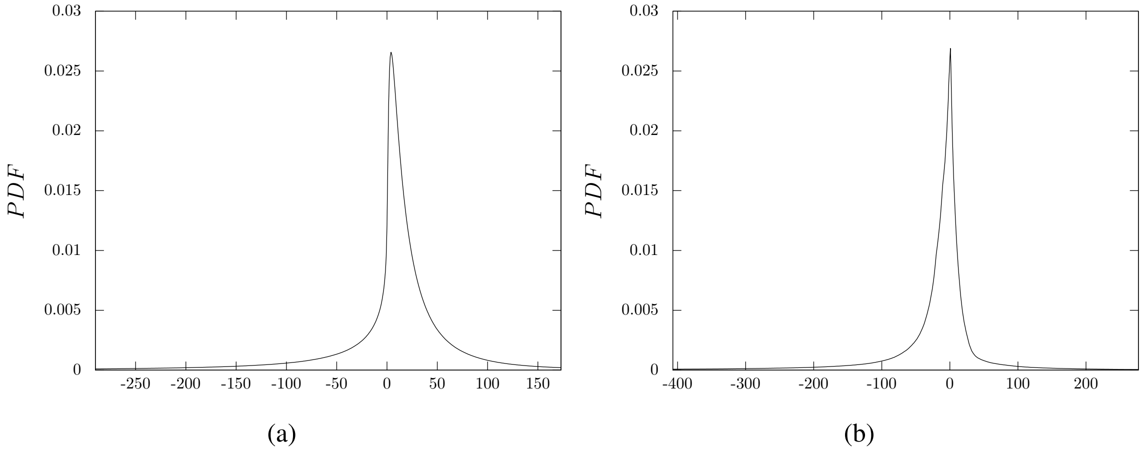

(a)

(b)

FIG. C.3: PDF of the real subgrid contribution with $\Delta_f = 6\Delta_{ref}$ and $\Delta_G = 8\Delta_{ref}$ in (a): M1 and (b): M2.

Bibliography

[1] J. Adanez, A. Abad, F. Garcia-Labiano, P. Gayan, and F. Luis. Progress in chemical-looping combustion and reforming technologies. *Progress in Energy and Combustion Science*, 38(2):215–282, 2012.

[2] K. Agrawal, P.N. Loezos, M. Syamlal, and S. Sundaresan. The role of meso-scale structures in rapid gas-solid flows. *J. Fluid Mech.*, 445:151–185, 2001.

[3] S.C. Alfaro, A. Gaudichet, L. Gomes, and M. Maillé. Mineral aerosol production by wind erosion: aerosol particle sizes and binding energies. *Geophysical Research Letters*, 25(7):991–994, 1998.

[4] E. Andresen. *Statistical Approach to Continuum Models for Turbulent Gas-Particle Flows*. PhD thesis, Technical University of Denmark, 1990.

[5] R. Andreux, G. Petit, M. Hemati, and O. Simonin. Hydrodynamic and solid residence time distribution in a circulating fluidized bed: Experimental and 3D computational study. *Chemical Engineering and Processing: Process Intensification*, 47(3):463–473, 2008.

[6] A.T. Andrews, P.N. Loezos, and S. Sundaresan. Coarse-grid simulation of gas-particle flows in vertical risers. *Ind. Eng. Chem. Res.*, 44:6022–6037, 2005.

[7] D. Archer. Fate of fossil fuel co2 in geologic time. *Journal of Geophysical Research Oceans*, 110, 2005.

[8] G. Balzer, A. Boëlle, and O. Simonin. Eulerian gas-solid flow modeling of dense fluidized bed. In *FLUIDIZATION VII, Proc International Symposium of the Engineering Foundation*, pages 1125–1134, 1995.

[9] J. Bardina, J.H. Ferziger, and W.C. Reynolds. Improved turbulence models based on large eddy simulation of homogeneous, incompressible turbulent flows. 1983.

[10] O. Batrak. *Etudes numérique et expérimentale de l'hyrdodynamique des lits fluidisés circulants gaz-particules avec prise en compte de la polydispersion granulométrique*. PhD thesis, Institut National Polytechnique de Toulouse, 2005.

[11] O. Batrak, G. Patino, O. Simonin, I. Flour, T. Le Guevel, and E. Perez. Unlike particle size model in 3d unsteady polydispersed simulation of circulating fluidized bed. In *8th International Conference on Circulating Fluidized Bed*, pages 370–378, CFB8, China, 2005.

[12] R. Beetstra, M.A. Van der Hoef, and J.A.M. Kuipers. Drag force of intermediate reynolds number flow past mono- and bidisperse arrays of spheres. *AIChE Journal*, 53:489–501, 2007.

[13] S. Benyahia. Analysis of model parameters affecting the pressure profile in a circulating fluidized bed. *AIChE Journal*, 58(2):427–439, 2012.

[14] S. Benyahia, H. Arastoopour, T.M. Knowlton, and H. Massah. Simulation of particles and gas flow behavior in the riser section of a circulating fluidized bed using the kinetic theory approach for the particulate phase. *Powder Technology*, 112:24–33, 2000.

[15] S. Benyahia and S. Sundaresan. Do we need sub-grid scale corrections for both continuum and discrete gas-particle flow models? *Powder Technology*, 220:2 – 6, 2012.

[16] N. Berguerand and A. Lyngfelt. Design and operation of a 10 kwth chemical-looping combustor for solid fuels - testing with south african coal. *Fuel*, 87(12):2713 – 2726, 2008.

[17] S. Bhavsar, M. Najera, R. Solunke, and G. Veser. Chemical looping: To combustion and beyond. *Catalysis Today*, 228:96 – 105, 2014.

[18] BP. Bp statistical review of world energy. Technical report, BP, 2014.

[19] S. Chapman and T.G. Cowling. *The Mathematical Theory of Non-Uniform Gases*. Cambridge University Press, Cambridge, 1970.

[20] J.W. Chew, R. Hays, J.G. Findlay, T.M. Knowlton, S.B. Reddy Karri, R.A. Cocco, and C.M. Hrenya. Cluster characteristics of geldart group b particles in a pilot-scale {CFB} riser. ii. polydisperse systems. *Chemical Engineering Science*, 68(1):82 – 93, 2012.

[21] S. Chiba, A.W. Nienow, T. Chiba, and H. Kobayashi. Fluidised binary mixtures in which the denser component may be flotsam. *Powder Technology*, 26(1):1 – 10, 1980.

[22] V. Ciais, R. Martin, H. Neau, and O. Simonin. 3d multiparticle simulation of volcanic dome collapse and pyroclastic flow: Application to 1984 and 1994 events at merapi volcano. In *7th International Conference on Multiphase Flow, ICMF 2010, Tampa, FL, May 30 - June 4*, 2007.

[23] J.S. Dahler and N.F. Sather. Kinetic theory of loaded spheres. *J. Chem. Physics*, 42:3445–3475, 1963.

[24] M. Das, B.C. Meikap, and R.K. Saha. Characteristics of axial and radial segregation of single and mixed particle system based on terminal settling velocity in the riser of a circulating fluidized bed. *Chemical Engineering Journal*, 145(1):32 – 43, 2008.

[25] S. Dasgupta, R. Jackson, and S. Sundaresan. Gas-particle flow invertical pipes with high mass loading of particles. *Powder Technology*, 96:6 – 23, 1998.

[26] F. Luis de Diego, F. Garcia-Labiano, P. Gayàn, J. Celaya, J.M. Palacios, and J. Adànez. Operation of a 10 kwth chemical-looping combustor during 200 h with a cuo-al2o3 oxygen carrier. *Fuel*, 86:1036 – 1045, 2007.

[27] L.F. de Diego, F. Garcia-Labiano, J. Adànez, P. Gayàn, A. Abad, B.M. Corbella, and J.M. Palacios. Development of cu-based oxygen carriers for chemical-looping combustion. *Fuel*, 83(13):1749 – 1757, 2004.

[28] M.A. Van der Hoef, R. Beetstra, and J.A.M. Kuipers. Lattice-boltzmann simulations of low-reynolds-number flow past mono- and bidisperse arrays of spheres: results for the permeability and drag force. *Journal of Fluid Mechanics*, 528:233–254, 4 2005.

[29] J. Ding and D. Gidaspow. A bubbling fluidization model using kinetic theory of granular flow. *AIChE Journal*, 36(4):523–538, 1990.

[30] R. G. Edwin and K.L. Warren. Production of pure carbon dioxide, January 12 1954. US Patent 2,665,972.

[31] EIA. Annual energy outlook with projection to 2040. Technical report, EIA, 2014.

[32] S. Ergun. Fluid flow through packed columns. *Chemical Engineering Progress*, 48:89–94, 1952.

[33] A. Fabre. *Etude de l'hydrodynamique sur un lit fluidisé circulant déchelle industrielle*. PhD thesis, 1995.

[34] R. Fan and R.O. Fox. Segregation in polydisperse fluidized beds: Validation of a multi-fluid model. *Chemical Engineering Science*, 63(1):272–285, 2008.

[35] P. Fede and O. Simonin. Application of a perturbated two-maxwellian approach for the modelling of kinetic stress transfer by collision in non-equilibrium binary mixture of inelastic particles. In *7th Int. Symp. on Gas-Particle Flows, ASME FEDSM2005-77127*, Houston, TX, USA, June 19-23 2005.

[36] P. Fede, O. Simonin, and I. Ghouila. 3d numerical simulation of polydisperse pressurized gas-solid fluidized bed. In *ASME-JSME-KSME 2011 Joint Fluids Engineering Conference*, pages 3199–3210. American Society of Mechanical Engineers, 2011.

[37] P. Fede, O. Simonin, and I. Ghouila. 3D numerical simulation of polydisperse pressurized gas-solid fluidized bed. In *Proceedings of AJK2011-FED, ASME-JSME-KSME Joint Fluids Engineering Conference 2011, July 24-29, 2011, Hamamatsu, Shizuoka, JAPAN*, 2011.

[38] J.D. Figueroa, Timothy Fout, Sean Plasynski, Howard McIlvried, and Rameshwar D. Srivastava. Advances in {CO2} capture technology the u.s. department of energy's carbon sequestration program. *International Journal of Greenhouse Gas Control*, 2(1):9 – 20, 2008.

[39] F. Fotovat, R. Ansart, M. Hemati, O. Simonin, and J. Chaouki. Sand-assisted fluidization of large cylindrical and spherical biomass particles: Experiments and simulation. *Chemical Engineering Science*, 126:543–559, 2015.

[40] R.O. Fox. On multiphase turbulence models for collisional fluid–particle flows. *Journal of Fluid Mechanics*, 742:368–424, 2014.

[41] D. Geldart. Types of gas fluidization. *Powder Technology*, 7:285–292, 1973.

[42] M. Germano. A proposal for a redefinition of the turbulent stresses in the filtered navier-stokes equations. *Phys. Fluids*, 29:2323–2324, 1986.

[43] M. Germano, U. Piomelli, P. Moin, and W.H. Cabot. A dynamic subgrid-scale eddy viscosity model. *Phys. of Fluids*, 3(7):1760–1765, 1991.

[44] D. Gidaspow. *Multiphase flow and fluidization: continuum and kinetic theory descriptions*. Academic press, 1994.

[45] D. Gidaspow, L. Huilin, and E. Manger. Kinetic theory of multiphase flow and fluidization: validation and extension to binary mixture. In *Nineteenth Int. Cong. of Theoretical and Appl. Mech., August, Kyoto, Japan,*, 1996.

[46] A. Gobin, H. Neau, O. Simonin, V. Reiling J.R. Llinas, and J.L. S élo. Phase polymerisation reactor. *International Journal for Numerical Methods in Fluids*, 43(2):1199–1220, 2003.

[47] A. Gobin, H. Neau, O. Simonin, J. R. Llinas, V. Reiling, and J. L. Sélo. Fluid dynamic numerical simulation of a gas phase polymerisation reactor. *International Journal for Numerical Methods in Fluids*, 43:1199–1220, 2003.

[48] C. Gourdel. *Modélisation et Simulations de Mélange Binaires de Particules En Interaction Avec un Champ Fluide Turbulent Pour L'application Aux Lits Fluidisés Circulants*. PhD thesis, Université de Technologie de Compiègne, 1999.

[49] C. Gourdel, O. Simonin, and E. Brunier. Modelling and simulation of gas-solid turbulents flows with a binary mixture of particles. In *Third International Conference on Multiphase Flow*, Lyon, France, 1998. ICFM'98.

[50] C. Gourdel, O. Simonin, and E. Brunier. Two-maxwellian equilibrium distribution function for the modelling of a binary mixture of particles. In *Proc. of the 6th Int. Conference on Circulating Fluidized Beds, Circulating Fluidized Bed Technology VI*, pages 205–210. J. Werther (Editor), DECHEMA, Frankfurt am Main, (Germany), 1999.

[51] H. Hasimoto. On the periodic fundamental solutions of the stokes equations and their application to viscous flow past a cubic array of spheres. *Journal of Fluid Mechanics*, 5(02):317–328, 1959.

[52] R.K. Helen. Chapter 38 - capture and separation technology gaps and priority research needs. In David C. Thomas, editor, *Carbon Dioxide Capture for Storage in Deep Geologic Formations*, pages 655 – 660. Elsevier Science, Amsterdam, 2005.

[53] R.J. Hill, D.L. Koch, and A.J.C. Ladd. The first effects of fluid inertia on flows in ordered and random arrays of spheres. *Journal of Fluid Mechanics*, 448:213–241, 2001.

[54] R.J. Hill, D.L. Koch, and A.J.C. Ladd. Moderate-reynolds-number flows in ordered and random arrays of spheres. *Journal of Fluid Mechanics*, 448:243–278, 2001.

[55] B. Hirschberg and J. Werther. Factors affecting solids segregation in circulating fluidized-bed riser. *AIChE Journal*, 44(1):25–34, 1998.

[56] W. Holloway, S. Benyahia, CM. Hrenya, and S. Sundaresan. Meso-scale structures of bidisperse mixtures of particles fluidized by a gas. *Chemical engineering science*, 66(19):4403–4420, 2011.

[57] W. Holloway and S. Sundaresan. Filtered models for bidisperse gas-particle flows. *Chemical Engineering Science*, 108:67–86, 2014.

[58] K. Horiuti. A new dynamic two-parameter mixed model for large-eddy simulation. *Physics of Fluids*, 9(11):3443–3464, 1997.

[59] L. Huilin and D. Gidaspow. Hydrodynamics of binary fluidization in a riser: Cfd simulation using two granular temperatures. *Chemical Engineering Science*, 58:3777 – 3792, 2003.

[60] L. Huilin, L. Wenti, B. Rushan, Y. Lidan, and D. Gidaspow. Kinetic theory of fluidized binary granular mixtures with unequal granular temperature. *Phys. A*, 284:265–276, 2000.

[61] IEA. Key world energy statistics. Technical report, International Energy Agency, 2012.

[62] Y. Igci, A.T. Andrews, S. Sundaresan, S. Pannala, and T. O'Brien. Filtered two-fluid models for fluidized gas-particle suspensions. *AIChE Journal*, 54:1431–1448, 2008.

[63] Y. Igci and S. Sundaresan. Verification of filtered two-fluid models for gas-particle flows in risers. *AIChE Journal*, 57(10):2691–2707, 2011.

[64] M. Ishida and J. Hongguang. A new advanced power-generation system using chemical-looping combustion. *Energy*, 19(4):415 – 422, 1994.

[65] M. Ishida and H. Jin. A novel chemical-looping combustor without nox formation. *Industrial & engineering chemistry research*, 35(7):2469–2472, 1996.

[66] M Ishida and H Jin. {CO2} recovery in a power plant with chemical looping combustion. *Energy Conversion and Management*, 38, Supplement:S187 – S192, 1997. Proceedings of the Third International Conference on Carbon Dioxide Removal.

[67] M. Ishida, D. Zheng, and T. Akehata. Evaluation of a chemical-looping-combustion power-generation system by graphic exergy analysis. *Energy*, 12(2):147 – 154, 1987.

[68] J.T. Jenkins and F. Mancini. Kinetic theory for binary mixtures of smooth, nearly elastic spheres. *Phys. of Fluids*, 12:2050–2057, 1989.

[69] A. Konan., H. Neau, O. Simonin, M. Dupoizat, and T. Le Goaziou. Reactive multiphase flow simulation of uranium hexafluoride conversion reactor. In *7th International Conference on Multiphase Flow, ICMF 2010, Tampa, FL, May 30 - June 4*, Tampa, FL, May 30 - June 4 2010.

[70] J.A.M. Kuipers and W.P.M. Van Swaaij. Computational fluid dynamics applied to chemical reaction engineering. *Advances in chemical engineering*, 24:227–328, 1998.

[71] D. Kunii and O. Levenspiel. *Fluidization Engineering*. Butterworth Heinemann, 1991.

[72] D. Lathouwers and J. Bellan. Modeling and simulation of bubbling fluidized beds containing particles mixture. In *Proceedings of the Combustion Institute*, volume 28, pages 2297–2304. ASME FED, 2000.

[73] W. Layton and R. Lewandowski. A simple and stable scale-similarity model for large eddy simulation: Energy balance and existence of weak solutions. *Applied Mathematics Letters*, 16(8):1205 – 1209, 2003.

[74] H. Leion, T. Mattisson, and A. Lyngfelt. Solid fuels in chemical-looping combustion. *International Journal of Greenhouse Gas Control*, 2(2):180–193, 2008.

[75] D.K. Lilly. A proposed modification of the germano subgrid scale closure method. *Phys. Fluids A*, 4:633–635, 1992.

[76] M. Liu, J. Li, and M. Kwauk. Application of the energy-minimization multiscale method to gas–liquid–solid fluidized beds. *Chemical Engineering Science*, 56(24):6805–6812, 2001.

[77] S. Liu, C. Menauvau, and J. Katz. On the properties of similarity subgrid-scale models as deduced from measurements in a turbulent jet. *Journal of Fluid Mechanics*, 275:83–119, 1994.

[78] B. Lu, W. Wang, and J. Li. Searching for a mesh-independent sub-grid model for cfd simulation of gas-solid riser flows. *Chemical Engineering Science*, 64:3437 – 3447, 2009.

[79] B. Lu, N. Zhang, W. Wang, J. Li, J.H. Chiu, and S.G. Kang. 3-d full-loop simulation of an industrial-scale circulating fluidized-bed boiler. *AIChE Journal*, 59(4):1108–1117, 2013.

[80] C.K.K. Lun and S.B. Savage. The effetcs of an impact velocity dependent coefficient of restitution on stresses developed by sheared granular materials. *Acta Mechanica*, 63:539–559, 1986.

[81] A. Lyngfelt. Chemical-looping combustion of solid fuels. *Applied Energy*, 113(0):1869 – 1873, 2014.

[82] A. Lyngfelt, B. Kronberger, J. Adànez, J.X. Morin, and P. Hurst. The grace project. development of oxygen carrier particles for chemical-looping combustion, design and operation of a 10 kw chemical-looping combustor. In *Proc 7th Int Conf Greenhouse Gas Control Technology (GHGT-7)*, Vancouver, Canada; 2004.

[83] E. Manger. *Modeling and simualtion of gas solid systmes in curvulinear coordinates*. PhD thesis, Telemark Institute of technology, 1996.

[84] A. Massol. *Simulations numériques d'écoulements à travers des réseaux fixes de sphères monodisperses et bidisperses, pour des nombres de Reynolds modérés*. PhD thesis, INPT - CERFACS, 2004.

[85] V. Mathiesen, T. Solberg, and B.H. Hjertager. An experimental and computational study of multiphase flow behavior in a circulating fluidized bed. *International Journal of Multiphase Flow*, 26(3):387 – 419, 2000.

[86] Vidar Mathiesen, Tron Solberg, Hamid Arastoopour, and Bjørn H Hjertager. Experimental and computational study of multiphase gas/particle flow in a cfb riser. *AIChE journal*, 45(12):2503–2518, 1999.

[87] T. Mattisson, A. Lyngfelt, and H.Leion. Chemical-looping with oxygen uncoupling for combustion of solid fuels. *International Journal of Greenhouse Gas Control*, 3(1):11 – 19, 2009.

[88] C.C. Milioli and F.E. Milioli. On the accuracy of two-fluid model predictions for a particular gas–solid riser flow. *Applied Mathematical Modelling*, 34(3):684 – 696, 2010.

[89] A. Miller and D. Gidaspow. Dense, vertical gas-solid flow in a pipe. *AIChE Journal*, 38:1801–1815, 1992.

[90] S. Morioka and T. Nakajima. Modeling of gas and solid particles two-phase flow and application to fluidized bed. *Journal of Theoretical and Applied Mechanics*, 6:77–88, 1987.

[91] H. Neau, P. Fede, J. Laviéville, and O. Simonin. High performance computing (hpc) for the fluidization of particle-laden reactive flows. In *The 14th International Conference on Fluidization - From Fundamentals to Products*, 2013.

[92] H. Neau, J. Laviéville, and O. Simonin. Neptune_CFD high parallel computing performances for particle-laden reactive flows. In *7th International Conference on Multiphase Flow, ICMF 2010, Tampa, FL, May 30 - June 4*, 2010.

[93] A. Neri and D. Gidaspow. Riser hydrodynamics: simulation using kinetic theory. *AIChE Journal*, 46(1):52–67, 2000.

[94] J.J. Nieuwland, M. van Sint Annaland, J.A.M. Kuipers, and W.P.M. Van Swaaij. Hydrodynamic modeling of gas/particle flows in riser reactors. *AIChE Journal*, 42(6):1569–1582, 1996.

[95] N. Nouyrigat. *Hydrodynamic modeling of poly-solid recative circulating fluidized beds: Application to Chemical Looping Combustion*. PhD thesis, M écanique, Energétique, Génie Civil et Procédéc (MEGeP), 2012.

[96] A. Ozel. *Simulation aux grandes échelles des lits fluidises circulant gaz-particule*. PhD thesis, Ecole doctorale Mécanique, Energétique, énie Civil et Procédés, 2011.

[97] A. Ozel, P. Fede, and O. Simonin. The effective drag closure for gas-solid flows in vertical risers. In *Aiche Meeting, Annual Meeting, Nashville, TN*, 2009.

[98] A. Ozel, P. Fede, and O. Simonin. Development of filtered euler–euler two-phase model for circulating fluidised bed: high resolution simulation, formulation and a priori analyses. *International Journal of Multiphase Flow*, 55:43–63, 2013.

[99] A. Ozel, P. Fede, and O. Simonin. Development of filtered euler-euler two-phase model for circulating fluidised bed: High resolution simulation, formulation and a priori analyses. *International Journal of Multiphase Flow*, 55:43 – 63, 2013.

[100] A. Ozel, P. Fede, and O. Simonin. Effect of unresolved structures on the euler-euler simulation of 3d periodic circulating fluidized of binary mixture. In *8th International Conference on Multiphase Flow, ICMF 2013, Jeju, Korea, May 26 - 31*, 2013.

[101] J.F. Parmentier. *Extension du formalisme Euler/Euler pour la simulation des lit fluidisés de particules du ggroup A dans la classification de Geldart*. PhD thesis, Mécanique, Energétique, Génie Civil et Procédés (MEGEP), 2010.

[102] J.F. Parmentier, O. Simonin, and O. Delsart. A numerical study of fluidization behavior of geldart B, A/B and A particles using an Eulerian multifluid modeling approach. In *Proc. of the 9th Int. Conference on Circulating Fluidized Beds*, pages 331–336. Circulating Fluidized Bed Technology IX, Mai 2008.

[103] J.F. Parmentier, O. Simonin, and O. Delsart. A functional subgrid drift velocity model for filtered drag prediction in dense fluidized bed. *AIChE Journal*, pages 1–15, 2011.

[104] G. Patino. *Modélisation numérique eulérienne des écoulements gaz-solide avec plusieurs espèces de particules*. PhD thesis, Institut National Polytechnique de Toulouse, 2007.

[105] G. Patino and O. Simonin. General derivation of eulerian-eulerian equations for multiphase flows. Technical report, IMFT, 2003. Rapport Interne.

[106] G. Petit. *Contribution A L'etude Experimentale Et Numerique du Comportement Des Phases Gaz Et Solide Dans Un Lit Fluidise Circulant: Application Au Procede FCC*. PhD thesis, 2005.

[107] T.S. Pugsley and F. Berruti. A predictive hydrodynamic model for circulating fluidized bed risers. *Powder Technology*, 89(1):57–69, 1996.

[108] Mohammad Fardausur Rahaman, Jamal Naser, and PJ Witt. An unequal granular temperature kinetic theory: description of granular flow with multiple particle classes. *Powder Technology*, 138(2):82–92, 2003.

[109] M.W. Reeks. On a kinetic equation for the transport of particles in turbulent flows. *Phys. of Fluids*, 3(3):446–456, 1991.

[110] M. Rhodes, M. Hideaki, and H. Toshimasa. Particle motion at the wall of a circulating fluidized bed. *Powder Technology*, 70(3):207 – 214, 1992.

[111] H.J. Richter and K.F. Knoche. Reversibility of combustion process. In *Efficiency and costing, second law analysis of process. ACS Symposium Series, vol. 235. Washington DC: American Chemical Society; 1983. p.*, 1983.

[112] S.S. Rodrigues. *Riser hydrodynamic study with Group B particles for Chemical Looping Combustion*. PhD thesis, Université Claude Bernard-Lyon I, 2014.

[113] M. Rydèn and A. Lyngfelt. Using steam reforming to produce hydrogen with carbon dioxide capture by chemical-looping combustion. *International Journal of Hydrogen Energy*, 31(10):1271 – 1283, 2006.

[114] A.S. Sangani and A. Acrivos. Slow flow through a periodic array of spheres. *International Journal of Multiphase Flow*, 8(4):343–360, 1982.

[115] A.S. Sangani, G. Mo, H.K. Tsao, and D.L. Koch. Simple shear flows of dense gas-solid suspensions at finite stokes numbers. *Journal of Fluid Mechanics*, 313:309–341, 1996.

[116] S. Sarkar, M.A. Van der Hoef, and J.A.M. Kuipers. Fluid–particle interaction from lattice boltzmann simulations for flow through polydisperse random arrays of spheres. *Chemical Engineering Science*, 64(11):2683–2691, 2009.

[117] L. Schiller and A. Nauman. A drag coefficient correlation. *V.D.I. Zeitung*, 77:318–320, 1935.

[118] S. Schneiderbauer, S. Puttinger, and S. Pirker. Comparative analysis of subgrid drag modifications for dense gas-particle flows in bubbling fluidized beds. *AICAIChe,59:4077-4099*, 2013.

[119] S. Schneiderbauer, D. Schellander, A. Löderer, and S. Pirker. Non-steady state boundary conditions for collisional granular flows at flat frictional moving walls. *International Journal of Multiphase Flow*, 43:149–156, 2012.

[120] A.K. Sharma, K. Tuzla, J. Matsen, and J.C. Chen. Parametric effects of particle size and gas velocity on cluster characteristics in fast fluidized beds. *Powder Technology*, 111(1-2):114 – 122, 2000.

[121] O. Simonin. Combustion and turbulence in two-phase flows. In *Lecture Series 1996-02*. Von Karman Institute for Fluid Dynamics, 1996.

[122] O. Simonin. Statistical and continuum modelling of turbulent reactive particulate flows. part 1 : Theoretical derivation of dispersed eulerian modelling from probability density function kinetic equation. In *Lecture Series 2000-06, Von Karman Institute for Fluid Dynamics, Rhodes Saint Genèse (Belgium)*. Von Karman Institute for Fluid Dynamics, 2000.

[123] O. Simonin, S. Chevrier, F. Audard, and P. Fede. Drag force modelling in dilute to dense particle-laden flows with mono-disperse or binary mixture of solid particles. In *9th International Conference on Multiphase Flow, ICMF 2010, Italy*, 2016.

[124] O. Simonin, P. Février, and J. Laviéville. On the spatial distribution of heavy particle velocities in turbulent flow : From continuous field to particulate chaos. *Journal of Turbulence*, 3(040):1 – 18, 2002.

[125] J. L. Sinclair and R. Jackson. Gas-particle flow in a vertical pipe with particle-particle interactions. *AIChE Journal*, 35:1473–1486, 1989.

[126] A.M. Squires, M. Kwauk, and A.A. Avidan. Fluid beds: at last, challenging two entrenched practices. *Science*, 230(4732):1329–1337, 1985.

[127] W. Stöber, A. Fink, and E. Bohn. Controlled growth of monodisperse silica spheres in the micron size range. *Journal of colloid and interface science*, 26(1):62–69, 1968.

[128] S. Sundaresan. Modeling the hydrodynamics of multiphase flow reactors: current status and challenges. *AIChE Journal*, 46(6):1102–1105, 2000.

[129] S. Tenneti, R. Garg, and S. Subramaniam. Drag law for monodisperse gas–solid systems using particle-resolved direct numerical simulation of flow past fixed assemblies of spheres. *International journal of multiphase flow*, 37(9):1072–1092, 2011.

[130] M.B. Toftegaard, J. Brix, P.A. Jensen, P. Glarborg, and A.D. Jensen. Oxy-fuel combustion of solid fuels. *Progress in energy and combustion science*, 36(5):581–625, 2010.

[131] H.K. Tsao and D.L. Koch. Simple shear flows of dilute gas–solid suspensions. *Journal of Fluid Mechanics*, 296:211–245, 1995.

[132] M van Sint Annaland, GA Bokkers, MJV Goldschmidt, OO Olaofe, MA Van Der Hoef, and JAM Kuipers. Development of a multi-fluid model for poly-disperse dense gas–solid fluidised beds, part i: model derivation and numerical implementation. *Chemical Engineering Science*, 64(20):4222–4236, 2009.

[133] S. Vincent, J.C.B. De Motta, A. Sarthou, J.L. Estivalezes, O. Simonin, and E. Climent. A lagrangian vof tensorial penalty method for the dns of resolved particle-laden flows. *Journal of Computational Physics*, 256:582–614, 2014.

[134] B.G.M. Van Wachem, J.C. Schouten, C.M. Van den Bleek, R. Krishna, and J.L. Sinclair. Cfd modeling of gas-fluidized beds with a bimodal particle mixture. *AIChE Journal*, 47(6):1292–1302, 2001.

[135] J. Wang. A review of eulerian simulation of geldart a particles in gas-fluidized beds. *Industrial & Engineering Chemistry Research*, 48(12):5567–5577, 2009.

[136] J. Wang, W. Ge, and J. Li. Eulerian simulation of heterogeneous gas-solid flows in cfb risers: Emms-based sub-grid scale model with a revised cluster description. *Chemical Engineering Science*, 63(6):1553–1571, 2008.

[137] W. Wang and J. Li. Simulation of gas-solid two-phase flow by a multi-scale cfd approach of the emms model to the sub-grid level. *Chemical Engineering Science*, 62(1):208–231, 2007.

[138] W. Wang, B. Lu, N. Zhang, Z. Shi, and J. Li. A review of multiscale cfd for gas–solid cfb modeling. *International Journal of Multiphase Flow*, 36(2):109–118, 2010.

[139] Y.C. Wen and Y.H. Yu. Mechanics of fluidization. *Chemical Engineering Symposium Series*, 62:100–111, 1965.

[140] J. Werther and J. Wein. Expansion behavior of gas fluidized bed in the turbulent regime. *AIChE Journal*, 90:31–44, 1994.

[141] J. Wang X. Chen and J. Li. Coarse grid simulation of heterogeneous gas solid flow in a cfb riser with polydisperse particles. *Chemical Engineering Journal*, 234:173 – 183, 2013.

[142] G. Xu and J. Li. Multi scale interfacial stresses in heterogeneous particle fluid systems. *Chemical Engineering Science*, 53(18):3335 – 3339, 1998.

[143] Y. Yamamoto, M. Potthoff, T. Tanaka, T. Kajishima, and Y. Tsuji. Large-eddy simulation of turbulent gas-particle flow in a vertical channel: effect of considering inter-particle collisions. *J. Fluid Mech.*, 442:303–334, 2001.

[144] H. Yang and M. Gautam. Experimental study on the interface of core-annulus flow in the riser of a circulating fluidized bed. *Powder Technology*, 85(1):57 – 64, 1995.

[145] W.C. Yang. *Handbook of fluidization and fluid-particle systems*. CRC press, 2003.

[146] W.C. Yang. Modification and re-interpretation of geldart's classification of powders. *Powder Technology*, 171(2):69 – 74, 2007.

[147] J.G. Yates and D. Newton. Fine particle effects in a fluidized-bed reactor. *Chemical engineering science*, 41(4):801–806, 1986.

[148] Y. Yang Y.F. Zhang and H. Arastoopour. Electrostatic effect on the flow behavior of a dilute gas/cohesive particle flow system. *AIChE journal*, 42(6):1590–1599, 1996.

[149] X. Yin and S. Sundaresan. Fluid-particle drag in low-reynolds-number polydisperse gas-solid suspensions. *AIChE Journal*, 55:1352–1368, 2009.

[150] L. I. Zaichik and A. A. Vinberg. Modelling of particle dynamics and heat transfer in turbulent flows using equations for first and second moments of velocity and temperature fluctuations. In *8th Int. Symp. on Turbulent Shear Flows*, volume 1, pages 1021–1026, Munich, 1991.

[151] L.I. Zaichik, P. Fede, O. Simonin, and V.M. Alipchenkov. Statistical models for predicting the effect of bidisperse particle collisions on particle velocities and stresses in homogeneous anisotropic turbulent flows. *International Journal of Multiphase Flow*, 35:868–878, 2009.

[152] D.Z. Zhang and W.B. VanderHeyden. High-resolution three-dimensional numerical simulation of a circulating fluidized bed. *Powder Technology*, 116:133–141, 2001.

[153] D.Z. Zhang and W.B.VanderHeyden. The effects of mesoscale structures on the macroscopic momentum equation for two-phase flows. *International Journal of Multiphase Flow*, 28(5):805 – 822, 2002.

[154] S.J Zhang and A.B Yu. Computational investigation of slugging behaviour in gas-fluidised beds. *Powder Technology*, 123(2-3):147 – 165, 2002.